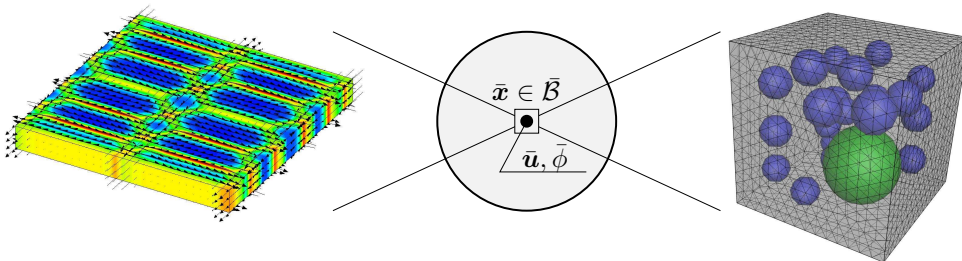


Variational Homogenization in Electro-Mechanics: From Micro-Electro-Elasticity to Electroactive Polymers

Dominic Zäh



$$\bar{\pi}^\tau(\bar{\boldsymbol{\varepsilon}}, \bar{\varphi}) = \inf_{\tilde{\boldsymbol{u}}} \sup_{\tilde{\phi}} \inf_P \frac{1}{|\mathcal{B}|} \int_{\mathcal{B}} \pi^\tau(\bar{\boldsymbol{\varepsilon}} + \nabla_s \tilde{\boldsymbol{u}}, \bar{\varphi} - \nabla \tilde{\phi}, P, \nabla P) dV$$

Bericht Nr.: I-32 (2014)
Institut für Mechanik (Bauwesen), Lehrstuhl I
Professor Dr.-Ing. C. Miehe
Stuttgart 2014

Variational Homogenization in Electro-Mechanics: From Micro-Electro-Elasticity to Electroactive Polymers

Von der Fakultät Bau- und Umweltingenieurwissenschaften der Universität Stuttgart
und dem Stuttgart Research Center for Simulation Technology
zur Erlangung der Würde eines Doktor-Ingenieurs (Dr.-Ing.)
genehmigte Abhandlung

von

Dominic Zäh

aus Bönningheim

Hauptberichter: Prof. Dr.-Ing. C. Miehe

Mitberichter: Prof. Dr.-Ing. P. Steinmann

Tag der mündlichen Prüfung: 31. Oktober 2014

Institut für Mechanik (Bauwesen) der Universität Stuttgart

2014

Herausgeber:

Prof. Dr.-Ing. habil. C. Miehe

Organisation und Verwaltung:

Institut für Mechanik (Bauwesen)

Lehrstuhl I

Universität Stuttgart

Pfaffenwaldring 7

70569 Stuttgart

Tel.: +49 (0)711 685-66378

Fax: +49 (0)711 685-66347

© Dominic Zäh
Institut für Mechanik (Bauwesen)
Lehrstuhl I
Universität Stuttgart
Pfaffenwaldring 7
70569 Stuttgart
Tel.: +49 (0)711 685-66326
Fax: +49 (0)711 685-66347

Alle Rechte, insbesondere das der Übersetzung in fremde Sprachen, vorbehalten. Ohne Genehmigung des Autors ist es nicht gestattet, dieses Heft ganz oder teilweise auf fotomechanischem Wege (Fotokopie, Mikrokopie) zu vervielfältigen.

ISBN 3-937859-20-9 (D 93 Stuttgart)

Acknowledgements

The present work is the result of my occupation at the Institute of Applied Mechanics (Civil Engineering) at the University of Stuttgart. I would like to acknowledge the great enthusiasm and commitment of my supervisor Prof. Dr.-Ing. Christian Miehe, the numerous fruitful discussions, his support and guidance in academic matters that contributed decisively to the successful completion of this work. He gave me the opportunity to work in his group and to deal with interesting and advanced research topics. I also would like to thank him for accepting the main referee position. A sincere thank you goes to Prof. Dr.-Ing. Paul Steinmann for his acceptance to become co-referee for this doctoral thesis and I am grateful for his constructive criticism as well as interest in this work.

Furthermore, I would like to thank all my colleagues from both chairs of the Institute of Applied Mechanics for the fruitful discussions, collaborations, and friendly working atmosphere. A particular thank you goes to my roommate Lisa Schänzel for her patience, support, and readiness to help during the last years. Additionally, I would like to convey my gratitude to my current and former colleagues Gautam Ethiraj, Steffen Mauthe, Daniele Rosato, and Fabian Welschinger for discussions and the help in many scientific questions. I am very grateful to Fadi Aldakheel and Daniel Vallicotti who provided me with significant support to my dissertation through their master theses. The supervision of these works was a true pleasure. I would also like to gratefully acknowledge the financial support of this work through the German Research Foundation (DFG) within the SimTech Cluster of Excellence (EXC 310/1).

Moreover, I would like to thank my girlfriend Alexandra Tittes for the motivation she provided and especially her patience during the last years. I am truly grateful to my father and my brother, Dittmar and Manuel, for their care and encouragement during the last decade. Despite difficult times that we lived through, it has always been possible for me to come home, where I received the support I needed.

Stuttgart, October 2014

Dominic Zäh

Table of Contents

Abstract	v
Zusammenfassung	ix
1. Introduction	1
1.1. Electro-mechanical coupling phenomena	1
1.2. Multiscale approaches and computational homogenization	3
1.3. Objectives and overview	6
2. Micromechanical Motivation	9
2.1. Piezoelectricity	9
2.2. Piezoceramics	11
2.3. Electroactive polymers	15
I Fundamentals of Electro-Mechanics and Homogenization	
3. Foundations of Continuum Mechanics and Electrostatics	21
3.1. Fundamentals of continuum mechanics	21
3.1.1. Motion of a material body	22
3.1.2. The deformation gradient	22
3.1.3. The Cauchy-Green strain tensors	23
3.1.4. Velocity gradient and Lie derivative	24
3.1.5. The concept of mechanical stresses	25
3.1.6. Mechanical power expressions	26
3.2. Fundamentals of electrostatics	27
3.2.1. Coulomb's and Faraday's law	27
3.2.2. The Gauss law of electrostatics	29
3.2.3. The electric field in matter	30
3.2.4. Boundary conditions at interfaces	32
3.2.5. Balance laws of coupled electro-mechanics	33
3.2.6. Electric force, couple, and energy supply	34
3.2.7. The concept of total stress	36

3.2.8.	Geometrical transformations	37
3.2.9.	Electrical power expressions	37
4.	The Concept of Micro-to-Macro Transition	39
4.1.	The concept of representative volume elements	40
4.2.	The problem of homogenization: A brief introduction	41
4.3.	Variational bounds on effective properties	43
4.4.	Fundamental averaging theorems of electro-mechanics	46
4.5.	The Hill-Mandel macrohomogeneity condition	46
 II Micro-Electro-Elasticity at Small Strains		
5.	Variational-Based Modeling of Micro-Electro-Elasticity	53
5.1.	Basic functionals in micro-electro-elasticity	55
5.1.1.	Displacement, polarization, and electric potential	55
5.1.2.	Boundary conditions and loading functionals	56
5.1.3.	Objective state variables: Theory of grade one	58
5.1.4.	Energy-enthalpy and dissipation potential functionals	58
5.1.5.	The energy-enthalpy function of micro-electro-elasticity	61
5.1.6.	Dissipation potential for micro-electric evolution	61
5.2.	Variational formulations of micro-electro-elasticity	61
5.2.1.	Variational formulation for stationary problems	62
5.2.2.	Variational formulation for dynamic problems	63
5.3.	Discrete incremental variational formulations	64
5.3.1.	Time-discrete field variables in incremental setting	64
5.3.2.	Time-discrete incremental variational principle	65
5.3.3.	Space-time-discrete incremental variational principle	66
5.4.	Representative numerical examples	68
5.4.1.	Definition of the boundary-value-problem	69
5.4.2.	Construction of an initial equilibrium state	70
5.4.3.	Electric field driven loading processes	70
5.4.4.	Stress driven loading process	73
6.	Computational Homogenization in Dissipative Electro-Mechanics	75
6.1.	Variational homogenization of micro-electro-elasticity	77
6.1.1.	Introduction of microscopic fields	77
6.1.2.	Microscopic rate-type variational principle of homogenization	78
6.1.3.	Microscopic incremental variational principle of homogenization	79
6.1.4.	Space-time discrete incremental variational principle	80
6.2.	Variational formulation of the macroscopic response	81

6.2.1.	Introduction of macroscopic fields	81
6.2.2.	Macroscopic incremental variational formulation	81
6.2.3.	Macroscopic space-time discrete incremental variational principle	83
6.3.	Generalized micro-to-macro transition	83
6.3.1.	Generalized macrohomogeneity condition	84
6.3.2.	Derivation of appropriate boundary conditions	85
6.3.3.	Deformation and electric field driven homogenization	86
6.4.	Representative numerical examples	90
6.4.1.	Analysis of different homogenization boundary conditions	90
6.4.2.	Homogenization analysis of polycrystalline aggregate	91
6.4.3.	Three-dimensional homogenization of thin single crystal	96

III Electroactive Polymers at Large Strains

7.	Multiplicative Electro-Elasticity of Electroactive Polymers	103
7.1.	General equations of finite electro-elasticity	105
7.1.1.	The variational principle and its Euler equations	105
7.1.2.	Finite element implementation of coupled problem	108
7.2.	Constitutive modeling of multiplicative electro-elasticity	111
7.2.1.	Ingredient 1: Additive split of energy-enthalpy density	111
7.2.2.	Ingredient 2: Volumetric-isochoric split of local deformation	111
7.2.3.	Ingredient 3: Local electrically-induced deformation	112
7.2.4.	Ingredient 4: Local isochoric elastic network kernel	112
7.2.5.	Ingredient 5: Local electrostatic contribution to the energy	113
7.2.6.	Stress and electric displacement with isochoric stress kernel	115
7.2.7.	The coupled electro-elastic tangent moduli	116
7.3.	Micromechanical kernel for elastic network response	116
7.4.	Representative numerical examples	119
7.4.1.	Model comparison and parameter identification	120
7.4.2.	Electroactive polymer as double-s-shaped actuator	121
7.4.3.	Electroactive polymer as starfish gripper	123
8.	Variational-Based Homogenization of Electro-Elasticity	125
8.1.	Variational formulation of the homogenization problem	127
8.1.1.	Constraints on fine-scale fluctuation fields	127
8.1.2.	Variational formulation of the coupled homogenization problem	128
8.1.3.	Finite element solution of homogenization problem	129
8.1.4.	Generalized macro-stress and moduli	131
8.2.	Variational formulation of the macroscopic response	132
8.2.1.	Variational formulation of finite electro-mechanics	132

8.2.2. Finite element discretization of the macroscopic response	133
8.3. Infinitesimal material stability analysis	134
8.3.1. Material stability analysis of the energy formulation	134
8.3.2. Material stability analysis of the enthalpy formulation	135
8.4. FE ² driver for homogeneous macro-problems	137
8.5. Representative numerical examples	138
8.5.1. Energy-enthalpy density function	139
8.5.2. Volume fraction of the inclusion	141
8.5.3. Shape of the inclusion	141
8.5.4. Material limit point analysis	142
9. Conclusion	145
Bibliography	147

Abstract

In recent years an increasing interest in functional or smart materials such as ferroelectric polymers and ceramics has been shown. Regarding the technical implementation of smart systems a broad variety of physically-based phenomena and materials are available, where some of the most important coupling effects are the shape memory effect, magnetostriction, electrostriction, and piezoelectricity. Typical fields of application are adaptive or controlled systems such as actuators and sensors, micro-electro-mechanical systems (MEMS), fuel injectors for common rail diesel engines, ferroelectric random access memories, and artificial muscles used in robotics. A highly interesting class of these materials are piezoceramics, coming up with short response times, high precision positioning, relatively low power requirements, and high generative forces, providing an excellent opportunity for mass production. Typical examples of such materials are barium titanate and lead zirconate titanate crystals and polycrystals, which exhibit linear and nonlinear coupling phenomena as well as hysteresis under high cyclic loading. At the microscale level, these materials are composed of several homogeneously polarized regions, called ferroelectric domains, whose evolution in time is driven by external electric fields and stresses applied to a sample of the material. Ferroelectric domains are regions of parallel and hence aligned polarization. Electric poling can be achieved by the application of a sufficiently strong electric field, inducing the reorientation and alignment of spontaneous polarization. As a consequence, piezoceramics exhibit a macroscopic remanent polarization. On the other hand, there are electroactive polymers (EAPs) responding by a (possibly large) deformation to an applied electrical stimulus, an effect discovered by the physicist Wilhem Röntgen in 1880 in an experiment on a rubber strip subjected to an electric field. They are divided into two main groups: electronic and ionic materials. The description of these effects through models of continuum physics is a subject of extensive research. The theoretical foundations for the analysis of electro-mechanical interactions in dielectric solids can be traced back to TOUPIN [190, 189], ERINGEN [42], TIERSTEN [187], MAUGIN [110], ERINGEN & MAUGIN [43, 44], and KOVETZ [94]. Continuum models for ferroelectrics may be broadly classified into two categories: *Phenomenological models* for the macroscopic response, which do not resolve the domain patterns, and *micro-electric approaches*, which involve the explicit characterization of these specific microstructures.

Physically predictive material modeling can be performed on different length- and time scales. The classical setting of continuum mechanics develops phenomenological material models “smeared” over some continuously distributed material, where the material parameters are determined from experimental data. Nowadays developed multiscale techniques focus predominantly on the efficient bridging of neighboring length- and time scales, e.g. the incorporation of the microscopic polarization in order to predict macroscopic hysteresis phenomena. With a continuous increase in computational power and the development of efficient numerical solvers, real multiscale simulations seem to be a reachable goal. *Computational homogenization schemes* determine, in contrast to initially developed Voigt and Reuss bounds, the effective properties numerically. No constitutive model is explicitly assumed at the macroscale, and the material response at each point is determined by performing a separate numerical analysis at the micro-level. The macroscopic material behavior in this *two-scale scenario* is then determined by separate FE computations at the microscale. Main ingredients of such a framework are, on the one hand, the solution of a microscopic material model describing mechanical behavior at the representative vol-

ume element and, on the other hand, a homogenization rule determining the macroscopic stress tensor by its microscopic counterpart. Goal of these computational homogenization techniques is the modeling of the overall response based on well-defined microstructural information. We refer to HILL [65] and SUQUET [177] for fundamental principles of local mechanical response. Concerning the scale transition for *functional materials*, it is necessary to extend the homogenization principles to coupled problems, incorporating besides the mechanical displacement further primary variables such as the electric potential and the electric polarization. An overview of homogenization theories is given in NEMAT-NASSER & HORI [140], where the additional incorporation of non-mechanical properties such as thermal, magnetic, or electric effects was also concerned. The key aspect of every homogenization scheme is the determination of macroscopic quantities in terms of their microscopic counterpart, driven by appropriate constraints or boundary conditions on the representative volume element. The micro-to-macro transition can be described in a canonical manner by variational principles of homogenization, determining *macroscopic potentials* in terms of their microscopic counterparts. A rigorous application to variational-based homogenization and the development of boundary conditions is performed in MIEHE [116] for the pure mechanical case. ZÄH & MIEHE [207] developed a non-standard homogenization scheme bridging a dissipative phase field model of domain switching on the microscale to a standard macroscopic Boltzmann continuum. The concepts originally proposed by MIEHE [116] were used and extended to electro-mechanics by outlining Lagrange and penalty methods for the incorporation of boundary conditions in the variational principles.

This work outlines aspects of electro-mechanically coupled material models on different scales and the development of new *variational-based homogenization techniques*. An important issue is the numerical implementation of coupled problems. The discretization of the multifield problem appears, as a consequence of the proposed incremental variational principles, in a symmetric and very compact format. This dissertation is subdivided into three parts, where [Part I](#) governs fundamentals of continuum mechanics as well as electrostatics and briefly outlines basic principles of homogenization theory. In particular, two classes of materials are addressed: [Part II](#) deals with piezoceramics, that are numerically investigated by a small strain theory of *micro-electro-elasticity*. The dissipative response caused by polarization switching is described by a Ginzburg-Landau-type phase field model. The resultant domain structure is fully resolved by the model. New rate-type and incremental *variational principles* for the coupled evolution problem are outlined and details of the micro-to-macro transition by an extended Hill-Mandel macrohomogeneity condition discussed. The Euler equations of these variational principles are the static stress equilibrium condition, the electrostatic equilibrium condition, often denoted as the second Maxwell equation or the Gauss law, and a Ginzburg-Landau-type equation for the evolution of the polarization. An important aspect for the design of a variational homogenization method is the definition of suitable boundary conditions at the micro-level, which also includes the phase field of electric polarization. The three classical types of surface conditions are discussed and consistently transferred to the electro-mechanical context. In addition, they are incorporated into the variational functionals by means of Lagrange and penalty methods. Besides, [Part III](#) develops *finite strain material models* and bridging theorems for polymers. General equations of finite electro-elasticity in a variational format are reviewed, accounting for geometric settings in both the Lagrangian as well as the Eulerian configuration. We cover all details of the modeling process, including the set up

of coupled electro-mechanical tangent moduli by a numerical perturbation technique. In addition, a macroscopic driver for the homogenization problem is developed, accounting for the consistent algorithmic tangent on the macroscale. Homogeneous macro-tests are performed and the relevant data transferred to the microscale via the boundary conditions. An innovative driving of the electric displacement as compared to the electric field is performed, allowing us to avoid points of electro-mechanical instability.

Zusammenfassung

In den letzten Jahren wurde ein gesteigertes Interesse an funktionalen oder intelligenten Materialien wie ferroelektrischen Polymeren und Keramiken gezeigt. Für die technische Umsetzung steht ein großes Spektrum an physikalischen Phänomenen und Materialien zur Verfügung, wobei die wichtigsten Kopplungseffekte der Formgedächtnis-Effekt, Magnetostriktion, Elektrostriktion und Piezoelektrizität sind. Typische Einsatzbereiche solcher Materialien sind adaptive Systeme wie Sensoren und Aktoren, Mikrosysteme aus miniaturisierten Bauteilen (MEMS), Einspritzdüsen für Common-Rail-Dieselmotoren, ferroelektrische Arbeits- oder Hauptspeicher für Computersysteme und künstliche Muskeln im Bereich der Robotertechnik. *Piezokeramiken* sind aufgrund ihrer kurzen Reaktionszeiten, relativ geringen Leistungsanforderung und hohen generierten Kräften von großem industriellen Interesse. Daraus resultiert unter anderem eine ausgezeichnete Eignung für die Massenproduktion. Typische Beispiele sind Bariumtitanat und Blei-Zirkonat-Titanat Ein- und Mehrkristalle, welche lineare und nichtlineare Kopplungsphänomene aufweisen, sowie Hysteresekurven bei zyklischen Belastungsprozessen zeigen. Mikroskopisch betrachtet bestehen diese Werkstoffe aus mehreren homogen polarisierten Bereichen, den so genannten ferroelektrischen Domänen, deren zeitliche Entwicklung durch externe elektrische Felder und Spannungen getrieben wird. Domänen sind Bereiche mit gleicher Polarisationsrichtung der Einheitszellen. Die elektrische Polung, d.h. Neuausrichtung der spontanen Polarisation, kann durch anlegen eines hinreichend starken elektrischen Feldes erreicht werden. Als Folge weisen Piezokeramiken eine makroskopische remanente Polarisation auf. Des weiteren gibt es *elektroaktive Polymere* (EAPs) welche mit einer (möglicherweise großen) Verformung auf elektrische Stimulation reagieren. Dieser Effekt wurde vom Physiker Wilhelm Röntgen 1880 entdeckt, indem er in einem Experiment einen Gummistreifen einem elektrischen Feld ausgesetzt hat. Solche Werkstoffe werden im Allgemeinen in zwei Hauptgruppen unterteilt, die elektronischen und ionischen EAPs. Die Beschreibung dieser Effekte durch physikalische Modelle der Kontinuumsmechanik ist ein umfangreiches Forschungsthema. Die theoretischen Grundlagen für die Analyse der elektromechanischen Wechselwirkungen dielektrischer Festkörper werden auf die Arbeiten von TOUPIN [190, 189], ERINGEN [42], TIERSTEN [187], MAUGIN [110], ERINGEN & MAUGIN [43, 44] und KOVETZ [94] zurückgeführt. Daraus abgeleitete Modelle zur Beschreibung von Ferroelektrika können in zwei Kategorien eingeteilt werden: *phänomenologische Modelle* zur Beschreibung von makroskopischem Materialverhalten, welche die elektrischen Domänen nicht explizit auflösen und *mikroelektrische Ansätze*, die die charakteristischen Mikrostrukturen und deren zeitliche Evolution explizit beschreiben.

Eine physikalisch aussagekräftige Materialbeschreibung kann auf unterschiedlichen Zeit- und Längenskalen durchgeführt werden. Die klassische Kontinuumsmechanik entwickelt phänomenologische Materialmodelle, welche über ein kontinuierlich verteiltes Gebiet verschmiert sind. Die daraus resultierenden Materialparameter müssen durch experimentelle Untersuchungen bestimmt werden. Derzeit entwickelte Multiskalenansätze konzentrieren sich vorwiegend auf die effiziente Überbrückung benachbarter Skalen, z.B. die Berücksichtigung der mikroskopischen Polarisation um makroskopische hysteretische Effekte vorherzusagen. Mit stetiger Leistungszunahme moderner Computer sowie der Entwicklung effizienter numerischer Löser scheint die Verwirklichung von Mehrskalensimulationen ein erreichbares Ziel zu sein. *Computerbasierte Homogenisierungsverfahren* bestimmen, im Gegensatz zu den ursprünglich entwickelt Verfahren nach Voigt und Reuss, die

effektiven Eigenschaften numerisch. Auf der Makroskala wird kein explizites konstitutives Modell entwickelt, hingegen wird die Materialantwort an jedem Punkt durch separate numerische Simulationen auf der Mikroebene bestimmt. Die numerische Lösung des *zwei Skalen Szenarios* erfolgt durch FE-Berechnungen eines repräsentativen Volumenelementes auf der Mikroskala. Die Lösung des mikroskopischen Problems auf der einen Seite sowie ein geeignetes Homogenisierungskonzept zur Bestimmung der makroskopischen Spannungen auf der anderen Seite sind die Hauptbestandteile eines solchen Konzepts. Ziel der computerbasierten Homogenisierungsverfahren ist die Modellierung der gesamtheitlichen Systemantwort aufgrund von klar definierten mikrostrukturellen Informationen. Wir beziehen uns auf HILL [65] and SUQUET [177], welche fundamentale Prinzipien für lokales mechanisches Verhalten behandeln. Bezüglich der Skalenübergänge für *funktionale Materialien* ist es notwendig die Homogenisierungsprinzipien auf gekoppelte Probleme zu erweitern. Dazu werden neben den mechanischen Verschiebungen weitere Primärvariablen einbezogen, wie beispielsweise das elektrische Potential sowie die elektrische Polarisierung. Eine Übersicht der Homogenisierungstheorien findet sich in NEMAT-NASSER & HORI [140], wobei der zusätzliche Einbau von nichtmechanischen Eigenschaften, wie thermische, magnetische oder elektrische Effekte, auch berücksichtigt werden. Der wichtigste Aspekt jeder Homogenisierungsmethode ist die Bestimmung der makroskopischen Größen in Bezug auf ihre mikroskopischen Pendanten, welche durch geeignete Wahl von Randbedingungen für das repräsentative Volumenelement getrieben werden. Der Mikro-Makro Übergang kann in kanonischer Weise durch Variationsprinzipien der Homogenisierung beschrieben werden, welche *makroskopische Potentiale* in Abhängigkeit ihrer mikroskopischen Gegenstücke bestimmen. Eine rigorose Anwendung solcher Homogenisierungsmethoden basierend auf Variationsprinzipien sowie die Entwicklung von Randbedingungen wird in MIEHE [116] für den rein mechanischen Fall diskutiert. ZÄH & MIEHE [207] erweitern dieses Schema der Homogenisierung, wobei ein dissipatives Phasenfeldmodell auf der Mikroebene zu einem makroskopischen Boltzmann-Kontinuum überbrückt wird. Das ursprünglich von MIEHE [116] vorgeschlagene Konzept wurde auf den Fall der Elektromechanik erweitert sowie der Einbau von Randbedingungen mittels Lagrange- und Strafmethode in den Variationsprinzipien diskutiert.

Diese Arbeit skizziert Aspekte elektro-mechanisch gekoppelter Materialmodelle auf verschiedenen Skalen sowie die Entwicklung von neuen *Homogenisierungstechniken basierend auf Variationsstrukturen*. Die numerische Umsetzung der gekoppelten Probleme ist ein wichtiges Thema. Die Diskretisierung der Mehrfeldprobleme tritt, als Folge der entwickelten inkrementellen Variationsprinzipien, in einer symmetrischen und sehr kompakten Form auf. Die Dissertation ist in drei Teile untergliedert, wobei [Abschnitt I](#) die Grundlagen der Kontinuumsmechanik sowie Elektrostatik beschreibt und kurz die Grundprinzipien und Theoreme der Homogenisierung darlegt. Die Materialklassen, Piezokeramiken und EAPs, sind von besonderem Interesse und werden in zwei getrennten Abschnitten behandelt. [Abschnitt II](#) beschäftigt sich mit Piezokeramiken, welche numerisch durch eine *mikro-elektro Elastizitätstheorie* bei kleinen Verzerrungen durchdrungen werden. Die durch Polarisationsumschaltungen verursachte dissipative Systemantwort wird durch ein Ginzburg-Landau Phasenfeldmodell beschrieben. Die resultierende Domänenstruktur wird vollständig durch das Modell aufgelöst. Neue ratenabhängige und inkrementelle *Variationsprinzipien* für das gekoppelte Evolutionsproblem werden umrissen und die Einzelheiten des Mikro-Makro Übergangs durch eine erweiterte Hill-Mandel Makrohomogenitätsbedingung diskutiert. Die Euler-Gleichungen dieser Variationsprinzi-

pien sind die statischen Gleichgewichtsbedingungen, das Gleichgewicht der Elektrostatik, welches oft als zweite Maxwell-Gleichung oder Gaußsches Gesetz bezeichnet wird, und eine Ginzburg-Landau Gleichung für die Evolution der Polarisierung. Ein wesentliches Merkmal für den Entwurf eines variationsbasierten Homogenisierungsverfahrens ist die Definition von geeigneten Randbedingungen auf der Mikroebene, welche das Phasenfeld der elektrischen Polarisierung einschließt. Die drei klassischen Arten von Oberflächenbedingungen werden diskutiert und konsequent auf den elektromechanischen Kontext übertragen. Darüber hinaus werden sie in den Variationsfunktionalen durch geeignete Lagrange- und Strafmethode berücksichtigt. [Abschnitt III](#) entwickelt *Materialmodelle für finite Deformationen* und Theoreme für Skalenübergänge elektroaktiver Polymere. Allgemeine Gleichungen finiter Elektroelastizität werden in einem variationellen Kontext, sowohl in einem Lagrangeschen als auch Eulerschen geometrischen Rahmen, besprochen. Die Modellbildung beinhaltet ebenfalls Details zur Bestimmung gekoppelter elektromechanischer Tangentenmoduli durch eine numerische Störungstechnik. Zusätzlich wird ein makroskopischer Treiber für das Homogenisierungsproblem entwickelt, welcher die konsistente algorithmische Tangente auf der Makroskala berücksichtigt. Auf der Makroebene werden homogene Tests durchgeführt, wobei alle relevanten Daten durch die Randbedingungen auf die Mikroebene übertragen werden. Eine innovative Belastung durch die dielektrische Verschiebung ermöglicht es, Punkte elektromechanischer Instabilität zu überwinden.

Introduction

With the continuous increase in computational power and the development of efficient numerical solvers, complex multiscale simulations seem to be a reachable goal. The nano-processing technique and consequently the capability of CPU and GPU computations makes the parallelization of modern computer codes very efficient and fast. Hence, the description of heterogeneous materials with electro-, magneto-, thermo-mechanical coupling is a task of intensive research. Even though there have been significant advances in the development of new materials for high-tech and high-performance applications in the past, these advances have been based mainly on trial and error experiments or simply serendipity. Such empirical approaches allow the realization of only a tiny fraction of all the materials that are theoretically possible without prior knowledge of the properties and the behavior. The predictive simulation of coupling effects allows the creation of tailor-made materials in the form of composites that have properties which are superior than those of the individual constituents.

1.1. Electro-mechanical coupling phenomena

Recently, an increasing amount of problems from varying fields of engineering are solved by smart or functional systems, harnessing the electro-magneto-mechanical coupling properties of the used materials. Typical fields of application are adaptive or controlled systems such as actuators and sensors, micro-electro-mechanical systems (MEMS), fuel injectors for common-rail diesel engines, ferroelectric random access memories, and artificial muscles used in robotics, see [Figure 1.1](#). Regarding the technical implementation of smart systems, a broad variety of physically-based phenomena and materials are available. Some of the most important of these coupling phenomena are the shape memory effect, magnetostriction, electrostriction, and piezoelectricity. The exploitation of such coupling effects and the adaptation to the specific needs requires the choice of a specific material. The phenomenon of *ferroelectricity* in solids is characterized on the macroscopic level by a local electric polarization that remains even after a complete withdrawal of the applied electric field or the stress. Poled ferroelectric materials exhibit the property of *piezoelectricity* for small applied stresses and electric fields, that is, they show a linear electro-mechanically



Figure 1.1: *Examples of industrial applications.* Piezo-inline injector for common-rail diesel engines from Bosch. Ferroelectric random-access memory (FRAM) uses a ferroelectric layer instead of a dielectric layer to achieve non-volatility. Concept study “fly like a bird” of an EAP-actuated unmanned aerial vehicle in the shape of an ornithopter or flapping-wing aircraft.

coupled response and hence find use as the active components in sensors and actuators.

A highly interesting class of these materials are piezoceramics, coming up with short response times, high precision positioning, relatively low power requirements, and high generative forces, providing an excellent opportunity for mass production. Typical examples of such materials are barium titanate (BaTiO_3) and lead zirconate titanate (PZT) crystals and polycrystals, which exhibit linear and nonlinear coupling phenomena as well as hysteresis under high cyclic loading. A specific coupling phenomenon is the direct piezoelectric effect, which describes the generation of electrical charges on the surface resulting from an applied mechanical force. The converse piezoelectric effect identifies the development of a mechanical strain by an electric stimulus. At the microscopic level, these materials are composed of many homogeneously polarized regions, called ferroelectric domains, whose evolution in time is driven by external electric fields and stresses applied to a sample of the material. Ferroelectric domains are regions of parallel and hence aligned polarization. Electric poling can be achieved by the application of a sufficiently strong electric field inducing the reorientation and alignment of spontaneous polarization. As a consequence, piezoceramics exhibit a macroscopic remanent polarization. The poling process of the microstructure is dissipative in nature and gives rise to macroscopic dielectric and butterfly hysteresis loops. An overview on the material science of ferroelectric piezoceramics is given in JAFFE ET AL. [76], LINES & GLASS [105], and MOULSON & HERBERT [138].

Another important class of electro-mechanically coupled materials are electroactive polymers (EAPs). They respond with a (possibly large) deformation to an applied electrical stimulus, an effect discovered by the physicist Wilhelm Röntgen in 1880 in an experiment on a rubber strip subjected to an electric field. EAP materials are divided into two main groups: electronic and ionic materials. In electronic EAPs, the activation is driven by Coulomb-type electrostatic forces between opposite charges (Maxwell stresses) which are created inside the dielectric as a result of an applied electric field. These materials allow fast response speeds, however, at the cost of high voltage. Ionic EAPs including gels and conductive polymers are actuated by electric field induced diffusion of mobile ions that cause deformation. They operate at low voltage, but also perform at a comparably low speed. Advanced electroactive polymer materials may achieve large electrically induced strains, making them the closest man-made materials to biological muscles. As a consequence, they could be used in many technological applications, e.g. in robotics, biomimetic and smart structures as sensors and actuators, see BAR-COHEN [7], BAR-COHEN & ZHANG [8], and SMITH [169].

The description of these effects through models of continuum mechanics is a subject of extensive research. The theoretical foundations for the analysis of electro-mechanical interactions in dielectric solids can be traced back to TOUPIN [190, 189], ERINGEN [42], TIERSTEN [187], MAUGIN [110], ERINGEN & MAUGIN [43, 44], and KOVETZ [94]. Continuum models for ferroelectrics may be broadly classified into two categories: *Phenomenological models* for the macroscopic response, which do not resolve the domain patterns, and *micro-electric approaches*, which involve the explicit modeling of microstructures. Purely phenomenological models for ferroelectric polycrystals undergoing small strains, where dissipative effects are described by internal macro-variables, are outlined for example in BASSIOUNY ET AL. [11, 12], BASSIOUNY & MAUGIN [9, 10], HUBER & FLECK [71], KAMLAH [81], LANDIS [102], McMEEKING & LANDIS [112], SCHRÖDER & ROMANOWSKI [163], KLINKEL [85], and MIEHE & ROSATO [123]. Recent developments with a particular focus on the constitutive modeling of field-activated EAPs and deformable dielectrics are given in DORFMANN & OGDEN [41], McMEEKING & LANDIS [113], VU & STEINMANN [196], ZHAO ET AL. [215], SUO ET AL. [176], PONTE CASTAÑEDA & SIBONI [151], THYLANDER ET AL. [186], JIMÉNEZ & McMEEKING [80], and ROSATO & MIEHE [156]. Numerical implementations of finite electro-mechanics combined with variational principles are proposed for non-dissipative response by VU ET AL. [197], VU & STEINMANN [196], and STEINMANN & VU [170] as well as for dissipative behavior by ROSATO [154] and ROSATO & MIEHE [156]. Micromechanically motivated theories investigate the behavior of single crystals and employ energy arguments as switching criteria, see for example HWANG ET AL. [73], CHEN & LYNCH [31], HUBER ET AL. [72], and HUBER & FLECK [71]. Micro-electric approaches *resolve the domain evolution* and are inspired by the domain theory of magnetization, cf. LANDAU & LIFSHITZ [100]. Here, the electric polarization is described by a *phase field* that acts as an order parameter or a generalized internal variable. The domain walls are interpreted as diffusive interfaces and their motion is described by the *Ginzburg-Landau* or *Allen-Cahn equation*, see for example ZHANG & BHATTACHARYA [210, 211], SU & LANDIS [174], SCHRADER ET AL. [159], and the recent work MIEHE ET AL. [133] on its variational structure. The latter provides, due to the rigorous exploitation of new rate-type and incremental variational principles, a frame that gives a canonical insight into the structure of the coupled problem. Micro-electro-elastic theories are based on three primary fields including the microscopic polarization to describe dissipative polarization switching. They are formulated in terms of a general framework of an objective, first-order gradient-type material. The energy density of solid matter contains the stored elastic energy including the electrostrictive coupling, the non-convex anisotropy density (Landau-Devonshire energy), and the exchange energy that incorporates the polarization gradient.

1.2. Multiscale approaches and computational homogenization

Physically predictive material modeling can be performed on different length- and time scales. The classical setting of continuum mechanics develops phenomenological material models “smeared” over some continuously distributed material, where the material parameters are identified from experimental data. The aim of multiscale simulation techniques is the reduction of uncertainties and empirical assumptions while simultaneously increasing the accuracy of the solution. Many developed multiscale techniques focus pre-

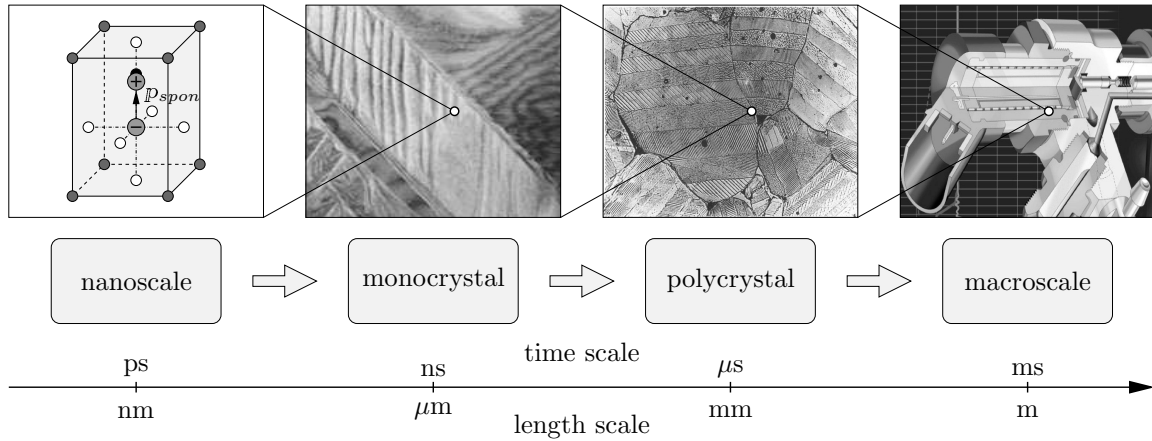


Figure 1.2: *Multiscale modeling on different length- and time scales.* Visualization of several scales for the simulation of piezoceramics. Continuum models may be broadly classified into two categories: Phenomenological models for the macroscopic response, which do not resolve the domain patterns, and micro-electric approaches, which involve the explicit characterization of these specific microstructures.

dominantly on the efficient bridging of neighboring length- and time scales, e.g. on the incorporation of microscopic polarization in order to predict macroscopic hysteresis phenomena, see Figure 1.2. Here, the multiscale character of piezoceramics is considered. On the nanoscale a typical perovskite unit cell gives rise to the development of a spontaneous polarization after cooling below a material-specific transition temperature. A ceramic material is per definition the agglomeration of small crystals fitted together randomly. While cooling to a ferroelectric phase, the minimization of intergranular stresses drives the formation of electric domains, which are regions of unit cells with equal spontaneous polarization. These domains are well separated by electric domain walls. On the next larger scale, a polycrystalline structure consisting of many single crystals can be observed. Macroscopically, industrial applications such as a piezo inline injectors for diesel engines are of interest, utilizing the micro-mechanisms in order to create the desired system output. Physical observations that determine the coupled behavior characterize the constitutive relations on every scale, but also change from one scale to another. Hence, the scale bridging by homogenization methods is a mathematical or computational problem, not a physical one.

If the determination of effective properties of micromechanically heterogeneous materials is concerned, the available approaches may be subdivided into two main categories, depending on the regularity of the microstructure. For *regular* or *nearly regular composites* with linear constitutive behavior, the effective properties can be determined by solving a finite number of unit cell problems with appropriate boundary conditions. If additionally the assumption of scale separation is met, an asymptotic homogenization approach can be applied, BENSOUSSAN ET AL. [13] and SANCHEZ-PALENCIA [157]. If, in contrast, the *microstructure is not regular*, the effective properties cannot be determined exactly. The available schemes are limited to the determination of ranges of the effective behavior in terms of bounds which depend on characteristics of the microstructure, such as for instance volume ratios. In the pioneering works of VOIGT [195] and REUSS [153], rigorous upper and lower bounds for the effective stiffness of composites were developed. An extension based on variational principles leading to better estimates was presented decades later by HASHIN & SHTRIKMAN [57, 58]. If we were dealing with nonlinear con-

stitutive behavior and composites with random microstructures instead, the first bounds are obtained by BISHOP & HILL [21, 22] for rigid, perfectly plastic polycrystals. An improved method was developed by BUDIANSKY [26] and HILL [64]. This self-consistent method is based on Eshelby's analysis and embeds a single inclusion into an infinite domain of the initially unknown effective matrix material. The work of TALBOT & WILLIS [180] and WILLIS [203] enhances the Hashin-Shtrikman variational principle for nonlinear composites to a nonlinear constitutive framework. The variational principles of PONTE CASTAÑEDA [149, 150] and TALBOT & WILLIS [182] for general classes of nonlinear composites or of SUQUET [178] for power-law composites deal with the determination of general bounds and estimates directly from corresponding estimates for linear composites by a proper choice of the linear comparison composites.

Two-scale computational homogenization schemes determine the effective properties numerically by two nested boundary-value-problems coupled by an appropriate scale transition law. No constitutive model is explicitly assumed on the macroscale, and the material response at each point (i.e. at each quadrature point within the finite element domain) is determined by performing a separate numerical analysis at the micro-level. For first- and second-order homogenization schemes in the purely mechanical context performed with the finite element method (FE²), see for instance SMIT ET AL. [168], MIEHE ET AL. [125, 126], MIEHE [116], FEYEL & CHABOCHE [46], TERADA & KIKUCHI [183], KOUZNETSOVA ET AL. [92], and GEERS ET AL. [50]. Main ingredients of such a framework are, on the one hand, the solution of a microscopic boundary-value-problem in consideration of the material behavior of the representative volume element and, on the other hand, a homogenization rule determining the macroscopic response. Goal of these computational homogenization techniques is the modeling of the overall response based on well-defined microstructural information. We refer to HILL [65] and SUQUET [177] for fundamental homogenization principles of local mechanical response.

The scale transition for *functional materials* from a heterogeneous microstructure towards a macroscopically homogeneous continuum is concerned in the following. It is necessary to extend the homogenization principles to coupled problems, incorporating besides the mechanical displacement further primary variables such as the electric potential and the electric polarization. An overview of homogenization theories is given in NEMAT-NASSER & HORI [140], where the additional incorporation of non-mechanical properties such as thermal, magnetic, or electric effects was concerned in a fundamental format. The key aspect of every homogenization scheme is the determination of macroscopic quantities in terms of their microscopic counterparts, driven by appropriate constraints or boundary conditions on a representative volume element. In the present work, a variational-based homogenization framework for electro-mechanically coupled materials based on a rigorous exploitation of variational principles is developed, see the work MIEHE [118] on variational principles for the mechanical response of gradient-extended standard dissipative solids. These principles serve as canonical ingredients for the micro-to-macro transition and determine *macroscopic potentials* in terms of their microscopic counterparts. We refer to the previous works MIEHE [116], LAHELLEC & SUQUET [99] and BRASSART ET AL. [24] on incremental variational principles for purely mechanical problems and BISEGNA & LUCIANO [19, 20] for piezoelectric composites. The derivation of basic equations for coupled electro-mechanical homogenization at small strains is treated in SCHRÖDER [161]. This two-scale homogenization approach is implemented into a FE²-method in SCHRÖDER & KEIP [162], allowing for the computation of macroscopic

boundary-value-problems in consideration of microscopic representative volume elements. An extension to determine configurational forces within piezoelectric materials is given in KHALAQUZZAMAN ET AL. [84]. KEIP ET AL. [83] proposed a framework for the simulation of electro-active solids at finite deformations. Furthermore, PONTE CASTAÑEDA & SIBONI [151] investigated the analytic homogenization of electro-active polymer composites at finite strains. For magneto-mechanical coupling in the large strain context, we refer to the papers by CHATZIGEORGIOU ET AL. [30] and JAVILI ET AL. [79]. In this context, recall the classical works on self-consistent *variational estimates* for nonlinear dielectrics by WILLIS [202, 204], TALBOT & WILLIS [181], and TOLAND & WILLIS [188]. Here, different bounds are generated starting from a Hashin-Shtrikman-type variational principle by a suitable choice of the 'comparison' energy function. A rigorous application to variational-based homogenization and the development of boundary conditions is performed in MIEHE [116] for the purely mechanical case. ZÄH & MIEHE [207] developed a non-standard homogenization scheme bridging a dissipative phase field model of domain switching on the microscale to a standard macroscopic Boltzmann continuum. The concepts originally proposed by MIEHE [116] were used and extended to electro-mechanics by outlining Lagrange and penalty methods for the incorporation of boundary conditions in the variational principles.

1.3. Objectives and overview

This work deals with the development of electro-mechanically coupled material models on different scales and the investigation of new variational-based homogenization techniques. Two classes of materials are addressed, piezoceramics simulated with a *small strain phase field* theory of micro-electro-elasticity and electroactive polymers (composites), where *finite strain* material models and bridging theorems need to be developed. A key feature of all scale bridging approaches is the particular investigation of boundary conditions. These constraints strongly influence the response of the microstructure. The three classical types of boundary conditions—stiff Dirichlet-type, soft Neumann-type, and periodic boundary conditions—are discussed in this work and consistently transferred to the electro-mechanical context. A short micromechanical motivation of electro-mechanics is given in [Chapter 2](#). We start by giving a description of the direct and inverse piezoelectric effect and outline the difference between piezo- and ferroelectricity. Afterwards, the focus is on dissipative mechanisms of polarization switching, both electric field and stress induced, which are the reason of hysteretic material behavior on macroscopic scales. The subsequent chapters are arranged into three main parts:

Part I deals with fundamentals of electro-mechanics and homogenization theory. Here, [Chapter 3](#) provides elementary knowledge of finite strain continuum mechanics and electrostatics, which is a key aspect to the modeling of coupled electro-mechanical problems. To enhance purely mechanical formulations, the electric field is physically motivated and fundamental laws of physics are presented. The main ingredients are provided by Coulomb's law, Gauss's law, and Faraday's law formulated for the electrostatic case. The mathematical description of purely mechanical balance principles is extended to electro-mechanical influences. The interaction of matter with electric fields is considered by additional electric force, couple, and energy supply terms within the balance equations. In [Chapter 4](#), we provide a brief introduction to the problem of homogenization and the

concept of micro-to-macro transition. Most materials which are attempted to be modeled by homogeneous continuum approaches are inhomogeneous on smaller length scales, that is on micro- or even nanoscale. The mathematical theory of variational-based homogenization can close the gap between neighboring length scales by the formulation of suitable micro-to-macro transition concepts, incorporating physically necessary information of the microscale on the macroscopic level. The key aspect of every homogenization scheme is the determination of macroscopic quantities in terms of their microscopic counterpart, driven by appropriate constraints or boundary conditions on the representative volume element. Extended averaging theorems are derived and various potentials proposed, leading to upper and lower bounds for the macroscopic potentials characterized by an appropriate choice of microscopic boundary conditions.

In **Part II** the modeling and homogenization of micro-electro-elasticity at *small strains* is addressed, where the polarization enters the modeling strategy as a phase field variable fully resolving the domain structure. [Chapter 5](#) develops new rate-type and incremental variational principles for the coupled evolution problem, in order to simulate electric field and stress driven switching processes. The Euler equations of these variational principles are the static stress equilibrium condition, the electrostatic equilibrium condition, often denoted as the second Maxwell equation or the Gauss law, and a Ginzburg-Landau-type equation for the evolution of the polarization. In the subsequent [Chapter 6](#), the previously developed model of micro-electro-elasticity is adopted as material model for the representative volume element. An important aspect for the design of variational-based homogenization methods is the definition of suitable boundary conditions at the micro-level, which also include the phase field of electric polarization. Here, the microscopic displacement and electric potential may be viewed to be driven by their macroscopic counterparts, which are considered the only primary variables on the macro-level. In contrast, the electric polarization has no counterpart on the macroscale. Details of the micro-to-macro transition are outlined by utilizing an extended version of the Hill-Mandel macrohomogeneity condition. Various boundary constraints are incorporated into the variational functionals by means of Lagrange and penalty methods.

Finally, **Part III** develops finite electro-elastic models at *large strains*, focusing on polymeric materials. [Chapter 7](#) summarizes general equations of finite electro-elasticity in a variational format, accounting for geometric settings in both the Lagrangian as well as the Eulerian configuration. A modular framework for the alternative incorporation of polymer network models is developed. This covers all details of the modeling, including the set up of coupled electro-mechanical tangent moduli by a numerical perturbation technique. We focus on the microsphere network model of rubber elasticity, that exploits a homogenization over a chain orientation space. This provides an advanced model problem for the application of the proposed constitutive framework for electroactive polymers. In addition, [Chapter 8](#) develops a macroscopic FE² driver for the homogenization problem, accounting for the consistent algorithmic tangent on the macroscale. The sensitivity of the microscopic fluctuation field with respect to macro-driven fields is the crucial ingredient of this numerical scheme. Homogeneous tests on the macroscale are performed and the relevant data transferred to the microscale via the boundary conditions. An innovative driving of the electric displacement as compared to the standard electric field driven homogenization is performed, allowing us to avoid points of electro-mechanic instability.

Micromechanical Motivation

Before dealing with the modeling and homogenization of electro-mechanically coupled materials, the micromechanical behavior of two classes of piezoelectric materials, that are piezoceramics and electroactive polymers, are discussed. The constitutive material response of these two classes of materials is based on two fundamental elements: First, the non-centrosymmetric molecular constitution, which result in the appearance of elementary micro-dipoles characterized by a certain spontaneous polarization in the microstructure and additionally is responsible for the piezoelectric behavior of the unit cells. Second, the capability of alignment and hence rotation of those elementary unit cells under a certain electro-mechanical loading and the ability of retaining the alignment after unloading. The first factor is responsible for the reversible part of the material response, while the second characteristic is the fundamental reason for the dissipative behavior of this class of materials. We start by giving a description of the direct and inverse piezoelectric effect and outline the difference between piezo- and ferroelectricity. Afterwards, the focus is on dissipative mechanisms of polarization switching, both electric field and stress induced, which are the reason of hysteretic material behavior on macroscopic scales.

2.1. Piezoelectricity

The term *piezoelectricity* originates from the Greek “pressure electricity” and describes the generation of an electric field in the material due to mechanical stresses. It was discovered in 1880 by the physicists Jacques and Pierre Curie using crystals of tourmaline. In order to show the piezoelectric effect, materials need to be polarizable, that is the centers of charges can be shifted with respect to each other by the application of external fields. Such poled piezoelectric materials possess a macroscopic polarization, whose direction remains constant. Piezoelectricity is a *linear electro-mechanical interaction* phenomenon possessing a direct and a converse effect. As such, it is a reversible process and no polarization develops in an unstressed state. If an electric field e is applied to a mechanically unloaded specimen, the *converse piezoelectric effect* causes the strain ε , that is

$$\varepsilon = d_{33}e, \tag{2.1}$$

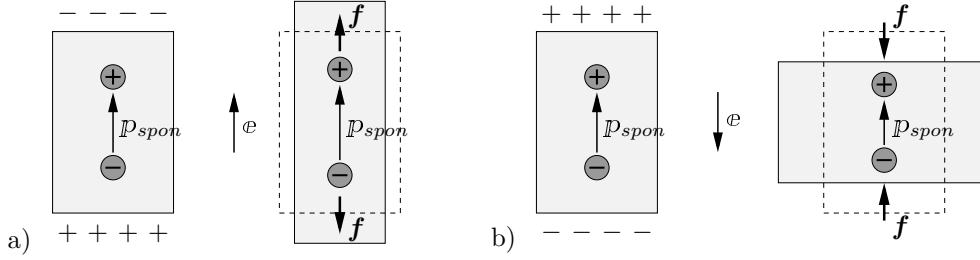


Figure 2.1: *Piezoelectric effects.* An electrically induced mechanical strain is caused by the force $\mathbf{f} = q\mathbf{e}$ acting on the barycenters of positive and negative charges. A piezoelectric material has an a priori given polarization \mathbf{p} . The electric field causes a mechanical a) elongation or b) compression of the unit cell in the direction of the polarization vector, depending on the sign of the electric field. This effect is transversely isotropic with respect to the polarization.

which is proportional to the electric field. The proportionality constant d_{33} is called piezoelectric constant. The electrically induced strain may be an elongation or a shortening, depending on the direction of the applied electric field in comparison to the direction of the polarization. To visualize this behavior, consider a unit cell of an unloaded polar material with a spontaneous polarization $\mathbf{p}_{\text{spont}}$, resulting from the different locations of the centers of positive and negative charges of a unit cell. Application of a constant voltage to the cell results in a shift of the barycenters of positive and negative ions with respect to each other. An electric field with the same direction as the spontaneous polarization will move the centers further apart from each other, while an electric field with opposite direction brings them closer together, see [Figure 2.1](#). The electro-mechanical coupling effect is caused by the fact that the shifting of the centers of the charges is accompanied by a corresponding elongation or shortening of the unit cell. In case the spontaneous polarization is oriented in the reverse direction with respect to a fixed frame of reference, the constant d_{33} has the same magnitude, but a different sign. As a consequence, the orientation of the electric field is an important ingredient of the effect. An exposure of the unit cell to mechanical pressure deforms the unit cell and, accordingly, displaces the relative positions of the centers of positive and negative charges. This displacement causes a transient current in the unit cell and, in turn, a change of polarization. The mechanically induced change of polarization is called *direct piezoelectric effect*

$$\Delta \mathbf{p} = d_{33} \sigma. \quad (2.2)$$

Here, $\Delta \mathbf{p}$ is the change in spontaneous polarization and $d_{33} = \Delta \mathbf{p} / \sigma = \varepsilon / e$ the above mentioned piezoelectric constant. As a result of the direct piezoelectric effect, application of even very small mechanical loads may lead to high electric voltages. This behavior suits to sensor applications. Besides, the converse piezoelectric effect may be employed in the actuator applications. The property of piezoelectricity is related to the polarity of the unit cell of a material and hence only possible in non-centrosymmetric crystals. For a PZT composite, the piezoelectric constant is $d_{33} = 400 \cdot 10^{-12} \frac{\text{m}}{\text{V}}$. If a tensile stress is applied perpendicular to the initial polarization direction, the change $\Delta \mathbf{p} = d_{31} \sigma$ is negative, where $d_{31} = -170 \cdot 10^{-12} \frac{\text{m}}{\text{V}}$, see SMITH [169].

A *ferroelectric material* has a polycrystalline structure as visualized in the micrographs depicted in [Figure 2.2](#). All ferroelectric materials are piezoelectric, but not vice versa. It is a material in which the polarization dipoles can be reoriented using an external electrical field of sufficient magnitude. Even if the applied field is removed, the spontaneous polarization remains in the switched state and the overall polycrystalline

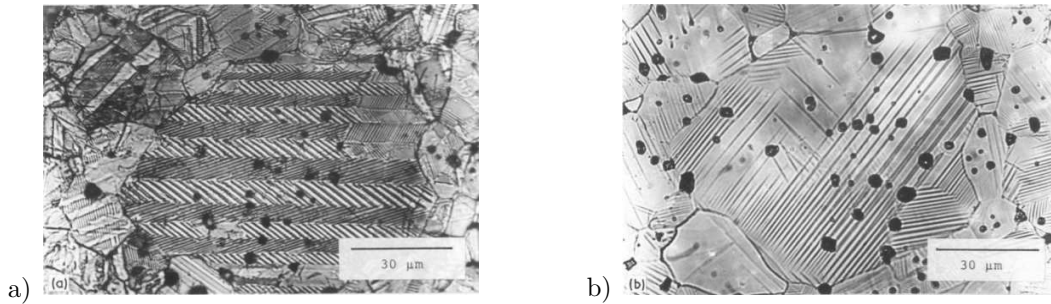


Figure 2.2: *Micrograph of a barium titanate ferroelectric ceramic crystal.* Representative BaTiO_3 domain patterns of a grain taken from ARLT [1]. a) The pattern is formed inside the ceramic body with three-dimensional clamping and b) the same grain when the pattern is formed under free surface conditions.

aggregate has a macroscopic polarization in a homogenized sense. The macroscopic behavior of an electrically poled ferroelectric material is then for a certain range of the electric field piezoelectric. This process is called poling and achieved by the temporarily application of strong electric fields, analogously to magnetization to create permanent magnets. The spontaneous polarization can be switched between two or more distinct crystallographic directions by an electric field above a threshold value and depends on the history of previous switching, yielding typical hysteresis loops. Materials demonstrate a ferroelectric behavior only below a certain transition temperature called the Curie temperature θ_c . Above that temperature in the paraelectric phase, the crystal structure is centrosymmetric without spontaneous polarization.

2.2. Piezoceramics

Ferroelectric ceramics are presently being used in a broad range of applications including sonar devices, micro-electro-mechanical systems (MEMS), fuel injectors for diesel engines, actuators for active control of helicopter rotor blades and underwater vehicle control surfaces, as well as ferroelectric nonvolatile random access memories (FRAMs) for computers. Accurate modeling tools are required for the reliable design and optimized performance of these devices. The common structure of typical materials with piezoelectric properties, like barium titanate (BaTiO_3) and lead zirconate titanate (PZT), is polycrystalline as a result of the ceramic processing techniques. For a more detailed description concerning the material science of ferroelectric piezoceramics see JAFFE ET AL. [76], LINES & GLASS [105], and MOULSON & HERBERT [138]. The polycrystalline structure comprises grains of differently oriented crystal lattices. A unit cell consists of a structure of positively and negatively charged ions typical for a specific material. In this structure, the centers of the positive and negative charges have a certain location within the cell. If the centers are at different positions in the absence of any load, a permanent dipole establishes and the cell possesses a *spontaneous polarization*. In ferroelectric materials, this spontaneous polarization can be switched hysteretically by the application of an external electric field. A ceramic material is per definition the agglomeration of small crystals, fitted together randomly. While cooling to a ferroelectric phase, the minimization of intergranular stresses benefits the formation of *electric domains*, which are regions of unit cells with equal spontaneous polarization. Micrographs of ferroelectric barium titanate crystals are depicted in Figure 2.2. Let us consider BaTiO_3 as a representative example for piezoceramics.

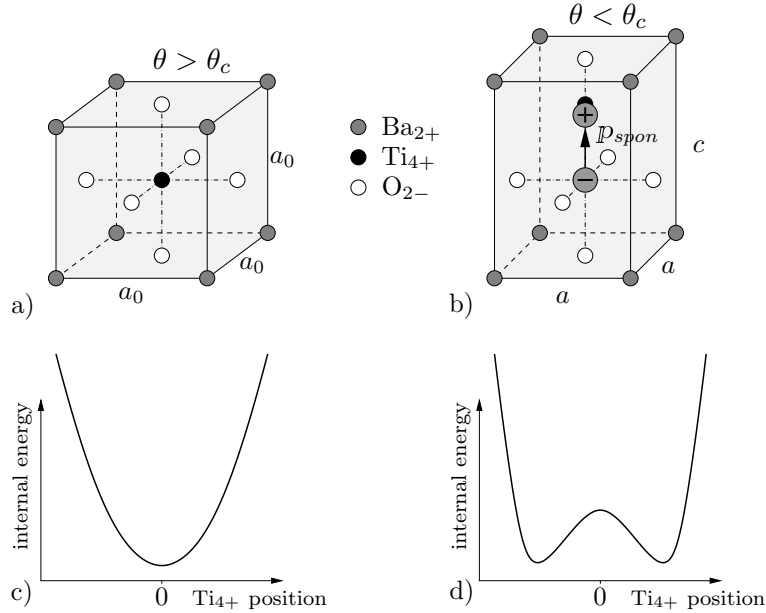


Figure 2.3: Non-centrosymmetric unit cell and energy profiles for barium titanate. a) Paraelectric phase above Curie temperature θ_c , where the cubic symmetry with dimension $a_0 = 4.009\text{\AA}$ does not allow for a spontaneous polarization. b) Distortion of perfect perovskite unit cell after cooling below θ_c . In this ferroelectric phase the spontaneous polarization vector P_{spon} orients in the direction of the displaced titanium ion. The dimension of the tetragonal polar lattice is $a = 4.003\text{\AA}$ and $c = 4.022\text{\AA}$ at the transition temperature of 130°C . c) Energy profile for cubic lattice structure with single well giving rise to a unique position of the titanium ion. d) Internal energy of ferroelectric phase exhibits double well profile, where minima correspond to equilibrium positions of titanium ion above or below unit cell center.

The crystal lattice of these materials has perovskite structure below the material dependent Curie temperature θ_c (BaTiO $_3$: $\theta_c = 120\text{--}130^\circ\text{C}$, PZT: $\theta_c = 250\text{--}350^\circ\text{C}$). Above the Curie temperature, Figure 2.3a, the unit cell has cubic shape with side length a_0 and the positive titanium ion (Ti $_{4+}$) located at the center. Since the centers of positive and negative charges coincide, the material possesses no spontaneous polarization. The lattice structure is centrosymmetric and the material is in the *paraelectric phase*. Below the Curie temperature, the cubic configuration becomes unstable due to the shifting of the centers parallel to one of the lattice axes leading to a *tetragonal* shape with the dimensions $a \times a \times c$, Figure 2.3b. Note that the upward displacement of the positive titanium ion is accompanied by the downward displacement of all surrounding negative oxygen ions. Two characteristic *energy profiles* for cubic and tetragonal perovskite lattice structures are plotted in Figure 2.3c,d. For the paraelectric phase, the internal energy has a single minimum and thus the position of the titanium ion is uniquely described. In the ferroelectric phase, the internal energy exhibits a double well profile, where the minima correspond to the equilibrium positions of the titanium ion above or below the unit cell center. The influx of enough energy makes it possible to overcome the energy barrier between the two minima and the ion moves to the other stable equilibrium state by a dipole switch. Additional lattice shapes beside the tetragonal are discussed in JAFFE ET AL. [76], but for the sake of simplicity we stay with the latter as is common practice in literature. Ferroelectric materials perform a phase transition from the paraelectric to the ferroelectric phase during cooling. There are six possible directions in each unit cell located along the originally cubic lattice axes for the rearrangement of the central ion. Hence, six different

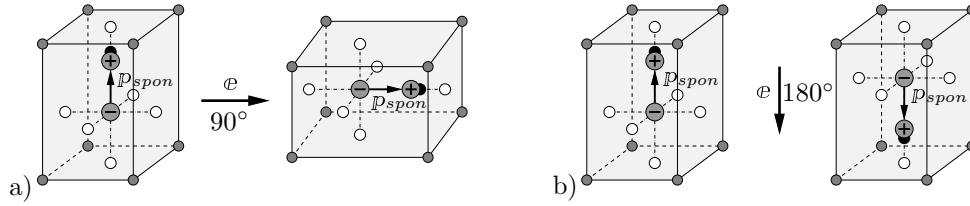


Figure 2.4: *Electric field driven switching of the spontaneous polarization.* The cooling of piezoceramics to a ferroelectric phase causes a random orientation of micro-dipoles characterized by the polarization vector P_{spon} . The mechanism of a) 90° and b) 180° electric field driven reorientation of the polarization causes an alignment with the prescribed electric field e .

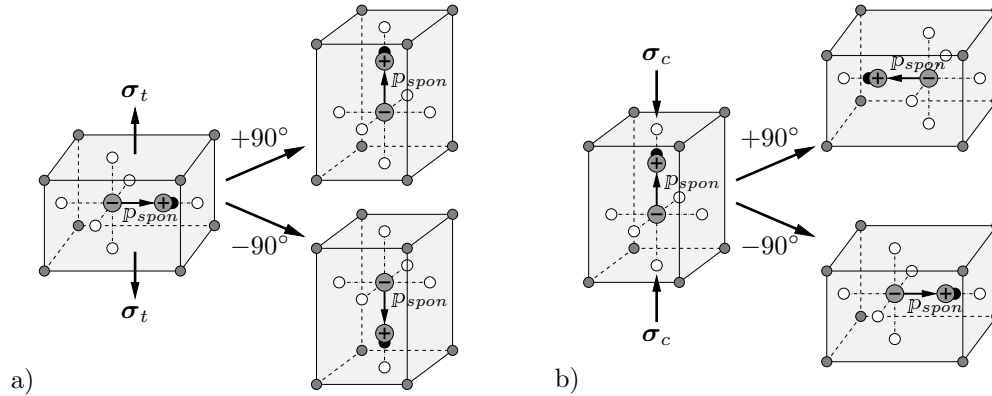


Figure 2.5: *Stress driven switching of the spontaneous polarization.* The application of a mechanical stress field to a non-centrosymmetric perovskite unit cell induces a switching process of $\pm 90^\circ$ of the spontaneous polarization P_{spon} . a) Tensile stress causing two possible reorientations and b) compressive loading with four possible orientation directions (reduced representation).

directions for the spontaneous polarization exist simultaneously and no unique direction exists for all unit cells of a grain during cooling. In fact, the spontaneous polarization forms locally within a grain electric domains with uniform directions, but within a whole grain the polarization distribution is random, see MOULSON & HERBERT [138] for further details. In contrast to ferromagnets, where the size of domain walls separating adjacent domains is about 10 nm, the walls of ferroelectric materials have a thickness of only a few nanometers. Transforming these characteristics to the macroscopic scale, the randomly distributed spontaneous polarization cancel each other such that there is no macroscopic piezoelectricity in this thermally depoled virgin state of the material. Although the individual unit cells are anisotropic, the macroscopically observable material behavior is isotropic due to the random distribution of the spontaneous polarization.

The macroscopic electrical and mechanical response is the outcome of the domain structure on the microscale. The orientation of domains of a ferroelectric material can be modified by electric and mechanical loading with sufficient magnitude by *domain switching*. The application of an electric field of magnitude greater than the *coercive field* e_c switches the directions of spontaneous polarization by 90° or 180° such that it is more closely aligned with the external field as illustrated in Figure 2.4. During a 180° inversion of the polarization, the tetragonal structure of the unit cell remains unchanged, while the 90° switching goes with the reorientation of the lattice. Since there exist six equivalent crystallographic directions in the tetragonal structure, there are always four possible 90° switches and one 180° switch. After removal of the loading, the switched configuration retains. In the completely unloaded state, that is zero electric field, the material will have

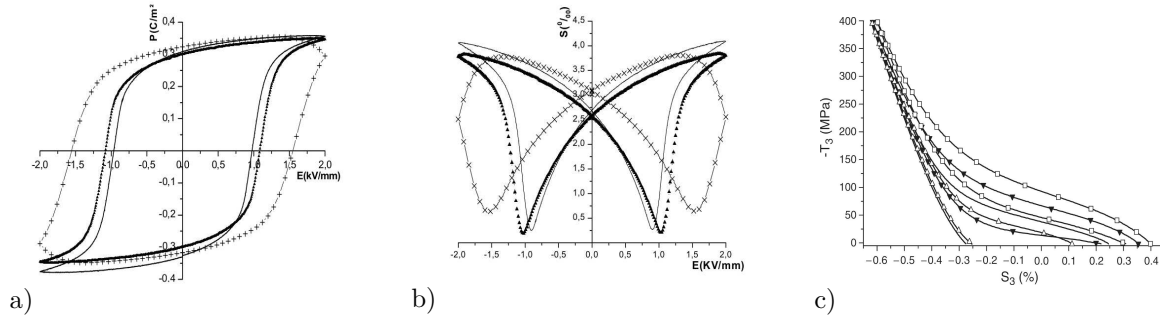


Figure 2.6: Typical hysteresis curves of ferroelectric materials. a) Dielectric hysteresis depicts polarization versus electric field curves and b) butterfly hysteresis for a cyclic electric loading shows strain against electric field curves for initially unpoled PIC151 soft PZT ceramics for different loading frequencies. c) Ferroelastic hysteresis comparing mechanical stress with longitudinal strain during first cycle of compressive stress loading characterizing the depolarization behavior of soft PZT piezoceramics. Experimental results taken from ZHOU ET AL. [216, 217].

a non-zero residual macroscopic polarization, which is called *irreversible* or *remanent polarization*. The process to reach this ordered microscopic polarization state is named poling. The remanent polarization is the average of the spontaneous polarization of a unit cell over all of the corresponding crystals. In an ideal crystal, the remanent polarization can achieve the value of spontaneous polarization as a maximum. However, in real ceramic structures the crystallographic axes are randomly distributed from grain to grain, leading to mismatches of the spontaneous polarization, HUBER ET AL. [72]. Because of defects like dislocations and impurities, the maximum possible value reachable for the remanent polarization is the *saturation polarization*, see JAFFE ET AL. [76] and MOULSON & HERBERT [138]. Arrangement of the formerly random state by a poling process in the direction of the external electric field causes a transversely isotropic material, whose anisotropy axis coincides with the remanent polarization vector, JAFFE ET AL. [76]. The average of the spontaneous polarization over all grains in a polycrystal does not vanish any more, and a macroscopic piezoelectricity exists.

The reorientation of the spontaneous polarization in the direction of the poling field is accompanied by a deformation of the polycrystal. The resultant macroscopic average of the spontaneous strain of the unit cells is called *irreversible* or *remanent strain*. As for the remanent polarization, there is also a maximum value for the remanent strain called the *saturation strain*. One of the most important characteristics of piezoceramics are the macroscopic hysteresis curves under purely electric loading. The so-called *dielectric hysteresis*, the plot of polarization (or electric displacement) versus applied electric field, represents the dielectric behavior of the ferroelectric ceramic. Figure 2.6a depicts typical experimental curves obtained for ferroelectric ceramics for a cyclic electric loading with varying frequencies. The polarization switching process also affects the deformation state of the material. In Figure 2.6b the *butterfly hystereses* are recorded for the normal strain in the direction of the electric field. The characteristic property of the butterfly curve is its symmetry with respect to the strain axis at zero electric field. The dielectric hysteresis and the butterfly curve clearly demonstrate a strong frequency dependence. Both types of hysteresis curves were already pointed out in the pioneering work of LYNCH [107] and are here extracted from the measurements in ZHOU ET AL. [216]. A qualitative discussion interpreting the underlying domain structure is given in KAMLAH [81]. A mechanical stress with adequate magnitude above the *coercive stress* can trigger domain switching

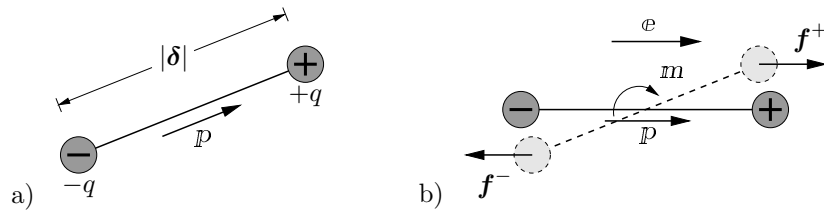


Figure 2.7: *Moment experienced by dipole in a uniform electric field.* The positive and negative electric charges $\pm q$ are separated by the distance $|\delta|$ resulting in a dipole $\mathbf{p} = q\delta$. a) Initial configuration of the dipole in the absence of an electric field. b) Opposing forces $\mathbf{f}^+ = q\mathbf{e}$ and $\mathbf{f}^- = -q\mathbf{e}$ create a moment $\mathbf{m} = \mathbf{p} \times \mathbf{e}$ causing the electric dipole to align with the electric field.

as well, but cannot give a unique switching direction of the spontaneous polarization, LINES & GLASS [105]. The longer c-axes of a unit cell are oriented randomly in the plane perpendicular to the compression loading, accompanied by an irreversible deformation. Spontaneous polarization of a unit cell may take an orientation from alternatives shown in Figure 2.5, where for the sake of simplicity solely two out of four possible switching directions are outlined. The resulting domain state is transversely isotropic and no macroscopic polarization is observed. Hence, such a process is called *mechanical depolarization*, see Figure 2.6c showing the compressive stresses versus strain hysteresis for a single loading cycle of an initially poled polycrystalline material. For further loading cycles, hardly any hysteretic behavior can be observed as the domain configuration finally reached by the depolarization process is stable. Although the induced deformations seem to be similar to those in metal plasticity caused by dislocation movement, the saturation limit for the strains due to domain switching mechanisms makes the crucial difference. For a detailed description of the microstructural and macrostructural material response of ferroelectric ceramics see the review articles of KAMLAH [81] and LANDIS [103] and references therein.

2.3. Electroactive polymers

The elastic response of cross-linked polymers is dominated by an extreme deformability and can be well explained by statistical micro-mechanics, see for example TRELOAR [192] for an introduction. Elasticity of polymers above the glass transition temperature is achieved by a molecular micro-structure consisting of very flexible and mobile long chain molecules and a three-dimensional network that is formed by occasional cross-links between molecules. The dominant contribution to the elastic response of rubber-like materials is due to changes in conformations of network constituents, yielding the so-called entropy elasticity theory. The entropy-based elasticity of chain molecules is well established in the context of statistical mechanics, see KUHN [96, 97], KUHN & GRÜN [98], TRELOAR [192], FLORY [47] and references cited therein. In the literature, many constitutive models for the macroscopic elastic response of rubbery polymers have been developed, see BOYCE & ARRUDA [23] and MIEHE ET AL. [129] for an overview. *Purely phenomenological macro-models* involve invariant or principal stretch based isotropic free energy functions, often having polynomial structures. The most advanced formulations are those of OGDEN [141, 142]. However, these approaches lack relations to the molecular structure of the material. This is achieved by *micro-mechanically based network models*, such as the three chain model proposed by JAMES & GUTH [77], the eight chain model suggested by ARRUDA & BOYCE [2], and the affine full network models considered in

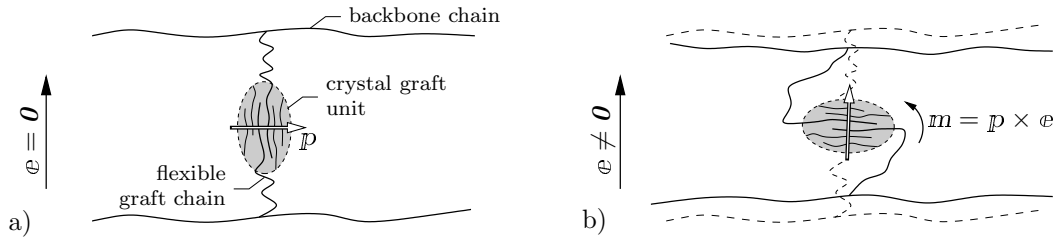


Figure 2.8: *Elastomer deformation induced by crystal unit rotation.* a) Location of backbone chains, flexible graft chains, and crystal graft unit prior to deformation. Crystal unit exhibits a dipole moment \mathbf{p} . b) Force moment $\mathbf{m} = \mathbf{p} \times \mathbf{e}$ rotates dipole moment in the direction of the electric field. Flexible graft chains wrap around the crystal unit pulling connected backbone chains closer together.

TRELOAR [191], TRELOAR & RIDING [193], and WU & VAN DER GIESSEN [206]. It is well-known that the affinity assumption between microscopic and macroscopic deformation is not in agreement with experimental observations, in particular in the range of large deformations. Consequently, BOYCE & ARRUDA [23] argued that the eight chain model yields more realistic results than the seemingly more precise affine full network models. A further improvement provides the non-affine microsphere model proposed in MIEHE ET AL. [129], which allows a flexible modeling of the locking stretches in multi-dimensional deformations. This microsphere model with a low number of physically-based material parameters shows an excellent fit to experimental results.

The stimulation of electroactive polymers by an electric field causes a change in size or shape. Due to their polymeric nature, EAP materials can be easily manufactured into various shapes, making them very versatile materials. Potential applications are artificial muscles, refreshable braille displays, drug delivery systems, or robotics applications such as flapping-wing ornithopters. The most common applications of smart materials are in actuators and sensors. A typical characteristic property is in contrast to piezoceramics that they will undergo a large amount of deformation while sustaining large forces. Some electroactive polymers can exhibit up to 380% strain. The existing electroactive materials are still exhibiting low conversion efficiency, that is to produce large deformations, a huge electric field needs to be applied. In addition, they are not robust, and there are no standard commercial materials available for consideration in practical applications.

The first scientific experiments with electroactive polymer materials emerged back in 1880. Wilhelm Röntgen fixed a rubber band at one end, attached a mass at the other as well as simultaneously charged and discharged the polymer to study the change in length. In 1925, the first piezoelectric polymer was discovered, consisting of a mixture of 45% carnauba wax, 45% white rosin, and 10% white beeswax. The ingredients were melted, mixed together, and left to cool in a static electric field. The mixture solidifies into a polymeric material that exhibits a piezoelectric effect. Recently, new electroactive materials emerged that exhibit large mechanical displacements in response to electric stimuli, enabling great potential as actuators in functional systems. To develop efficient and robust EAP materials for practical applications, the microscopic behavior needs to be understood and taken into account during the simulation process. Electroactive polymers are currently mainly distinguished by their activation mechanism: *Electronic EAPs* are deformed by electrostatic forces between adjacent electrodes while loaded by an electric

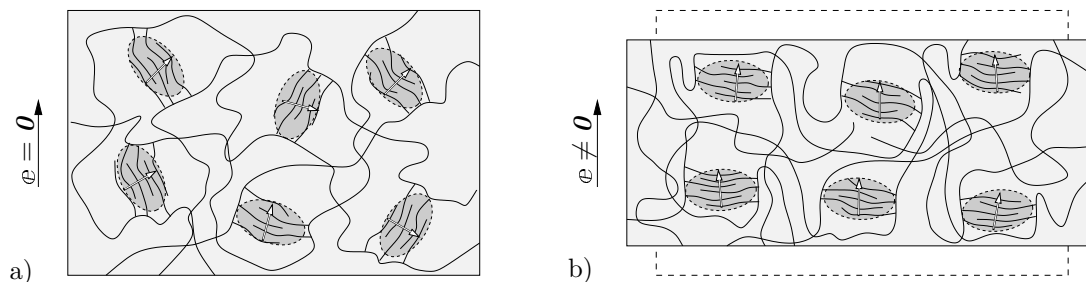


Figure 2.9: Schematic representation of the EAP deformation mechanism at the microscale. a) Randomly oriented dipole moments of the graft elastomer in zero electric field. b) The rotation of the graft units in an applied electric field causes shrinking in a parallel direction.

field. The material compresses in thickness (parallel to field) and expands in area (perpendicular to field). *Ionic EAPs* exhibit a mechanical deformation due to the diffusion of ions, however, require an electrolyte for the actuation process. The focus is on *electrostrictive graft elastomers*, an electronic EAP developed by NASA Langley Research Center, SU ET AL. [171, 172]. Their specific low mass, high performance, and ease of manufacturing makes them attractive for usage in aerospace and bio-mimetic applications (robotic hands, facial expressions). A comparison with other EAP materials reveals that the mechanical behavior is approximately 30 times stiffer than polyurethane (polyurethane: 15–20 MPa, electrostrictive graft elastomers: ~ 550 MPa), WANG ET AL. [201]. In the following, we will give a brief micromechanical motivation for graft elastomers. Consider the electric dipole in Figure 2.7 consisting of a positive and a negative charge separated by the distance $|\delta|$. Associated with this system is the dipole moment $p = q\delta$, where q is the magnitude of the charges while δ is the vector from the negative to the positive charge. Such a dipole in a uniform electric field e experiences a moment $m = p \times e$. This moment tends to rotate the dipole in the direction of the electric field, since this can be shown to be a stable configuration, see Figure 2.7. Consider next the deformation mechanism occurring in polymers, where crystalline particles are embedded in an amorphous matrix of cross-linked polymer chains. Such a microstructure appears in electrostrictive graft elastomer, consisting of flexible backbone chains (chlorotrifluoroethylene-vinylidene fluoride copolymer) with branching side chains (poly(vinylidene fluoride-trifluoroethylene) copolymer), see SU ET AL. [171, 173], WANG ET AL. [201], and SUN ET AL. [175]. Here, the side chains are cross-linked to adjacent backbone polymers and form crystal units. These grafted polar crystalline moieties are responsible for the shape changes induced by the electric field as visualized in Figure 2.8. Backbone chains as well as graft moieties contain atoms with two partial electric charges (positive and negative) generating a dipole moment. The dipole moments of backbone chains orient randomly and nullify each other. The graft dipoles, however, form grafted polar crystalline moieties by arranging in patterns such that the individual dipole moments of the monomers do not cancel out. As a result, the crystalline graft units have a net dipole moment. In a sufficiently strong electric field, these crystalline graft units rotate in order to orient their dipole moment along the field, see Figure 2.8b. In this process, they cause the flexible graft chains to wrap around the moieties, which pulls the backbone chains towards the crystal unit. The rotation causes a shrinking in the direction parallel to the applied electric field. As a consequence, Figure 2.9 depicts the resulting overall shrinking of the microstructure in the direction parallel to the applied electric field. This behavior is identical for an electric field pointing in the opposite direction, hence, representing an *electrostrictive effect*.

— Part I —

**Fundamentals of Electro-Mechanics
and Homogenization**

Foundations of Continuum Mechanics and Electrostatics

This chapter provides fundamental knowledge of finite strain continuum mechanics and electrostatics, which is the basis to the modeling of coupled electro-mechanical problems. The focus is on a geometric setting of large strain continuum mechanics, where metric tensors appear as natural elements for the connection between tangent and cotangent spaces. The stress- and strain-like quantities of electro-mechanics are presented, and transformations between reference and actual configuration reviewed. To enhance purely mechanical formulations, the electric field is physically motivated and fundamental laws of physics are presented. The main ingredients are provided by Coulomb's law, Gauss's law, and Faraday's law formulated for the electrostatic case. The mathematical description of purely mechanical balance principles is extended to electro-mechanical influences. The interaction of matter with electric fields is considered by additional electric force, couple, and energy supply terms within the balance equations.

3.1. Fundamentals of continuum mechanics

The mechanics of continuous media is a fundamental field of knowledge used to describe certain phenomena in deforming systems and lays the groundwork for all advanced fields of applied mechanics. Kinematics in large strain continuum mechanics are based on the introduction of the nonlinear deformation map, describing the motion from the Lagrangian to the Eulerian manifold. The focus is on a geometric setting, using the nomenclature of co- and contravariant objects for the description in a general base system. Hence, material and spatial metric coefficients are introduced to connect tangent and cotangent spaces and act as index lowering or raising operators. This viewpoint is mainly adopted from the lectures MIEHE [119, 120] on advanced mechanics held at the Institute of Applied Mechanics at the University of Stuttgart. This section has an introductory character and is by no means complete. For further explanations including an introduction to tensor algebra and analysis, the interested reader is referred to the classical textbooks TRUESDELL & NOLL [194], GURTIN [53], MARSDEN & HUGHES [109], OGDEN [142], HOLZAPFEL [67], BAŞAR & WEICHERT [3], HAUPT [59], and GURTIN ET AL. [55].

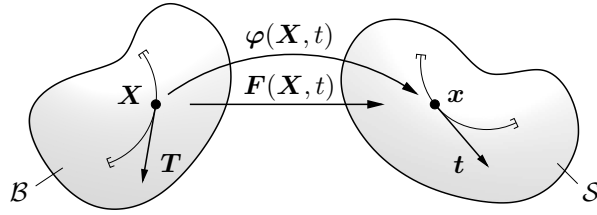


Figure 3.1: *The deformation map and deformation gradient.* The motion of the body \mathcal{B} in the Euclidean space is described by the deformation map $\varphi(\mathbf{X}, t)$, mapping points from the reference to the current configuration $\varphi : (\mathbf{X}, t) \mapsto \mathbf{x} = \varphi(\mathbf{X}, t)$. The deformation gradient $\mathbf{F}(\mathbf{X}, t)$ maps material tangent vectors \mathbf{T} at Lagrangian curves onto spatial tangent vectors $\mathbf{t} = \mathbf{F}\mathbf{T}$ at deformed material curves.

3.1.1. Motion of a material body

A material body B is a physical object mathematically described by a set of material points $P \in B$ that are in a *one-to-one relationship* to a domain in the Euclidean space \mathcal{R}^3 . The placement or configuration of the material body in \mathcal{R}^3 is characterized by the map

$$\chi : \begin{cases} B \rightarrow \mathcal{B} \subset \mathcal{R}^3, \\ P \mapsto \mathbf{X} = \chi(P), \end{cases} \quad (3.1)$$

where $\mathbf{X} \in \mathcal{B}$ is the place a particle occupies in the Euclidean space. The parametrization of the placement by the time gives us the motion of the body χ_t as a family of configurations. It is common practice to label an arbitrary placement of the body at a time t_0 as the reference or Lagrangian configuration $\chi_{t_0}(B) = \mathcal{B}$ with Lagrangian coordinates $\chi_{t_0}(P) = \mathbf{X} \in \mathcal{B} \subset \mathcal{R}^3$ with respect to the global Cartesian frame $\{\mathbf{E}_i\}_{i=1,3}$. The current or Eulerian configuration is likewise denoted as $\chi_t(B) = \mathcal{S}$ with the spatial coordinates $\chi_t(P) = \mathbf{x} \in \mathcal{S} \subset \mathcal{R}^3$ at the current time t . In order to describe the motion of the body in the Euclidean space, the *nonlinear deformation map* $\varphi(\mathbf{X}, t)$ is introduced as a point map of the reference to the current position

$$\varphi : \begin{cases} \mathcal{B} \rightarrow \mathcal{S} = \varphi_t(\mathcal{B}), \\ \mathbf{X} \mapsto \mathbf{x} = \varphi(\mathbf{X}, t), \end{cases} \quad (3.2)$$

see [Figure 3.1](#) for an image of the mapping between reference and current configuration.

3.1.2. The deformation gradient: Line, area, and volume map

It is now of interest how material tangent vectors to material curves are transformed to spatial tangent vectors to the deformed curves. To achieve such a mapping one needs to introduce the so-called *deformation gradient* \mathbf{F} as the Fréchet derivative of the deformation map with respect to material coordinates

$$\boxed{\mathbf{F}(\mathbf{X}) = \nabla_{\mathbf{X}}\varphi(\mathbf{X}, t)} \quad (3.3)$$

which is understood as the partial derivative of the motion $\varphi(\mathbf{X}, t)$ with respect to the material coordinate \mathbf{X} . The deformation gradient plays the central role in the kinematics of finite strains and is constrained by the condition $J := \det[\mathbf{F}] > 0$ to avoid material

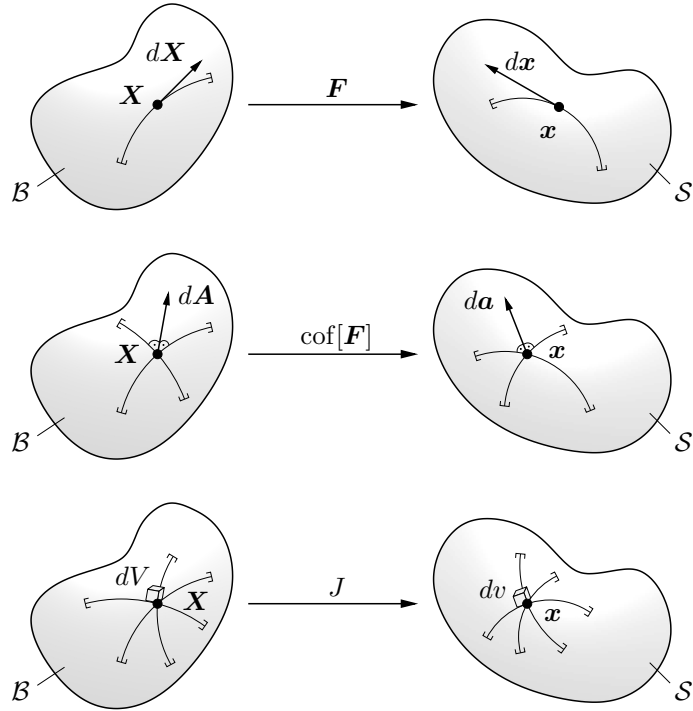


Figure 3.2: Three basic mappings of continuum mechanics. The tangent map $d\mathbf{x} = \mathbf{F}d\mathbf{X}$ maps line elements from the material to the current configuration by the deformation gradient, the area map or Nanson's formula $d\mathbf{a} = \text{cof}[\mathbf{F}]d\mathbf{A}$ transforms area elements, and the volume map $dv = JdV$ by the Jacobian shifts material volume elements to their spatial counterpart.

penetration and grant a one-to-one bijective relation between material and spatial position \mathbf{X} and \mathbf{x} , respectively. It is understood as a linear mapping of material tangents $\mathbf{T} \in \mathcal{B}$ to spatial tangents $\mathbf{t} \in \mathcal{S}$. Next, consider a material area element $d\mathbf{A} = \mathbf{N}dA$. Employing *Nanson's formula*, one obtains its Eulerian counterpart $d\mathbf{a} = \mathbf{n}da = \text{cof}[\mathbf{F}] \cdot d\mathbf{A}$ in terms of the cofactor $\text{cof}[\mathbf{F}] := J\mathbf{F}^{-T}$ of the deformation gradient. Hence, the normal map connecting normals to material areas with normals to spatial areas is identified as \mathbf{F}^{-T} . In the same manner, we investigate the material volume element dV . Multiplication with the determinant of the deformation gradient J gives the Eulerian counterpart $dv = JdV$. A summary of the tangent, normal, and volume map is given by

$$\mathbf{F} : \begin{cases} T_X \mathcal{B} \rightarrow T_x \mathcal{S}, \\ \mathbf{T} \mapsto \mathbf{t} = \mathbf{F}\mathbf{T}, \end{cases} \quad \mathbf{F}^{-T} : \begin{cases} T_X^* \mathcal{B} \rightarrow T_x^* \mathcal{S}, \\ \mathbf{N} \mapsto \mathbf{n} = \mathbf{F}^{-T}\mathbf{N}, \end{cases} \quad J : \begin{cases} \mathcal{R}^3 \rightarrow \mathcal{R}^3, \\ dV \mapsto dv = JdV. \end{cases} \quad (3.4)$$

Figure 3.2 shows the graphical counterpart of the three basic geometric mappings of non-linear continuum mechanics.

3.1.3. The Cauchy-Green strain tensors

Given is a Lagrangian direction $\mathbf{T}(\mathbf{X})$ with unit length $|\mathbf{T}|_{\mathbf{G}} = \sqrt{\mathbf{T} \cdot \mathbf{G}\mathbf{T}} = 1$, where $\mathbf{G} = \delta_{AB}$ is the material metric tensor. The spatial object $\boldsymbol{\lambda}$ determines the stretch tensor in the Eulerian manifold and is given by the change of deformation in the direction of \mathbf{T} , yielding $\boldsymbol{\lambda} := \mathbf{F}\mathbf{T}$. The length of the stretch tensor can be computed in the Eulerian setting as $|\boldsymbol{\lambda}|_{\mathbf{g}} = \sqrt{\boldsymbol{\lambda} \cdot \mathbf{g}\boldsymbol{\lambda}}$ with $\mathbf{g} = \delta_{ab}$ being the spatial metric. Inserting the definition

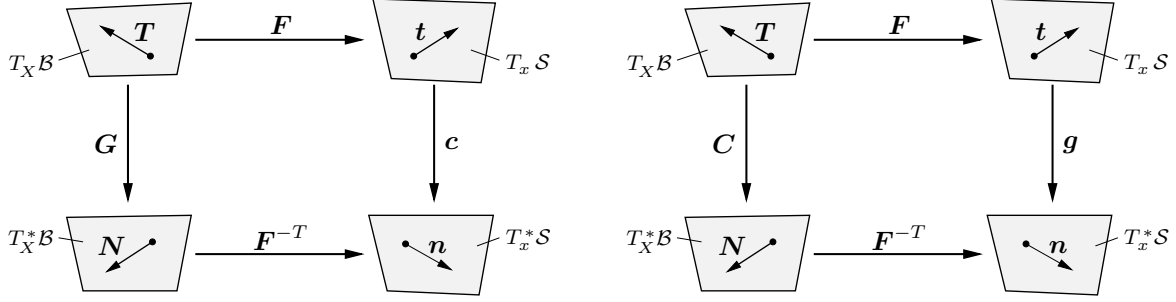


Figure 3.3: Mapping properties of metric tensors. Natural Lagrangian G and Eulerian metric tensor g map tangents onto normals in the respective manifold. The Lagrangian representation of the current metric is the right Cauchy-Green tensor $C = \varphi^*(g) = F^T g F$. The Eulerian representation of the reference metric is the left Cauchy-Green tensor $c = \varphi_*[G] = F^{-T} G F^{-1}$.

of λ allows the computation of this length $|\lambda|_g = \sqrt{T \cdot F^T g F T} = \sqrt{T \cdot C T} = |T|_C$ in the Lagrangian setting by the *right Cauchy-Green tensor*

$$C := \varphi^*(g) = F^T g F, \quad (3.5)$$

as the pull-back $\varphi^*(\cdot)$ of the current metric in the material setting. In a dual manner, $\varphi_*[\cdot]$ is introduced as the push-forward of Lagrangian objects to the Eulerian configuration, resulting in the *left Cauchy-Green tensor* as the representation of the material metric in the spatial setting

$$c := \varphi_*[G] = F^{-T} G F^{-1}. \quad (3.6)$$

For convenience, its inverse is referred to as the *Finger tensor* $b := c^{-1} = F G^{-1} F^T$. The geometric interpretation of these tensors leads us to the commutative diagrams shown in [Figure 3.3](#), visualizing the pull-back and push-forward operations of the Eulerian and Lagrangian metrics.

3.1.4. Velocity gradient and Lie derivative

Consider the material time derivative of the spatial stretch vector $\dot{\lambda} = \dot{F} T$. It is governed by the material velocity gradient $L := \dot{F}$, reflecting the total time derivative of the deformation gradient for a time-independent reference configuration. On the other hand, the temporal change $\dot{\lambda}$ in terms of the stretch itself reads $\dot{\lambda} = \dot{F}(F^{-1} \lambda) = l \lambda$, where the spatial velocity gradient

$$l = \dot{F} F^{-1} = \nabla_x v(x, t) \quad (3.7)$$

characterizes the relative change of a spatial object with respect to its current state in the Eulerian configuration. The Lie derivative of a spatial object describes its relative change with respect to time, keeping the basis vectors fixed. It is associated with that part of the total time derivative ascertained by an observer sitting in the moving frame of the current configuration and is thus a priori objective. Consider a spatial object (\cdot) , the Lie derivative is defined in three steps

$$\mathcal{L}_v(\cdot) = \varphi_* \left[\frac{d}{dt} \{ \varphi^*(\cdot) \} \right]. \quad (3.8)$$

First, a pull-back operation of the Eulerian object to its material counterpart is performed. Then, the material time derivative of the Lagrangian object is performed and finally the

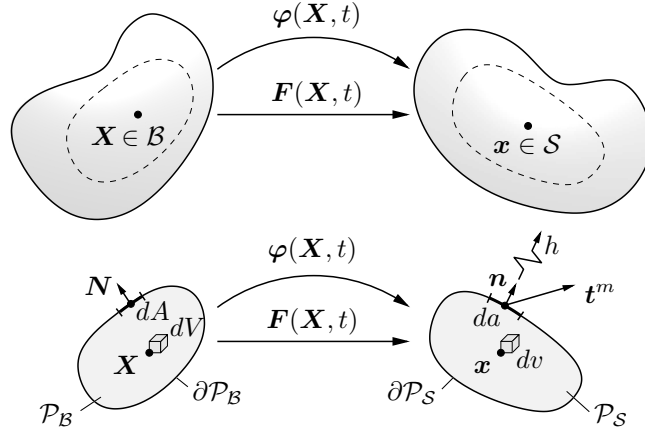


Figure 3.4: *Euler's cut principle.* Lagrangian and Eulerian parts \mathcal{P}_B and \mathcal{P}_S cut out of the whole body \mathcal{B} and \mathcal{S} . At a point $\mathbf{x} \in \partial\mathcal{P}_S$, the mechanical and thermal actions of the remaining part of \mathcal{S} are replaced by the mechanical traction vector $\mathbf{t}^m = \boldsymbol{\sigma}^m \mathbf{n}$ and the heat flux $h = \mathbf{q}\mathbf{n}$.

resultant quantity is pushed-forward to the spatial configuration. In particular, the Lie derivation of the spatial metric \mathbf{g} , representing the constant Kronecker symbol in Cartesian coordinate systems, is considered. It coincides with the spatial rate-of-deformation tensor \mathbf{d} , that is the symmetric part of the spatial velocity gradient

$$\mathcal{L}_{\mathbf{v}}\mathbf{g} = \mathbf{F}^{-T}\dot{\mathbf{C}}\mathbf{F}^{-1} = \mathbf{g}\mathbf{l} + \mathbf{l}^T\mathbf{g} = 2\mathbf{d}. \quad (3.9)$$

Note that the Lie derivative yields objective rates of tensors, that is, they are invariant under superimposed rigid body motions.

3.1.5. The concept of mechanical stresses

Consider a material body in its deformed configuration \mathcal{S} and an arbitrary subdomain $\mathcal{P}_S \subset \mathcal{S}$ that is cut out of the material body, see Figure 3.4. Following the methodology of *Euler's cut principle*, the effects of the rest body on \mathcal{P}_S are replaced by the surface traction \mathbf{t}^m and the heat flux h , governing mechanical and thermal effects, respectively. According to *Cauchy's theorem*, the contact force \mathbf{t}^m , as a function of its spatial position $\mathbf{x} \in \partial\mathcal{P}_S$ at time t , is a linear function of the outward normal \mathbf{n}

$$\mathbf{t}^m(\mathbf{x}, t; \mathbf{n}) = \boldsymbol{\sigma}^m(\mathbf{x}, t)\mathbf{n} \quad (3.10)$$

with $\boldsymbol{\sigma}^m : \mathbf{n} \mapsto \mathbf{t}^m = \boldsymbol{\sigma}^m \mathbf{n}$ being the mechanical *true* or *Cauchy stress* that relates the actual force to the deformed area. The Cauchy stress can therefore be seen as an Eulerian object that describes a mapping between the two vector spaces. It is the canonical stress tensor with basic physical meaning, however, not the convenient one for modeling purposes. Multiplication of $\boldsymbol{\sigma}^m$ with the Jacobian J reveals the so-called *Kirchhoff stress* tensor $\boldsymbol{\tau}^m = J\boldsymbol{\sigma}^m$. This weighted stress $\boldsymbol{\tau}^m$ is also an Eulerian object that maps spatial normals onto volumetrically scaled spatial tangents

$$\boldsymbol{\tau}^m : \begin{cases} T_x^* \mathcal{S} \rightarrow T_x \mathcal{S}, \\ \mathbf{n} \mapsto J\mathbf{t}^m = \boldsymbol{\tau}^m \mathbf{n}. \end{cases} \quad (3.11)$$

Relating the actual force to the reference area, one obtains by the Cauchy-type relation

$$\mathbf{T}^m(\mathbf{X}, t; \mathbf{N}) = \tilde{\mathbf{P}}^m(\mathbf{X}, t)\mathbf{N} \quad (3.12)$$

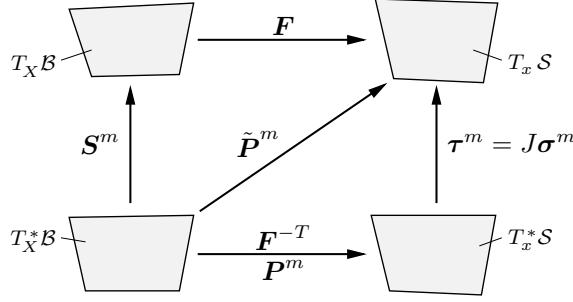


Figure 3.5: Mapping properties of mechanical stress tensors. Lagrangian second Piola-Kirchhoff stress $\mathbf{S}^m : \mathbf{N} \mapsto \tilde{\mathbf{T}}^m = \mathbf{S}^m \mathbf{N}$, Eulerian Kirchhoff stress $\boldsymbol{\tau}^m : \mathbf{n} \mapsto \mathbf{J} \mathbf{t}^m = \boldsymbol{\tau}^m \mathbf{n}$, and two-point first Piola-Kirchhoff stress tensor $\tilde{\mathbf{P}}^m : \mathbf{N} \mapsto \mathbf{T}^m = \tilde{\mathbf{P}}^m \mathbf{N}$.

the *nominal* or *first Piola-Kirchhoff stress* as a two-field tensor interpreted as a mapping between the material cotangent space $T_X^* \mathcal{B}$ and the spatial tangent space $T_x \mathcal{S}$

$$\tilde{\mathbf{P}}^m : \begin{cases} T_X^* \mathcal{B} \rightarrow T_x \mathcal{S}, \\ \mathbf{N} \mapsto \mathbf{T}^m = \tilde{\mathbf{P}}^m \mathbf{N}. \end{cases} \quad (3.13)$$

The first Piola-Kirchhoff stress is the conveniently used stress for experimental investigations, that is in standard tensile tests of metallic specimens. A transformation between $\boldsymbol{\tau}^m$ and $\tilde{\mathbf{P}}^m$ is achieved by employing the normal map $\tilde{\mathbf{P}}^m = \mathbf{J} \boldsymbol{\sigma}^m \mathbf{F}^{-T} = \boldsymbol{\tau}^m \mathbf{F}^{-T}$. Considering a purely Eulerian and a mixed-variant stress tensor, the purely Lagrangian *second Piola-Kirchhoff stress* \mathbf{S}^m is introduced as the relation between the fictitious reference force to the reference area. It is defined as the pull-back of the Kirchhoff stress to the Lagrangian setting $\mathbf{S}^m := \mathbf{F}^{-1} \boldsymbol{\tau}^m \mathbf{F}^{-T}$. Note that the Lagrangian stress tensor \mathbf{S}^m is a purely geometric object with no physical meaning. In particular, no Cauchy-type theorem exists as the reference configuration is meant to be stress-free and no surface traction exists a priori, whereas the tractions \mathbf{t}^m and \mathbf{T}^m are Eulerian objects. A geometric summary of the mapping properties of mechanical stresses is shown in Figure 3.5.

3.1.6. Mechanical power expressions

The mechanical stress power \mathcal{P}^m per unit mass of the reference configuration can be expressed in three different geometric settings. The full work needed by an (in)elastic continuum to deform from the reference to the current configuration in the time interval $[0, t]$ can be measured by

$$W := \int_{\mathcal{B}} w_0^t dV \quad \text{with} \quad w_0^t := \int_0^t \varrho_0 \mathcal{P}^m d\tau, \quad (3.14)$$

with w being the work per unit reference volume. The stress power is defined as stress times strain-rate, leading to the necessity of dual stress and strain objects in the respective geometric settings

$$\boxed{\varrho_0 \mathcal{P}^m := \underbrace{\mathbf{P}^m : \dot{\mathbf{F}}}_{\text{two-point}} = \underbrace{\mathbf{S}^m : \frac{1}{2} \dot{\mathbf{C}}}_{\text{Lagrangian}} = \underbrace{\boldsymbol{\tau}^m : \frac{1}{2} \mathcal{L}_v \mathbf{g}}_{\text{Eulerian}}} \quad (3.15)$$

As mechanical work conjugated or dual objects, we identify in the *geometric two-point setting* the alternative mixed-variant first Piola-Kirchhoff stress \mathbf{P}^m and the deformation gradient \mathbf{F} ¹. In the *Lagrangian setting* the second Piola-Kirchhoff stress \mathbf{S}^m and the right Cauchy-Green tensor \mathbf{C} and in the *Eulerian setting* the Kirchhoff stress $\boldsymbol{\tau}^m$ and the spatial metric \mathbf{g} are work conjugate. These are the input for a constitutive formulation based on the second axiom of thermodynamics. Observe that all subsequent treatments can be performed in the three basic and equivalent geometric settings.

3.2. Fundamentals of electrostatics

To enhance purely mechanical formulations, the electric field is physically motivated and added as additional independent variable to be taken into account. The elementary electro-mechanical laws and quantities are introduced, that is the Gauss law, Coulomb's law, and Faraday's law of electrostatics. The point charges involved within the derivation are assumed to be stationary with respect to each other. Interactions with magnetic quantities are a priori excluded. This section is a conglomerate of ideas presented in TOUPIN [190], LANDAU & LIFSHITZ [101], ERINGEN [42], PENFIELD & HAUS [146], IRODOV [74], MAUGIN [110], JACKSON [75], and GRIFFITHS [52]. The first part deals with the theory of electrostatics in free space, where no matter is present. The fundamental physical principles are introduced and later on extended to ponderable media placed in an external electric field.

3.2.1. Coulomb's and Faraday's law

The fundamental laws of electromagnetic field theory are the result of observations and experiments. The existence of two different charges, positive and negative ones, was postulated to explain simple experiments with amber and fur. Charges of the same sign repel each other while charges of opposite sign attract or in case of equal charge neutralize each other as far as external action is concerned. The force on a test charge q at position \mathbf{x} due to a single source charge Q at position \mathbf{x}' is defined by *Coulomb's law*

$$\mathbf{f} = kqQ \frac{\mathbf{x} - \mathbf{x}'}{|\mathbf{x} - \mathbf{x}'|^3}. \quad (3.16)$$

Coulomb's constant is given in SI-units by $k = 1/(4\pi\epsilon_0)$ in terms of the permittivity of free space $\epsilon_0 = 8.854 \cdot 10^{-12}$ [F/m]. The force is repulsive if test charge q and source Q have same sign, attractive for opposite ones. The fact that charges repel or attract each other implies the existence of a quantity that measures the intensity of such an interaction. We observe that a test charge q , placed in an electric field generated by an arbitrary system of charges experiences a force \mathbf{f} that depends on the location in the field \mathbf{x} and the sign of the charge, see [Figure 3.6a](#). This force can be approximated by the polynomial form

$$\mathbf{f}(\mathbf{x}, q) = q\mathbf{e}(\mathbf{x}) + q^2\mathbf{g}(\mathbf{x}) + \mathcal{O}(q) \quad (3.17)$$

¹According to (3.13), the first Piola-Kirchhoff stress $\tilde{\mathbf{P}}^m$ is a contravariant two-point tensor mapping Lagrangian covariant normals \mathbf{N} onto Eulerian contravariant tractions \mathbf{T}^m . For the stress power, an alternative mixed-variant representation $\mathbf{P}^m = \mathbf{g}\tilde{\mathbf{P}}^m$ is used dual to the deformation gradient \mathbf{F} . Within this work, the description is related to Cartesian frames and metric tensors coincide with identity maps. Consequently, it appears to be appropriate to renounce the distinction between both representations.

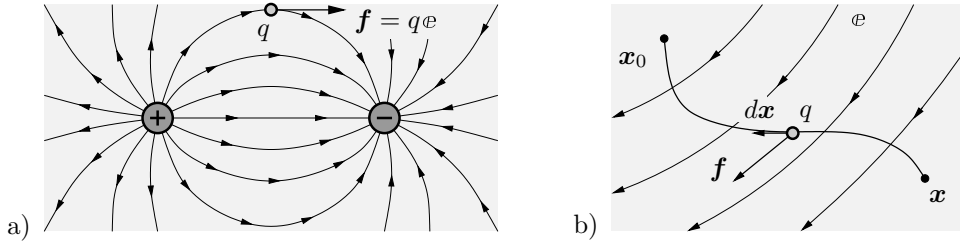


Figure 3.6: *The electric field and electric potential.* a) Consider the test charge q in an electric field induced by other charges. The point charge is subjected to a force $\mathbf{f} = q\mathbf{e}$, depending on its position in the electric field, with direction tangential to the field line. b) The point charge q moves along the path between the point \mathbf{x} and reference point \mathbf{x}_0 due to the electric field \mathbf{e} indicated by its field lines. For conservative fields with $\text{curl } \mathbf{e} = \mathbf{0}$ the line integral $\oint_C \mathbf{e} \cdot d\mathbf{x} = 0$ is path independent.

with \mathbf{e} and \mathbf{g} being vectorial coefficients and $\mathcal{O}(q)$ representing higher order terms in q . Assuming small values $q \rightarrow 0$ so that its presence does not alter appreciably the field configuration, equation (3.17) reduces to $\mathbf{f}(\mathbf{x}, q) = q\mathbf{e}(\mathbf{x})$, that is force equals to charge times electric field, yielding the *spatial electric field vector*

$$\mathbf{e}(\mathbf{x}) = \lim_{q \rightarrow 0} \frac{\mathbf{f}(\mathbf{x}, q)}{q} \quad (3.18)$$

given in units Newton per Coulomb or Volt per meter. Combining (3.16) and (3.18), the electric field at position \mathbf{x} due to a single source charge Q at position \mathbf{x}' is

$$\mathbf{e}(\mathbf{x}) = \frac{Q}{4\pi\epsilon_0} \frac{\mathbf{x} - \mathbf{x}'}{|\mathbf{x} - \mathbf{x}'|^3}. \quad (3.19)$$

Note that inserting test charges into the electric field of a source charge alters the position of the source due to repulsion or attraction. For simplicity we assume that in the limit of $q \rightarrow 0$ the positional distortion of the source is negligible. Keep in mind that this simplification is physically unreasonable regarding the fact that the smallest possible charge is the charge of an electron which has a discrete value. The *principle of superposition* states that the resultant force on a test particle due to several source charges Q_i at position \mathbf{x}'_i for $i = 1, \dots, n$ is the vector sum of the forces due to the charges individually. Henceforth, the electric field produced by a continuous distribution of charges can be described by the volume charge density $\rho^e(\mathbf{x}')$ confined to a volume \mathcal{S} , that is

$$\mathbf{e}(\mathbf{x}) = \frac{1}{4\pi\epsilon_0} \sum_{i=1}^n Q_i \frac{\mathbf{x} - \mathbf{x}'_i}{|\mathbf{x} - \mathbf{x}'_i|^3} = \frac{1}{4\pi\epsilon_0} \int_{\mathcal{S}} \rho^e(\mathbf{x}') \frac{\mathbf{x} - \mathbf{x}'}{|\mathbf{x} - \mathbf{x}'|^3} dv'. \quad (3.20)$$

Due to convenient mathematical properties of the electrostatic field, its computation can be reduced to the determination of a scalar field instead of the unknown electric vector field. Identifying the relation $\frac{\mathbf{x} - \mathbf{x}'}{|\mathbf{x} - \mathbf{x}'|^3} = -\nabla_{\mathbf{x}} \left(\frac{1}{|\mathbf{x} - \mathbf{x}'|} \right)$ from vector calculus allows a significant simplification of Coulomb's law (3.20). Since the gradient operator is with respect to \mathbf{x} , but the integration variable is the location of the source charge \mathbf{x}' , it can be taken outside the integral

$$\mathbf{e}(\mathbf{x}) = -\nabla_{\mathbf{x}} \left(\frac{1}{4\pi\epsilon_0} \int \frac{\rho^e(\mathbf{x}')}{|\mathbf{x} - \mathbf{x}'|} dv' \right). \quad (3.21)$$

In consideration of the property $\nabla \times \nabla a = 0$, that holds for all scalar functions a , it follows directly the important property

$$\boxed{\text{curl } e = \mathbf{0}} \quad (3.22)$$

known as *Faraday's law* in electrostatics, also referred to as electric compatibility, together with the definition $\text{curl}(\cdot) = \nabla_{\mathbf{x}} \times (\cdot)$. It is much easier to deal with a scalar potential than to determine all three components of the electric field. To this end, we introduce the *electric potential*

$$e = -\nabla\phi(\mathbf{x}) \quad \text{with} \quad \phi(\mathbf{x}) := \frac{1}{4\pi\epsilon_0} \int \frac{\rho^e(\mathbf{x}')}{|\mathbf{x} - \mathbf{x}'|} dv'. \quad (3.23)$$

A physical interpretation of the electric potential ϕ is performed by considering the work done in moving a charge from an arbitrary point \mathbf{x} to a reference point \mathbf{x}_0 in the presence of an electric field. The force on the charge is according to Coulomb's law $\mathbf{f} = qe$, so that the work done moving the charge is

$$w^e = \int_{\mathbf{x}}^{\mathbf{x}_0} \mathbf{f} \cdot d\mathbf{x} = - \int_{\mathbf{x}_0}^{\mathbf{x}} \mathbf{f} \cdot d\mathbf{x} = -q \int_{\mathbf{x}_0}^{\mathbf{x}} e \cdot d\mathbf{x}. \quad (3.24)$$

The minus sign indicates that the work done on moving the test charge against the field is computed. By taking into account (3.23), the work becomes

$$w^e = -q \int_{\mathbf{x}_0}^{\mathbf{x}} e \cdot d\mathbf{x} = q \int_{\mathbf{x}_0}^{\mathbf{x}} \nabla\phi \cdot d\mathbf{x} = q(\phi(\mathbf{x}) - \phi(\mathbf{x}_0)) \quad (3.25)$$

showing that $q\phi$ is the potential energy of a test charge in an electric field, see Figure 3.6b. Furthermore, the line integral does not depend on a specific path, yielding a conservative electric field. If now $\mathbf{x} = \mathbf{x}_0$, the total work around the closed curve \mathcal{C} is zero and $\oint_{\mathcal{C}} e \cdot d\mathbf{x} = 0$. Note that path independence does not hold for non-conservative fields as for instance in electromagnetism. The reference point is usually chosen at infinity $\mathbf{x}_0 \rightarrow \infty$, where the electric potential is assumed to vanish. Hence, the electric potential can be written as

$$\phi(\mathbf{x}) = - \int_{\mathbf{x}_0}^{\mathbf{x}} e \cdot d\mathbf{x}, \quad (3.26)$$

which will be used later on to determine the geometric transformation of the electric field from the current to the reference configuration.

3.2.2. The Gauss law of electrostatics

The *Gauss law* or *Gauss's flux theorem* is also known as the *first law of electrostatics* and states that “the total electric flux through any closed surface of any shape in an electric field is proportional to the total electric charge enclosed within the surface”. Consider a point charge Q in the center of a sphere with radius $|\mathbf{x} - \mathbf{x}'|$ enclosed by a Gaussian surface $\partial\mathcal{S}$. The electric field due to the source Q , see equation (3.19), is pointing in radial direction of the sphere

$$e = \frac{Q}{4\pi\epsilon_0} \frac{1}{|\mathbf{x} - \mathbf{x}'|^2} \mathbf{n} \quad \text{with} \quad \mathbf{n} := \frac{\mathbf{x} - \mathbf{x}'}{|\mathbf{x} - \mathbf{x}'|}, \quad (3.27)$$

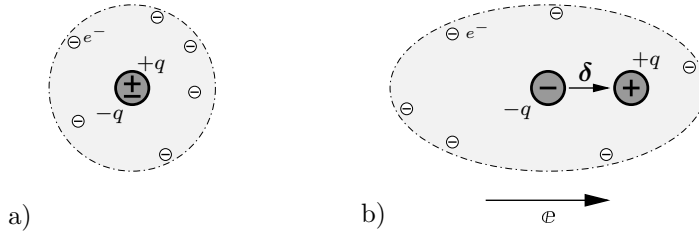


Figure 3.7: *The polarization effect of electrically neutral atoms.* a) The charge center of electrons coincides in the absence of an external electric field with the positive nucleus. b) Application of an electrical field separates the centers of charge. The electron cloud will be pulled in the direction of the positive pole of the field. The resultant electric dipole moment is $\tilde{p} = q\delta$. For illustrative purposes the deformation of the electron cloud is magnified.

where \mathbf{n} is the unit normal pointing radially outward. The area element on the sphere is considered in spherical coordinates as $da = |\mathbf{x} - \mathbf{x}'|^2 \sin\theta d\theta d\phi$. The electric flux through the surface is defined as the electric field multiplied by the area of the surface projected in a plane perpendicular to the field. For the single source charge under consideration

$$\mathbf{e} \cdot d\mathbf{a} = \mathbf{e} \cdot \mathbf{n} da = \frac{Q}{4\pi\epsilon_0} \sin\theta d\theta d\phi. \quad (3.28)$$

Integration of the normal component gives the total flux through the entire Gaussian surface

$$\oint_{\partial S} \mathbf{e} \cdot d\mathbf{a} = \frac{Q}{4\pi\epsilon_0} \int_0^\pi \sin\theta d\theta \int_0^{2\pi} d\phi = \frac{Q}{\epsilon_0}. \quad (3.29)$$

Note that this result is valid for a single source charge. It turns out that the choice of the closed surface is arbitrary and the application of the superposition principle for many charges Q_i distributed continuously by the volume charge density ρ^e results in

$$\oint_{\partial S} \mathbf{e} \cdot d\mathbf{a} = \sum_{i=1}^n \left(\oint_{\partial S} \mathbf{e}_i \cdot d\mathbf{a} \right) = \frac{1}{\epsilon_0} \sum_{i=1}^n Q_i = \frac{Q_{enc}}{\epsilon_0}, \quad (3.30)$$

where Q_{enc} is the total charge enclosed by the surface. The differential form of Gauss's law is obtained by the application of the divergence theorem for arbitrary volumes with $Q_{enc} = \int_S \rho^e dv$ as

$$\boxed{\epsilon_0 \operatorname{div} \mathbf{e} = \rho^e} \quad (3.31)$$

and relates the volume distribution of electric charges to the resulting electric field.

3.2.3. The electric field in matter

In the preceding, the electric field in vacuum was considered. These concepts will be extended to the case where matter is put into an electric field. To this end, the structure of an electrically neutral atom is reconsidered, where the average center of positive charges (protons) and negative charges (electrons) are located at the center due to symmetry of the nucleus and electron shell, respectively. The absence of external electric fields and the overlapping nature of charge centers is the reason for the electric neutrality of the atom, see Figure 3.7a. According to Coulomb's law, the existence of an external field deforms the orbit of the electrons and the symmetry of the shell will be broken. Hence, the average

center of the electrons will be shifted and the atom will not be electrically neutral any more. The atom has been polarized and became a dipole, see [Figure 3.7b](#). The dipole moment is defined as a vector containing the information about the electric charge and the distance between the average centers of opposite charges within the dipole. Since every material contains a huge number of atoms and hence also electric dipoles, a macroscopic quantity representing this effect is introduced. The vector of *electric polarization* is considered as the dipole moment per unit volume given by

$$\mathbb{P}(\mathbf{x}) = \lim_{\Delta v \rightarrow 0} \frac{\sum_i \tilde{\mathbb{P}}_i}{\Delta v}, \quad (3.32)$$

where $\tilde{\mathbb{P}}_i$ is the dipole moment of the i th type of molecule in the medium and Δv an infinitesimal volume element. Materials in which the polarization attains non zero values are called *dielectric materials* as $\mathbb{P} = \mathbf{0}$ in vacuum. The electric potential at position \mathbf{x} due to the electric charge and dipole moment of an infinitesimal volume is

$$\Delta\phi(\mathbf{x}, \mathbf{x}') = \frac{1}{4\pi\epsilon_0} \frac{\mathbb{P}(\mathbf{x}') \cdot (\mathbf{x} - \mathbf{x}')}{|\mathbf{x} - \mathbf{x}'|^3} \Delta v, \quad (3.33)$$

where \mathbf{x} is outside the volume Δv and the polarization characterizes the interaction of material and electric field. Passing to an integral version gives the potential of a polarized dielectric body \mathcal{S} , that is

$$\phi(\mathbf{x}) = \frac{1}{4\pi\epsilon_0} \int_{\mathcal{S}} \frac{\mathbb{P}(\mathbf{x}') \cdot (\mathbf{x} - \mathbf{x}')}{|\mathbf{x} - \mathbf{x}'|^3} dv'. \quad (3.34)$$

Using the integration factor given in the previous subsection and applying the divergence theorem, the latter is transformed into the more useful form

$$\phi(\mathbf{x}) = \frac{1}{4\pi\epsilon_0} \int_{\mathcal{S}} \frac{\rho_b^e}{|\mathbf{x} - \mathbf{x}'|} dv' + \frac{1}{4\pi\epsilon_0} \int_{\partial\mathcal{S}} \frac{\sigma_b^e}{|\mathbf{x} - \mathbf{x}'|} da', \quad (3.35)$$

where $\rho_b^e := -\operatorname{div} \mathbb{P}$ is the volume density of bound charges and $\sigma_b^e := \mathbb{P} \cdot \mathbf{n}$ the surface density of bound charges. Analyzing this equation shows that the electric potential produced by matter placed in an electric field has two kinds of sources. The first is the bound charge distributed over the volume of the material and the second the polarized charge distributed over the surface. The total charge density of a dielectric has now contributions due to bound and free charges $\rho^e = \rho_f^e + \rho_b^e$, where the bound charges are caused by the polarization and the free charges by everything else. With this at hand, the *Gauss law* in differential form becomes

$$\boxed{\operatorname{div} \mathbf{d} = \rho_f^e} \quad (3.36)$$

by defining the electric displacement or electric induction $\mathbf{d} := \epsilon_0 \mathbf{e} + \mathbb{P}$. In integral form, the Gauss law can be written as

$$\oint_{\partial\mathcal{S}} \mathbf{d} \cdot d\mathbf{a} = Q_{f,enc} \quad (3.37)$$

in terms of the total free charges $Q_{f,enc} = \int_{\mathcal{S}} \rho_f^e dv$ enclosed in the volume \mathcal{S} . It is noteworthy that one of the three fields (electric field, displacement, or polarization) introduced so far is redundant due to its dependency on the two others, outlining the auxiliary character

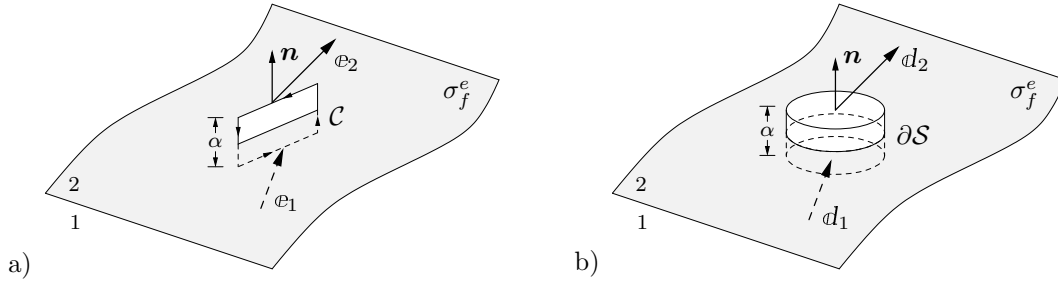


Figure 3.8: *Boundary conditions at an interface.* a) Thin rectangular loop \mathcal{C} and b) Gaussian pillbox $\partial\mathcal{S}$ with surface charge density of free charges σ_f^e . The normal \mathbf{n} points from medium 1 into medium 2 and the height $\alpha \rightarrow 0$ tends to zero.

of the electric displacement without deep physical meaning, IRODOV [74]. However, for the modeling purposes in focus of this work, it simplifies the description of the deformation in a dielectric medium.

Suppose a linear isotropic dielectric medium is placed in an electric field. The induced polarization is proportional to the external electric field such that $\mathbf{p} = \epsilon_0\chi\mathbf{e}$, where χ is the dimensionless *electric susceptibility* of the material. The electric displacement is hence also proportional to the applied field

$$\mathbf{d} = \epsilon_0\mathbf{e} + \epsilon_0\chi\mathbf{e} = \epsilon_0(1 + \chi)\mathbf{e} = \epsilon\mathbf{e}, \quad (3.38)$$

where $\epsilon_r = (1 + \chi)$ is the relative permittivity or dielectric constant of the material. For matter $\epsilon_r > 1$ and for vacuum $\epsilon_r = 1$. The values of the relative permittivity vary significantly depending on the material, that is approximately one for various gases and up to several thousand for ceramics. Examples are water with $\epsilon_r = 80.1$ or barium titanate with $\epsilon_r = 1250$ at room temperature.

3.2.4. Boundary conditions at interfaces between materials

Consider a material interface where the electric field and displacement in the respective materials are labeled by $\{\mathbf{e}_1, \mathbf{d}_1\}$ and $\{\mathbf{e}_2, \mathbf{d}_2\}$. The tangential boundary condition for the electric field is derived starting from the local form of Faraday's law $\text{curl } \mathbf{e} = \mathbf{0}$ applied to a closed rectangular loop \mathcal{C} as shown in Figure 3.8a. As the height $\alpha \rightarrow 0$ tends to zero, Stoke's theorem results in the continuity of the tangential component of the electric field over the interface

$$\oint_{\mathcal{C}} \mathbf{e} \cdot d\mathbf{x} = 0 \quad \longrightarrow \quad (\mathbf{e}_2 - \mathbf{e}_1) \times \mathbf{n} = \mathbf{0}. \quad (3.39)$$

The boundary condition for the normal component of the electric displacement is derived from Gauss's law applied to an elementary pillbox. Due to $\alpha \rightarrow 0$, the flux through the sides has no contribution, see Figure 3.8b. If free surface charges are present on the interface, the normal component has a discontinuity

$$\int_{\partial\mathcal{S}} \mathbf{d} \cdot \mathbf{n} da = \int_{\partial\mathcal{S}} \sigma_f^e da \quad \longrightarrow \quad (\mathbf{d}_2 - \mathbf{d}_1) \cdot \mathbf{n} = \sigma_f^e, \quad (3.40)$$

where σ_f^e is the surface charge density of free charges at the interface. An important special case is the interface between a dielectric (medium 1) and a conductor (medium 2). The external electric field acts on all charges inside the conductor and displaces the

negative ones in the direction against the field. This displacement continues till the charge distribution inside the conductor cancels the external field, hence the electric field and polarization are zero in a conductor. Equation (3.40) becomes

$$\boxed{-d \cdot \mathbf{n} = \sigma_f^e} \quad (3.41)$$

which can be interpreted as *Cauchy-type theorem* for the electric displacement. The subscript 1 is omitted here. This special case is important for electrode materials (e.g. graphite powder) used to apply the electric field to a dielectric medium.

3.2.5. Balance laws of coupled electro-mechanics

The fundamental laws in continuum mechanics are expressions of the conservation of physical quantities such as mass, linear and angular momentum as well as energy. They must be satisfied for all bodies and are usually formulated as global relationships in integral form. The electro-mechanical balance laws are formulated such that they incorporate additional contributions due to the interaction of the solid with the electric field, see for example TIERSTEN [187] and ERINGEN & MAUGIN [43]. Assuming a generic part \mathcal{P}_S cut out of the full body \mathcal{S} , the action of the rest body $\mathcal{S} \setminus \mathcal{P}_S$ is expressed in terms of phenomenological quantities such as heat flux and mechanical tractions, see Figure 3.4. The *global balance laws* in the spatial configuration are

$$\begin{aligned} 1. \text{ mass} & \quad \frac{d}{dt} \int_{\mathcal{P}_S} \varrho \, dv = 0, \\ 2. \text{ linear momentum} & \quad \frac{d}{dt} \int_{\mathcal{P}_S} \varrho \mathbf{v} \, dv = \int_{\mathcal{P}_S} \varrho \boldsymbol{\gamma} \, dv + \int_{\partial \mathcal{P}_S} \mathbf{t}^m \, da, \\ 3. \text{ angular momentum} & \quad \frac{d}{dt} \int_{\mathcal{P}_S} \mathbf{x} \times \varrho \mathbf{v} \, dv = \int_{\mathcal{P}_S} \mathbf{x} \times \varrho \boldsymbol{\gamma} + \varrho \boldsymbol{\omega}^e \, dv + \int_{\partial \mathcal{P}_S} \mathbf{x} \times \mathbf{t}^m \, da, \\ 4. \text{ energy} & \quad \frac{d}{dt} \int_{\mathcal{P}_S} \frac{1}{2} \varrho \mathbf{v} \cdot \mathbf{v} + \varrho e \, dv = \int_{\mathcal{P}_S} \varrho \boldsymbol{\gamma} \cdot \mathbf{v} + \varrho r \, dv + \int_{\partial \mathcal{P}_S} \mathbf{t}^m \cdot \mathbf{v} - h \, da, \end{aligned} \quad (3.42)$$

in terms of the mass density in the current configuration ϱ , the mechanical tractions $\mathbf{t}^m = \boldsymbol{\sigma}^m \mathbf{n}$, and the *total body force* per unit mass $\boldsymbol{\gamma} := \boldsymbol{\gamma}^m + \boldsymbol{\gamma}^e$ as sum of externally applied part and that caused by electric fields. Furthermore, we observe the *body couple* $\boldsymbol{\omega}^e$ due to electric fields per unit mass, the internal energy density per unit mass e , the heat flux $h = \mathbf{q} \mathbf{n}$, and the *total energy supply* per unit mass $r := r^m + r^e$ as sum of the prescribed part and that caused by electric fields. The body force, couple, and energy supply are generated by the interaction with the electric field and explicitly determined in the next subsection. If the considered fields are sufficiently smooth, these global laws can be transformed to *local statements*, valid at every point $\mathbf{x} \in \mathcal{S}$, by applying the Gauss and localization theorem

$$\begin{aligned} 1. \text{ mass} & \quad \dot{\varrho} + \varrho \operatorname{div}[\mathbf{v}] = 0 \quad \text{in } \mathcal{S}, \\ 2. \text{ linear momentum} & \quad \varrho \dot{\mathbf{v}} = \operatorname{div}[\boldsymbol{\sigma}^m] + \varrho \boldsymbol{\gamma}^m + \varrho \boldsymbol{\gamma}^e \quad \text{in } \mathcal{S}, \\ 3. \text{ angular momentum} & \quad \operatorname{skew}[\boldsymbol{\sigma}^m] = \varrho \hat{\boldsymbol{\omega}}^e \quad \text{in } \mathcal{S}, \\ 4. \text{ energy} & \quad \varrho \dot{e} = \boldsymbol{\sigma}^m : \mathbf{gl} + \varrho r^m + \varrho r^e - \operatorname{div}[\mathbf{q}] \quad \text{in } \mathcal{S}, \end{aligned} \quad (3.43)$$

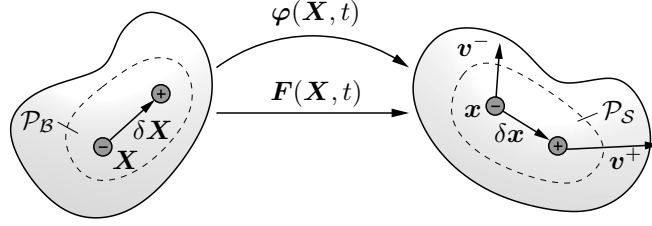


Figure 3.9: *The two-dipole model.* The cut out parts of the moving body in the reference \mathcal{P}_B and the current configuration \mathcal{P}_S possess at every point an electric dipole. Electric charges $\pm q$ in the current configuration at positive and negative poles move with velocity $\mathbf{v}^- = \mathbf{v} = \dot{\mathbf{x}}$ and $\mathbf{v}^+ = \mathbf{v} + \delta\mathbf{v} = \dot{\mathbf{x}} + \delta\dot{\mathbf{x}}$.

with the skew-symmetric second order tensor $\hat{\omega}_{ij}^e = \frac{1}{2} \epsilon_{ijk} \omega_k^e$, where $\boldsymbol{\omega}^e$ is the axial vector of $\hat{\boldsymbol{\omega}}^e$, and the spatial velocity gradient $\mathbf{l} = \dot{\mathbf{F}}\mathbf{F}^{-1}$. Note that the mechanical Cauchy stress $\boldsymbol{\sigma}^m$ is no longer symmetric ².

3.2.6. Electric force, couple, and energy supply

The electric body force $\boldsymbol{\gamma}^e$, the couple $\boldsymbol{\omega}^e$, and energy supply r^e are determined for electric fields satisfying the Maxwell equations, see TIERSTEN [187], MAUGIN & ERINGEN [111], and ERINGEN & MAUGIN [43]. In literature, there exist various approaches all including additional postulates, cf. PENFIELD & HAUS [146] for further details. In this work, we follow the approach used by PAO & HUTTER [143] who employ a *two-dipole model* of non-interacting dipoles to evaluate electric forces, see Figure 3.9. Such an approach is applicable solely to *macroscopic models*. On the micro-level, additional contributions need to be taken into account. Each point in the continuum has attached an electric dipole of positive and negative charges representing the polarization. Electric charges $\pm q$ are attached to the dipoles separated by the distance $\delta\mathbf{x}$. For the limit case, where $|\delta\mathbf{x}| \rightarrow 0$, the *polarization* \mathbb{p} is defined by

$$\mathbb{p} := \lim_{|\delta\mathbf{x}| \rightarrow 0} N^e q \delta\mathbf{x}, \quad (3.44)$$

where N^e is the total number of electric dipoles per unit volume. The forces acting on the charges of the dipoles are derived starting from a general expression of the *Lorentz*

²*Remark on balance of angular momentum:* In order to perform the total time derivative we use the volume map $dv = JdV$ and the time independent density in the reference frame $\rho_0 = J\rho$, yielding $\frac{d}{dt} \int_{\mathcal{P}_S} \mathbf{x} \times \rho \mathbf{v} dv = \int_{\mathcal{P}_S} \mathbf{x} \times \rho \dot{\mathbf{v}} dv$. For the term involving the traction vector we get in index notation after applying divergence theorem

$$\int_{\partial\mathcal{P}_S} \mathbf{x} \times \mathbf{t}^m da = \int_{\mathcal{P}_S} \epsilon_{ijk} x_i \sigma_{jl,l}^m + \epsilon_{ijk} \sigma_{ji}^m dv = \int_{\mathcal{P}_S} \epsilon_{ijk} x_i \sigma_{jl,l}^m - \epsilon_{ijk} \sigma_{ij}^m dv,$$

where we used the permutation property of the Levi-Civita symbol $\epsilon_{ijk} = -\epsilon_{jik}$. Insertion into the global form of the balance of angular momentum and application of localization theorem allows us to identify the local form of the balance of linear momentum (3.43)₂, reducing the equation to $\sigma_{ij}^m \epsilon_{ijk} = \rho \omega_k^e$. With the identity $\epsilon_{ijk} \epsilon_{mnk} = \delta_{im} \delta_{jn} - \delta_{in} \delta_{jm}$ we finally arrive at

$$\frac{1}{2} (\sigma_{ij}^m - \sigma_{ji}^m) = \frac{1}{2} \rho \epsilon_{ijk} \omega_k^e = \rho \hat{\omega}_{ij}^e,$$

defining the skew-symmetric tensor $\hat{\omega}_{ij}^e = \frac{1}{2} \epsilon_{ijk} \omega_k^e$ in terms of the electric body couple.

force $\mathbf{f}_L = q(\mathbf{e} + \mathbf{v} \times \mathbf{b})$. For a point charge q moving with velocity \mathbf{v} due to the electric field \mathbf{e} and the magnetic induction \mathbf{b} this force becomes

$$\mathbf{f}_q = q\mathbf{e} + q\mathbf{v} \times \mu_0\mathbf{h}, \quad (3.45)$$

where \mathbf{v} is the velocity of the material particle and (3.45) is only valid in free space where $\mathbf{b} = \mu_0\mathbf{h}$. Thus, using the Lorentz force for macroscopic charges inside a continuum is only a postulate. According to the two-dipole model under consideration, the negative electric charge $-q$ is considered at position \mathbf{x} , the positive $+q$ at $\mathbf{x} + \delta\mathbf{x}$. The velocities of the moving charges are $\mathbf{v}^- = \mathbf{v}$ and $\mathbf{v}^+ = \mathbf{v} + \delta\dot{\mathbf{x}}$. A Taylor series expansion of (3.45) yields the forces on the charges as

$$\begin{aligned} \mathbf{f}_q^- &= -q\mathbf{e}(\mathbf{x}) - q\mathbf{v} \times \mu_0\mathbf{h}(\mathbf{x}), \\ \mathbf{f}_q^+ &= q\mathbf{e}(\mathbf{x} + \delta\mathbf{x}) + q[\mathbf{v} + \delta\dot{\mathbf{x}}] \times \mu_0\mathbf{h}(\mathbf{x} + \delta\mathbf{x}) \\ &= q\mathbf{e}(\mathbf{x}) + q\nabla_{\mathbf{x}}\mathbf{e}(\mathbf{x}) \cdot \delta\mathbf{x} + q\mathbf{v} \times \mu_0\mathbf{h}(\mathbf{x}) \\ &\quad + q\mathbf{v} \times \mu_0\nabla_{\mathbf{x}}\mathbf{h}(\mathbf{x}) \cdot \delta\mathbf{x} + q\delta\dot{\mathbf{x}} \times \mu_0\mathbf{h}(\mathbf{x}) + \dots \end{aligned} \quad (3.46)$$

A unit material volume element contains N^e electric dipoles and no broken dipoles are considered. The force on each dipole can be written as the sum of the forces on the charges and thus we get the total force on the volume element due to polarization as

$$\begin{aligned} \varrho\gamma_{pol}^e &= \lim_{|\delta\mathbf{x}| \rightarrow 0} N^e(\mathbf{f}_q^- + \mathbf{f}_q^+) \\ &= \lim_{|\delta\mathbf{x}| \rightarrow 0} N^e [q\nabla_{\mathbf{x}}\mathbf{e} \cdot \delta\mathbf{x} + q\mathbf{v} \times \mu_0\nabla_{\mathbf{x}}\mathbf{h} \cdot \delta\mathbf{x} + q\delta\dot{\mathbf{x}} \times \mu_0\mathbf{h}] \\ &= \nabla_{\mathbf{x}}\mathbf{e} \cdot \mathbf{p} + \mu_0\mathbf{v} \times \nabla_{\mathbf{x}}\mathbf{h} \cdot \mathbf{p} + \mu_0\varrho \frac{d}{dt} \left(\frac{\mathbf{p}}{\varrho} \right) \times \mathbf{h}, \end{aligned} \quad (3.47)$$

where we used the definition of the polarization (3.44) and the relation $\lim_{|\delta\mathbf{x}| \rightarrow 0} N^e q\delta\dot{\mathbf{x}} = \varrho \frac{d}{dt} \left(\frac{\mathbf{p}}{\varrho} \right) = \frac{\partial}{\partial t} \mathbf{p} + \text{div}[\mathbf{p} \otimes \mathbf{v}]$. In addition to the body forces due to polarization, there is the force due to free charges $\rho_f^e \mathbf{e}$. Thus, the total force on an element of unit volume turns out to be $\varrho\gamma^e = \varrho\gamma_{pol}^e + \rho_f^e \mathbf{e}$. For the quasi-static case with $\mathbf{v} \approx \mathbf{0}$, the total *electric body* or *ponderomotive force* reduces to

$$\boxed{\varrho\gamma^e = \nabla_{\mathbf{x}}\mathbf{e} \cdot \mathbf{p} + \rho_f^e \mathbf{e}} \quad (3.48)$$

The electric couple is determined by evaluating the torque exerted by the force of the positive charge. From (3.46), the torque on an electric dipole is

$$\delta\mathbf{x} \times \mathbf{f}_q^+ = \delta\mathbf{x} \times [q\mathbf{e} + q\mathbf{v} \times \mu_0\mathbf{h} + \dots]. \quad (3.49)$$

In the limit case, the torque on a unit volume with N^e electric dipoles is given by $\varrho\boldsymbol{\omega}^e = \lim_{|\delta\mathbf{x}| \rightarrow 0} N^e(\delta\mathbf{x} \times \mathbf{f}_q^+) = \mathbf{p} \times \mathbf{e} + \mathbf{p} \times (\mathbf{v} \times \mu_0\mathbf{h})$, indicating the asymmetry of the mechanical Cauchy stress. In the quasi-static case, the *electric body couple* and its skew-symmetric part $\hat{\boldsymbol{\omega}}_{ij}^e = \frac{1}{2} \epsilon_{ijk} \omega_k^e$ reduce to

$$\boxed{\varrho\boldsymbol{\omega}^e = \mathbf{p} \times \mathbf{e} \quad \text{and} \quad \varrho\hat{\boldsymbol{\omega}}^e = \text{skew}[\mathbf{p} \otimes \mathbf{e}]} \quad (3.50)$$

Evaluating the *rate of work* done on an electric dipole by the forces \mathbf{f}_q^- and \mathbf{f}_q^+ with velocities $\mathbf{v}_e^- = \mathbf{v}$ and $\mathbf{v}_e^+ = \mathbf{v} + \delta\dot{\mathbf{x}}$ we get

$$\begin{aligned} \mathbf{f}_q^- \cdot \mathbf{v}_e^- + \mathbf{f}_q^+ \cdot \mathbf{v}_e^+ &= -q[\mathbf{e}(\mathbf{x}) + \mathbf{v} \times \mu_0 \mathbf{h}(\mathbf{x})] \cdot \mathbf{v} \\ &\quad + q[\mathbf{e}(\mathbf{x} + \delta\mathbf{x}) + (\mathbf{v} + \delta\dot{\mathbf{x}}) \times \mu_0 \mathbf{h}(\mathbf{x} + \delta\mathbf{x})] \cdot (\mathbf{v} + \delta\dot{\mathbf{x}}) \\ &= q\mathbf{e}(\mathbf{x}) \cdot \delta\dot{\mathbf{x}} + q(\nabla_{\mathbf{x}}\mathbf{e} \cdot \delta\mathbf{x}) \cdot \mathbf{v} + q(\nabla_{\mathbf{x}}\mathbf{e} \cdot \delta\mathbf{x}) \cdot \delta\dot{\mathbf{x}} + \dots \end{aligned} \quad (3.51)$$

Taking the limit $|\delta\mathbf{x}| \rightarrow 0$ and multiplying with the number of dipoles N^e , we obtain the work done per unit volume due to polarization $\varrho r^e = \lim_{|\delta\mathbf{x}| \rightarrow 0} N^e [\mathbf{f}_q^- \cdot \mathbf{v}_e^- + \mathbf{f}_q^+ \cdot \mathbf{v}_e^+] = \varrho\mathbf{e} \cdot \frac{d}{dt}\left(\frac{\mathbf{p}}{\varrho}\right) + (\nabla_{\mathbf{x}}\mathbf{e} \cdot \mathbf{p}) \cdot \mathbf{v}$. For the quasi-static case, the electric energy supply reduces to

$$\boxed{\varrho r^e = \varrho\mathbf{e} \cdot \frac{d}{dt}\left(\frac{\mathbf{p}}{\varrho}\right)} \quad (3.52)$$

The electric body force and couple are now used to introduce the concept of a total stress tensor combining mechanical and electric influences.

3.2.7. The concept of total stress

The electro-mechanical balance laws can be reformulated in terms of a *symmetric total stress tensor*. The interaction between solid matter and electric field is taken into account by the electric body force, couple, and energy supply. We define the additional stress tensor $\boldsymbol{\sigma}^e$ such that its divergence determines the electric body force and its skew-symmetric part the negative body couple tensor

$$\operatorname{div}[\boldsymbol{\sigma}^e] = \varrho\boldsymbol{\gamma}^e \quad \text{and} \quad \operatorname{skew}[\boldsymbol{\sigma}^e] = -\varrho\hat{\boldsymbol{\omega}}^e. \quad (3.53)$$

It is often referred to as the Maxwell stress tensor³ taking the form $\boldsymbol{\sigma}^e = \mathbf{e} \otimes \mathbf{d} - \frac{1}{2}\epsilon_0|\mathbf{e}|^2\mathbf{1}$. Insertion of equation (3.53) into the balance of linear and angular momentum gives

$$\operatorname{div}[\boldsymbol{\sigma}] + \varrho\boldsymbol{\gamma}^m = \mathbf{0} \quad \text{and} \quad \operatorname{skew}[\boldsymbol{\sigma}] = \mathbf{0} \quad (3.54)$$

in terms of the *symmetric total stress tensor* $\boldsymbol{\sigma} = \boldsymbol{\sigma}^m + \boldsymbol{\sigma}^e$ as sum of the mechanical Cauchy stress and electric Maxwell stress combining the interaction of matter and electric field.

³ *Proof of Maxwell stress:* Starting with the Maxwell equation $\operatorname{div}[\mathbf{d}] = \rho_f^e$ where the electric displacement is defined as $\mathbf{d} = \epsilon_0\mathbf{e} + \mathbf{p}$, the divergence of the Maxwell stress reads

$$\operatorname{div}[\boldsymbol{\sigma}^e] = \nabla_{\mathbf{x}}\mathbf{e} \cdot \mathbf{d} + \mathbf{e} \operatorname{div}[\mathbf{d}] - \epsilon_0\nabla_{\mathbf{x}}^T\mathbf{e} \cdot \mathbf{e} = \epsilon_0(\nabla_{\mathbf{x}}\mathbf{e} - \nabla_{\mathbf{x}}^T\mathbf{e}) \cdot \mathbf{e} + \nabla_{\mathbf{x}}\mathbf{e} \cdot \mathbf{p} + \rho_f^e\mathbf{e} = \nabla_{\mathbf{x}}\mathbf{e} \cdot \mathbf{p} + \rho_f^e\mathbf{e} \equiv \varrho\boldsymbol{\gamma}^e,$$

where we used Faraday's circuital law in the form $\operatorname{curl}(\cdot) \times \mathbf{a} = [\nabla_{\mathbf{x}}(\cdot) - \nabla_{\mathbf{x}}^T(\cdot)] \cdot \mathbf{a} = \mathbf{0}$. The skew-symmetric part of the Maxwell stress is

$$\operatorname{skew}[\boldsymbol{\sigma}^e] = \frac{1}{2}(\mathbf{e} \otimes \mathbf{p} - \mathbf{p} \otimes \mathbf{e}) = \operatorname{skew}[\mathbf{e} \otimes \mathbf{p}] = -\operatorname{skew}[\mathbf{p} \otimes \mathbf{e}] \equiv -\varrho\hat{\boldsymbol{\omega}}^e,$$

coinciding with the skew-symmetric tensor $\varrho\hat{\boldsymbol{\omega}}^e$ defined by the electric body couple $\hat{\omega}_{ij}^e = \frac{1}{2}\epsilon_{ijk}\omega_k^e$.

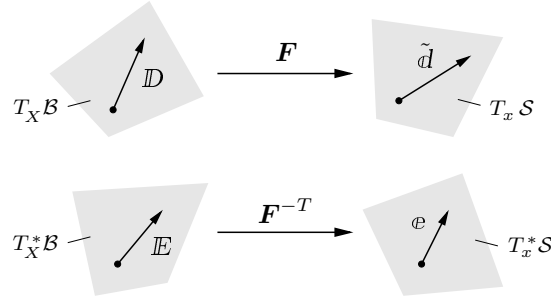


Figure 3.10: Geometric mapping properties of electric displacement and electric field. The contravariant Kirchhoff-type electric displacement $\tilde{\mathbf{d}} := J\mathbf{d} = \mathbf{F}\mathbf{D}$ is mapped via the deformation gradient. The covariant electric field $\mathbf{e} = \mathbf{F}^{-T}\mathbf{E}$ is mapped by the normal map.

3.2.8. Geometrical transformations of electric objects

In analogy to the transformation of mechanical objects, the Lagrangian counterparts of the electric field and electric displacement can be obtained. Employing the transformation of line elements, the spatial integration of the electric field in (3.26) can be rewritten as

$$\phi(\mathbf{x}) = - \int_{\mathbf{x}_0}^{\mathbf{x}} \mathbf{e} \cdot d\mathbf{x} = - \int_{\mathbf{X}_0}^{\mathbf{X}} \mathbf{e} \cdot \mathbf{F} d\mathbf{X} = - \int_{\mathbf{X}_0}^{\mathbf{X}} \mathbf{E} \cdot d\mathbf{X}, \quad (3.55)$$

yielding the pull-back of the Eulerian electric field to the Lagrangian configuration

$$\mathbf{E} = \mathbf{F}^T \mathbf{e} \quad \longrightarrow \quad \mathbf{e} = \mathbf{F}^{-T} \mathbf{E}. \quad (3.56)$$

Following the definition of the electric displacement in equation (3.37) and applying Nanson's area transformation

$$\int_{\partial S} \mathbf{d} \cdot d\mathbf{a} = \int_{\partial B} \mathbf{d} \cdot J\mathbf{F}^{-T} d\mathbf{A} = \int_{\partial B} \mathbf{D} \cdot d\mathbf{A}, \quad (3.57)$$

we can define the Lagrangian electric displacement \mathbf{D} as the pull-back

$$\mathbf{D} = J\mathbf{F}^{-1} \mathbf{d} \quad \longrightarrow \quad \tilde{\mathbf{d}} := J\mathbf{d} = \mathbf{F}\mathbf{D}, \quad (3.58)$$

which is a typical inverse Piola-transformation. The polarization vector \mathbf{p} transforms in an analogous manner $\mathbf{P} = J\mathbf{F}^{-1} \mathbf{p}$. Following the geometric interpretation of the mappings in Figure 3.10, it is obvious that we need to modify the definition of the polarization vector $\mathbf{p} = \mathbf{d} - \epsilon_0 \mathbf{g}^{-1} \mathbf{e}$ to be geometrically exact yielding $\mathbf{P} = \mathbf{D} - \epsilon_0 J\mathbf{C}^{-1} \mathbf{E}$.

3.2.9. Electrical power expressions

In analogy to the mechanical stress power expression discussed in Subsection 3.1.6, the electrical power \mathcal{P}^e per unit mass is defined as negative electric displacement times rate of the electric field in the material and spatial setting

$$\boxed{\varrho_0 \mathcal{P}^e := \underbrace{-\mathbf{D} \cdot \dot{\mathbf{E}}}_{\text{Lagrangian}} = \underbrace{-\tilde{\mathbf{d}} \cdot \mathcal{L}_{\mathbf{v}} \mathbf{e}}_{\text{Eulerian}}} \quad (3.59)$$

Note that in the Eulerian configuration, the dual quantities for the computation of the electric power are the Kirchhoff-type electric displacement and the Lie derivative of the electric field $\mathcal{L}_{\mathbf{v}} \mathbf{e} = \mathbf{F}^{-T} \frac{d}{dt} (\mathbf{F}^T \mathbf{e}) = \dot{\mathbf{e}} + \mathbf{l}^T \mathbf{e}$.

The Concept of Micro-to-Macro Transition

This chapter provides a brief introduction to the problem of homogenization and the concept of micro-to-macro transition as outlined in the fundamental works of VOIGT [195], REUSS [153], HILL [63, 66], HASHIN & SHTRIKMAN [58], WILLIS [202], SUQUET [177], PONTE CASTAÑEDA & SUQUET [152] and the textbooks by NEMAT-NASSER & HORI [140], ZOHDI & WRIGGERS [218], BURYACHENKO [27]. An overview on various homogenization techniques is given in KANOUTÉ ET AL. [82] and GEERS ET AL. [50] including asymptotic homogenization, mean field approaches, multiscale computational techniques of multi-physics problems as well as first and second order schemes. *Multiscale techniques* were initially developed in the field of mechanics, but recently fundamental advances for coupled multi-physics problems are achieved. Most materials which are attempted to be modeled by homogeneous continuum approaches are inhomogeneous on smaller length scales, that is on micro- or even nano-size. Typical examples within the context of this work are piezoelectrics, consisting of grains built up of electric domains with aligned polarization on the micro-level. On the one hand, there exist complex *micromechanically*

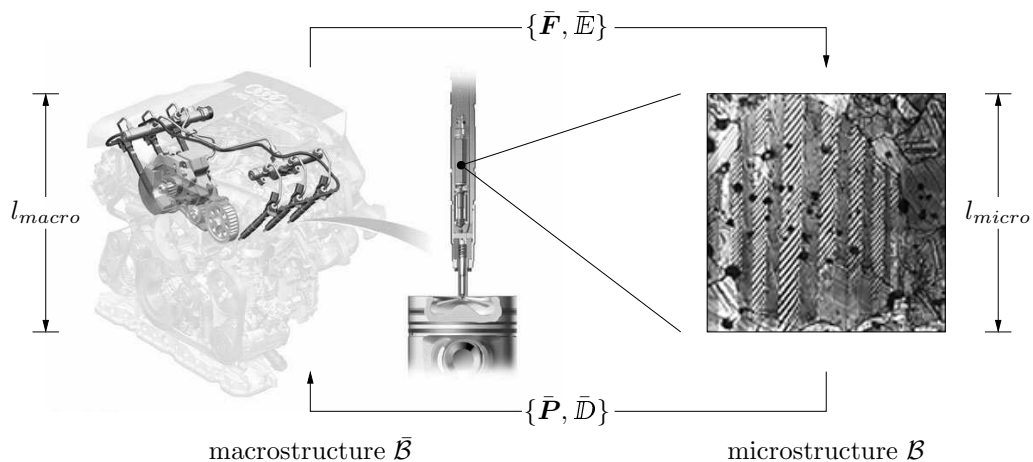


Figure 4.1: *Micro-to-macro transition concept.* Common-rail fuel injection systems with piezo inline injectors and barium titanate microstructure are depicted. The macroscopic deformation gradient and electric field $\{\bar{\mathbf{F}}, \bar{\mathbf{E}}\}$ drive the microstructure \mathcal{B} . Output are the homogenized nominal stress and electric displacement $\{\bar{\mathbf{P}}, \bar{\mathbf{D}}\}$ at a material point of the macrostructure $\bar{\mathcal{B}}$.

motivated modeling concepts such as phase field models describing explicitly the dissipative nature of polarization switching and thus the movement of domain walls. On the other hand, there are macroscopic *phenomenological* approaches neglecting the underlying microstructure and focusing on a homogeneous medium instead. Both concepts are relevant and can be adapted to experimental results. The mathematical theory of computational homogenization can close the gap between micro- and macroscale by the formulation of suitable micro-to-macro transition concepts, incorporating physically necessary information of the microscale (e.g. the domain switching) on the macroscopic level, see [Figure 4.1](#). In the pioneering work of VOIGT [195] and REUSS [153] rigorous upper and lower bounds for the effective stiffness of composites were developed. An extension based on variational principles leading to better estimates was presented later by HASHIN & SHTRIKMAN [57, 58]. A computational homogenization approach coupling the macroscopic scale to the microscopic scale is in the following extended to electro-mechanically coupled materials. The key aspect of every homogenization scheme is the determination of macroscopic quantities in terms of their microscopic counterparts, driven by appropriate constraints or boundary conditions on the representative volume element. In NEMAT-NASSER & HORI [140, p.59], the additional incorporation of non-mechanical properties such as thermal, magnetic, or electric effects was concerned. Extended averaging theorems are derived and various potentials proposed leading to upper and lower bounds for the macroscopic potentials characterized by an appropriate choice of boundary conditions.

Within this chapter, upper and lower bounds for the effective properties of the material are developed by considering a simple one-dimensional purely mechanical model problem. The fundamental assumptions such as the concept of representative volume elements and the separation of length scales of computational homogenization are reviewed and extended to the electro-mechanically coupled regime.

4.1. The concept of representative volume elements

The description of macroscopic material behavior takes the heterogeneous microstructure as a basis. Hence, the macroscopic material behavior is fully characterized by microscopic geometry and composition of particular constituents, e.g. fibers, particles, inclusions, and voids. The goal of computational homogenization schemes is to describe macroscopic behavior by considering an underlying *representative volume element*, see HILL [63], HASHIN [56], and NEMAT-NASSER & HORI [140]. Rodney Hill defined a representative volume element as a sample of a heterogeneous material that is typical of the whole mixture on average, and contains a sufficient number of micro-inhomogeneities for the material properties to be independent of surface values. They are large compared to typical phase region dimensions, that is a fiber diameter or the distance between inclusions. The overall properties fluctuate about a mean value with a wavelength much smaller than the dimensions of the sample, and the effect of such fluctuations becomes insignificant in a small layer close to the surface. The contribution of this surface layer to any volume average can be made negligible by taking the sample large enough. A graphical interpretation of the non-uniqueness of representative volume elements is given in [Figure 4.2](#). Hence, the choice of the sample is ambiguous, albeit some geometric structures are more favorable for the numerical treatment than others, see for instance MICHEL ET AL. [114] regarding the numerical treatment of hexagonal representative volume elements.

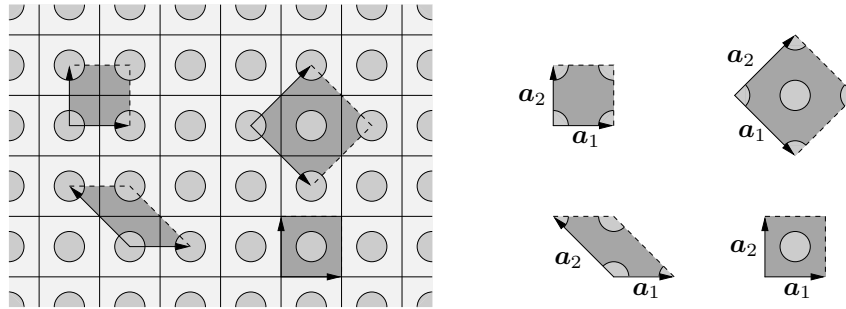


Figure 4.2: *Non-uniqueness of representative volume elements.* The dashed lines indicate four possible representative volume elements in a heterogeneous, periodic microstructure. The two linearly independent vectors \mathbf{a}_1 and \mathbf{a}_2 build up a coordinate system to describe the periodicity of the unit cells, see SCHRÖDER [160].

A crucial requirement for the application of the concept of representative volume elements is the existence of different length scales. The *separation of length scale* assumption implies that the microscopic length scale identifying the size of a representative volume element varies on a much smaller scale than the characteristic length of the macroscopic loading

$$l_{micro} \ll l_{macro}, \quad (4.1)$$

see for instance GEERS ET AL. [50]. Note that it is not the size of the macroscopic body which is important, rather the spatial variation of the kinematic and stress fields as well as external loading within that domain. This hypothesis causes two key consequences for the homogenization analysis. First, the macroscopic gradients $\{\bar{\mathbf{F}}, \bar{\mathbb{E}}\}$ and stress-like quantities $\{\bar{\mathbf{P}}, \bar{\mathbb{D}}\}$ are uniform (constant) over the spatial length scale l_{micro} associated with the size of the microstructure. Second, the body force, external surface traction, volume density, and free surface density fluctuate on a length scale much larger than that of the microscale and thus can be neglected. Hence, the mechanical equilibrium equation and the Gauss law reduce to $\text{Div}[\mathbf{P}] = \mathbf{0}$ and $\text{Div}[\mathbb{D}] = 0$ in \mathcal{B} , that are homogeneous balance equations without source terms.

4.2. The problem of homogenization: A brief introduction

This section serves as a brief introduction to the problem of homogenization, focusing on a one-dimensional bar with periodic microstructure and constant cross section A . The body consists of a sequence of alternating pieces with two different Young moduli satisfying the separation of length scale hypothesis. The elongation in longitudinal direction for an inhomogeneous Young modulus $E(x)$ and displacement $u(x)$ are determined by the principle of minimum potential energy, see Figure 4.3. Let $\varepsilon := du/dx$ be the strain in the bar, $\sigma = E(x)\varepsilon$ a one-dimensional stress state governed by Hooke's law, and F an external force at its right end. Then, the *internal energy density* at a point of a linear-elastic material is $\mathcal{U} = \frac{1}{2} \sigma \varepsilon$. The total internal energy is obtained by integration over the volume of the bar

$$\mathcal{U}_{tot} = \int_{\mathcal{B}} \mathcal{U} dV = \int_{\mathcal{B}} \frac{1}{2} \sigma \varepsilon dV = \int_0^L \frac{1}{2} E(x) A \varepsilon^2 dx. \quad (4.2)$$

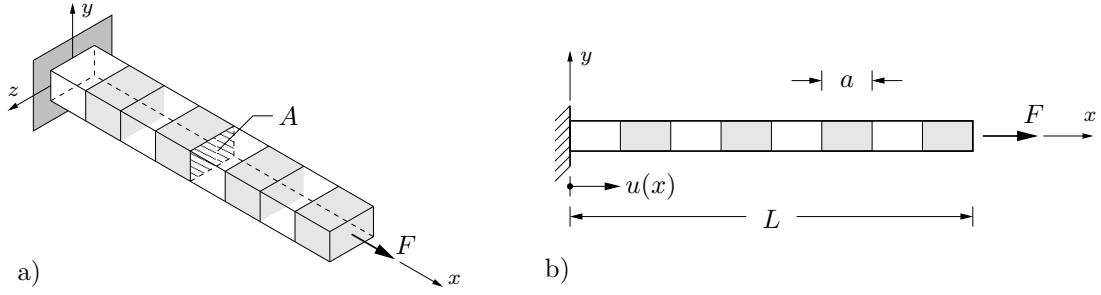


Figure 4.3: *Elastic bar with periodic microstructure.* a) Three-dimensional and b) two-dimensional view of undeformed configuration. The constant cross section is A and the Young modulus $E(x)$ is inhomogeneous in consecutive parts. The beam is loaded by the force F at its right end and clamped at its left, acting as Dirichlet boundary condition with $u(0) = 0$. The length of alternating pieces is $a \ll L$, which is much smaller than the total length of the bar L .

The *external work potential* $\mathcal{W} = Fu(L)$ is the work performed by the applied end load F on the displacements. The displacement field is then obtained by the *principle of minimum potential energy*

$$u = \arg \left\{ \inf_{u \in \mathcal{W}_u} \Pi(u) \right\} \quad \text{with} \quad \Pi(u) = \mathcal{U}_{\text{tot}}(\varepsilon) - \mathcal{W}(u), \quad (4.3)$$

where $\mathcal{W}_u := \{u \mid u(0) = 0\}$ restricts the displacement to satisfy the Dirichlet boundary conditions and the functional Π is the total potential energy. The Euler equations of this variational principle describe the boundary-value-problem

$$\frac{d}{dx} [E(x)A\varepsilon] = 0, \quad u(0) = 0, \quad E(x)A\varepsilon|_{x=L} = F. \quad (4.4)$$

Assuming a constant stress distribution within the bar, the analytic solution for this problem is obtained in accordance with BERDICHEVSKY [14] as

$$u(x) = \frac{F}{A} \int_0^x \frac{dx}{E(x)}. \quad (4.5)$$

By introducing the average strain $\bar{\varepsilon}$ as the total relative elongation of the rod, the effective Young modulus can be defined by the relation

$$F = \bar{E}_{\text{eff}} A \bar{\varepsilon} \quad \text{with} \quad \bar{\varepsilon} := \frac{u(L)}{L}. \quad (4.6)$$

The determination of effective moduli will be the main task of the homogenization analysis in order to replace a microscopically inhomogeneous material by a *homogeneous idealization* on the macroscale. Using the exact solution (4.5), the constant effective modulus

$$\bar{E}_{\text{eff}} = \left(\frac{1}{L} \int_0^L \frac{dx}{E(x)} \right)^{-1} \quad (4.7)$$

is obtained as the Reuss bound. More details regarding Reuss, Voigt, and Hashin-Shtrikman bounds are given in the subsequent section. The minimizing element of the variational principle (4.3) can be analogously determined by a homogenized functional of

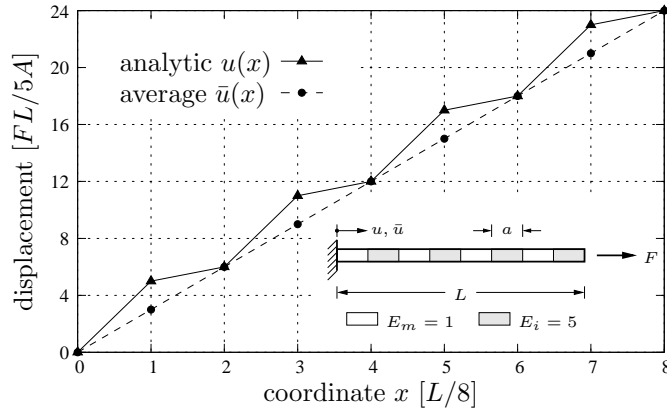


Figure 4.4: *The problem of homogenization.* Analytic solution $u(x)$ and average solution $\bar{u}(x)$ for the elastic rod with periodically alternating Young moduli and piece length $a = L/8$. For the given material parameters the effective stiffness is computed as the Reuss bound $1/\bar{E}_{\text{eff}} = \frac{1}{L} \int_0^L 1/E(x)dx = 3/5$ and hence the average displacement is $\bar{u}(x) = F/\bar{E}_{\text{eff}}A \cdot x = 3/5 \cdot F/A \cdot x$ with $x \in [0, L]$.

a homogeneous elastic bar in terms of the effective Young modulus \bar{E}_{eff} and the homogenized displacement $\bar{u}(x)$. Hence, let the homogenized strain be determined by $\bar{\varepsilon} := d\bar{u}/dx$. The variational principle of homogenization then reads

$$\bar{u} = \arg \left\{ \inf_{\bar{u} \in \mathcal{W}_{\bar{u}}} \bar{\Pi}(\bar{u}) \right\} \quad \text{with} \quad \bar{\Pi}(\bar{u}) = \int_0^L \frac{1}{2} \bar{E}_{\text{eff}} A \bar{\varepsilon}^2 dx - F \bar{u}(L), \quad (4.8)$$

where $\mathcal{W}_{\bar{u}} := \{\bar{u} \mid \bar{u}(0) = 0\}$. The minimization of the functional $\bar{\Pi}(\bar{u})$ for arbitrary variations gives as solution the homogenized displacement field

$$\bar{u}(x) = \frac{F}{\bar{E}_{\text{eff}} A} x. \quad (4.9)$$

The cornerstone of every homogenization problem is the determination of the effective properties describing the inhomogeneous material behavior for its homogeneous counterpart. For the one-dimensional bar under consideration, the differences between the two solutions of the variational principles (4.3) and (4.8) are given in Figure 4.4.

4.3. Variational bounds on effective properties

This section develops bounds on effective properties for a one-dimensional continuum governed by Hooke's law. The classical Voigt and Reuss bounds are derived and compared with the more sophisticated Hashin-Shtrikman estimates. Consider a microscopic representative volume element with inhomogeneous Young modulus such that Hooke's law becomes $\sigma = E(x)\varepsilon$. This results in the need to solve complicated partial differential equations for the displacement field of the body. A more efficient approach is to derive homogeneous estimates on the macroscale with average (effective) material properties

$$\sigma = E(x)\varepsilon \quad \longrightarrow \quad \bar{\sigma} = \bar{E}_{\text{eff}} \bar{\varepsilon}, \quad (4.10)$$

where \bar{E}_{eff} is a constant effective Young modulus. For a graphical representation of the idea of using homogeneous idealizations with effective-properties we refer to Figure 4.5.

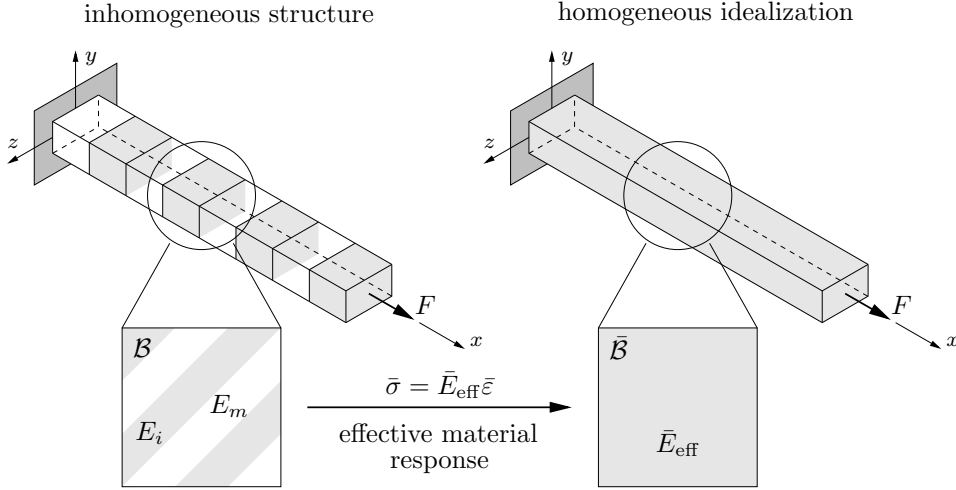


Figure 4.5: *Effective properties in structural engineering.* The actual structure is inhomogeneous with varying Young modulus in consecutive parts. This inhomogeneous material is replaced by a homogeneous idealization with effective material properties.

In the pioneering works of VOIGT [195] and REUSS [153], either the strain or the stress field was assumed to be uniform within an aggregate of polycrystalline material. These assumptions lead to simple bounds for two-phase composites, where an inclusion phase is embedded into a matrix. The Young modulus is constant within each phase such that $\sigma_m = E_m \varepsilon_m$ and $\sigma_i = E_i \varepsilon_i$ in the matrix and the inclusion, respectively. These bounds generally provide rough estimates of the effective stiffness of the material. The Voigt assumption usually overestimates the effective stiffness because the tractions at the phase boundaries cannot be in equilibrium (static inadmissibility), while the Reuss assumption leads to an underestimation of the stiffness, where the matrix-inclusion composite cannot be perfectly bonded (kinematic inadmissibility).

The fractional volume concentration of the inclusion and matrix phases are denoted by c_i and c_m such that $c_i + c_m = 1$. Hence, the average stress in the composite is

$$\bar{\sigma} = c_m \bar{\sigma}_m + c_i \bar{\sigma}_i = c_m E_m \bar{\varepsilon}_m + c_i E_i \bar{\varepsilon}_i, \quad (4.11)$$

see HILL [63]. A representative volume element is assumed to be structurally typical for the whole mixture on average and contains a sufficient number of inclusions for the effective modulus to be independent of the surface tractions and displacements. VOIGT [195] assumes that the *strain in the composite is uniform*, that is $\varepsilon_m = \varepsilon_i = \bar{\varepsilon}$. Insertion into (4.11) gives the Voigt bound for the effective stiffness of the composite

$$\bar{\sigma} = \bar{E}_{\text{Voigt}} \bar{\varepsilon} \quad \text{with} \quad \bar{E}_{\text{Voigt}} = c_m E_m + c_i E_i. \quad (4.12)$$

Obviously this is tantamount to a simple volume weight of the phase stiffnesses. In complete analogy, a similar ansatz to (4.11) for the strain field in the composite is

$$\bar{\varepsilon} = c_m \bar{\varepsilon}_m + c_i \bar{\varepsilon}_i = c_m E_m^{-1} \bar{\sigma}_m + c_i E_i^{-1} \bar{\sigma}_i. \quad (4.13)$$

The assumption of *uniform stress in the composite* $\sigma_m = \sigma_i = \bar{\sigma}$ according to REUSS [153] specifies the Reuss bound for the stiffness of the mixture

$$\bar{\sigma} = \bar{E}_{\text{Reuss}} \bar{\varepsilon} \quad \text{with} \quad \bar{E}_{\text{Reuss}} = (c_m E_m^{-1} + c_i E_i^{-1})^{-1}, \quad (4.14)$$

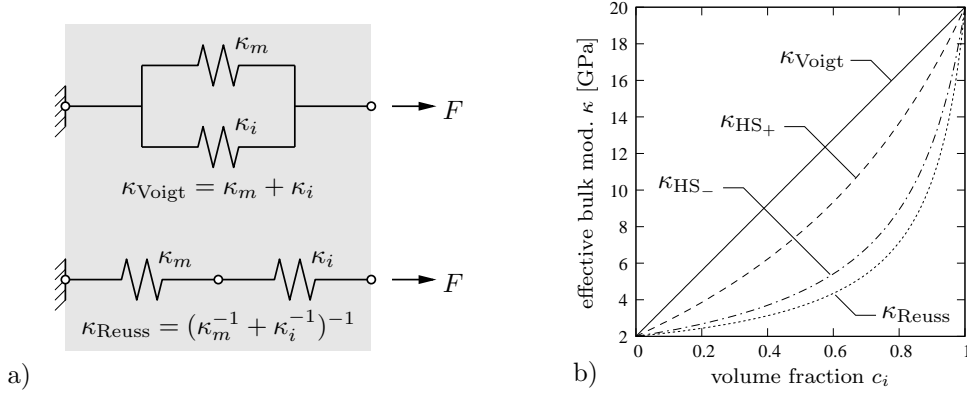


Figure 4.6: *Bounds on effective properties.* a) For the springs in parallel the strain (displacement) is uniform $\varepsilon(x) = \bar{\varepsilon}$ leading to the Voigt bound $\kappa_{\text{Voigt}} = \kappa_m + \kappa_i$ for the effective spring constant. The two springs in series render a uniform stress (force) state $\sigma(x) = \bar{\sigma}$ and give the Reuss bound $\kappa_{\text{Reuss}} = (\kappa_m^{-1} + \kappa_i^{-1})^{-1}$. b) Comparison of upper Voigt and lower Reuss bounds with Hashin-Shtrikman bounds for a fictitious matrix-inclusion material. The bulk and shear moduli are $\kappa_m = 2$ GPa, $\kappa_i = 20$ GPa, $\mu_m = 1$ GPa, and $\mu_i = 10$ GPa.

which are weights of the phase compliances. Within the fundamental work HILL [60] it is shown that the previously derived Voigt and Reuss estimates for the overall properties of composite materials are strict upper and lower bounds of the true effective elastic moduli

$$\bar{E}_{\text{Reuss}} \leq \bar{E}_{\text{eff}} \leq \bar{E}_{\text{Voigt}}. \quad (4.15)$$

For a simple isotropic material described by the bulk modulus κ and the shear modulus μ in each phase the previously mentioned bounds on the effective stiffness are given. The Voigt bounds arise as

$$\kappa_{\text{Voigt}} = (1 - c_i)\kappa_m + c_i\kappa_i \quad \text{and} \quad \mu_{\text{Voigt}} = (1 - c_i)\mu_m + c_i\mu_i \quad (4.16)$$

and the Reuss bounds as

$$\kappa_{\text{Reuss}} = \left((1 - c_i)\kappa_m^{-1} + c_i\kappa_i^{-1} \right)^{-1} \quad \text{and} \quad \mu_{\text{Reuss}} = \left((1 - c_i)\mu_m^{-1} + c_i\mu_i^{-1} \right)^{-1}, \quad (4.17)$$

which are simple weights of the stiffness or compliances. The stiff Voigt bound can be interpreted by two springs in parallel while the soft Reuss bound resembles springs in series, see Figure 4.6a. In a sequence of papers HASHIN & SHTRIKMAN [57, 58] developed improved bounds based on variational principles using a split of the stress field according to the concept of filtering of micro-macro fields. These are useful for infinite sample sizes compared to the length scale of micro-constituents. Due to their complicated nature, only the upper and lower Hashin-Shtrikman bounds for the bulk modulus are shown here

$$\kappa_{\text{HS-}} = \kappa_m + \frac{(\kappa_i - \kappa_m)c_i}{1 + \alpha_m \left(\frac{\kappa_i}{\kappa_m} - 1 \right) (1 - c_i)} \quad \text{and} \quad \kappa_{\text{HS+}} = \kappa_i + \frac{(\kappa_m - \kappa_i)(1 - c_i)}{1 + \alpha_i \left(\frac{\kappa_m}{\kappa_i} - 1 \right) c_i}, \quad (4.18)$$

where $\alpha = \kappa / (\kappa + \frac{4}{3}\mu)$ in each phase. For details regarding the bounds on bulk and shear moduli see HILL [63]. The results obtained for isotropic solids are compared in Figure 4.6b, where both the Voigt and the Reuss bound as well as the more sophisticated Hashin-Shtrikman bounds are shown exemplary for the bulk modulus.

4.4. Fundamental averaging theorems of electro-mechanics

The fundamental averaging theorems for finite strains, see HILL [66], NEMAT-NASSER [139], and MIEHE ET AL. [126], discussed within this section are necessary to extract macroscopic information from an underlying representative volume element. The results are independent of constitutive relations, material properties, and linear or nonlinear material response. The first theorem concerns the micro-to-macro transition of kinematic quantities. The macroscopic deformation gradient is completely defined in terms of the average of boundary displacements taken over the volume of the microstructure

$$\bar{\mathbf{F}} = \frac{1}{|\mathcal{B}|} \int_{\partial\mathcal{B}} \boldsymbol{\varphi} \otimes \mathbf{N} dA = \frac{1}{|\mathcal{B}|} \int_{\mathcal{B}} \mathbf{F} dV. \quad (4.19)$$

For the simple microstructures under consideration, the macroscopic deformation gradient is the volume average of its microscopic counterpart. For more complex microstructures including e.g. holes or discontinuities, the reader is referred to SCHRÖDER [160], where the macroscopic deformation gradient has additional contributions due to internal boundaries. The difficulty within large strain kinematics is the nonlinear relation between kinematic objects. Hence, not all macroscopic kinematic quantities may be obtained as the volume average of their microscopic counterparts, e.g. the Green-Lagrange strain tensor. In analogy to kinematics, the macroscopic nominal stress is governed by the prescribed boundary tractions $\mathbf{T} = \mathbf{P} \cdot \mathbf{N}$, that is

$$\bar{\mathbf{P}} = \frac{1}{|\mathcal{B}|} \int_{\partial\mathcal{B}} \mathbf{T} \otimes \mathbf{X} dA = \frac{1}{|\mathcal{B}|} \int_{\mathcal{B}} \mathbf{P} dV. \quad (4.20)$$

Again we conclude that the macro stress is the volume average of the microscopic one. Extending the small strain version developed in SCHRÖDER [161] or ZÄH & MIEHE [207] to finite deformations results in the determination of the macroscopic electric field and electric induction. Hence, for a body without discontinuities the electric field is defined in terms of the electric potential on the boundary

$$\bar{\mathbb{E}} = \frac{1}{|\mathcal{B}|} \int_{\partial\mathcal{B}} -\phi \mathbf{N} dA = \frac{1}{|\mathcal{B}|} \int_{\mathcal{B}} \mathbb{E} dV \quad (4.21)$$

and the macroscopic electric induction

$$\bar{\mathbb{D}} = \frac{1}{|\mathcal{B}|} \int_{\partial\mathcal{B}} -\Sigma_f^e \mathbf{X} dA = \frac{1}{|\mathcal{B}|} \int_{\mathcal{B}} \mathbb{D} dV \quad (4.22)$$

in terms of the prescribed free surface charge density $\Sigma_f^e = -\mathbb{D} \cdot \mathbf{N}$. The average theorem for the mechanical stress and electric displacement can be derived solely if the separation of length scale hypothesis holds, that is, the mechanical equilibrium and the Gauss law reduce to their homogeneous form without source terms. An analogous ansatz is outlined in KEIP ET AL. [83] for electro-mechanics and CHATZIGEORGIOU ET AL. [30] for magneto-mechanically coupled materials.

4.5. The Hill-Mandel macrohomogeneity condition

The Hill-Mandel condition was originally developed by HILL [63] and MANDEL [108]. In words, HILL [63] explained it as follows: “The average strain energy in any region can

be calculated from the average stress and strain, when the surface constraints are of the specified kind". The macrohomogeneity has become one of the fundamental principles in computational homogenization analysis due to the fact that the boundary conditions applied to the representative volume element are directly derived from it. Mathematically, it can be formulated in the electro-mechanical context as the equivalence of total virtual macroscopic stress power including electric contributions and volume average of its total microscopic counterpart

$$\bar{\mathbf{P}} : \delta \bar{\mathbf{F}} - \bar{\mathbb{D}} \cdot \delta \bar{\mathbb{E}} = \frac{1}{|\mathcal{B}|} \int_{\mathcal{B}} \mathbf{P} : \delta \mathbf{F} - \mathbb{D} \cdot \delta \mathbb{E} dV. \quad (4.23)$$

Note that for the sake of simplicity, any dissipative effects are neglected here. It can be shown that the macrohomogeneity condition solely holds in conjunction with the separation of length scale hypothesis. In order to derive more accurate averaging strategies than the previously discussed Voigt and Reuss estimates, the Hill-Mandel condition is used transferring the given macroscopic variables to the microstructure via the boundary conditions, see HILL [66] for the purely mechanical case. In a first step, the right hand side of (4.23) gives

$$\frac{1}{|\mathcal{B}|} \int_{\mathcal{B}} \mathbf{P} : \delta \mathbf{F} - \mathbb{D} \cdot \delta \mathbb{E} dV = \frac{1}{|\mathcal{B}|} \int_{\partial \mathcal{B}} \mathbf{T} \cdot \delta \boldsymbol{\varphi} - \Sigma_f^e \delta \phi dA \quad (4.24)$$

with the traction vector $\mathbf{T} = \mathbf{P} \cdot \mathbf{N}$, the free surface charge density $\Sigma_f^e = -\mathbb{D} \cdot \mathbf{N}$, and the outward unit normal $\mathbf{N} \in \partial \mathcal{B}$. Three additional reformulations of the macroscopic power expression

$$\begin{aligned} \bar{\mathbf{P}} : \delta \bar{\mathbf{F}} - \bar{\mathbb{D}} \cdot \delta \bar{\mathbb{E}} &= \frac{1}{|\mathcal{B}|} \int_{\partial \mathcal{B}} (\bar{\mathbf{P}} \cdot \mathbf{N}) \cdot \delta \boldsymbol{\varphi} + (\bar{\mathbb{D}} \cdot \mathbf{N}) \delta \phi dA, \\ \bar{\mathbf{P}} : \delta \bar{\mathbf{F}} - \bar{\mathbb{D}} \cdot \delta \bar{\mathbb{E}} &= \frac{1}{|\mathcal{B}|} \int_{\partial \mathcal{B}} \mathbf{T} \cdot (\delta \bar{\mathbf{F}} \cdot \mathbf{X}) + \Sigma_f^e (\delta \bar{\mathbb{E}} \cdot \mathbf{X}) dA, \\ \bar{\mathbf{P}} : \delta \bar{\mathbf{F}} - \bar{\mathbb{D}} \cdot \delta \bar{\mathbb{E}} &= \frac{1}{|\mathcal{B}|} \int_{\partial \mathcal{B}} (\bar{\mathbf{P}} \cdot \mathbf{N}) \cdot (\delta \bar{\mathbf{F}} \cdot \mathbf{X}) - (\bar{\mathbb{D}} \cdot \mathbf{N}) (\delta \bar{\mathbb{E}} \cdot \mathbf{X}) dA, \end{aligned} \quad (4.25)$$

give, together with an extension of (4.23), the following form

$$\frac{1}{|\mathcal{B}|} \int_{\partial \mathcal{B}} (\delta \boldsymbol{\varphi} - \delta \bar{\mathbf{F}} \cdot \mathbf{X}) \cdot (\mathbf{T} - \bar{\mathbf{P}} \cdot \mathbf{N}) - (\delta \phi + \delta \bar{\mathbb{E}} \cdot \mathbf{X}) (\Sigma_f^e + \bar{\mathbb{D}} \cdot \mathbf{N}) dA = 0. \quad (4.26)$$

The modifications performed above result in two obvious boundary conditions, that are the uniform displacements (Dirichlet) and uniform tractions (Neumann) on the surface of the microstructure

$$(D) : \begin{cases} \boldsymbol{\varphi} = \bar{\mathbf{F}} \cdot \mathbf{X}, \\ -\phi = \bar{\mathbb{E}} \cdot \mathbf{X}, \end{cases} \quad \text{and} \quad (N) : \begin{cases} \mathbf{T} = \bar{\mathbf{P}} \cdot \mathbf{N}, \\ -\Sigma_f^e = \bar{\mathbb{D}} \cdot \mathbf{N}. \end{cases} \quad (4.27)$$

Non-trivial periodic boundary conditions are obtained by additive decomposing the deformation map and electric potential into a linear, homogeneous part governed by the macroscopic deformation and a superimposed fine scale fluctuation field

$$\boldsymbol{\varphi} = \bar{\mathbf{F}} \cdot \mathbf{X} + \tilde{\boldsymbol{\varphi}} \quad \text{and} \quad -\phi = \bar{\mathbb{E}} \cdot \mathbf{X} - \tilde{\phi}, \quad (4.28)$$

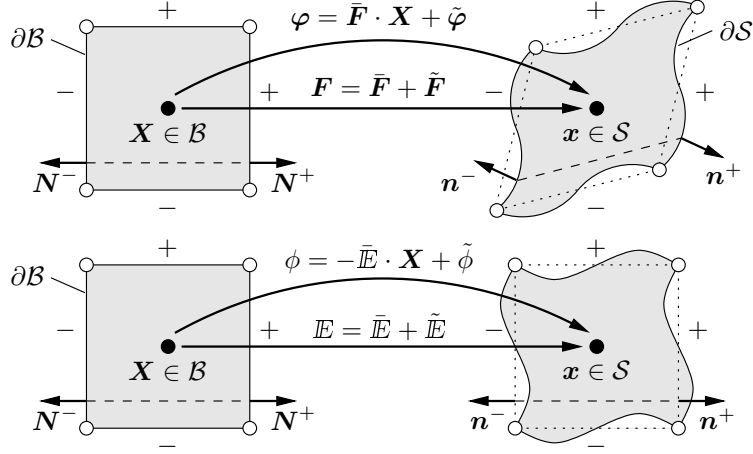


Figure 4.7: *Non-trivial periodic boundary conditions.* The microscopic deformation and electric potential are decomposed into homogeneous macroscopic parts and superimposed fine-scale fluctuations according to $\varphi = \bar{\mathbf{F}} \cdot \mathbf{X} + \tilde{\varphi}$ and $\phi = -\bar{\mathbf{E}} \cdot \mathbf{X} + \tilde{\phi}$. Periodic boundary conditions are applied for the superimposed fluctuation fields. The deformation map and electric potential at the edges are prescribed. Normal vectors on opposite faces '+' and '-' are related by $\mathbf{N}^+ = -\mathbf{N}^-$ at associated points $\mathbf{X}^+ \in \partial\mathcal{B}^+$ and $\mathbf{X}^- \in \partial\mathcal{B}^-$.

resulting in the kinematics $\mathbf{F} = \bar{\mathbf{F}} + \nabla_{\mathbf{X}}\tilde{\varphi}$ and $\mathbf{E} = \bar{\mathbf{E}} - \nabla_{\mathbf{X}}\tilde{\phi}$, see Figure 4.7. Taking (4.23), (4.24), and (4.25)₂, the macrohomogeneity condition can be reformulated as

$$\frac{1}{|\mathcal{B}|} \int_{\partial\mathcal{B}} (\delta\varphi - \delta\bar{\mathbf{F}} \cdot \mathbf{X}) \cdot \mathbf{T} - (\delta\phi + \delta\bar{\mathbf{E}} \cdot \mathbf{X}) \Sigma_f^e dA = 0. \quad (4.29)$$

Due to the extension of the primary fields (4.28) by fine scale fluctuations and the split of the boundary into points $\mathbf{X}^+ \in \partial\mathcal{B}^+$ and $\mathbf{X}^- \in \partial\mathcal{B}^-$, we finally obtain

$$\frac{1}{|\mathcal{B}|} \int_{\partial\mathcal{B}^+} \delta\tilde{\varphi}^+ \cdot \mathbf{T}^+ - \delta\tilde{\phi}^+ \Sigma_f^{e+} dA + \frac{1}{|\mathcal{B}|} \int_{\partial\mathcal{B}^-} \delta\tilde{\varphi}^- \cdot \mathbf{T}^- - \delta\tilde{\phi}^- \Sigma_f^{e-} dA = 0. \quad (4.30)$$

This results in the non-trivial periodic boundary conditions with anti-periodic tractions and surface charges

$$(P) : \begin{cases} \tilde{\varphi}^+ = \tilde{\varphi}^-, \\ \tilde{\phi}^+ = \tilde{\phi}^-, \end{cases} \quad \text{with} \quad \begin{cases} \mathbf{T}^+ = -\mathbf{T}^-, \\ \Sigma_f^{e+} = -\Sigma_f^{e-}. \end{cases} \quad (4.31)$$

Note that the uniform displacement constraints are recovered for $\tilde{\varphi} = \mathbf{0}$ and $\tilde{\phi} = 0$ on $\partial\mathcal{B}$ and that zero fluctuation fields in the entire domain \mathcal{B} also satisfy the Hill-Mandel condition, usually referred to as Taylor assumption. Periodic boundary conditions are the most reasonable choice for the computational homogenization analysis, even for microstructures which are non-periodic, see TERADA ET AL. [184] and SEGURADO & LLORCA [164].

— Part II —

Modeling and Homogenization of
Micro-Electro-Elasticity at Small
Strains

Variational-Based Modeling of Micro-Electro-Elasticity with Electric Field and Stress Driven Domain Evolution

In order to improve the predictive quality of macroscale models and to have a better understanding of the underlying micromechanical driving forces, a greater emphasis on the construction of micro-mechanically motivated experiments and associated microscale models is called for. The development of *micro-electric continuum approaches* for ferroelectric crystals at small strains may be inspired by concepts for the phenomenological description of magnetic domains, such as the seminal work of LANDAU & LIFSHITZ [100], where the fundamentals of the so-called *domain theory* of magnetization in rigid bodies have been laid based on energy minimization concepts. Let \mathbb{p} denote the vector field of electric polarization defined on the solid domain \mathcal{B} . When ignoring for a moment the electro-mechanical coupling effects, a theory of electric domains for *rigid bodies* may be obtained by converting the Landau-Lifschitz energy functional of micro-magnetics to ferroelectrics

$$E(\mathbb{p}) = \int_{\mathcal{B}} \left[\frac{\alpha}{2} |\nabla \mathbb{p}|^2 + \varphi(\mathbb{p}) - \mathbb{p} \cdot \bar{\mathbf{e}} \right] dV + \frac{\epsilon_0}{2} \int_{\mathcal{R}^3} |\nabla \tilde{\phi}|^2 dV, \quad (5.1)$$

the minimization of which, for a given external electric field $\bar{\mathbf{e}}$, gives the shape of the electric domains. This functional is valid along with the additional constraint $\text{div}[\mathbb{p} - \epsilon_0 \nabla \tilde{\phi}] = 0$, that is the second Maxwell equation or the Gauss law, where $\tilde{\phi}$ is the electric potential induced by the electric polarization \mathbb{p} in the full space \mathcal{R}^3 and ϵ_0 the electric permittivity of vacuum. The key aspect in the solution of such *equilibrium theories* is the presence of the non-convex energy term $\varphi(\mathbb{p})$, which is typically formulated in a polynomial form as outlined in the pioneering works on ferroelectrics by DEVONSHIRE [38, 39]. This applies equally to non-rigid, that are micro-electro-elastic theories, where additionally elastic and electrostrictive terms in the energy functional appear. As already mentioned, the multi-well non-convex structure of the problem (5.1) and of its micro-electro-elastic extension gives rise to minimizers that consist of domains of differently oriented polarization. As outlined in SHU & BHATTACHARYA [165] and BHATTACHARYA & RAVICHANDRAN [17], based on arguments formulated in DESIMONE [35] and DESIMONE & JAMES [36] for

ferromagnetic bodies, these domains form very characteristic patterns in ferroelectrics. In [165] domain patterns in a large ferroelectric single crystal in the absence of external loading were studied. In this so-called 'large body limit', the gradient term in (5.1) and thus the boundary of the microstructure is neglected ($\alpha = 0$). We refer in this context to the overview on relaxation methods for rigid ferromagnetic materials in DESIMONE ET AL. [37]. In contrast, classical approaches to *dynamic theories* (or more correctly, quasi-static viscous theories) of domain evolution consider the Landau-Ginzburg equation, see GURTIN [54] for a general overview, which describes for rigid solids the temporal evolution of the electric polarization in the domain \mathcal{B} by the equation

$$\int_{\mathcal{B}} \eta \dot{p} dV = -\frac{\delta}{\delta t} E(p), \quad (5.2)$$

where $\delta E(\cdot)/\delta t$ denotes the variational derivative of the functional E . This equation characterizes p to be a *phase field-like order parameter*. The modeling of evolving electric domains in ferroelectric crystals conceptually in line with phase field approaches of diffusive interfaces are considered for example in CAO & CROSS [28], HU & CHEN [68], WANG ET AL. [200], ZHANG & BHATTACHARYA [210, 211], SU & LANDIS [174], SCHRADER ET AL. [158], CHOUDHURY ET AL. [32], WANG & ZHANG [199], WANG & KAMLAH [198], and KONTOSOS & LANDIS [87, 88]. These works mostly report on processes driven by prescribed electric potentials and displacements and do not directly control the homogenized electric field and the homogenized stress. Phase field models are typical examples for the constitutive modeling of *size effects*, such as the width of moving domain walls, which characterize the diffusive phase field-type interface. This needs non-standard continuum theories which incorporate *length-scales*, such as considered in FRIED & GURTIN [48, 49] and SU & LANDIS [174].

The literature of micro-electro-elasticity seems to be lacking fundamental *variational principles* of incremental nature. Hence, an important challenge on the theoretical side is the formulation of a variational principle in terms of the rates of the primary variables governing the micro-electro-elastic multi-field problem, which returns a Ginzburg-Landau-type evolution equation similar to (5.2) and the other governing equations of the coupled problem as the *Euler equations*. Variational principles based on rate-type, incremental structures were recently proposed for the macroscopic description of ferroelectrics in MIEHE & ROSATO [123] and MIEHE ET AL. [132]. The aim of this chapter is to extend these variational macro-concepts for materials with *locally defined* ordinary differential equations for the evolution of internal variables to a model of micro-electro-elasticity, that describes the time evolution of electric polarization parameters by *balance-type partial differential equations*. A guideline for this extension is given in the recent work MIEHE [118] on variational principles for the mechanical response of gradient-extended standard dissipative solids. The variational concepts proposed in the present work will serve as a natural starting point for the discrete solution of the micro-electro-elastic problem by means of the finite element method. On the computational side, the key challenge is the construction of a fully implicit monolithic finite element method for the multi-field problem, where the variational nature is reflected in the symmetry of the algebraic system.

The rigorous exploitation of new rate-type and incremental variational principles provides a frame that gives a canonical insight in the structure of the coupled problem. Section 5.1 starts by constructing functionals of micro-electro-elasticity governing the coupled problem. With these functionals at hand, Section 5.2 develops the variational

principles for the coupled evolution problem. To this end, we first outline in a continuous setting a *principle for stationary problems*, in line with the classical work of BROWN [25] for micro-magnetics, however, formulated in terms of average macro-stress and average macro-field loading functionals. A central new aspect of this paper is the formulation of a *variational principle for dynamic (quasi-static) evolution problems*. The Euler equations of this variational principle are the static stress equilibrium condition, the electrostatic equilibrium condition, often denoted as the second Maxwell equation or the Gauss law, and a Ginzburg-Landau-type evolution equation of the polarization. Based on these continuous formulations, Section 5.3 develops a consistent finite element model of micro-electro-elasticity. An algorithmic version of the variational principle for dynamic evolution problems associated with finite time increments is constructed. This time-space-discrete formulation is variational in nature, yielding a symmetric monolithic system of the coupled problem. Numerical simulations in Section 5.4 demonstrate the modeling capacity of the proposed formulation for domain wall motions in electric field and stress driven loading processes including their coupling with the surrounding free space.

5.1. Basic functionals in micro-electro-elasticity

Let $\Omega \subset \mathcal{R}^d$ denote a vacuum free space box with dimension $d \in [2, 3]$ and $\mathcal{B} \subset \Omega$ the domain occupied by the material solid as depicted in Figure 5.1a. Ω is considered to be large enough such that the electric field induced by the polarization of the body \mathcal{B} is decayed at its surface $\partial\Omega \subset \mathcal{R}^{d-1}$. We study the deformation and the polarization of the body under quasi-static, electro-mechanical loading in the time interval $\mathcal{T} \subset \mathcal{R}_+$.

5.1.1. Primary fields: Displacement, polarization, and electric potential

The boundary-value-problem of electro-mechanics is a coupled multi-field problem. On the mechanical side, the primary variable field is the *displacement field* \mathbf{u} of the material point $\mathbf{x} \in \mathcal{B}$ at time $t \in \mathcal{T}$. On the electric side, the *microscopic polarization* \mathbf{p} describes the polarization of the solid material at $\mathbf{x} \in \mathcal{B}$ and $t \in \mathcal{T}$. Hence, we focus on the two primary variable fields

$$\mathbf{u} : \begin{cases} \mathcal{B} \times \mathcal{T} \rightarrow \mathcal{R}^d, \\ (\mathbf{x}, t) \mapsto \mathbf{u}(\mathbf{x}, t), \end{cases} \quad \text{and} \quad \mathbf{p} : \begin{cases} \mathcal{B} \times \mathcal{T} \rightarrow \mathcal{R}^d, \\ (\mathbf{x}, t) \mapsto \mathbf{p}(\mathbf{x}, t), \end{cases} \quad (5.3)$$

defined on the solid domain $\mathcal{B} \subset \Omega$. The electric field in the full free space box Ω induced by the polarization \mathbf{p} is described by a third field, the *electric potential*

$$\tilde{\phi} : \begin{cases} \Omega \times \mathcal{T} \rightarrow \mathcal{R}, \\ (\mathbf{x}, t) \mapsto \tilde{\phi}(\mathbf{x}, t). \end{cases} \quad (5.4)$$

This potential field is assumed to be continuous across the interface $\partial\mathcal{B}$ between the solid domain \mathcal{B} and the surrounding free space $\Omega \setminus \mathcal{B}$, that is

$$[[\tilde{\phi}]] = 0 \quad \text{on } \partial\mathcal{B}, \quad (5.5)$$

where $[[(\cdot)]] := (\cdot)_+ - (\cdot)_-$ denotes the jump between the sides $\partial\mathcal{B}_+$ and $\partial\mathcal{B}_-$ of the interface between matter and free space as depicted in Figure 5.1a. The gradients of the

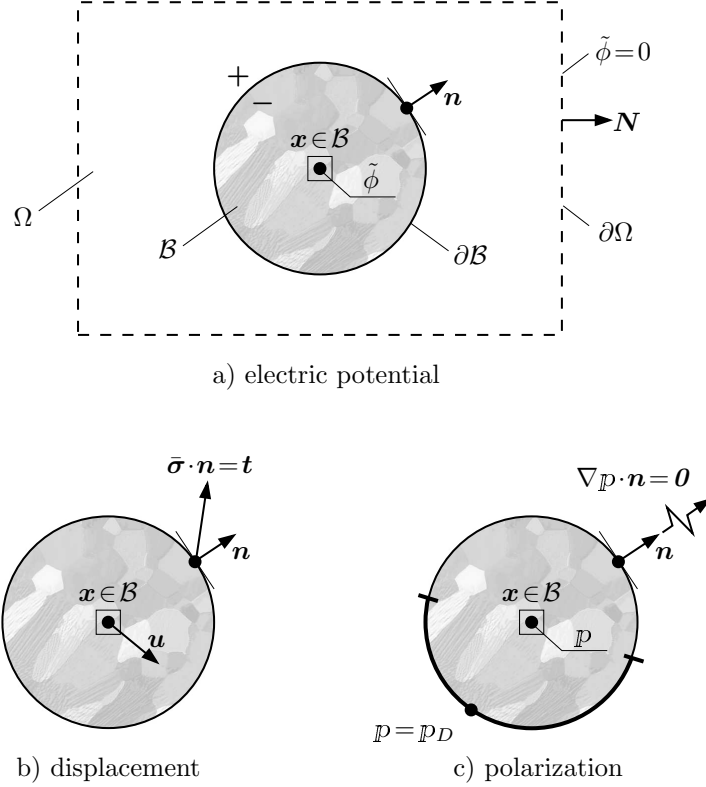


Figure 5.1: *Primary fields in micro-electro-elasticity.* The solid $\mathcal{B} \subset \Omega$ is embedded into a free space box $\Omega \subset \mathcal{R}^d$. a) The electric potential field $\tilde{\phi}$ in Ω induced by the electric polarization of the solid is continuous across the interface $\partial\mathcal{B}$, that is $[[\tilde{\phi}]] := \tilde{\phi}^+ - \tilde{\phi}^- = 0$ on $\partial\mathcal{B}$, and zero on the boundary $\partial\Omega$ of the free space box. b) Associated with the displacement field \mathbf{u} defined on \mathcal{B} are Neumann-type boundary conditions for the macro tractions $\bar{\boldsymbol{\sigma}} \cdot \mathbf{n} = \mathbf{t}$ on $\partial\mathcal{B}$. c) The polarization field \mathbf{p} on \mathcal{B} is constrained by the boundary conditions $\mathbf{p} = \mathbf{p}_D$ on $\partial\mathcal{B}_p$ and its normal flux $\nabla_{\mathbf{p}} \cdot \mathbf{n} = \mathbf{0}$ on $\partial\mathcal{B}_t$, with $\partial\mathcal{B} = \partial\mathcal{B}_p \cup \partial\mathcal{B}_t$.

displacement field \mathbf{u} and the potential $\tilde{\phi}$ define the displacement gradient and the electric field induced by the polarization

$$\mathbf{f} := \nabla \mathbf{u} \quad \text{in } \mathcal{B} \quad \text{and} \quad \tilde{\mathbf{e}} := -\nabla \tilde{\phi} \quad \text{in } \Omega, \quad (5.6)$$

respectively. These definitions satisfy automatically the *deformation compatibility* condition $\text{curl}[\mathbf{f}] = \mathbf{0}$ in \mathcal{B} and *Faraday's law of induction*, the third Maxwell equation, $\text{curl}[\tilde{\mathbf{e}}] = \mathbf{0}$ in Ω for the quasi-static problem under consideration. The strains are assumed to be small, that is $|\nabla \mathbf{u}| < \epsilon$ is bounded by a small number ϵ . In contrast, the norm of the gradients of the polarization $|\nabla_{\mathbf{p}}|$ and the electric potential $|\nabla \tilde{\phi}|$ are not bounded.

5.1.2. Boundary conditions and loading functionals

Mechanical loading by average macro-stress. We consider the polarized body \mathcal{B} to be mechanically loaded by a *constant external stress function* $\bar{\boldsymbol{\sigma}}(t)$, i.e. we assume the given traction

$$\mathbf{t} = \bar{\boldsymbol{\sigma}} \cdot \mathbf{n} \quad \text{on } \partial\mathcal{B} \quad (5.7)$$

on the *full surface* of the body, where \mathbf{n} is the outward normal on $\partial\mathcal{B}$. As a consequence, the stresses inside the solid domain decompose according to

$$\boldsymbol{\sigma}(\mathbf{x}, t) = \bar{\boldsymbol{\sigma}}(t) + \tilde{\boldsymbol{\sigma}}(\mathbf{x}, t) \quad \text{in } \mathcal{B} \quad (5.8)$$

into the external part $\bar{\boldsymbol{\sigma}}$ and the stress fluctuation $\tilde{\boldsymbol{\sigma}}$. The stress fluctuation is governed by the mechanical equilibrium equation

$$\operatorname{div}[\tilde{\boldsymbol{\sigma}}] = \mathbf{0} \quad \text{in } \mathcal{B}. \quad (5.9)$$

As a consequence of (5.7)–(5.9), we obtain

$$\int_{\mathcal{B}} \tilde{\boldsymbol{\sigma}} \, dV = \int_{\partial\mathcal{B}} (\tilde{\boldsymbol{\sigma}} \cdot \mathbf{n}) \otimes \mathbf{x} \, dA - \int_{\mathcal{B}} \operatorname{div}[\tilde{\boldsymbol{\sigma}}] \otimes \mathbf{x} \, dV = \mathbf{0}. \quad (5.10)$$

With this result at hand, it is clear that the above introduced external stress

$$\bar{\boldsymbol{\sigma}} = \frac{1}{|\mathcal{B}|} \int_{\mathcal{B}} \boldsymbol{\sigma} \, dV \quad (5.11)$$

is the *average stress* in the solid domain \mathcal{B} . We consider the polarized body to be mechanically loaded by this average stress. It induces the *mechanical load functional*

$$L_{\bar{\boldsymbol{\sigma}}}(\mathbf{u}; t) = \int_{\partial\mathcal{B}} \mathbf{u} \cdot (\bar{\boldsymbol{\sigma}}(t) \cdot \mathbf{n}) \, dA = \int_{\mathcal{B}} \nabla_s \mathbf{u} : \bar{\boldsymbol{\sigma}}(t) \, dV \quad (5.12)$$

Note that the pure Neumann-type loading (5.7) determines the displacement field \mathbf{u} up to rigid body motions. They can be suppressed by suitable Dirichlet conditions, which do not give constraints on the deformation of the solid. Examples are single nodal supports in typical finite element discretizations.

Electric loading by average macro-field. The polarized solid with polarization \mathbb{p} *generates* the electric field $\tilde{\mathbf{e}}$, which is therefore also called depolarization field. Let the total electric field be decomposed according to

$$\mathbf{e}(\mathbf{x}, t) = \bar{\mathbf{e}}(t) + \tilde{\mathbf{e}}(\mathbf{x}, t) \quad \text{in } \Omega, \quad (5.13)$$

where $\bar{\mathbf{e}}(t)$ is the *constant external contribution*. Considering the polarization \mathbb{p} in the domain as given, $\tilde{\mathbf{e}}$ follows from Faraday's and Gauss's law in the absence of electric fields, free currents, and electric charges

$$\operatorname{curl}[\tilde{\mathbf{e}}] = \mathbf{0} \quad \text{and} \quad \operatorname{div}[\epsilon_0 \tilde{\mathbf{e}} + \hat{\mathbb{p}}] = 0 \quad \text{in } \Omega, \quad (5.14)$$

where the formal extension of the polarization to the free space box Ω is obtained by defining the function

$$\hat{\mathbb{p}}(\mathbf{x}) = \begin{cases} \mathbb{p} & \text{for } \mathbf{x} \in \mathcal{B}, \\ \mathbf{0} & \text{otherwise.} \end{cases} \quad (5.15)$$

Condition (5.14)₁ is satisfied by equation (5.6)₂ in terms of the electric potential $\tilde{\phi}$, which is formally assumed to satisfy the Dirichlet condition

$$\tilde{\phi} = 0 \quad \text{on } \partial\Omega \quad (5.16)$$

on the boundary $\partial\Omega$ of the free space box Ω . As a consequence, we have

$$\int_{\Omega} \bar{e} dV = - \int_{\partial\Omega} \tilde{\phi} \mathbf{N} dA = \mathbf{0}, \quad (5.17)$$

where \mathbf{N} is the outward normal on the surface $\partial\Omega$ of the free space box. Hence, we may view the external field \bar{e} as the *average* of the total electric field in Ω

$$\bar{e} = \frac{1}{|\Omega|} \int_{\Omega} e dV. \quad (5.18)$$

We consider the polarized body to be loaded by the external *electric load functional*

$$L_{\bar{e}}(\mathbb{P}; t) = \int_{\mathcal{B}} \mathbb{P} \cdot \bar{e}(t) dV \quad (5.19)$$

Note again that the external loading field $\bar{e}(t)$ is assumed to be constant over the element domain \mathcal{B} .

5.1.3. Objective state variables: Theory of grade one

The three fields \mathbf{u} , \mathbb{P} , and $\tilde{\phi}$ defined in (5.3) and (5.4) are the primary variable fields for the coupled electro-mechanical problem of a solid embedded into the free space. We consider a constitutive theory for simple materials of the grade one by assuming constitutive functions to be dependent on these primary variables and their first gradient. For a generic scalar constitutive variable f , we constitute the functional dependence

$$f = \hat{f}(\mathbf{f}_0) \quad \text{with} \quad \mathbf{f}_0 := \{\mathbf{u}, \nabla \mathbf{u}, \tilde{\phi}, \nabla \tilde{\phi}, \mathbb{P}, \nabla \mathbb{P}\}. \quad (5.20)$$

For the quasi-static problem under consideration, these functions are constrained to satisfy the invariance condition

$$\hat{f}(\mathbf{f}_0^+) = \hat{f}(\mathbf{f}_0) \quad (5.21)$$

for superimposed rigid body motions $\mathbf{u}^+ = \mathbf{u} + \mathbf{w}\mathbf{x} + \mathbf{c}$ and a shift of the electric potential $\tilde{\phi}^+ = \tilde{\phi} + c$. Thus, we have $\mathbf{f}_0^+ := \{\mathbf{u} + \mathbf{w}\mathbf{x} + \mathbf{c}, \nabla \mathbf{u} + \mathbf{w}, \tilde{\phi} + c, \nabla \tilde{\phi}, \mathbb{P}, \nabla \mathbb{P}\}$ for arbitrary skew tensors \mathbf{w} , vectors \mathbf{c} , and scalars c , respectively. The immediate consequence of (5.21) is that the constitutive function \hat{f} cannot depend on the displacement \mathbf{u} , the skew part of the displacement gradient skew $[\nabla \mathbf{u}]$, and the electric potential $\tilde{\phi}$. A reduced constitutive equation of the grade one can be specified to

$$f = \hat{f}_{red}(\mathbf{f}) \quad \text{with} \quad \mathbf{f} := \{\nabla_s \mathbf{u}, -\nabla \tilde{\phi}, \mathbb{P}, \nabla \mathbb{P}\} =: \{\boldsymbol{\varepsilon}, \tilde{e}, \mathbb{P}, \nabla \mathbb{P}\}, \quad (5.22)$$

depending on the *set of objective state variables* \mathbf{f} that satisfy a priori the constraint (5.21). Recall that the symmetric part of the displacement gradient is the classical small-strain tensor $\boldsymbol{\varepsilon} := \nabla_s \mathbf{u} = \frac{1}{2} [\mathbf{f} + \mathbf{f}^T]$ in $Sym(d)$.

5.1.4. Energy-enthalpy and dissipation potential functionals

In order to describe the energy storage in micro-electrics in terms of the objective constitutive state defined in (5.22), we first introduce a constitutive free energy function and transform it later by a Legendre-Fenchel transformation to a mixed energy-enthalpy function suitable for the above choice of the primary variables.

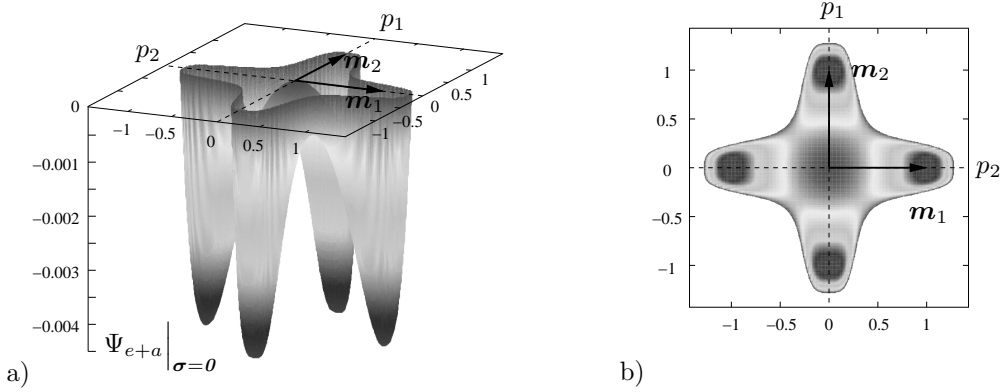


Figure 5.2: Landau-Devonshire four-well potential. Landau-Devonshire energy and corresponding structural vectors $\{\mathbf{m}_i\}_{i=1,2}$ pointing to the minima of the four wells. a) Three dimensional plot of Ψ_{e+a} evaluated at a zero stress state and b) projection onto the $p_1 p_2$ -plane at $\Psi_{e+a} = 0$.

Contributions to the energy density. Two contributions to the energy density need to be described: A part Ψ'_{vac} due to the presence of an electric field in the full free space box Ω and the additional part Ψ_{mat} in the domain $\mathcal{B} \subset \Omega$ due to the elastic deformation and the polarization of the solid. Hence, in the solid domain \mathcal{B} , the total free energy density of the solid material embedded into the free space decomposes according to

$$\Psi'(\boldsymbol{\varepsilon}, \tilde{\mathbf{d}}, \mathbf{p}, \nabla \mathbf{p}) = \Psi_{mat}(\boldsymbol{\varepsilon}, \mathbf{p}, \nabla \mathbf{p}) + \Psi'_{vac}(\mathbf{p}, \tilde{\mathbf{d}}) \quad (5.23)$$

into contributions from the material and the free space. $\tilde{\mathbf{d}}$ is the electric displacement induced by the polarization, see definition (5.29) below. The material part of the free energy is a function of the strain $\boldsymbol{\varepsilon}$, the polarization \mathbf{p} , and its gradient $\nabla \mathbf{p}$. It is assumed to consist of the three contributions

$$\Psi_{mat}(\boldsymbol{\varepsilon}, \mathbf{p}, \nabla \mathbf{p}) = \Psi_e(\boldsymbol{\varepsilon}, \mathbf{p}) + \Psi_a(\mathbf{p}) + \Psi_{ex}(\nabla \mathbf{p}), \quad (5.24)$$

where Ψ_e is the elastic and electrostriction energy, Ψ_a the anisotropy energy, often denoted as the Landau contribution, and Ψ_{ex} the exchange energy, often referred to as the Ginzburg contribution.

Elastic energy density. The elastic energy $\Psi_e : Sym(d) \times \mathcal{R}^d \mapsto \mathcal{R}_+$ describes the energy storage due to elastic lattice distortions. Associated with the polarization \mathbf{p} , there exists a preferred local distortion of the crystalline solid. In line with ZHANG & BHATTACHARYA [210, 211], we introduce the elastic energy density to be a quadratic, isotropic tensor function represented in terms of trace-type invariants

$$\Psi_e(\boldsymbol{\varepsilon}, \mathbf{p}) = \frac{\lambda}{2} \text{tr}^2[\boldsymbol{\varepsilon}] + \mu \text{tr}[\boldsymbol{\varepsilon}^2] - \frac{\alpha}{2} \text{tr}[\boldsymbol{\varepsilon}] \text{tr}[\mathbf{p} \otimes \mathbf{p}] - \beta \text{tr}[\boldsymbol{\varepsilon} \cdot (\mathbf{p} \otimes \mathbf{p})]. \quad (5.25)$$

For simplicity, we modeled the elastic response to be isotropic based on the two Lamé constants $\lambda > 0$ and $\mu > 0$. For the coupling term the material parameters are chosen to be the electrostrictive coefficients α and β .

Anisotropy energy density. In a crystalline solid, there exist preferred directions of the polarization often denoted as the *easy directions*. They are modeled by the even,

anisotropy energy density $\Psi_a : \mathcal{R}^d \mapsto \mathcal{R}$. The minima of Ψ_a define the easy directions, that are the directions along which the material is polarized most easily. Specific polynomial representations of this non-convex energy contribution Ψ_a for different crystals are reported in DEVONSHIRE [38, 39]. For the three dimensional case $d = 3$, the set of minima of the anisotropy energy is at the preferred direction $\mathcal{K} := \{\pm \mathbf{m}_1, \pm \mathbf{m}_2, \pm \mathbf{m}_3\}$, characterized by the three orthonormal structural vectors $\{\mathbf{m}_i\}_{i=1,3}$. Then, a possible anisotropy energy density can be specified to be a function satisfying the constraint

$$0 = \Psi_a(\pm \mathbf{m}_i) < \Psi_a(\mathbf{m}) \quad \forall \quad \mathbf{m} \notin \{\pm \mathbf{m}_i\}. \quad (5.26)$$

Without loss of generality, the minimum values of Ψ_a are set to zero, which can be achieved by a shift of the coordinate axis. Hence, the latter restriction is satisfied by an energy density up to the eighth-order in components of microscopic polarization

$$\begin{aligned} \Psi_a(\mathbb{P}) = & \frac{a_1}{2} [(\mathbf{m}_1 \cdot \mathbb{P})^2 + (\mathbf{m}_2 \cdot \mathbb{P})^2 + (\mathbf{m}_3 \cdot \mathbb{P})^2] \\ & + \frac{a_2}{4} [(\mathbf{m}_1 \cdot \mathbb{P})^4 + (\mathbf{m}_2 \cdot \mathbb{P})^4 + (\mathbf{m}_3 \cdot \mathbb{P})^4] \\ & + \frac{a_3}{2} [(\mathbf{m}_1 \cdot \mathbb{P})^2 (\mathbf{m}_2 \cdot \mathbb{P})^2 + (\mathbf{m}_2 \cdot \mathbb{P})^2 (\mathbf{m}_3 \cdot \mathbb{P})^2 + (\mathbf{m}_1 \cdot \mathbb{P})^2 (\mathbf{m}_3 \cdot \mathbb{P})^2] \\ & + \frac{a_4}{6} [(\mathbf{m}_1 \cdot \mathbb{P})^6 + (\mathbf{m}_2 \cdot \mathbb{P})^6 + (\mathbf{m}_3 \cdot \mathbb{P})^6] \\ & + \frac{a_5}{4} [(\mathbf{m}_1 \cdot \mathbb{P})^4 (\mathbf{m}_2 \cdot \mathbb{P})^4 + (\mathbf{m}_2 \cdot \mathbb{P})^4 (\mathbf{m}_3 \cdot \mathbb{P})^4 + (\mathbf{m}_1 \cdot \mathbb{P})^4 (\mathbf{m}_3 \cdot \mathbb{P})^4]. \end{aligned} \quad (5.27)$$

Ψ_a governs the anisotropic energy landscape with four wells at the easy directions of the polarization. A graphical representation of the elastic, electrostriction, and anisotropy energy evaluated at a zero stress state is given in [Figure 5.2](#).

Exchange energy density. The exchange energy $\Psi_{ex} : Lin(d) \mapsto [0, +\infty]$ models the tendency of neighboring polarized states to align. Focusing on an isotropic response, we consider the standard expression

$$\Psi_{ex}(\nabla \mathbb{P}) = \frac{A}{2} \text{tr}[\nabla \mathbb{P} \cdot \nabla^T \mathbb{P}], \quad (5.28)$$

where the material parameter $A > 0$ is the exchange energy coefficient. It is a material length scale related to the width of the electric domain walls.

Energy density of the free space. The polarization \mathbb{P} defines, together with the depolarizing electric field $\tilde{\mathbf{e}}$, the electric displacement induced by the polarization

$$\tilde{\mathbf{d}} = (\epsilon_0 \tilde{\mathbf{e}} + \hat{\mathbb{P}}) \quad \text{in } \Omega \quad (5.29)$$

with $\hat{\mathbb{P}}$ defined in (5.15). The energy $\Psi'_{vac} : \mathcal{R}^d \times \mathcal{R}^d \mapsto [0, +\infty]$ describes the energy due to the presence of an electric field in the free space in the absence of an external source including the embedded solid material. Resolving (5.29) for the electric field $\tilde{\mathbf{e}} = \hat{\mathbf{e}}(\mathbb{P}, \tilde{\mathbf{d}})$, we define the quadratic form

$$\Psi'_{vac}(\tilde{\mathbf{d}}, \mathbb{P}) = \frac{\epsilon_0}{2} \text{tr}[\hat{\mathbf{e}} \otimes \hat{\mathbf{e}}] = \frac{1}{2\epsilon_0} \text{tr}[(\tilde{\mathbf{d}} - \hat{\mathbb{P}}) \otimes (\tilde{\mathbf{d}} - \hat{\mathbb{P}})] \quad (5.30)$$

governed by the permittivity of free space $\epsilon_0 > 0$.

5.1.5. The energy-enthalpy function of micro-electro-elasticity

With the above definition of the free energy function at hand, the mixed energy-enthalpy function is obtained by the partial Legendre-Fenchel transformation

$$\Psi(\nabla_s \mathbf{u}, \tilde{\mathbf{e}}, \mathbb{P}, \nabla \mathbb{P}) = \inf_{\tilde{\mathbf{d}}} [\Psi'(\nabla_s \mathbf{u}, \tilde{\mathbf{d}}, \mathbb{P}, \nabla \mathbb{P}) - \tilde{\mathbf{e}} \cdot \tilde{\mathbf{d}}] \quad (5.31)$$

with respect to the electric slot. This transformation affects only the free space part Ψ_{vac} of the free energy. The necessary condition of (5.31) gives (5.29). Using this as an elimination equation for $\tilde{\mathbf{d}}$, we get from (5.31) the energy-enthalpy function

$$\Psi(\nabla_s \mathbf{u}, \tilde{\mathbf{e}}, \mathbb{P}, \nabla \mathbb{P}) = \Psi_{mat}(\nabla_s \mathbf{u}, \mathbb{P}, \nabla \mathbb{P}) - \frac{\epsilon_0}{2} \tilde{\mathbf{e}} \cdot \tilde{\mathbf{e}} - \tilde{\mathbf{e}} \cdot \mathbb{P} \quad (5.32)$$

governed by the free energy density Ψ_{mat} of the solid material defined in (5.24). Note that the energy-enthalpy function Ψ is formulated in terms of the objective constitutive state variables \mathbf{f} defined in (5.22). With this function at hand and the definition (5.6)₂ of the electric field $\tilde{\mathbf{e}}$, we finally obtain the *energy-enthalpy functional* of the polarized solid \mathcal{B} embedded into the free space Ω

$$E(\mathbf{u}, \tilde{\phi}, \mathbb{P}) = \int_{\mathcal{B}} \{ \Psi_{mat}(\nabla_s \mathbf{u}, \mathbb{P}, \nabla \mathbb{P}) + \nabla \tilde{\phi} \cdot \mathbb{P} \} dV - \frac{\epsilon_0}{2} \int_{\Omega} |\nabla \tilde{\phi}|^2 dV \quad (5.33)$$

5.1.6. Dissipation potential for micro-electric evolution

For a time-dependent, dynamic modeling of the evolution of the polarization \mathbb{P} a kinetic law needs to be defined. This is achieved by the definition of a constitutive dissipation potential. We assume the simple quadratic structure

$$\Phi(\dot{\mathbb{P}}) = \frac{\eta}{2} \text{tr}[\dot{\mathbb{P}} \otimes \dot{\mathbb{P}}], \quad (5.34)$$

where the scalar parameter η is an inverse mobility coefficient, which governs the kinetics of the domain wall evolution. With the above function at hand, the *dissipation potential functional* is introduced as

$$D(\dot{\mathbb{P}}) = \frac{\eta}{2} \int_{\mathcal{B}} |\dot{\mathbb{P}}|^2 dV \quad (5.35)$$

The four functionals $L_{\bar{\sigma}}$, $L_{\bar{\mathbf{e}}}$, E , and D defined in (5.12), (5.19), (5.33), and (5.35) govern the variational principles of micro-electro-elasticity outlined in the subsequent sections.

5.2. Variational formulations of micro-electro-elasticity

Based on the functionals introduced in the section above, we consider now variational principles which govern the coupled electro-mechanical problem. Here, we first focus on stationary problems and extend them in a second step to dissipative dynamic problems.

5.2.1. Variational formulation for stationary problems

Consider a variational principle for stationary problems, whose variation is conceptually in line with the principle of virtual work for dielectrics proposed by TOUPIN [190]. Based on the energy-enthalpy functional (5.33), the mechanical loading functional (5.12), and the electric loading functional (5.19), we define the *stationary electro-elastic potential*

$$\Pi_{stat}(\mathbf{u}, \tilde{\phi}, \mathbb{P}; t) := E(\mathbf{u}, \tilde{\phi}, \mathbb{P}) - L_{\bar{\sigma}}(\mathbf{u}; t) - L_{\bar{e}}(\mathbb{P}; t) \quad (5.36)$$

yielding the explicit form

$$\Pi_{stat} = \int_{\mathcal{B}} \Psi_{mat}(\nabla_s \mathbf{u}, \mathbb{P}, \nabla \mathbb{P}) - \nabla_s \mathbf{u} : \bar{\sigma}(t) dV - \int_{\Omega} [\bar{e}(t) - \nabla \tilde{\phi}] \cdot \hat{\mathbb{P}} + \frac{\epsilon_0}{2} |\nabla \tilde{\phi}|^2 dV, \quad (5.37)$$

where $\hat{\mathbb{P}}$ defined in (5.15) is used for the extension of the polarization to the full space Ω . The displacement, the polarization, and the electric potential are assumed to be governed by the *variational principle*

$$\boxed{\{\mathbf{u}, \tilde{\phi}, \mathbb{P}\} = \arg \left\{ \inf_{\mathbf{u}} \sup_{\tilde{\phi}} \inf_{\mathbb{P}} \Pi_{stat}(\mathbf{u}, \tilde{\phi}, \mathbb{P}; t) \right\}} \quad (5.38)$$

The necessary condition of this principle is provided by the variation

$$\begin{aligned} \delta \Pi_{stat} &= \int_{\mathcal{B}} \left\{ -\operatorname{div}[\partial_{\nabla_s \mathbf{u}} \Psi_{mat}] \cdot \delta \mathbf{u} + [\delta_{\mathbb{P}} \Psi_{mat} - (\bar{e}(t) - \nabla \tilde{\phi})] \cdot \delta \mathbb{P} \right\} dV \\ &+ \int_{\partial \mathcal{B}} [(\partial_{\nabla_s \mathbf{u}} \Psi_{mat} - \bar{\sigma}(t)) \cdot \mathbf{n}] \cdot \delta \mathbf{u} dA + \int_{\partial \mathcal{B}_t} (\partial_{\nabla \mathbb{P}} \Psi_{mat} \cdot \mathbf{n}) \cdot \delta \mathbb{P} dA \\ &- \int_{\Omega} \operatorname{div}[-\epsilon_0 \nabla \tilde{\phi} + \hat{\mathbb{P}}] \cdot \delta \tilde{\phi} dV + \int_{\partial \mathcal{B}} [(-\epsilon_0 \nabla \tilde{\phi} + \hat{\mathbb{P}}) \cdot \mathbf{n}] \cdot \delta \tilde{\phi} dA = 0 \end{aligned} \quad (5.39)$$

for the virtual fields $\{\delta \mathbf{u}, \delta \tilde{\phi}, \delta \mathbb{P}\}$ with $\delta \mathbb{P} = \mathbf{0}$ on $\partial \mathcal{B}_p$ and $\delta \tilde{\phi} = 0$ on $\partial \Omega$. Thus, we end up with the Euler equations

$$\left. \begin{aligned} \operatorname{div}[\partial_{\nabla_s \mathbf{u}} \Psi_{mat}] &= \mathbf{0} \\ \delta_{\mathbb{P}} \Psi_{mat} - (\bar{e}(t) - \nabla \tilde{\phi}) &= \mathbf{0} \\ \operatorname{div}[-\epsilon_0 \nabla \tilde{\phi} + \mathbb{P}] &= 0 \end{aligned} \right\} \text{ in } \mathcal{B} \quad (5.40)$$

in the solid domain \mathcal{B} , along with the boundary conditions

$$\partial_{\nabla_s \mathbf{u}} \Psi_{mat} \cdot \mathbf{n} = \bar{\sigma}(t) \cdot \mathbf{n} \quad \text{on } \partial \mathcal{B} \quad \text{and} \quad \partial_{\nabla \mathbb{P}} \Psi_{mat} \cdot \mathbf{n} = \mathbf{0} \quad \text{on } \partial \mathcal{B}_t, \quad (5.41)$$

the jump condition

$$[-\epsilon_0 \nabla \tilde{\phi} + \hat{\mathbb{P}}] \cdot \mathbf{n} = 0 \quad \text{on } \partial \mathcal{B} \quad (5.42)$$

at the interface between the solid domain and the surrounding free space, and the field equation

$$\Delta \tilde{\phi} = 0 \quad \text{in } \Omega \setminus \mathcal{B} \quad (5.43)$$

in the surrounding free space $\Omega \setminus \mathcal{B}$, where $\Delta(\cdot) = \operatorname{div}[\operatorname{grad}(\cdot)]$ is the Laplace operator. Here, we introduced the variational or functional derivative of the material free energy function with respect to the polarization

$$\delta_{\mathbb{P}} \Psi_{mat} := \partial_{\mathbb{P}} \Psi_{mat} - \operatorname{div}[\partial_{\nabla \mathbb{P}} \Psi_{mat}]. \quad (5.44)$$

The set (5.40)–(5.43) of equations is consistent with those outlined in TOUPIN [190, p.883] for dielectrics. Note that (5.40)₁ and (5.40)₃ reflect the stress equilibrium equation and the Gauss law. The third equation (5.40)₂ governs the evolution of the polarization, but is *not well posed* due to the non-convexity of the free energy function Ψ_{mat} . This has motivated researchers to approach formally similar problems in micro-magnetics based on relaxation and convexification methods.

Optimizing the functional (5.37) with respect to the electric potential $\tilde{\phi}$, the Maxwell equation (5.14)₂ is obtained. This equation expresses the fact that the potential $\tilde{\phi}$ in Ω is determined by the polarization \mathbb{p} in $\mathcal{B} \subset \Omega$. The Gauss law (5.14)₂ implies the condition

$$\int_{\Omega} \epsilon_0 |\nabla \tilde{\phi}|^2 dV = \int_{\Omega} \hat{\mathbb{p}} \cdot \nabla \tilde{\phi} dV, \quad (5.45)$$

as pointed out for the equivalent problem of micro-magnetics by JAMES & KINDERLEHRER [78, p.220]. Substituting this result into (5.37) and setting $A = 0$ in the exchange term yields the energy functional

$$E_{stat} = \int_{\mathcal{B}} \{ \Psi_e(\nabla_s \mathbf{u}, \mathbb{p}) + \Psi_a(\mathbb{p}) - \nabla_s \mathbf{u} : \bar{\boldsymbol{\sigma}}(t) - \mathbb{p} \cdot \bar{\mathbf{e}}(t) \} dV + \frac{\epsilon_0}{2} \int_{\Omega} |\nabla \tilde{\phi}|^2 dV, \quad (5.46)$$

which is quite similar to the constrained theory of magnetization for large bodies proposed by DESIMONE & JAMES [36, p.288]. The functional understood to be constrained by Gauss's law (5.14)₂, which determines the electric potential $\tilde{\phi}$ for a given polarization \mathbb{p} . In [36], this functional served as a starting point for the computation of laminate-type magnetic domains based on relaxation concepts in the calculus of direct variation of non-convex problems. Relaxation methods for the solution of non-convex variational problems based on (5.46) for the analysis of domain patterns in ferroelectrics are considered in SHU & BHATTACHARYA [165] and BHATTACHARYA & RAVICHANDRAN [17]. Here, laminate-type structures are adopted to characterize the electric microstructure.

5.2.2. Variational formulation for dynamic problems

For dynamic problems, which govern the evolution in time of the polarization in the solid, we define a *rate-type variational principle* governing the rates $\{\dot{\mathbf{u}}, \dot{\tilde{\phi}}, \dot{\mathbb{p}}\}$ at a *given state* $\{\mathbf{u}, \tilde{\phi}, \mathbb{p}\}$. This treatment also includes the *kinetics* of the polarization, which is assumed to be dissipative in nature. It is described by the dissipation potential functional D introduced in (5.35). Based on the energy-enthalpy functional (5.33), the dissipation potential functional (5.35), the mechanical loading functional (5.12), and the electric loading functional (5.19), the rate-type *dynamic electro-elastic potential* is defined as

$$\Pi(\dot{\mathbf{u}}, \dot{\tilde{\phi}}, \dot{\mathbb{p}}; t) := \frac{d}{dt} E(\mathbf{u}, \tilde{\phi}, \mathbb{p}) + D(\dot{\mathbb{p}}) - L_{\bar{\boldsymbol{\sigma}}}(\dot{\mathbf{u}}; t) - L_{\bar{\mathbf{e}}}(\dot{\mathbb{p}}; t) \quad (5.47)$$

at a given state $\{\mathbf{u}, \tilde{\phi}, \mathbb{p}\}$. Note the appearance of the dissipation functional D in the potential. Using integration by parts, the rate-functional takes the explicit form

$$\begin{aligned} \Pi = & \int_{\mathcal{B}} \{ -\operatorname{div}[\partial_{\nabla_s \mathbf{u}} \Psi_{mat}] \cdot \dot{\mathbf{u}} + [\delta_{\mathbb{p}} \Psi_{mat} - (\bar{\mathbf{e}}(t) - \nabla \tilde{\phi}) + \frac{\eta}{2} \dot{\mathbb{p}}] \cdot \dot{\mathbb{p}} \} dV \\ & + \int_{\partial \mathcal{B}} [(\partial_{\nabla_s \mathbf{u}} \Psi_{mat} - \bar{\boldsymbol{\sigma}}(t)) \cdot \mathbf{n}] \cdot \dot{\mathbf{u}} dA + \int_{\partial \mathcal{B}_t} (\partial_{\nabla_{\mathbb{p}}} \Psi_{mat} \cdot \mathbf{n}) \cdot \dot{\mathbb{p}} dA \\ & - \int_{\Omega} \{ \operatorname{div}[-\epsilon_0 \nabla \tilde{\phi} + \hat{\mathbb{p}}] \cdot \dot{\tilde{\phi}} \} dV + \int_{\partial \mathcal{B}} ([-\epsilon_0 \nabla \tilde{\phi} + \hat{\mathbb{p}}] \cdot \mathbf{n}) \cdot \dot{\tilde{\phi}} dA. \end{aligned} \quad (5.48)$$

Note that this functional is linear in the rates $\{\dot{\mathbf{u}}, \dot{\phi}, \dot{\mathbb{P}}\}$ up to the quadratic term $\eta \dot{\mathbb{P}} \cdot \dot{\mathbb{P}}/2$, which comes from the dissipation function. We assume that the *rates* of the displacement, the polarization, and the electric potential at a given state are governed by the variational principle

$$\boxed{\{\dot{\mathbf{u}}, \dot{\phi}, \dot{\mathbb{P}}\} = \arg \left\{ \inf_{\dot{\mathbf{u}}} \sup_{\dot{\phi}} \inf_{\dot{\mathbb{P}}} \Pi(\dot{\mathbf{u}}, \dot{\phi}, \dot{\mathbb{P}}; t) \right\}} \quad (5.49)$$

The necessary condition of this principle is provided by the variation

$$\begin{aligned} \delta \Pi = & \int_{\mathcal{B}} \left\{ -\operatorname{div}[\partial_{\nabla_{s\mathbf{u}}} \Psi_{mat}] \cdot \delta \dot{\mathbf{u}} + [\delta_{\mathbb{P}} \Psi_{mat} - (\bar{\mathbf{e}}(t) - \nabla \tilde{\phi}) + \eta \dot{\mathbb{P}}] \cdot \delta \dot{\mathbb{P}} \right\} dV \\ & + \int_{\partial \mathcal{B}} [(\partial_{\nabla_{s\mathbf{u}}} \Psi_{mat} - \bar{\boldsymbol{\sigma}}(t)) \cdot \mathbf{n}] \cdot \delta \dot{\mathbf{u}} dA + \int_{\partial \mathcal{B}_t} (\partial_{\nabla_{\mathbb{P}}} \Psi_{mat} \cdot \mathbf{n}) \cdot \delta \dot{\mathbb{P}} dA \\ & - \int_{\Omega} \left\{ \operatorname{div}[-\epsilon_0 \nabla \tilde{\phi} + \hat{\mathbb{P}}] \cdot \delta \dot{\phi} \right\} dV + \int_{\partial \mathcal{B}} ([-\epsilon_0 \nabla \tilde{\phi} + \hat{\mathbb{P}}] \cdot \mathbf{n}) \cdot \delta \dot{\phi} dA = 0 \end{aligned} \quad (5.50)$$

for the virtual fields $\{\delta \dot{\mathbf{u}}, \delta \dot{\phi}, \delta \dot{\mathbb{P}}\}$ with $\delta \dot{\mathbb{P}} = \mathbf{0}$ on $\partial \mathcal{B}_p$ and $\delta \dot{\phi} = 0$ on $\partial \Omega$. Note that (5.50) is identical to (5.39) up to the term that results from the dissipation. Hence, the Euler equations are identical with (5.40)–(5.43) of the stationary variational principle up to (5.40)₂, which now appears in the form

$$\eta \dot{\mathbb{P}} + [\delta_{\mathbb{P}} \Psi_{mat} - (\bar{\mathbf{e}}(t) - \nabla \tilde{\phi})] = \mathbf{0} \quad \text{in } \mathcal{B}. \quad (5.51)$$

It extends the stationary equation (5.40)₂ by the kinetic term $\eta \dot{\mathbb{P}}$. Hence, this equation determines the rate of the polarization by the kinetic equation

$$\dot{\mathbb{P}} = -\frac{1}{\eta} [\delta_{\mathbb{P}} \Psi_{mat} - (\bar{\mathbf{e}}(t) - \nabla \tilde{\phi})] \quad \text{in } \mathcal{B}. \quad (5.52)$$

This is consistent with a Ginzburg-Landau-type equation of phase field models such as reviewed in GURTIN [54].

5.3. Discrete incremental variational formulations

5.3.1. Time-discrete field variables in incremental setting

We now outline variational principles for time-discrete problems. To this end, we consider time-discrete solutions of the field variables at the discrete times $0, t_1, t_2, \dots, t_n, t_{n+1}, \dots, T$ of the process interval $[0, T]$. In order to advance the solution within a typical time step, we focus on the finite time increment $[t_n, t_{n+1}]$, where

$$\tau_{n+1} := t_{n+1} - t_n > 0 \quad (5.53)$$

denotes the step length. In the subsequent treatment, all field variables at time t_n are assumed to be *known*. The goal then is to determine the fields at time t_{n+1} based on variational principles valid for the time increment under consideration. In particular, we assemble the time-discrete spatial fields (displacement, polarization, electric potential) at the discrete times t_n and t_{n+1} in the discrete solution vectors

$$\mathbf{d}_{n+1} := \{\mathbf{u}_{n+1}, \tilde{\phi}_{n+1}, \mathbb{P}_{n+1}\} \quad \text{and} \quad \mathbf{d}_n := \{\mathbf{u}_n, \tilde{\phi}_n, \mathbb{P}_n\}. \quad (5.54)$$

The rates of the field variables are considered to be *constant* in the time increment (5.53) under consideration and defined by the algorithmic expression

$$\dot{\mathbf{d}}_{n+1} := [\mathbf{d}_{n+1} - \mathbf{d}_n]/\tau_{n+1}. \quad (5.55)$$

Note carefully that due to the given fields at time t_n , this rate is a linear function of variables \mathbf{d}_{n+1} at the current time t_{n+1} . As a consequence of the finite-step-sized algorithmic representation of rates such as (5.55), the discrete counterpart of the rate-type, dynamic variational principle outlined in Subsection 5.2.2 determines the *discrete state variables* \mathbf{d}_{n+1} at the current time t_{n+1} . In order to obtain a compact notation, the subscript $n + 1$ is dropped and all variables without subscript are considered to be evaluated at time t_{n+1} .

5.3.2. Time-discrete incremental variational principle

The counterpart of the dynamic functional (5.47) in the incremental setting associated with the time interval $[t_n, t_{n+1}]$ is defined by

$$\Pi^\tau(\mathbf{u}, \tilde{\phi}, \mathbb{P}) = ALGO \left\{ \int_{t_n}^{t_{n+1}} \Pi(\dot{\mathbf{u}}, \dot{\tilde{\phi}}, \dot{\mathbb{P}}; t) d\tau \right\}, \quad (5.56)$$

depending on the variable fields \mathbf{d} at the *current time* $t = t_{n+1}$ defined in (5.54)₁. The algorithmic assumption (5.55) then defines a *linear path* of the variables in the time increment $[t_n, t_{n+1}]$, yielding the *algorithmic form*

$$\begin{aligned} \Pi^\tau(\mathbf{u}, \tilde{\phi}, \mathbb{P}) &= E(\mathbf{u}, \tilde{\phi}, \mathbb{P}) - E_n + \tau D([\mathbb{P} - \mathbb{P}_n]/\tau) \\ &\quad - \tau L_{\bar{\sigma}}([\mathbf{u} - \mathbf{u}_n]/\tau; t) - \tau L_{\bar{\epsilon}}([\mathbb{P} - \mathbb{P}_n]/\tau; t) \end{aligned} \quad (5.57)$$

of (5.56). Here, $E_n := E(\mathbf{u}_n, \mathbb{P}_n, \tilde{\phi}_n)$ is a constant. The insertion of the energy-enthalpy functional (5.33), the dissipation potential functional (5.35), the mechanical loading functional (5.12), and the electric loading functional (5.19) gives the representation

$$\begin{aligned} \Pi^\tau(\mathbf{u}, \tilde{\phi}, \mathbb{P}) &= \int_{\mathcal{B}} \{ \Psi_{mat}(\nabla_s \mathbf{u}, \mathbb{P}, \nabla \mathbb{P}) + \nabla \tilde{\phi} \cdot \mathbb{P} \} dV - \frac{\epsilon_0}{2} \int_{\Omega} |\nabla \tilde{\phi}|^2 dV \\ &\quad - E(\mathbf{u}_n, \tilde{\phi}_n, \mathbb{P}_n) + \int_{\mathcal{B}} \frac{\eta}{2\tau} |\mathbb{P} - \mathbb{P}_n|^2 dV \\ &\quad - \int_{\mathcal{B}} \{ \bar{\sigma}(t) : \nabla_s(\mathbf{u} - \mathbf{u}_n) + (\mathbb{P} - \mathbb{P}_n) \cdot \bar{\epsilon}(t) \} dV. \end{aligned} \quad (5.58)$$

Again, note carefully, that due to the algorithmic assumption (5.55), the rate-type incremental potential is considered to be a functional of the fields $\mathbf{d} := \{\mathbf{u}, \tilde{\phi}, \mathbb{P}\}$ at the current time t_{n+1} . These fields are then determined by the *incremental variational principle*

$$\boxed{\{\mathbf{u}, \tilde{\phi}, \mathbb{P}\} = \arg \left\{ \inf_{\mathbf{u}} \sup_{\tilde{\phi}} \inf_{\mathbb{P}} \Pi^\tau(\mathbf{u}, \tilde{\phi}, \mathbb{P}) \right\}} \quad (5.59)$$

The variation of the functional (5.58) takes the form

$$\begin{aligned} \delta\Pi^\tau &= \int_{\mathcal{B}} \left\{ -\operatorname{div}[\partial_{\nabla_s \mathbf{u}} \Psi_{mat}] \cdot \delta \mathbf{u} + [\delta_{\mathbb{P}} \Psi_{mat} - (\bar{\mathbf{e}}(t) - \nabla \tilde{\phi}) + \frac{\eta}{\tau}(\mathbb{P} - \mathbb{P}_n)] \cdot \delta \mathbb{P} \right\} dV \\ &+ \int_{\partial \mathcal{B}} [(\partial_{\nabla_s \mathbf{u}} \Psi_{mat} - \bar{\boldsymbol{\sigma}}(t)) \cdot \mathbf{n}] \cdot \delta \mathbf{u} dA + \int_{\partial \mathcal{B}_t} (\partial_{\nabla_{\mathbb{P}}} \Psi_{mat} \cdot \mathbf{n}) \cdot \delta \mathbb{P} dA \\ &- \int_{\Omega} \left\{ \operatorname{div}[-\epsilon_0 \nabla \tilde{\phi} + \hat{\mathbb{P}}] \cdot \delta \tilde{\phi} \right\} dV + \int_{\partial \mathcal{B}} [(-\epsilon_0 \nabla \tilde{\phi} + \hat{\mathbb{P}}) \cdot \mathbf{n}] \cdot \delta \tilde{\phi} dA = 0 \end{aligned} \quad (5.60)$$

similar to (5.50), however, now for the variations $\{\delta \mathbf{u}, \delta \tilde{\phi}, \delta \mathbb{P}\}$ of the field variables at the discrete time t_{n+1} with $\delta \mathbb{P} = \mathbf{0}$ on $\partial \mathcal{B}_p$ and $\delta \tilde{\phi} = 0$ on $\partial \Omega$. Hence, the Euler equations of the incremental variational principle (5.59) are

$$\left. \begin{aligned} \operatorname{div}[\partial_{\nabla_s \mathbf{u}} \Psi_{mat}] &= \mathbf{0} \\ \frac{\eta}{\tau}(\mathbb{P} - \mathbb{P}_n) + [\delta_{\mathbb{P}} \Psi_{mat} - (\bar{\mathbf{e}}(t) - \nabla \tilde{\phi})] &= \mathbf{0} \\ \operatorname{div}[-\epsilon_0 \nabla \tilde{\phi} + \mathbb{P}] &= 0 \end{aligned} \right\} \text{ in } \mathcal{B} \quad (5.61)$$

in the solid domain \mathcal{B} , along with the boundary conditions

$$\partial_{\nabla_s \mathbf{u}} \Psi_{mat} \cdot \mathbf{n} = \bar{\boldsymbol{\sigma}}(t) \cdot \mathbf{n} \quad \text{on } \partial \mathcal{B} \quad \text{and} \quad \partial_{\nabla_{\mathbb{P}}} \Psi_{mat} \cdot \mathbf{n} = \mathbf{0} \quad \text{on } \partial \mathcal{B}_t, \quad (5.62)$$

the jump condition

$$[[-\epsilon_0 \nabla \tilde{\phi} + \hat{\mathbb{P}}] \cdot \mathbf{n}] = 0 \quad \text{on } \partial \mathcal{B} \quad (5.63)$$

at the interface of the solid domain with the surrounding free space, and the field equation

$$\Delta \tilde{\phi} = 0 \quad \text{in } \Omega \setminus \mathcal{B} \quad (5.64)$$

in the free space. Note that the Euler equations (5.61)–(5.64) of the incremental variational principle (5.59) are the *time-discrete, algorithmic counterparts* of the Euler equations (5.40)–(5.43) and (5.52) of the rate-type variational principle (5.49).

5.3.3. Space-time-discrete incremental variational principle

Consider now the spatial discretization of the coupled problem by the finite element method. To this end, we write the time-discrete incremental potential (5.58) in the form

$$\Pi^\tau(\mathbf{u}, \tilde{\phi}, \mathbb{P}) = \int_{\mathcal{B}} \pi^\tau(\mathbf{f}; \mathbf{f}_n) dV - \frac{\epsilon_0}{2} \int_{\Omega \setminus \mathcal{B}} |\nabla \tilde{\phi}|^2 dV + C_n \quad (5.65)$$

in terms of the *effective potential density* π^τ per unit volume of the solid domain \mathcal{B} and the additional contribution of the free space. C_n is a constant that assembles contributions at time t_n . The incremental effective potential

$$\begin{aligned} \pi^\tau(\mathbf{f}; \mathbf{f}_n) &= \Psi_{mat}(\nabla_s \mathbf{u}, \nabla_{\mathbb{P}}, \mathbb{P}) + \nabla \tilde{\phi} \cdot \mathbb{P} + \frac{\eta}{2\tau} |\mathbb{P} - \mathbb{P}_n|^2 \\ &- \bar{\boldsymbol{\sigma}}(t) : \nabla_s(\mathbf{u} - \mathbf{u}_n) - \bar{\mathbf{e}}(t) \cdot (\mathbb{P} - \mathbb{P}_n) \end{aligned} \quad (5.66)$$

is a function of the objective set of constitutive state variables $\mathbf{f} := \{\nabla_s \mathbf{u}, -\nabla \tilde{\phi}, \mathbb{P}, \nabla_{\mathbb{P}}\}$ introduced in (5.22). Now let \mathfrak{T}^h denote a finite element triangulation of the domain Ω .

Table 5.1: Ferroelectric material parameters and their normalization.

no.	par.	name	unit	normalization	value
1.	λ	Lamé parameter	N/m ²	$\lambda' = \lambda/\sigma_0$	111.0
2.	μ	Lamé parameter	N/m ²	$\mu' = \mu/\sigma_0$	37.0
3.	α	electrostrictive coefficient	Nm ² /C ²	$\alpha' = \alpha p_s^2/\sigma_0$	-0.185
4.	β	electrostrictive coefficient	Nm ² /C ²	$\beta' = \beta p_s^2/\sigma_0$	0.8066
5.	ϵ_0	electric permittivity	C ² /(Nm ²)	$\epsilon'_0 = \epsilon_0 \sigma_0 / p_s^2$	0.131
6.	a_1	anisotropy energy coefficient	Nm ² /C ²	$a'_1 = a_1 p_s^2/\sigma_0$	-0.007
7.	a_2	anisotropy energy coefficient	Nm ⁶ /C ⁴	$a'_2 = a_2 p_s^4/\sigma_0$	-0.009
8.	a_3	anisotropy energy coefficient	Nm ⁶ /C ⁴	$a'_3 = a_3 p_s^4/\sigma_0$	0.018
9.	a_4	anisotropy energy coefficient	Nm ¹⁰ /C ⁶	$a'_4 = a_4 p_s^6/\sigma_0$	0.0261
10.	a_5	anisotropy energy coefficient	Nm ¹⁴ /C ⁸	$a'_5 = a_5 p_s^8/\sigma_0$	5.0

in terms of the monolithic tangent matrix of the coupled problem

$$\Pi_{\underline{\mathbf{d}}\underline{\mathbf{d}}}^h := \int_{\mathcal{B}^h} \underline{\mathbf{B}}^T [\partial_{\underline{\mathbf{f}}\underline{\mathbf{f}}}^2 \pi^\tau] \underline{\mathbf{B}} dV - \epsilon_0 \int_{\Omega^h \setminus \mathcal{B}^h} \underline{\mathbf{G}}^T \underline{\mathbf{G}} dV. \quad (5.75)$$

Observe the *symmetry of the tangent matrix* $\Pi_{\underline{\mathbf{d}}\underline{\mathbf{d}}}^h$ induced by the incremental variational structure of the coupled three-field problem. The update (5.74) is performed until convergence is achieved in the sense $|\Pi_{\underline{\mathbf{d}}\underline{\mathbf{d}}}^h| < \text{tol}$. Observe further that the finite element residual and tangent are governed by the *generalized stress* and *tangent arrays*

$$\underline{\mathbf{S}}^h := \partial_{\underline{\mathbf{f}}\pi^\tau}(\underline{\mathbf{f}}^h; \underline{\mathbf{f}}_n^h, t) \quad \text{and} \quad \underline{\mathbf{C}}^h := \partial_{\underline{\mathbf{f}}\underline{\mathbf{f}}}^2 \pi^\tau(\underline{\mathbf{f}}^h; \underline{\mathbf{f}}_n^h, t), \quad (5.76)$$

that are the first and second derivatives of the incremental internal work density π^τ defined in (5.66) by the discretized constitutive state vector $\underline{\mathbf{f}}^h$ at current time t_{n+1} . These arrays are a critical ingredient of the proposed variational formulation and make the notation extremely compact.

5.4. Representative numerical examples

The subsequent numerical simulations demonstrate the modeling capacity of the proposed formulation. They treat domain wall movements in a piezoceramic material, such as barium titanate ($BaTiO_3$) or lead zirconate titanate (PZT), within electric field- as well as stress driven scenarios. In what follows, we focus in particular on barium titanate in a polarized tetragonal state below the Curie-Weiss transition temperature. In the subsequent treatment all variables are normalized referring to four physical variables: the equivalent stress σ_0 , the saturation polarization p_s , the inverse mobility parameter η , and the exchange energy coefficient A . The values of σ_0 and p_s for single crystal barium titanate under consideration are $\sigma_0 = 1 \cdot 10^9$ N/m² and $p_s = 0.26$ C/m². The primary variables (\cdot) are expressed in terms of their normalized counterparts (\cdot)' via

$$\mathbf{x} = \mathbf{x}' p_s / \sqrt{\sigma_0/A}, \quad \mathbb{p} = \mathbb{p}' p_s, \quad \phi = \phi' \sqrt{A\sigma_0}, \quad \mathbf{t} = \mathbf{t}' \eta p_s^2 / \sigma_0. \quad (5.77)$$

With these definitions at hand, the normalized material parameters are listed in Table 5.1, cf. the work of ZHANG & BHATTACHARYA [210, 211]. Note that the normalized values A' , η' , p'_s , and σ'_0 of the four chosen physical normalization parameters have the value one.

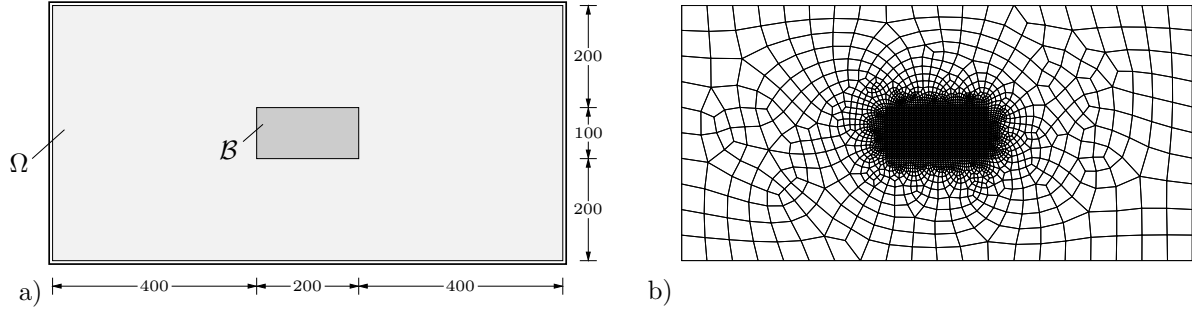


Figure 5.3: *Boundary-value-problem embedded in free space box.* a) Dimension of boundary-value-problem and b) discretization of free space box Ω surrounding the solid domain \mathcal{B} . The solid part is discretized by a structured mesh with 60×30 quadrilateral elements. For the surrounding vacuum a coarse, unstructured mesh due to numerical efficiency is used.

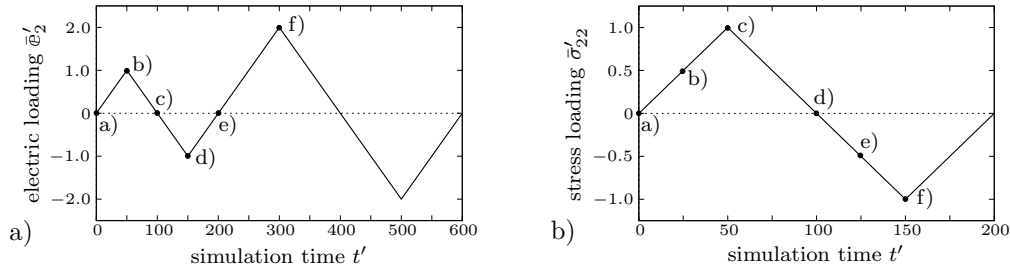


Figure 5.4: *Sawtooth-type loading functions.* a) Electric loading \bar{e}'_2 in two cycles with increasing amplitude and b) stress loading $\bar{\sigma}'_{22}$ with single cycle for tension as well as compression of the solid part embedded into the free space.

5.4.1. Definition of the boundary-value-problem

The proposed variational-based finite element formulation is applied to cyclic electric field- and stress driven loading processes. We deal with a solid \mathcal{B} embedded in a free space box Ω described by the boundary-value-problem shown in Figure 5.3, which highlights the geometry of the specimen as well as the finite element discretization. The solid part in the center of the free space box describes the electro-mechanically coupled material and is discretized by a structured mesh with 60×30 quadrilateral finite elements. In contrast, the free space is discretized by a coarse, unstructured mesh resulting in a total number of 3616 four node elements. We apply sawtooth-type loading paths for either the homogenized electric field \bar{e}' or homogenized stress $\bar{\sigma}'$. The electric field driven loading process is shown in Figure 5.4a consisting of two cycles. Here, the second cycle doubles the amplitude of the first one. The total simulation time is chosen to be $t'_{max} = 600$, resulting in periods of $T'_1 = 200$ and $T'_2 = 400$, respectively. Selected states during the deformation procedure are marked with labels a)–f), which will be commented on later. The stress driven loading in Figure 5.4b is performed in a single cycle with period $T'_1 = 200$. Again, important domain states are marked with labels a)–f). The two loading cycles considered produce either $90^\circ/180^\circ$ domain switching for electric field driven processes or solely 90° switching for the stress driven scenario. In the subsequent Subsection 5.4.2, we start from a random noise of the microscopic polarization vector p' and compute a vortex-like *equilibrium state*, which enforces Neumann-type boundary conditions for the order parameter at the interface between solid matter and free space. This equilibrium state is then used in Subsection 5.4.3 and Subsection 5.4.4 as the starting configuration for the analysis of electric field- and stress driven domain evolutions.

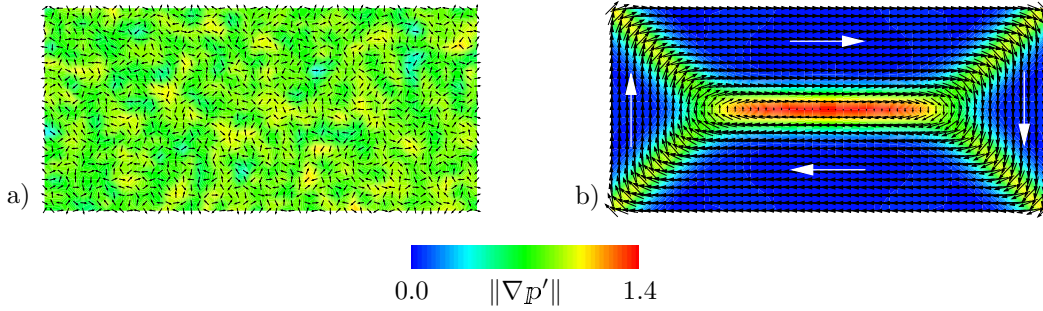


Figure 5.5: *Equilibrium state relaxation.* Relaxation of a) randomly distributed polarization p' to b) vortex-like equilibrium state at zero external load. The contours show the polarization gradient $\|\nabla p'\|$, white arrows indicate the average direction of the polarization in a domain. The surrounding free space box $\Omega \setminus \mathcal{B}$ is not visualized.

5.4.2. Construction of an initial equilibrium state

The equilibrium state of the electro-mechanically coupled material is determined in order to have a feasible starting point for subsequent computations. To this end, the normalized polarization p' is initialized by a random noise, that is an arbitrary orientation distribution of the order parameter in the solid domain \mathcal{B} . It should be pointed out that this initial random structure is not necessarily physical, but it rather serves as a reasonable, directionally-unbiased starting point for the equilibrium state computation. The normalized time step is chosen to be $\Delta t' = 1.0$ and the system is relaxed within 1000 time steps. Due to the dissipative nature of the incremental variational formulation, the motion of the domain walls is directly influenced by the inverse mobility coefficient η' . It influences the speed of the domain wall motion and thus the way how we reach a certain domain state. During the equilibrium computations only the final state matters and hence we choose for this particular case without loss of generality a normalized coefficient of $\eta' = 0.1$. Figure 5.5 shows the random initialization of the order parameter field p' and the final stage of the vortex-like equilibrium state. The progressing relaxation process causes the polarization to adjust in certain regions. A *rudimentary structure* of domains and domain walls starts to appear. After completion of the nucleation stage the domain walls are clearly visible. The final stage of the equilibrium state shows four 90° and one 180° domain wall. This is due to the fact that the constraint of a vanishing polarization in the free space acts as Neumann-type boundary condition. Hence, it is energetically unfavorable to have polarization components perpendicular to the surface $\partial\mathcal{B}$ of the solid domain. The equilibrium domain structure serves as the starting point for the subsequent numerical simulations involving electric field- and stress driven domain wall motions.

5.4.3. Electric field driven loading processes

Having determined the vortex-like domain structure in Figure 5.5b as a feasible starting point of the numerical simulations, the first example deals with microscopic domain wall motions caused by an applied electric field \bar{e}' . During such an electric field driven processes, the material under consideration is capable of 90° as well as 180° switching of the unit cells. The kind of switching depends on the direction of the external loading \bar{e}' and the current orientation of the polarization. In order to show the domain wall motion driven by the electric loading \bar{e}' , we apply the two phase sawtooth-type loading history

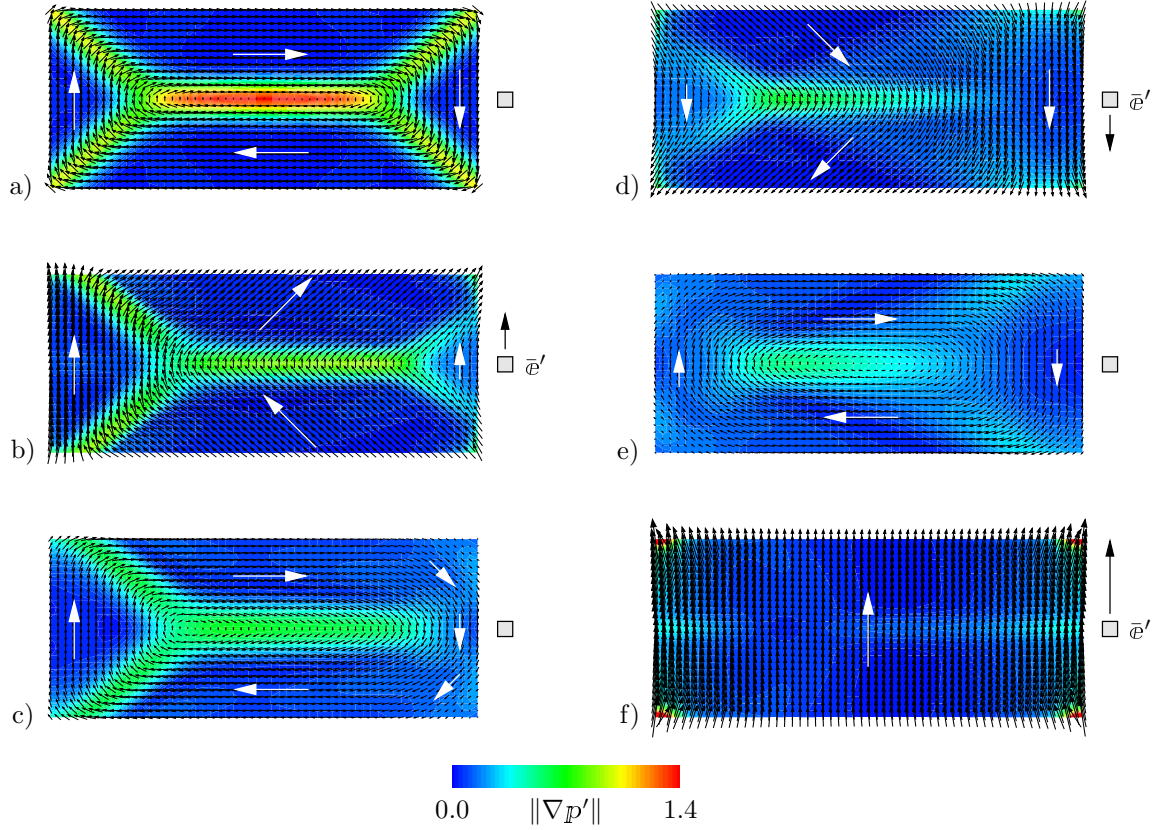


Figure 5.6: *Electric field driven domain wall movement.* The average direction of the polarization in each domain is indicated by white arrows. The direction and the amount of the electric loading \bar{e}' are shown alongside each contour plot corresponding to time a) $t' = 0$, b) $t' = 50$, c) $t' = 100$, d) $t' = 150$, e) $t' = 200$, and f) $t' = 300$. The free space box $\Omega \setminus \mathcal{B}$ is not visualized.

depicted in Figure 5.4a. The doubling of the field applied in the second cycle causes a full alignment of the polarization with the loading field and further switching processes do not cause neither nucleation nor motion of domain walls. This circumstance may be explained by the fact that in the perfect single crystal sample that has been modeled here, it is energetically more favorable for the material to reverse the polarization in a homogeneous manner, rather than nucleate new domain walls. Recall that due to (5.18), the applied electric loading \bar{e}' can be considered as the *averaged homogenized field* within the full space Ω . For the subsequent computations, we choose an electric loading field of $\bar{e}'_2 = 2.5$ which will be further increased to $\bar{e}'_2 = 5.0$ during the second cycle.

Domain wall motion. The subsequent numerical simulation deals with the domain wall motion of an electric field driven process. We specify the inverse mobility parameter to be $\eta' = 1.0$ and the normalized time step is chosen as $\Delta t' = 1.0$. These parameters are also applied in all subsequent numerical simulations. The plots of the domain configurations associated with the characteristic loading states are visualized in Figure 5.6. The surrounding free space $\Omega \setminus \mathcal{B}$ is not shown due to the fact that the polarization is solely defined in the solid part \mathcal{B} . Starting from the equilibrium state at time $t' = 0$, the domain walls are driven through the specimen as shown in the first loading sequence. After reaching the maximum positive applied electric field in the first cycle, the field is decreased until reaching zero again. Due to the viscous character of the microscopic bal-

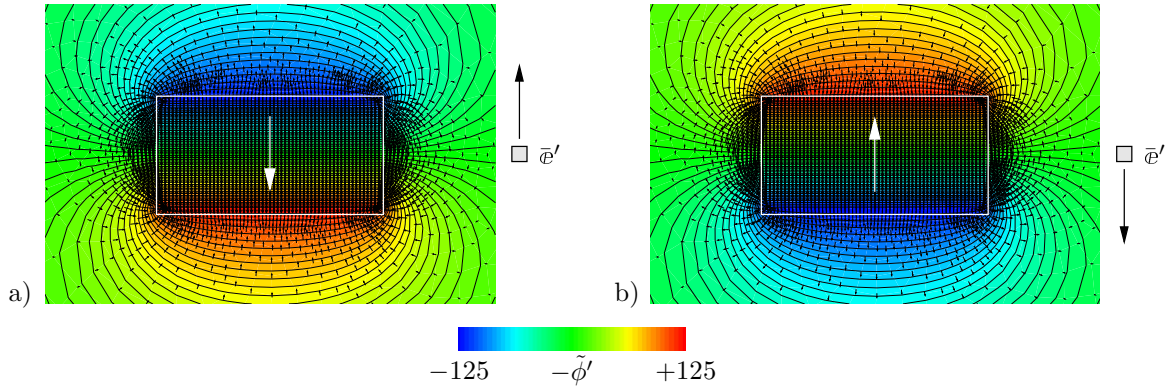


Figure 5.7: *The depolarizing electric field.* Depolarizing electric field \tilde{e}' and corresponding negative electric potential $-\tilde{\phi}'$ for sawtooth-type loading \tilde{e}' at time $t' = 50$ and $t' = 150$ for a partition of the free space box Ω . The white rectangle indicates the boundary of the solid domain $\partial\mathcal{B}$. Isolines in matter and free space refer to the electric potential. The depolarization field \tilde{e}' is represented by black arrows, white arrows indicate the average direction of \tilde{e}' in the solid domain.

ance equation describing the evolution of the order parameter, the decrease of the electric loading has a delayed influence on the domain wall motion. The polarization aligns further with the decreasing upwardly oriented field, that is driving the domain walls still in the direction of the left edge. Accordingly, the full inversion of the load causes the motion of the walls towards the opposite edge. Again, it should be pointed out that if one were to drive the domain walls completely out of the specimen, it would not reappear upon subsequent load reversal. Figure 5.6e–f depict the second loading cycle with a doubling of the electric field up to its maximum value of $\tilde{e}'_2 = 5.0$. Here, all the positive and negative barycenters move such that the polarization in each unit cell aligns with the external electric field resulting in a single domain sample, where the remaining domain walls have completely vanished. Due to this fact, the switching process is no longer caused by domain wall motions rather than a direct 180° switching. If no defects or grain boundaries with a lattice orientation mismatch are included, the nucleation of new domain walls is energetically not necessary. The main characteristics of electric field driven domain wall motion investigated in this section are in qualitative agreement with results reported in the literature ZHANG & BHATTACHARYA [210, 211] and SCHRADER ET AL. [159].

Electric potential and electric field in free space. The incorporation of the free space Ω allows the investigation of the evolving electric potential $\tilde{\phi}'$ as well as the resulting depolarizing electric field \tilde{e}' in the vacuum. The aforementioned fields spread out in the whole free space and are not restricted to the solid domain \mathcal{B} . From literature it is well known that placing a polarizable body into an electric field causes surface charges. These charges produce an electric field which is oriented oppositely to the polarization and thus called depolarization field \tilde{e}' . Schematic sketches are shown for instance in IRODOV [74, p.80] and DAMJANOVIC [34, p.1282]. The focus of the subsequent discussion is put on the behavior of the electric field in vacuum. The depolarization field opposed to the loading direction can be observed in Figure 5.7 by comparing the given loading direction with the average direction of the electric field \tilde{e}' indicated by the white arrow. Solely a cutout of the whole free space box is illustrated, where the contour plot clearly shows the formation of varying positive and negative poles related to the varying loading directions of the

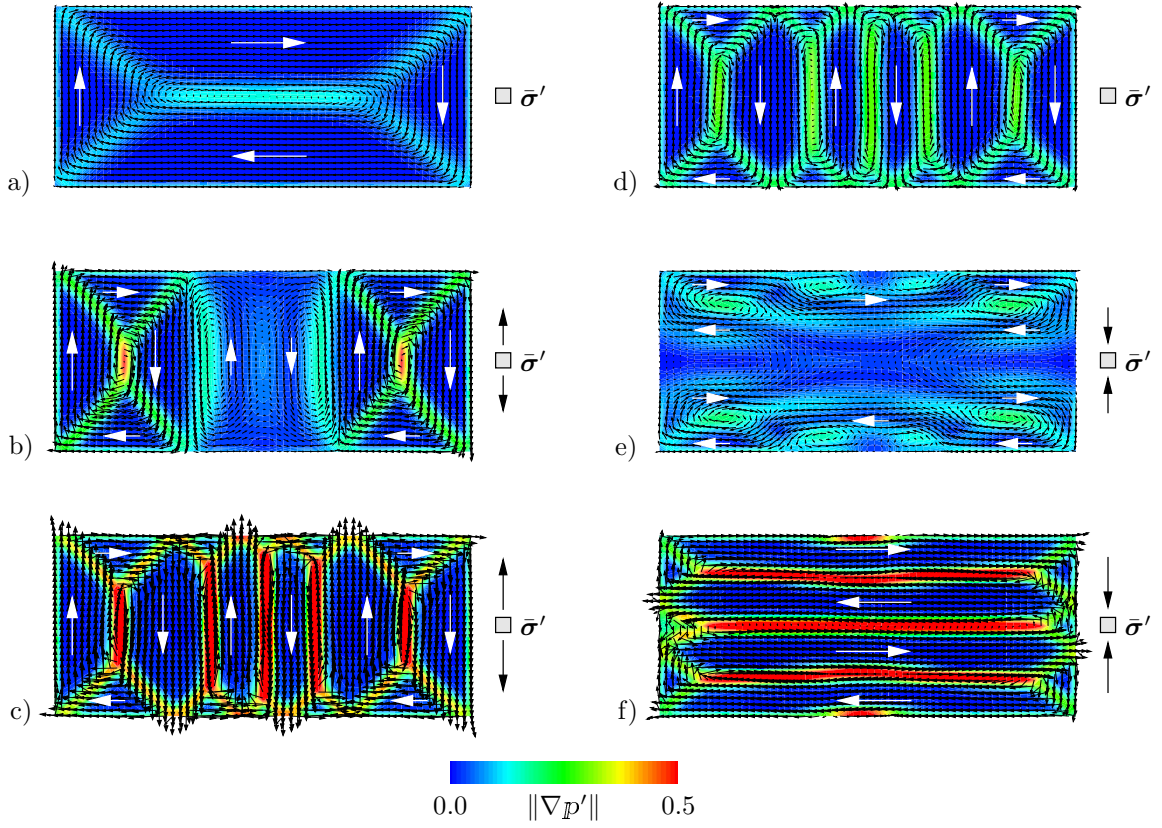


Figure 5.8: *Stress driven domain wall movement.* Domain wall movement and polarization p' caused by tensile and compressive stress $\bar{\sigma}'_{22}$. The average polarization direction is indicated by white arrows. The direction and amount of the loading $\bar{\sigma}'$ are shown at the right side of each contour plot corresponding to time a) $t' = 0$, b) $t' = 25$, c) $t' = 50$, d) $t' = 100$, e) $t' = 125$, and f) $t' = 150$. The surrounding free space $\Omega \setminus \mathcal{B}$ is not visualized.

external field. On the right hand side of each plot, the current loading status is shown. Note that the polarization in a unit cell remains after eliminating the electric loading and hence, a non-vanishing depolarization field for a preceding electric field could be observed.

5.4.4. Stress driven loading process

When applying an external stress field to a ferroelectric material in the tetragonal state below the Curie-Weiss transition temperature, a switching of the microscopic polarization by solely $\pm 90^\circ$ is possible. Here, a mechanical tensile stress $\bar{\sigma}'_t$ causes, due to the electro-mechanical coupling, an elongation of the unit cell in the direction of the applied stress, accompanied with a switching of the barycenters of positive and negative charges. However, the direction of the resulting polarization switching inside the microscopic unit cell is arbitrary. Similar characteristics can be observed for a compressive stress field $\bar{\sigma}'_c$, where a switching in the horizontal direction occurs.

The subsequent numerical simulation investigates a single cycle of a sawtooth-type stress driven loading process according to Figure 5.4b. Again, we have marked the characteristic loading points in the sawtooth-type loading cycle. The normalized maximum loading level is specified to $\bar{\sigma}'_{22} = 50$, which causes a stress driven reorientation of the internal polarization. The evolution of the polarization vector p' and its gradient $\|\nabla p'\|$ are

illustrated in [Figure 5.8](#). Similar to the electric field driven loading process, we start from the vortex-like equilibrium state, which consists of four 90° as well as one 180° domain walls separating the top and the bottom domain. The tensile part of the stress driven loading with a linear increase of the applied field up to its maximum value of $\bar{\sigma}'_{22} = 50$ is shown in the left panel of the picture. Due to arbitrary reorientations of the polarization by either $+90^\circ$ or -90° , the domains rearrange according to [Figure 5.8c](#). Here, the formation of domains oriented from the top to the bottom or vice versa is preferred, yielding several parallel vortex-like domains. We do not observe any alignment with the applied stress field in contrast to the electric field driven loading process treated in the previous section. Decreasing the loading to zero causes only minor changes in the domain structure and the strength of the polarization field decreases accordingly. The domain state is still in the linear range of piezoelectrics and thus no motion is observed. The compressive part of the stress loading process is shown in the right panel. The jumbled state [Figure 5.8e](#) is followed by an ordering of the polarization in a horizontal direction. For the maximum compressive stress $\bar{\sigma}'_{22} = -50$, vortex-like domains form in a horizontal manner, that is the polarization aligns either from the left to the right side of the sample or vice versa.

Computational Homogenization in Dissipative Electro-Mechanics of Functional Materials

The homogenization of the complex microscopic response of functional materials with electro-mechanical coupling is of utmost importance for technological design. In dissipative electro-mechanics, microstructures occur with complex electric domain patterns. The homogenization of microstructural properties then determines the overall response that governs macroscopic devices. The argument of scale separation allows to perform a bridging from a heterogeneous microstructure towards a macroscopically homogeneous continuum, see [Figure 6.1](#). In order to treat *functional materials with dissipative electric domain evolution*, it is necessary to extend standard homogenization principles to coupled problems, incorporating besides the mechanical displacement further primary variables such as the electric potential and the electric polarization. To this end, a *computational homogenization framework* of dissipative, electro-mechanically coupled materials based on a rigorous exploitation of rate-type and incremental variational principles is developed. These principles serve as canonical ingredients for the micro-to-macro transition and determine *macroscopic potentials* in terms of their microscopic counterparts. We refer to the previous works MIEHE [\[116\]](#), LAHELLEC & SUQUET [\[99\]](#), and BRASSART ET AL. [\[24\]](#) on incremental variational principles for purely mechanical problems and BISEGNA & LUCIANO [\[19, 20\]](#) for piezoelectric composites. SCHRÖDER [\[161\]](#) and SCHRÖDER & KEIP [\[162\]](#) have derived specific boundary conditions for electro-mechanical homogenization of non-dissipative materials in the context of the FE² approach, see also KHALAQUZZAMAN ET AL. [\[84\]](#). PONTE CASTAÑEDA & SIBONI [\[151\]](#) investigated the homogenization of electro-active polymer composites at finite strains. In this context, recall the classical works on self-consistent *variational estimates* for nonlinear dielectrics by WILLIS [\[202, 204\]](#), TALBOT & WILLIS [\[181\]](#) and TOLAND & WILLIS [\[188\]](#). Here, different bounds are generated starting from a Hashin-Shtrikman-type variational principle by a suitable choice of the 'comparison' energy function.

At the microscale level, ferroelectric materials such as BaTiO₃ or PZT are composed of several homogeneously polarized regions, called *ferroelectric domains*, whose evolution in time is driven by external electric fields and stresses applied to a sample of the material. *Electric poling* can be achieved by the application of a sufficiently strong electric

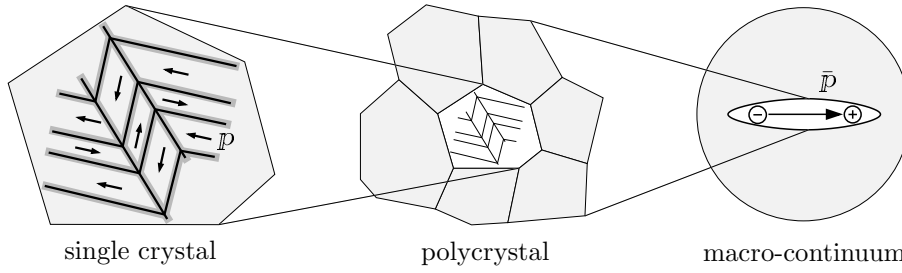


Figure 6.1: *Scale bridging to homogenized macro-continuum.* Electrically polarized domains with uniform micro-polarization \underline{p} separated by domain walls evolve in the grains of the microstructure as dissipative micro-processes driven by macroscopic strains $\bar{\epsilon}$ and electric fields \bar{e} . The spatial average of the micro-polarization gives the electric macro-polarization $\bar{\underline{P}} := \frac{1}{|\mathcal{B}|} \int_{\mathcal{B}} \underline{p} dV$ of the homogenized continuum.

field inducing the reorientation and alignment of the microscopic polarization. As a consequence, piezoceramics exhibit a macroscopic *remanent polarization*. The poling process of the microstructure is *dissipative in nature* and gives rise to so-called *dielectric* and *butterfly* hysteresis loops at the macroscale. The description of these effects through models of continuum physics has been a subject of extensive research.

In this chapter, the representative microstructure is modeled as a micro-electro-elastic solid, where the *electric polarization is described by a phase field*, see [Chapter 5](#) for a detailed discussion. An important aspect for the design of a computational homogenization method is the definition of suitable *boundary conditions at the micro-level*, which also include the phase field of electric polarization. Here, the microscopic displacement and electric potential may be considered to be driven by their macroscopic counterparts, which are considered the only primary variables on the macro-level. In contrast, the electric polarization has no external counterpart on the macroscale. Hence, the scale transition is performed between a gradient-extended dissipative micro-model and a standard Boltzmann continuum on the macroscale. The surface constraints at the microstructure are derived from an extension of the *Hill-Mandel-type micro-macro compatibility condition*, see HILL [65] and SUQUET [177] for *local* mechanical problems. The Hill-Mandel condition equates the macroscopic power of external variables with the volume average of its microscopic counterpart *extended* by contributions of the phase field of electric polarization. Note that this scenario is opposite to the works KOUZNETSOVA [91] and KOUZNETSOVA ET AL. [92, 93], which bridge local microstructures towards gradient-extended macro-continua. The incorporation of boundary constraints into the proposed variational principles of homogenization is achieved by Lagrange multiplier or penalty methods, conceptually similar to the purely mechanical treatments in MIEHE [117] and MIEHE & BAYREUTHER [121].

This chapter is organized as follows: [Section 6.1](#) develops rate-type as well as incremental *variational principles of homogenization* for the microstructure, which determine the macroscopic potential by an averaging procedure. The phase field model of electric domain evolution used for the description of the micro-response is borrowed from [Chapter 5](#). The mechanical and electric loading functionals are neglected within this homogenization treatment. In addition, all overlined characters are associated with macroscopic quantities instead of prescribed ones as compared to the previous chapter. Furthermore, the split of the electric field into prescribed and induced one is ignored, and the total electric potential

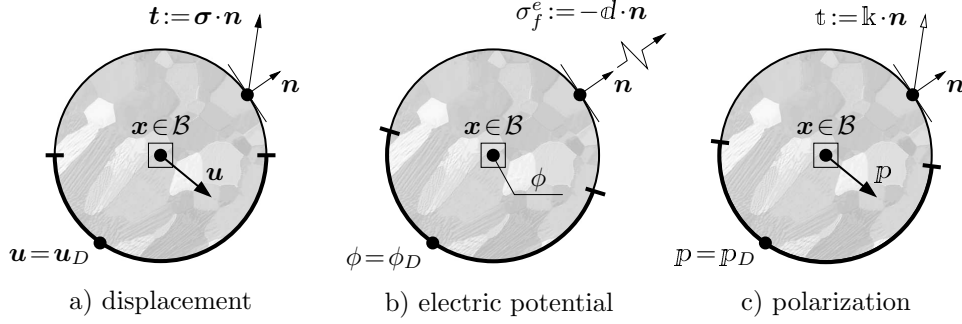


Figure 6.2: *Microscopic primary variables for the homogenization problem.* a) Mechanical displacement field \mathbf{u} , b) electric potential ϕ , and c) electric polarization \mathbb{p} with Dirichlet- and Neumann-type boundary conditions. The polarization \mathbb{p} describes the dissipative response in the sense of a generalized internal variable and has no external counterpart at the macro-level.

is treated as primary variable. [Section 6.2](#) outlines variational principles for the coupled macroscopic problem. To this end, an algorithmic *incremental variational principle* is derived for the update problem in a discrete time interval, which is then discretized by finite elements. [Section 6.3](#) outlines details of the *micro-to-macro transition* by utilizing an extended version of the Hill-Mandel condition. Furthermore, this section covers the incorporation of the boundary constraints into the variational functionals by means of Lagrange and penalty extensions. Finally, [Section 6.4](#) outlines two- and three-dimensional numerical examples of typical microstructures in micro-electrics and discusses the overall hysteresis effects as well as the phenomenon of mechanical depolarization.

6.1. Variational homogenization of micro-electro-elasticity

Let $\mathcal{B} \subset \mathcal{R}^d$ denote a microstructure with dimension $d \in [2, 3]$ as depicted in [Figure 6.2](#). We study the electro-mechanical response due to the *electric polarization* of this microstructure. The material model of micro-electro-elasticity investigated in the previous [Chapter 5](#) is used as a particular model on the microscale. The free space box is neglected and the total electric potential is assumed to be restricted to the microstructure.

6.1.1. Introduction of microscopic fields

The material is modeled by using a gradient-extended dissipative continuum formulation, where the electric polarization is described by an order parameter or generalized internal variable field, see SU & LANDIS [174], SCHRADE ET AL. [159], and MIEHE ET AL. [133]. We consider a *three field formulation* in terms of the displacement, the total electric potential, and a vectorial generalized internal variable for the microscopic polarization

$$\mathbf{u} : \begin{cases} \mathcal{B} \times \mathcal{T} \rightarrow \mathcal{R}^d, \\ (\mathbf{x}, t) \mapsto \mathbf{u}(\mathbf{x}, t), \end{cases} \quad \phi : \begin{cases} \mathcal{B} \times \mathcal{T} \rightarrow \mathcal{R}, \\ (\mathbf{x}, t) \mapsto \phi(\mathbf{x}, t), \end{cases} \quad \mathbb{p} : \begin{cases} \mathcal{B} \times \mathcal{T} \rightarrow \mathcal{R}^d, \\ (\mathbf{x}, t) \mapsto \mathbb{p}(\mathbf{x}, t). \end{cases} \quad (6.1)$$

The a priori objective constitutive state depends on the symmetric part of the displacement gradient and the electric field

$$\boldsymbol{\varepsilon} = \nabla_s \mathbf{u} = \frac{1}{2} [\nabla \mathbf{u} + \nabla^T \mathbf{u}] \quad \text{and} \quad \mathbf{e} := -\nabla \phi. \quad (6.2)$$

The strains are assumed to be small, that is $|\nabla \mathbf{u}| < \epsilon$ is bounded by a small number ϵ . In contrast, the norm of the gradients of the polarization vector $|\nabla \mathbf{p}|$ and the electric potential $|\nabla \phi|$ are not bounded.

6.1.2. Microscopic rate-type variational principle of homogenization

We postulate a *rate-type variational principle of homogenization* that determines the macroscopic potential density $\bar{\pi}$. This definition includes the *kinetics* of the generalized internal variable for the material polarization, which is assumed to be dissipative in nature. In a time continuous setting, the macroscopic potential density $\bar{\pi}$ is determined by

$$\boxed{\bar{\pi}(\dot{\bar{\boldsymbol{\epsilon}}}, \dot{\bar{e}}) = \inf_{\dot{\mathbf{u}}} \sup_{\dot{\phi}} \inf_{\dot{\mathbf{p}}} \Pi(\dot{\mathbf{u}}, \dot{\phi}, \dot{\mathbf{p}}; \dot{\bar{\boldsymbol{\epsilon}}}, \dot{\bar{e}})} \quad (6.3)}$$

governed by the rate-type potential

$$\Pi(\dot{\mathbf{u}}, \dot{\phi}, \dot{\mathbf{p}}; \dot{\bar{\boldsymbol{\epsilon}}}, \dot{\bar{e}}) = \frac{1}{|\mathcal{B}|} \int_{\mathcal{B}} \pi(\dot{\boldsymbol{\epsilon}}, \dot{e}, \dot{\mathbf{p}}, \nabla \dot{\mathbf{p}}; \dot{\bar{\boldsymbol{\epsilon}}}, \dot{\bar{e}}) dV. \quad (6.4)$$

The principle is characterized by the optimization of an *average* microscopic rate-type potential density π , that takes into account the *energy storage* and the *dissipative mechanisms* of the micro-material

$$\underbrace{\pi(\dot{\boldsymbol{\epsilon}}, \dot{e}, \dot{\mathbf{p}}, \nabla \dot{\mathbf{p}}; \dot{\bar{\boldsymbol{\epsilon}}}, \dot{\bar{e}})}_{\text{potential}} = \underbrace{\frac{d}{dt} \Psi(\boldsymbol{\epsilon}, e, \mathbf{p}, \nabla \mathbf{p}; \bar{\boldsymbol{\epsilon}}, \bar{e})}_{\text{rate of energy function}} + \underbrace{\Phi(\dot{\mathbf{p}})}_{\text{dissipation potential}} \quad (6.5)$$

The potential density is defined by the rate of the mixed energy-enthalpy function and the dissipation function

$$\Psi(\boldsymbol{\epsilon}, e, \mathbf{p}, \nabla \mathbf{p}; \bar{\boldsymbol{\epsilon}}, \bar{e}) = \Psi_{mat}(\boldsymbol{\epsilon}, \mathbf{p}, \nabla \mathbf{p}) - \frac{\epsilon_0}{2} e \cdot e - e \cdot \mathbf{p} \quad \text{and} \quad \Phi(\dot{\mathbf{p}}) = \frac{\eta}{2} \dot{\mathbf{p}} \cdot \dot{\mathbf{p}}, \quad (6.6)$$

which were discussed in more detail in [Section 5.1](#) of the previous chapter. Note again that the loading functionals are neglected due to the homogenization framework and the induced electric field replaced by the total one. Taking the variation of both sides of equation (6.3), the extended version of the Hill-Mandel macrohomogeneity condition is derived as

$$\underbrace{\bar{\boldsymbol{\sigma}} : \delta \dot{\bar{\boldsymbol{\epsilon}}} - \bar{\mathbf{d}} \cdot \delta \dot{\bar{e}}}_{\text{macro-power}} = \frac{1}{|\mathcal{B}|} \int_{\mathcal{B}} \underbrace{\{\boldsymbol{\sigma} : \delta \dot{\boldsymbol{\epsilon}} - \mathbf{d} \cdot \delta \dot{e} + \mathbf{q} \cdot \delta \dot{\mathbf{p}} + \mathbf{k} : \nabla \delta \dot{\mathbf{p}}\}}_{\text{extended micro-power}} dV \quad (6.7)$$

for the dissipative electro-mechanical problem under consideration, where we inserted the macroscopic quantities $\bar{\boldsymbol{\sigma}} = \partial_{\bar{\boldsymbol{\epsilon}}} \bar{\pi}$ and $\bar{\mathbf{d}} = -\partial_{\bar{e}} \bar{\pi}$. At the micro-level, we identify the stresses, the electric displacement, as well as the conjugate forces dual to the polarization vector and its gradient

$$\boldsymbol{\sigma} := \partial_{\boldsymbol{\epsilon}} \Psi, \quad \mathbf{d} := -\partial_e \Psi, \quad \mathbf{q} := \partial_{\mathbf{p}} \Psi + \partial_{\dot{\mathbf{p}}} \Phi, \quad \mathbf{k} := \partial_{\nabla \mathbf{p}} \Psi \quad (6.8)$$

governed by the constitutive enthalpy function Ψ and dissipation function Φ . Note that the microstructure is *loaded* by the macroscopic strain $\bar{\boldsymbol{\epsilon}}$ and the electric field \bar{e} , which are

considered to be *prescribed* and constant over the representative volume element. Taking the variation of the principle (6.3) at these prescribed values, the right hand side of (6.7) must vanish and we end up with the necessary microscopic equations

$$\begin{aligned} \delta\Pi = & \int_{\mathcal{B}} (-\operatorname{div}[\partial_{\varepsilon}\Psi]) \cdot \delta\mathbf{u} \, dV + \int_{\partial\mathcal{B}} (\partial_{\varepsilon}\Psi \cdot \mathbf{n}) \cdot \delta\mathbf{u} \, dA \\ & - \int_{\mathcal{B}} \operatorname{div}[-\partial_e\Psi] \delta\dot{\phi} \, dV + \int_{\partial\mathcal{B}} (-\partial_e\Psi \cdot \mathbf{n}) \delta\dot{\phi} \, dA \\ & + \int_{\mathcal{B}} (\partial_p\Psi + \partial_{\dot{p}}\Phi - \operatorname{div}[\partial_{\nabla p}\Psi]) \cdot \delta\dot{\mathbf{p}} \, dV + \int_{\partial\mathcal{B}} (\partial_{\nabla p}\Psi \cdot \mathbf{n}) \cdot \delta\dot{\mathbf{p}} \, dA = 0 . \end{aligned} \quad (6.9)$$

Hence, the Euler-Lagrange equations are the static form of the balance of linear momentum, the Gauss law, and a partial differential equation for the evolution of the polarization vector

$$\operatorname{div}[\partial_{\varepsilon}\Psi] = \mathbf{0} , \quad \operatorname{div}[-\partial_e\Psi] = 0 , \quad \operatorname{div}[\partial_{\nabla p}\Psi] = \partial_p\Psi + \partial_{\dot{p}}\Phi \quad (6.10)$$

in the microstructure \mathcal{B} . So far, we did not specify boundary constraints on the surface $\partial\mathcal{B}$ of the microstructure. As a consequence, the above treatment gives the Neumann-type conditions $\partial_{\varepsilon}\Psi \cdot \mathbf{n} = \mathbf{0}$, $-\partial_e\Psi \cdot \mathbf{n} = 0$ and $\partial_{\nabla p}\Psi \cdot \mathbf{n} = \mathbf{0}$. Sophisticated boundary conditions incorporated by Lagrange multiplier and penalty methods are considered in Section 6.3 below.

6.1.3. Microscopic incremental variational principle of homogenization

To provide a starting point for the numerical setting, an incremental variational principle which governs the electro-mechanical problem at discrete time t_{n+1} is considered. We propose the *incremental variational principle of homogenization*

$$\boxed{\bar{\pi}^{\tau}(\bar{\varepsilon}, \bar{e}) = \inf_{\mathbf{u}} \sup_{\phi} \inf_{\mathbf{p}} \Pi^{\tau}(\mathbf{u}, \phi, \mathbf{p}; \bar{\varepsilon}, \bar{e})} \quad (6.11)$$

where the incremental version of the rate-type potential (6.4) is given by

$$\Pi^{\tau}(\mathbf{u}, \phi, \mathbf{p}; \bar{\varepsilon}, \bar{e}) = \frac{1}{|\mathcal{B}|} \int_{\mathcal{B}} \pi^{\tau}(\varepsilon, e, \mathbf{p}, \nabla\mathbf{p}; \bar{\varepsilon}, \bar{e}) \, dV . \quad (6.12)$$

The variational principle defines the macroscopic incremental potential density $\bar{\pi}^{\tau}$ by optimizing the volume average of the microscopic potential π^{τ} with respect to all three microscopic primary fields. This definition is conceptually in line with formulations for nonlinear mechanical problems in MIEHE [116], PONTE CASTAÑEDA & SUQUET [152] and self-consistent variational estimates for nonlinear dielectrics by WILLIS and coworkers [181, 188, 202, 204]. The incremental potential density π^{τ} is related to the rate-type potential π by the algorithm

$$\pi^{\tau}(\varepsilon, e, \mathbf{p}, \nabla\mathbf{p}; \bar{\varepsilon}, \bar{e}) := \text{ALGO} \left\{ \int_{t_n}^{t_{n+1}} \pi(\dot{\varepsilon}, \dot{e}, \dot{\mathbf{p}}, \nabla\dot{\mathbf{p}}; \dot{\bar{\varepsilon}}, \dot{\bar{e}}) \, d\tau \right\} . \quad (6.13)$$

Application of an implicit backward Euler time integration scheme gives the time-discrete counterpart of (6.5), that is

$$\underbrace{\pi^{\tau}(\varepsilon, e, \mathbf{p}, \nabla\mathbf{p}; \bar{\varepsilon}, \bar{e})}_{\text{potential}} = \underbrace{\Psi(\varepsilon, e, \mathbf{p}, \nabla\mathbf{p}; \bar{\varepsilon}, \bar{e}) - \Psi_n}_{\text{incremental energy}} + \underbrace{\tau\Phi([\mathbf{p} - \mathbf{p}_n]/\tau)}_{\text{dissipation potential}} , \quad (6.14)$$

where Ψ_n is the energy-enthalpy function evaluated at t_n . The necessary conditions of the incremental variational principle are identical to those of the rate-type formulation

$$\operatorname{div}[\partial_{\varepsilon}\Psi] = \mathbf{0}, \quad \operatorname{div}[-\partial_e\Psi] = 0, \quad \operatorname{div}[\partial_{\nabla p}\Psi] = \partial_p\Psi + \tau\partial_p\Phi, \quad (6.15)$$

however, now in algorithmic form for the updates at the discrete time t_{n+1} .

Remark: Note that the above *gradient-extended* variational framework of dissipative electro-mechanical response degenerates to a *local* theory if the free energy function Ψ does not depend on the gradient ∇p . Then, the partial differential equation (6.10)₃ with update (6.15)₃ degenerates to an ordinary evolution equation for an internal variable p , e.g. a remanent strain or polarization. This covers phenomenological theories of dissipative electro-mechanics, see for example MIEHE ET AL. [131] and references cited therein. Hence, our subsequent treatment *includes locally dissipative microstructures*, where no additional boundary conditions for the internal variable field p appear. \square

6.1.4. Space-time discrete incremental variational principle

For the space discretization of the incremental potential (6.14), consider the set of constitutive state variables assembled in $\mathbf{f} := \{\nabla_s \mathbf{u}, -\nabla\phi, p, \nabla p\}$. The finite element interpolations of the microscale are then written in the compact form

$$\mathbf{f} \approx \underline{\mathbf{f}}^h = \underline{\mathbf{B}}(\mathbf{x})\underline{\mathbf{d}} \quad \text{with} \quad \underline{\mathbf{d}} := [\mathbf{u}, -\phi, p]^T \in \mathcal{R}^{(2d+1)N^h} \quad (6.16)$$

in terms of the space-time-discrete *nodal variable vector* $\underline{\mathbf{d}}$, containing the displacement, the electric potential, and the polarization vector at a typical nodal point of the microstructure. The finite-step-sized discrete stationary principle

$$\boxed{\bar{\pi}^\tau(\bar{\varepsilon}, \bar{\varphi}) = \operatorname{stat}_{\underline{\mathbf{d}}} \Pi^h(\underline{\mathbf{d}}; \bar{\varepsilon}, \bar{\varphi})} \quad (6.17)$$

determines the macroscopic potential density at current time t_{n+1} . The space-time discrete function

$$\Pi^h(\underline{\mathbf{d}}; \bar{\varepsilon}, \bar{\varphi}) = \frac{1}{|\mathcal{B}^h|} \int_{\mathcal{B}^h} \pi^\tau(\underline{\mathbf{B}}\underline{\mathbf{d}}; \bar{\varepsilon}, \bar{\varphi}) dV \quad (6.18)$$

is obtained by inserting the finite element approximation (6.16) into the time-discrete potential (6.12). The necessary condition of the discrete variational problem (6.17) reads

$$\Pi_{,\underline{\mathbf{d}}}^h = \int_{\mathcal{B}^h} \underline{\mathbf{B}}^T [\partial_{\mathbf{f}}\Psi] + \tau \underline{\mathbf{G}}^T [\partial_p\Phi] dV = \mathbf{0}, \quad (6.19)$$

where we inserted $p = \underline{\mathbf{G}}(\mathbf{x})\underline{\mathbf{d}}$ as an extraction of (6.16), and provides a nonlinear algebraic system for the determination of the microscopic nodal variables $\underline{\mathbf{d}}$. The system is solved by Newton-Raphson updates for the discrete nodal values

$$\underline{\mathbf{d}} \Leftarrow \underline{\mathbf{d}} - [\Pi_{,\underline{\mathbf{d}}\underline{\mathbf{d}}}^h]^{-1} [\Pi_{,\underline{\mathbf{d}}}^h] \quad \text{with} \quad \Pi_{,\underline{\mathbf{d}}\underline{\mathbf{d}}}^h = \int_{\mathcal{B}^h} \underline{\mathbf{B}}^T [\partial_{\mathbf{f}\mathbf{f}}^2\Psi] \underline{\mathbf{B}} + \tau \underline{\mathbf{G}}^T [\partial_{pp}^2\Phi] \underline{\mathbf{G}} dV \quad (6.20)$$

in terms of the *symmetric* monolithic tangent matrix $\Pi_{,\underline{\mathbf{d}}\underline{\mathbf{d}}}^h$.

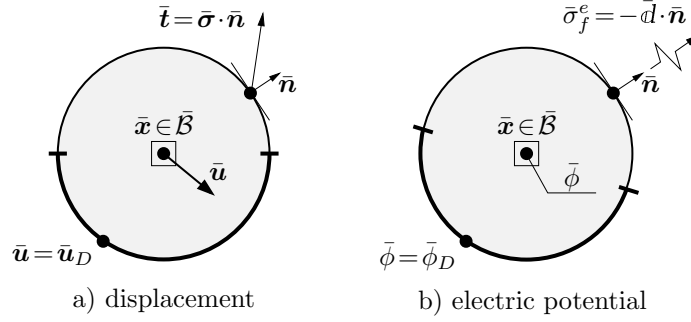


Figure 6.3: *Macroscopic primary variables for the homogenization problem.* a) Mechanical displacement field $\bar{\mathbf{u}}$ and b) electric potential $\bar{\phi}$ with Dirichlet- and Neumann-type boundary conditions due to prescribed tractions $\bar{\mathbf{t}} = \bar{\boldsymbol{\sigma}} \cdot \bar{\mathbf{n}}$ and given surface charge density $\bar{\sigma}_f^e = -\bar{\mathbf{d}} \cdot \bar{\mathbf{n}}$.

6.2. Variational formulation of the macroscopic response

Let $\bar{\mathcal{B}} \subset \mathcal{R}^d$ denote a macroscopic body with dimension $d \in [2, 3]$ as depicted in Figure 6.3. We study mechanical deformations coupled with electric displacements of the body under quasi-static, electro-mechanical external loading in the time interval $\bar{\mathcal{T}} \subset \mathcal{R}_+$. We dispense with a macroscopic rate-type variational principle and focus on the incremental setting at discrete times t_{n+1} . This principle is discretized by the finite element method in order to determine space-time-discrete solutions for the macroscopic boundary-value problem. For further details we refer to ZÄH & MIEHE [207].

6.2.1. Introduction of macroscopic fields

The macroscopic boundary-value problem of electro-mechanics is a coupled multifield problem. Primary variables are the displacement field $\bar{\mathbf{u}}$ and the electric potential $\bar{\phi}$ visualized in Figure 6.3 of the material point $\bar{\mathbf{x}} \in \bar{\mathcal{B}}$ at time $t \in \bar{\mathcal{T}}$, that is

$$\bar{\mathbf{u}} : \begin{cases} \bar{\mathcal{B}} \times \bar{\mathcal{T}} \rightarrow \mathcal{R}^d, \\ (\bar{\mathbf{x}}, t) \mapsto \bar{\mathbf{u}}(\bar{\mathbf{x}}, t), \end{cases} \quad \text{and} \quad \bar{\phi} : \begin{cases} \bar{\mathcal{B}} \times \bar{\mathcal{T}} \rightarrow \mathcal{R}, \\ (\bar{\mathbf{x}}, t) \mapsto \bar{\phi}(\bar{\mathbf{x}}, t). \end{cases} \quad (6.21)$$

The gradients of the fields $\bar{\mathbf{u}}$ and $\bar{\phi}$ define the objective constitutive state depending on the symmetric part of the displacement gradient and the electric field

$$\bar{\boldsymbol{\varepsilon}} = \bar{\nabla}_s \bar{\mathbf{u}} = \frac{1}{2} (\bar{\nabla} \bar{\mathbf{u}} + \bar{\nabla}^T \bar{\mathbf{u}}) \quad \text{and} \quad \bar{\boldsymbol{\varepsilon}} = -\bar{\nabla} \bar{\phi}. \quad (6.22)$$

These definitions satisfy automatically the deformation compatibility $\text{curl}[\bar{\nabla} \bar{\mathbf{u}}] = \mathbf{0}$ in \mathcal{B} and Faraday's law of induction $\text{curl}[\bar{\boldsymbol{\varepsilon}}] = \mathbf{0}$ in \mathcal{B} for the quasi-static problem under consideration. The strains are assumed to be small, that is $|\bar{\nabla} \bar{\mathbf{u}}| < \bar{\varepsilon}$ is bounded by a small number $\bar{\varepsilon}$. In contrast, the norm of the electric potential $|\bar{\nabla} \bar{\phi}|$ is not bounded.

6.2.2. Macroscopic incremental variational formulation

In order to provide a starting point for the numerical implementation, a time-discrete variational principle in a typical time step $[t_n, t_{n+1}]$ with step length $\tau_{n+1} = t_{n+1} - t_n > 0$ is considered. In what follows, all variables without subscript are evaluated at time

t_{n+1} . The update problem for the macro-fields at the current time t_{n+1} is defined by the *incremental variational principle*,

$$\boxed{\{\bar{\mathbf{u}}, \bar{\phi}\} = \arg \left\{ \inf_{\bar{\mathbf{u}}} \sup_{\bar{\phi}} \bar{\Pi}^\tau(\bar{\mathbf{u}}, \bar{\phi}) \right\}} \quad (6.23)$$

governed by the incremental macroscopic potential

$$\bar{\Pi}^\tau(\bar{\mathbf{u}}, \bar{\phi}) = \int_{\bar{\mathcal{B}}} \bar{\pi}^\tau(\bar{\boldsymbol{\varepsilon}}, \bar{\varrho}) dV - \bar{\mathcal{P}}_m(\bar{\mathbf{u}} - \bar{\mathbf{u}}_n) - \bar{\mathcal{P}}_e(\bar{\phi} - \bar{\phi}_n). \quad (6.24)$$

Note that the latter is formulated in terms of the incremental macroscopic potential density $\bar{\pi}^\tau$, determined by the variational principle of homogenization in (6.11). As a consequence, the macro problem depends on the microscopic polarization which describes the dissipative reorientation of microscopic electric domains. The external loading contributions are

$$\begin{aligned} \bar{\mathcal{P}}_m(\bar{\mathbf{u}} - \bar{\mathbf{u}}_n) &= \int_{\bar{\mathcal{B}}} \bar{\boldsymbol{\gamma}} \cdot (\bar{\mathbf{u}} - \bar{\mathbf{u}}_n) dV + \int_{\partial\bar{\mathcal{B}}_t} \bar{\mathbf{t}} \cdot (\bar{\mathbf{u}} - \bar{\mathbf{u}}_n) dA, \\ \bar{\mathcal{P}}_e(\bar{\phi} - \bar{\phi}_n) &= \int_{\bar{\mathcal{B}}} -\bar{\rho}^e(\bar{\phi} - \bar{\phi}_n) dV + \int_{\partial\bar{\mathcal{B}}_d} -\bar{\sigma}_f^e(\bar{\phi} - \bar{\phi}_n) dA. \end{aligned} \quad (6.25)$$

Here, $\bar{\boldsymbol{\gamma}}$ is the macroscopic body force per unit volume and $\bar{\mathbf{t}}$ are prescribed tractions. On the electric side, $\bar{\rho}^e$ is the volume density of free charges and $\bar{\sigma}_f^e$ a surface density of free charges. For the quasi-static problem under consideration, we have chosen a backward Euler algorithm for the discretization of the rates $\dot{\bar{\mathbf{u}}} = (\bar{\mathbf{u}} - \bar{\mathbf{u}}_n)/\tau$ and $\dot{\bar{\phi}} = (\bar{\phi} - \bar{\phi}_n)/\tau$, respectively. Consistent with these assumptions are the approximations of mechanical and electric source terms, see also MIEHE ET AL. [133], where the full set including rate-type formulations is outlined. The incremental macroscopic variational principle (6.23) gives the necessary condition

$$\begin{aligned} \delta\bar{\Pi}^\tau &= \int_{\bar{\mathcal{B}}} (\operatorname{div}[\partial_{\bar{\boldsymbol{\varepsilon}}}\bar{\pi}^\tau] + \bar{\boldsymbol{\gamma}}) \cdot \delta\bar{\mathbf{u}} dV - \int_{\partial\bar{\mathcal{B}}_t} (\partial_{\bar{\boldsymbol{\varepsilon}}}\bar{\pi}^\tau \cdot \bar{\mathbf{n}} - \bar{\mathbf{t}}) \cdot \delta\dot{\bar{\mathbf{u}}} dA \\ &+ \int_{\bar{\mathcal{B}}} (\operatorname{div}[-\partial_{\bar{\varrho}}\bar{\pi}^\tau] - \bar{\rho}^e)\delta\bar{\phi} dV - \int_{\partial\bar{\mathcal{B}}_d} (-\partial_{\bar{\varrho}}\bar{\pi}^\tau \cdot \bar{\mathbf{n}} + \bar{\sigma}_f^e)\delta\bar{\phi} dA = 0, \end{aligned} \quad (6.26)$$

where $\bar{\mathbf{n}}$ is the outward normal depicted in Figure 6.3. For arbitrary variations, this results in the macroscopic Euler-Lagrange equations

$$\operatorname{div}[\partial_{\bar{\boldsymbol{\varepsilon}}}\bar{\pi}^\tau] + \bar{\boldsymbol{\gamma}} = \mathbf{0} \text{ in } \bar{\mathcal{B}} \quad \text{and} \quad \operatorname{div}[-\partial_{\bar{\varrho}}\bar{\pi}^\tau] = \bar{\rho}^e \text{ in } \bar{\mathcal{B}}, \quad (6.27)$$

along with the Neumann-type boundary conditions $\partial_{\bar{\boldsymbol{\varepsilon}}}\bar{\pi}^\tau \cdot \bar{\mathbf{n}} = \bar{\mathbf{t}}$ on $\partial\bar{\mathcal{B}}_t$ and $\partial_{\bar{\varrho}}\bar{\pi}^\tau \cdot \bar{\mathbf{n}} = \bar{\sigma}_f^e$ on $\partial\bar{\mathcal{B}}_d$. Here, we identified the macroscopic stresses and electric displacement at the discrete time t_{n+1} as

$$\bar{\boldsymbol{\sigma}} = \partial_{\bar{\boldsymbol{\varepsilon}}}\bar{\pi}^\tau(\bar{\boldsymbol{\varepsilon}}, \bar{\varrho}) \quad \text{and} \quad \bar{\mathbf{d}} = -\partial_{\bar{\varrho}}\bar{\pi}^\tau(\bar{\boldsymbol{\varepsilon}}, \bar{\varrho}), \quad (6.28)$$

where the incremental potential $\bar{\pi}^\tau$ is defined in (6.11). Hence, this potential includes the homogenized information of the microstructure including elastic and dissipative material behavior due to domain wall motion characterized by the microscopic polarization.

6.2.3. Macroscopic space-time discrete incremental variational principle

Consider the spatial discretization of the coupled macroscopic problem by the finite element method. To this end, we assemble the set of constitutive state variables in the array $\bar{\mathbf{f}} := \{\bar{\nabla}_s \bar{\mathbf{u}}, -\bar{\nabla} \bar{\phi}\}$. Now let $\bar{\mathfrak{T}}^h$ denote a finite element triangulation of the domain $\bar{\mathcal{B}}$. The index h indicates a typical mesh size based on \bar{E}^h finite element domains $\bar{\mathcal{B}}_e^h \in \bar{\mathfrak{T}}^h$ and \bar{N}^h global nodal points. Associated with the triangulation $\bar{\mathfrak{T}}^h$, we write the finite element interpolation of the constitutive state vector in the compact form

$$\bar{\mathbf{f}} \approx \bar{\mathbf{f}}^h = \bar{\mathbf{B}}(\bar{\mathbf{x}}) \bar{\mathbf{d}} \quad \text{with} \quad \bar{\mathbf{d}} := [\bar{\mathbf{u}}, -\bar{\phi}]^T \in \mathcal{R}^{(d+1)\bar{N}^h}. \quad (6.29)$$

It is formulated in terms of the macroscopic space-time-discrete *nodal variable vector* $\bar{\mathbf{d}}$, which contains the displacement and electric potential at a typical nodal point of the finite element mesh. Then, for pure Dirichlet problems with $\bar{\mathcal{P}}_m = \bar{\mathcal{P}}_e = 0$, the finite-step-sized discrete stationary principle

$$\boxed{\bar{\mathbf{d}} = \arg \left\{ \text{stat} \bar{\Pi}^h(\bar{\mathbf{d}}) \right\}} \quad (6.30)$$

determines the macroscopic nodal displacements at current time t_{n+1} . It is formulated in terms of the discrete macroscopic potential

$$\bar{\Pi}^h(\bar{\mathbf{d}}) = \int_{\bar{\mathcal{B}}^h} \bar{\pi}^\tau(\bar{\mathbf{B}} \bar{\mathbf{d}}) dV \quad (6.31)$$

obtained by inserting the finite element approximation (6.29) into (6.24). The discrete variational principle is fully governed by the potential density $\bar{\pi}^\tau$ determined by the variational principle of the homogenization problem. The necessary condition reads

$$\bar{\Pi}_{\bar{\mathbf{d}}}^h = \int_{\bar{\mathcal{B}}^h} \bar{\mathbf{B}}^T [\partial_{\bar{\mathbf{f}}} \bar{\pi}^\tau] dV = \mathbf{0} \quad (6.32)$$

and provides a nonlinear algebraic system for the determination of the macroscopic nodal variables $\bar{\mathbf{d}}$. A standard Newton-type iteration of the nonlinear algebraic system (6.32) updates the generalized displacements by the algorithm

$$\bar{\mathbf{d}} \leftarrow \bar{\mathbf{d}} - [\bar{\Pi}_{\bar{\mathbf{d}}\bar{\mathbf{d}}}^h]^{-1} [\bar{\Pi}_{\bar{\mathbf{d}}}^h] \quad \text{with} \quad \bar{\Pi}_{\bar{\mathbf{d}}\bar{\mathbf{d}}}^h = \int_{\bar{\mathcal{B}}^h} \bar{\mathbf{B}}^T [\partial_{\bar{\mathbf{f}}\bar{\mathbf{f}}}^2 \bar{\pi}^\tau] \bar{\mathbf{B}} dV \quad (6.33)$$

in terms of the monolithic tangent matrix $\bar{\Pi}_{\bar{\mathbf{d}}\bar{\mathbf{d}}}^h$ of the coupled problem. The *symmetry of the tangent matrix* is induced by the incremental variational principle for the coupled problem. The update is performed until convergence is achieved in the sense $|\bar{\Pi}_{\bar{\mathbf{d}}}^h| < \text{tol}$.

6.3. Generalized micro-to-macro transition

As depicted in Figure 6.4, the microstructural boundary-value-problem of Section 6.1 is now linked to the macrostructure of Section 6.2 by homogenization. In order to do so, boundary conditions must be defined for the three primary fields on the micro-level, that

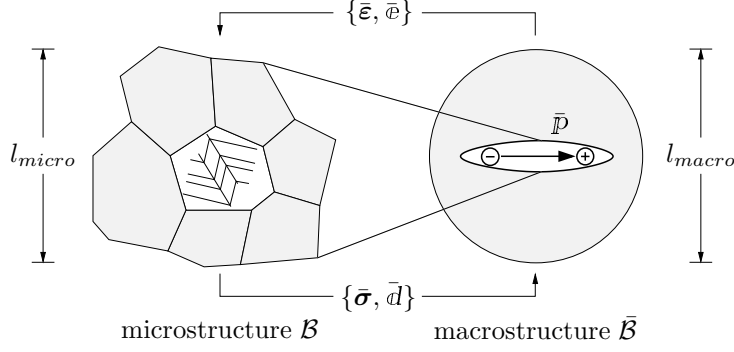


Figure 6.4: *Strain and electric field driven scale bridging approach.* Local strains and electric fields $\{\bar{\epsilon}, \bar{e}\}$ on the macrostructure $\bar{\mathcal{B}}$ drive the microstructure \mathcal{B} , inducing dissipative domain wall motions. Output are the homogenized stress and electric displacement $\{\bar{\sigma}, \bar{d}\}$ at a material point of the macrostructure. The average of the micro-polarization gives the electric macro-polarization $\bar{p} = \frac{1}{|\bar{\mathcal{B}}|} \int_{\bar{\mathcal{B}}} p \, dV$ of the homogenized continuum.

is the displacement \mathbf{u} , the electric potential ϕ , and the polarization p . The micro-to-macro transition concept derived in Chapter 4 for finite deformations is boiled down to the small strain regime. The macro-strains and macro-stresses are given by

$$\bar{\epsilon} = \frac{1}{|\mathcal{B}|} \int_{\partial\mathcal{B}} \text{sym}[\mathbf{u} \otimes \mathbf{n}] \, dA \quad \text{and} \quad \bar{\sigma} = \frac{1}{|\mathcal{B}|} \int_{\partial\mathcal{B}} \text{sym}[\mathbf{t} \otimes \mathbf{x}] \, dA, \quad (6.34)$$

where $\mathbf{t} = \partial_{\epsilon} \Psi \cdot \mathbf{n}$ is the traction vector. The macroscopic electric field and the electric displacement are

$$\bar{e} = \frac{1}{|\mathcal{B}|} \int_{\partial\mathcal{B}} -\phi \mathbf{n} \, dA \quad \text{and} \quad \bar{d} = \frac{1}{|\mathcal{B}|} \int_{\partial\mathcal{B}} -\sigma_f^e \mathbf{x} \, dA, \quad (6.35)$$

where $\sigma_f^e = \partial_e \Psi \cdot \mathbf{n}$ is the surface charge density. These can be transformed to volume averages by application of the Gauss theorem, such that the macroscopic quantities coincide with the volume average of their microscopic counterparts.

6.3.1. Generalized macrohomogeneity condition

Appropriate boundary conditions for the microstructure are derived from a Hill-Mandel-type macrohomogeneity condition, see HILL [63] for the purely mechanical case, and recent extension by SCHRÖDER [161] to non-dissipative electro-mechanical problems. We extend this to the dissipative case by postulating the equivalence of the total macroscopic power including electric contributions with the volume average of its microscopic counterpart *extended* by the phase field terms

$$\bar{\sigma} : \dot{\bar{\epsilon}} - \bar{d} \cdot \dot{\bar{e}} = \frac{1}{|\mathcal{B}|} \int_{\mathcal{B}} \{\boldsymbol{\sigma} : \dot{\boldsymbol{\epsilon}} - \mathbf{d} \cdot \dot{\mathbf{e}} + \mathbf{q} \cdot \dot{\mathbf{p}} + \mathbf{k} : \nabla \dot{\mathbf{p}}\} \, dV \quad (6.36)$$

Note that this statement is a direct outcome of the above proposed variational principle of homogenization, see (6.7). The average extended microscopic power can be transformed to the boundary of the microstructure by application of the Gauss theorem and utilizing the microscopic equilibrium equations (6.10), yielding

$$\frac{1}{|\mathcal{B}|} \int_{\mathcal{B}} \{\boldsymbol{\sigma} : \dot{\boldsymbol{\epsilon}} - \mathbf{d} \cdot \dot{\mathbf{e}} + \mathbf{q} \cdot \dot{\mathbf{p}} + \mathbf{k} : \nabla \dot{\mathbf{p}}\} \, dV = \frac{1}{|\mathcal{B}|} \int_{\partial\mathcal{B}} \{\mathbf{t} \cdot \dot{\mathbf{u}} - \sigma_f^e \dot{\phi} + \boldsymbol{\tau} \cdot \dot{\mathbf{p}}\} \, dA \quad (6.37)$$

in terms of the *micro-tractions* $\mathfrak{t} = \mathbb{k} \cdot \mathbf{n}$. This expression serves as the starting point for the construction of electro-mechanical boundary conditions of the microstructure.

6.3.2. Derivation of appropriate boundary conditions

For the micro-electro-elastic model under consideration, we focus on three classes of boundary constraints on the boundary $\partial\mathcal{B}$ of the microstructure:

- (D) *Dirichlet*: Linear displacement and electric potential, constant polarization.
- (N) *Neumann*: Constant stress and electric displacement, zero micro-tractions.
- (P) *Periodic*: Periodic primary fields with regard to opposite faces of microstructure.

These conditions are obtained from the extended Hill-Mandel condition as follows.

Dirichlet-type boundary conditions. Insertion of the overall macroscopic stresses (6.34)₂ and the macroscopic electric displacement (6.35)₂ into the above Hill-Mandel macrohomogeneity condition gives $\bar{\boldsymbol{\sigma}} : \dot{\boldsymbol{\varepsilon}} - \bar{\mathbf{d}} \cdot \dot{\boldsymbol{\varepsilon}} = \frac{1}{|\mathcal{B}|} \int_{\partial\mathcal{B}} \{\mathfrak{t} \cdot (\dot{\boldsymbol{\varepsilon}} \cdot \mathbf{x}) + \sigma_f^e(\dot{\boldsymbol{\varepsilon}} \cdot \mathbf{x})\} dA$. A combination with (6.37) results in a modified statement of the Hill-Mandel condition valid on the surface of the microstructure

$$\frac{1}{|\mathcal{B}|} \int_{\partial\mathcal{B}} \{\mathfrak{t} \cdot (\dot{\mathbf{u}} - \dot{\boldsymbol{\varepsilon}} \cdot \mathbf{x}) - \sigma_f^e(\dot{\phi} + \dot{\boldsymbol{\varepsilon}} \cdot \mathbf{x}) + \mathfrak{t} \cdot \dot{\mathbf{p}}\} dA = 0. \quad (6.38)$$

We conclude *uniform displacement-type (Dirichlet)* boundary constraints

$$(D) : \left. \begin{array}{l} \mathbf{u} = \bar{\boldsymbol{\varepsilon}} \cdot \mathbf{x} \\ -\phi = \bar{\boldsymbol{\varepsilon}} \cdot \mathbf{x} \\ \mathbf{p} = \mathbf{0} \end{array} \right\} \text{ on } \partial\mathcal{B} \quad (6.39)$$

which satisfy the macrohomogeneity condition. Here, the mechanical displacement and the electric potential on the boundary of the microstructure are fully determined due to the prescribed macro-variables. The polarization is set to zero (constant) on the full boundary of the microstructure.

Neumann-type boundary conditions. Here, we reformulate the macroscopic power in (6.36) by insertion of the homogenized strains (6.34)₁ and the electric field (6.35)₁, respectively. We end up with $\bar{\boldsymbol{\sigma}} : \dot{\boldsymbol{\varepsilon}} - \bar{\mathbf{d}} \cdot \dot{\boldsymbol{\varepsilon}} = \frac{1}{|\mathcal{B}|} \int_{\partial\mathcal{B}} \{(\bar{\boldsymbol{\sigma}} \cdot \mathbf{n}) \cdot \dot{\mathbf{u}} + (\bar{\mathbf{d}} \cdot \mathbf{n})\dot{\phi}\} dA$, yielding by a combination with (6.37) a modified Hill-Mandel condition of the form

$$\frac{1}{|\mathcal{B}|} \int_{\partial\mathcal{B}} \{(\mathfrak{t} - \bar{\boldsymbol{\sigma}} \cdot \mathbf{n}) \cdot \dot{\mathbf{u}} - (\sigma_f^e + \bar{\mathbf{d}} \cdot \mathbf{n})\dot{\phi} + \mathfrak{t} \cdot \dot{\mathbf{p}}\} dA = 0. \quad (6.40)$$

Hence, we identify the *traction-type (Neumann)* boundary conditions

$$(N) : \left. \begin{array}{l} \mathfrak{t} = \bar{\boldsymbol{\sigma}} \cdot \mathbf{n} \\ -\sigma_f^e = \bar{\mathbf{d}} \cdot \mathbf{n} \\ \mathfrak{t} = \mathbf{0} \end{array} \right\} \text{ on } \partial\mathcal{B} \quad (6.41)$$

for the thermodynamical forces dual to the primary fields on the surface. Note that no macroscopic dual to the micro-traction is considered. As a consequence, we assumed zero micro-tractions $\mathfrak{t} = \mathbf{0}$.

Periodic boundary conditions. Non-trivial constraints satisfying the Hill-Mandel condition are obtained for periodic microstructures according to Figure 4.7. The surface of the microstructure $\partial\mathcal{B} = \partial\mathcal{B}^+ \cup \partial\mathcal{B}^-$ decomposes into opposite faces with normals \mathbf{n}^+ and $\mathbf{n}^- = -\mathbf{n}^+$ at associated points $\mathbf{x}^+ \in \partial\mathcal{B}^+$ and $\mathbf{x}^- \in \partial\mathcal{B}^-$. *Periodicity* means ¹

$$\llbracket \mathbf{u} \rrbracket = \bar{\boldsymbol{\varepsilon}} \cdot \llbracket \mathbf{x} \rrbracket, \quad \llbracket -\phi \rrbracket = \bar{\varrho} \cdot \llbracket \mathbf{x} \rrbracket, \quad \llbracket \mathcal{P} \rrbracket = \mathbf{0}. \quad (6.42)$$

Note that a macro-mode for the polarization vector does not exist. We rewrite the Hill-Mandel condition by inserting the assumption (6.42) into (6.38) as an additional constraint for the mechanical tractions, the electric surface charge density, and the micro-tractions

$$\frac{1}{|\mathcal{B}|} \int_{\partial\mathcal{B}^+} \{ (\mathbf{t}^+ + \mathbf{t}^-) \cdot (\dot{\mathbf{u}}^+ - \dot{\bar{\boldsymbol{\varepsilon}}} \cdot \mathbf{x}^+) - (\sigma_f^{e+} + \sigma_f^{e-}) (\dot{\phi}^+ + \dot{\bar{\varrho}} \cdot \mathbf{x}^+) + (\mathfrak{t}^+ + \mathfrak{t}^-) \cdot \dot{\mathcal{P}}^+ \} dA = 0. \quad (6.43)$$

This is satisfied for *periodic primary fields* and *anti-periodic tractions*

$$(P) : \left. \begin{array}{l} \llbracket \mathbf{u} \rrbracket = \bar{\boldsymbol{\varepsilon}} \cdot \llbracket \mathbf{x} \rrbracket \\ \llbracket -\phi \rrbracket = \bar{\varrho} \cdot \llbracket \mathbf{x} \rrbracket \\ \llbracket \mathcal{P} \rrbracket = \mathbf{0} \end{array} \right\} \text{ on } \partial\mathcal{B} \left\{ \begin{array}{l} \mathbf{t}^+ = -\mathbf{t}^- \\ \sigma_f^{e+} = -\sigma_f^{e-} \\ \mathfrak{t}^+ = -\mathfrak{t}^- \end{array} \right. \quad (6.44)$$

at associated points $\mathbf{x}^+ \in \partial\mathcal{B}^+$ and $\mathbf{x}^- \in \partial\mathcal{B}^-$. Such periodic microscopic boundary conditions are the most reasonable choice for the homogenization analysis under consideration, even for microstructures which are non-periodic, see for instance TERADA ET AL. [184] and SEGURADO & LLORCA [164].

6.3.3. Deformation and electric field driven homogenization

We construct a *deformation and electric field driven implementation of homogenization* based on alternative boundary constraints. The attractive feature of such a setting is that the structure of the average variational principle (6.11) is preserved. The boundary constraints can be taken into account in the variational framework by means of *Lagrange multipliers* or *penalty terms* in line with the treatments MIEHE [117], MIEHE & BAYREUTHER [121], and MIEHE ET AL. [130] for purely mechanical formulations.

Formulation based on Lagrange functionals. The boundary constraints $I = D, P, N$ can be incorporated in the incremental variational framework of homogenization by adding additional Lagrange terms. The *extended form* of the incremental variational principle

$$\bar{\pi}_{\mathcal{L},I}^{\tau}(\bar{\boldsymbol{\varepsilon}}, \bar{\varrho}) = \inf_{\mathbf{u}} \sup_{\phi} \inf_{\mathcal{P}} \sup_{\boldsymbol{\lambda}_I} \sup_{\boldsymbol{\mu}_I} \sup_{\boldsymbol{\xi}_I} \Pi_{\mathcal{L},I}^{\tau}(\mathbf{u}, \phi, \mathcal{P}, \nabla \mathcal{P}, \boldsymbol{\lambda}_I, \boldsymbol{\mu}_I, \boldsymbol{\xi}_I; \bar{\boldsymbol{\varepsilon}}, \bar{\varrho}) \quad (6.45)$$

¹The mechanical and electric fields can be also expressed by fine scale fluctuation fields $\tilde{\mathbf{u}}$ and $\tilde{\phi}$ in the form $\mathbf{u} = \bar{\boldsymbol{\varepsilon}} \cdot \mathbf{x} + \tilde{\mathbf{u}}$ and $-\phi = \bar{\varrho} \cdot \mathbf{x} - \tilde{\phi}$. Note that on the macro-level the polarization does not exist. Then, periodic boundary conditions are achieved by considering periodic fluctuations

$$\tilde{\mathbf{u}}^+ = \tilde{\mathbf{u}}^-, \quad \tilde{\phi}^+ = \tilde{\phi}^-, \quad \mathcal{P}^+ = \mathcal{P}^-.$$

is governed by the incremental potential density π^τ defined in (6.14) and additional *Lagrange terms*

$$\Pi_{\mathcal{L},I}^\tau := \frac{1}{|\mathcal{B}|} \int_{\mathcal{B}} \pi^\tau(\nabla_s \mathbf{u}, -\nabla \phi, \mathbb{P}, \nabla \mathbb{P}; \bar{\boldsymbol{\varepsilon}}, \bar{e}) dV - \mathcal{L}_I(\mathbf{u}, \phi, \mathbb{P}, \boldsymbol{\lambda}_I, \boldsymbol{\mu}_I, \boldsymbol{\xi}_I; \bar{\boldsymbol{\varepsilon}}, \bar{e}) \quad (6.46)$$

for the alternative constraints $I = D, P, N$. These Lagrange terms are defined by

$$\mathcal{L}_I = \begin{cases} \frac{1}{|\mathcal{B}|} \int_{\partial \mathcal{B}} \boldsymbol{\lambda}_D(\mathbf{u} - \bar{\boldsymbol{\varepsilon}} \mathbf{x}) dA & + \frac{1}{|\mathcal{B}|} \int_{\partial \mathcal{B}} \mu_D(\phi + \bar{e} \mathbf{x}) dA & + \int_{\partial \mathcal{B}} \boldsymbol{\xi}_D \mathbb{P} dA \\ \frac{1}{|\mathcal{B}|} \int_{\partial \mathcal{B}^+} \boldsymbol{\lambda}_P(\llbracket \mathbf{u} \rrbracket - \bar{\boldsymbol{\varepsilon}} \llbracket \mathbf{x} \rrbracket) dA & + \frac{1}{|\mathcal{B}|} \int_{\partial \mathcal{B}^+} \mu_P(\llbracket \phi \rrbracket + \bar{e} \llbracket \mathbf{x} \rrbracket) dA & + \int_{\partial \mathcal{B}^+} \boldsymbol{\xi}_P \llbracket \mathbb{P} \rrbracket dA \\ \frac{1}{|\mathcal{B}|} \int_{\partial \mathcal{B}} \mathbf{u}(\boldsymbol{\lambda}_N \mathbf{n}) dA - \boldsymbol{\lambda}_N : \bar{\boldsymbol{\varepsilon}} & + \frac{1}{|\mathcal{B}|} \int_{\partial \mathcal{B}} -\phi(\boldsymbol{\mu}_N \mathbf{n}) dA - \boldsymbol{\mu}_N \bar{e} & + \frac{1}{|\mathcal{B}|} \int_{\partial \mathcal{B}} \mathbb{P}(\boldsymbol{\xi}_N \mathbf{n}) dA \end{cases} \quad (6.47)$$

The Euler-Lagrange equations of the extended variational principle of homogenization (6.45) are identical with (6.15) above. However, in addition, boundary constraints are obtained:

Mechanical displacement constraints. The three boundary conditions $I = D, P, N$ associated with the mechanical displacement field \mathbf{u} can be summarized as

$$\begin{aligned} \mathbf{u} &= \bar{\boldsymbol{\varepsilon}} \cdot \mathbf{x} \text{ on } \partial \mathcal{B} & \partial_e \Psi \cdot \mathbf{n} &= \boldsymbol{\lambda}_D \text{ on } \partial \mathcal{B} \\ \llbracket \mathbf{u} \rrbracket &= \bar{\boldsymbol{\varepsilon}} \cdot \llbracket \mathbf{x} \rrbracket \text{ on } \partial \mathcal{B}^+ & \text{and } \pm(\partial_e \Psi \cdot \mathbf{n})^\pm &= \boldsymbol{\lambda}_P \text{ on } \partial \mathcal{B}^\pm \\ \bar{\boldsymbol{\varepsilon}} &= \frac{1}{|\mathcal{B}|} \int_{\partial \mathcal{B}} \text{sym}[\mathbf{u} \otimes \mathbf{n}] dA & \partial_e \Psi \cdot \mathbf{n} &= \boldsymbol{\lambda}_N \cdot \mathbf{n} \text{ on } \partial \mathcal{B} \end{aligned} \quad (6.48)$$

Equation (6.48)_{1,4} and (6.48)_{2,5} are the (D) Dirichlet-type and (P) periodic representations, where we identify the Lagrange multiplier as the surface tractions. For (N) Neumann-type constraints (6.48)_{3,6}, the Lagrange parameter turns out to be the macroscopic stress tensor $\boldsymbol{\lambda}_N = \bar{\boldsymbol{\sigma}}$.

Electric potential constraints. The Lagrange terms (6.47) result in the boundary conditions for the electric potential ϕ

$$\begin{aligned} -\phi &= \bar{e} \cdot \mathbf{x} \text{ on } \partial \mathcal{B} & -\partial_e \Psi \cdot \mathbf{n} &= \mu_D \text{ on } \partial \mathcal{B} \\ \llbracket -\phi \rrbracket &= \bar{e} \cdot \llbracket \mathbf{x} \rrbracket \text{ on } \partial \mathcal{B}^+ & \text{and } \pm(-\partial_e \Psi \cdot \mathbf{n})^\pm &= \mu_P \text{ on } \partial \mathcal{B}^\pm \\ \bar{e} &= \frac{1}{|\mathcal{B}|} \int_{\partial \mathcal{B}} -\phi \mathbf{n} dA & -\partial_e \Psi \cdot \mathbf{n} &= -\boldsymbol{\mu}_N \cdot \mathbf{n} \text{ on } \partial \mathcal{B} \end{aligned} \quad (6.49)$$

We identify in (6.49)_{1,4} and (6.49)_{2,5} the linear electric potential conditions (D) and periodic conditions (P), respectively. The Lagrange parameter is in both cases the surface charge. For (N) uniform surface charges (6.49)_{3,6}, the Lagrange multiplier is determined as the negative macroscopic electric displacement $\boldsymbol{\mu}_N = -\bar{\mathbf{d}}$.

Constraints for the electric polarization. The boundary constraints for the electric polarization are

$$\begin{aligned} \mathbb{P} &= \mathbf{0} \text{ on } \partial \mathcal{B} & \partial_{\nabla \mathbb{P}} \Psi \cdot \mathbf{n} &= \boldsymbol{\xi}_D \text{ on } \partial \mathcal{B} \\ \llbracket \mathbb{P} \rrbracket &= \mathbf{0} \text{ on } \partial \mathcal{B}^+ & \text{and } \pm(\partial_{\nabla \mathbb{P}} \Psi \cdot \mathbf{n})^\pm &= \boldsymbol{\xi}_P \text{ on } \partial \mathcal{B}^\pm \\ \mathbf{0} &= \frac{1}{|\mathcal{B}|} \int_{\partial \mathcal{B}} \mathbb{P} \otimes \mathbf{n} dA & \partial_{\nabla \mathbb{P}} \Psi \cdot \mathbf{n} &= \boldsymbol{\xi}_N \cdot \mathbf{n} \text{ on } \partial \mathcal{B} \end{aligned} \quad (6.50)$$

Equation (6.50)_{1,4} and (6.50)_{2,5} represent the (D) Dirichlet and the (P) periodic representation of the boundary conditions for the electric polarization, where the Lagrange parameter is the micro-traction on the surface. For (N) Neumann-type constraints (6.50)_{3,6} the micro-tractions are zero.

Macroscopic stresses and electric displacement. The macroscopic stresses and electric displacement follow in a straightforward manner from the variational principle of homogenization (6.45) by $\bar{\boldsymbol{\sigma}}_I = \partial_{\bar{\boldsymbol{\varepsilon}}} \bar{\pi}_{\mathcal{L},I}^\tau$ and $\bar{\mathbf{d}}_I = -\partial_{\bar{\mathbf{e}}} \bar{\pi}_{\mathcal{L},I}^\tau$, respectively. For the three types of boundary conditions, we obtain the macro-stress and the macroscopic electric displacement as

$$\bar{\boldsymbol{\sigma}}_I = \begin{cases} \frac{1}{|\mathcal{B}|} \int_{\partial\mathcal{B}} \text{sym}[\boldsymbol{\lambda}_D \otimes \mathbf{x}] dA \\ \frac{1}{|\mathcal{B}|} \int_{\partial\mathcal{B}^+} \text{sym}[\boldsymbol{\lambda}_P \otimes \llbracket \mathbf{x} \rrbracket] dA \\ \boldsymbol{\lambda}_N \end{cases} \quad \text{and} \quad \bar{\mathbf{d}}_I = \begin{cases} \frac{1}{|\mathcal{B}|} \int_{\partial\mathcal{B}} \mu_D \mathbf{x} dA \\ \frac{1}{|\mathcal{B}|} \int_{\partial\mathcal{B}^+} \mu_P \llbracket \mathbf{x} \rrbracket dA \\ -\boldsymbol{\mu}_N \end{cases} \quad (6.51)$$

These expressions are derivatives of the Lagrange terms (6.47). Again, this highlights the Lagrange multipliers as the traction vector and surface charge for Dirichlet-type and periodic boundary conditions $I = D, P$. For the case of uniform traction boundary conditions, the Lagrange parameters $\boldsymbol{\lambda}_N$ and $\boldsymbol{\mu}_N$ are identical to the homogenized overall stresses $\bar{\boldsymbol{\sigma}}$ and the negative macroscopic electric displacement vector $-\bar{\mathbf{d}}$.

Formulation based on penalty functionals. An alternative approach to the implementation of the boundary conditions are *penalty terms*. The incremental variational statement (6.11) is then extended to

$$\boxed{\bar{\pi}_{\mathcal{P},I}^\tau(\bar{\boldsymbol{\varepsilon}}, \bar{\mathbf{e}}) = \inf_{\mathbf{u}} \sup_{\phi} \inf_P \Pi_{\mathcal{P},I}^\tau(\mathbf{u}, \phi, P, \nabla P; \bar{\boldsymbol{\varepsilon}}, \bar{\mathbf{e}})} \quad (6.52)$$

governed by the incremental potential π^τ in (6.14) and additional penalty functionals

$$\Pi_{\mathcal{P},I}^\tau := \frac{1}{|\mathcal{B}|} \int_{\mathcal{B}} \pi^\tau(\nabla_s \mathbf{u}, -\nabla \phi, P, \nabla P; \bar{\boldsymbol{\varepsilon}}, \bar{\mathbf{e}}) dV - \mathcal{P}_I(\mathbf{u}, \phi, P; \bar{\boldsymbol{\varepsilon}}, \bar{\mathbf{e}}) \quad (6.53)$$

for the constraints $I = D, P, N$. These penalty terms are defined via

$$\mathcal{P}_I = \begin{cases} \frac{\alpha_D}{2|\mathcal{B}|} \int_{\partial\mathcal{B}} |\mathbf{u} - \bar{\boldsymbol{\varepsilon}} \mathbf{x}|^2 dA & + \frac{\beta_D}{2|\mathcal{B}|} \int_{\partial\mathcal{B}} |\phi + \bar{\mathbf{e}} \mathbf{x}|^2 dA & + \frac{\gamma_D}{2|\mathcal{B}|} \int_{\partial\mathcal{B}} |P|^2 dA \\ \frac{\alpha_P}{2|\mathcal{B}|} \int_{\partial\mathcal{B}^+} |\llbracket \mathbf{u} \rrbracket - \bar{\boldsymbol{\varepsilon}} \llbracket \mathbf{x} \rrbracket|^2 dA & + \frac{\beta_P}{2|\mathcal{B}|} \int_{\partial\mathcal{B}^+} |\llbracket \phi \rrbracket + \bar{\mathbf{e}} \llbracket \mathbf{x} \rrbracket|^2 dA & + \frac{\gamma_P}{2|\mathcal{B}|} \int_{\partial\mathcal{B}^+} |\llbracket P \rrbracket|^2 dA \\ \frac{\alpha_N}{2} \left| \frac{1}{|\mathcal{B}|} \int_{\partial\mathcal{B}} \text{sym}[\mathbf{u} \otimes \mathbf{n}] dA - \bar{\boldsymbol{\varepsilon}} \right|^2 & + \frac{\beta_N}{2} \left| \frac{1}{|\mathcal{B}|} \int_{\partial\mathcal{B}} \phi \mathbf{n} dA + \bar{\mathbf{e}} \right|^2 & + \frac{\gamma_N}{2} \left| \frac{1}{|\mathcal{B}|} \int_{\partial\mathcal{B}} P \otimes \mathbf{n} dA \right|^2 \end{cases} \quad (6.54)$$

where $\{\alpha_I, \beta_I, \gamma_I\}$ are scalar penalty parameters. The Euler-Lagrange equations of the extended variational principle of homogenization (6.52) are identical with (6.15) above. In addition, boundary expressions are obtained as follows:

Mechanical displacement constraints. The three types of surface conditions $I = D, P, N$ of the mechanical displacement field \mathbf{u} can be summarized as

$$\begin{aligned} \partial_\varepsilon \Psi \cdot \mathbf{n} &= \alpha_D (\mathbf{u} - \bar{\varepsilon} \cdot \mathbf{x}) \text{ on } \partial\mathcal{B} \\ \pm(\partial_\varepsilon \Psi \cdot \mathbf{n})^\pm &= \alpha_P (\llbracket \mathbf{u} \rrbracket - \bar{\varepsilon} \cdot \llbracket \mathbf{x} \rrbracket) \text{ on } \partial\mathcal{B}^\pm \\ \partial_\varepsilon \Psi \cdot \mathbf{n} &= \alpha_N \left(\frac{1}{|\mathcal{B}|} \int_{\partial\mathcal{B}} \text{sym}[\mathbf{u} \otimes \mathbf{n}] dA - \bar{\varepsilon} \right) \mathbf{n} \text{ on } \partial\mathcal{B} \end{aligned} \quad (6.55)$$

They provide approximate representations of the exact conditions (6.48) obtained by the Lagrange functionals. In particular, (6.55)₁ provides an approximate solution (D) for the traction vector on the surface of the microstructure in terms of the penalty parameters α_D . This parameter penalizes deviations from the exact enforcement of the Dirichlet constraints for the displacement field \mathbf{u} . Similarly, (6.55)₂ determines non-trivial periodic boundary constraints (P) due to the traction vector on the contour $\partial\mathcal{B}^\pm$. The boundary condition (6.55)₃ approximates uniform tractions (N) by the determination of the macroscopic stress tensor $\bar{\boldsymbol{\sigma}}$ in terms of the penalty parameter α_N .

Electric potential constraints. The penalty formulation for electric field driven homogenization for the constraints $I = D, N, P$ results in the boundary conditions

$$\begin{aligned} -\partial_e \Psi \cdot \mathbf{n} &= \beta_D (\phi + \bar{e} \cdot \mathbf{x}) \text{ on } \partial\mathcal{B} \\ \pm(-\partial_e \Psi \cdot \mathbf{n})^\pm &= \beta_P (\llbracket \phi \rrbracket + \bar{e} \cdot \llbracket \mathbf{x} \rrbracket) \text{ on } \partial\mathcal{B}^\pm \\ -\partial_e \Psi \cdot \mathbf{n} &= \beta_N \left(\frac{1}{|\mathcal{B}|} \int_{\partial\mathcal{B}} \phi \mathbf{n} dA + \bar{e} \right) \mathbf{n} \text{ on } \partial\mathcal{B} \end{aligned} \quad (6.56)$$

Equation (6.56)₁ determines an approximative formulation of (D) Dirichlet-type boundary conditions, where the surface charge is expressed in terms of penalized deviations from the exact enforcement of the boundary conditions in (6.49)₁. An approximated version of the (P) non-trivial periodic boundary conditions is given in (6.56)₂. For the (N) Neumann-type constraints an approximation is given by (6.56)₃, where the overall electric displacement vector $\bar{\mathbf{d}}$ is directly computed by a constitutive function penalized by β_N .

Constraints for the electric polarization. The constraints for the electric polarization are governed by the penalty parameter γ_I in the form

$$\begin{aligned} \partial_{\nabla_P} \Psi \cdot \mathbf{n} &= \gamma_D P \text{ on } \partial\mathcal{B} \\ \pm(\partial_{\nabla_P} \Psi \cdot \mathbf{n})^\pm &= \gamma_P \llbracket P \rrbracket \text{ on } \partial\mathcal{B}^\pm \\ \partial_{\nabla_P} \Psi \cdot \mathbf{n} &= \gamma_N \left(\frac{1}{|\mathcal{B}|} \int_{\partial\mathcal{B}} P \otimes \mathbf{n} dA \right) \mathbf{n} \text{ on } \partial\mathcal{B} \end{aligned} \quad (6.57)$$

For the (D) Dirichlet-type as well as (P) periodic boundary conditions, we observe a representation in terms of the order parameter penalized by $\gamma_{D,P}$. The (N) Neumann-type representation is given due to an integral expression resulting in zero micro-tractions.

Macroscopic stresses and electric displacement. The variational principle of homogenization (6.52) determines directly the macroscopic stresses $\bar{\boldsymbol{\sigma}}_I = \partial_{\bar{\varepsilon}} \bar{\pi}_{P,I}^\tau$ and the electric

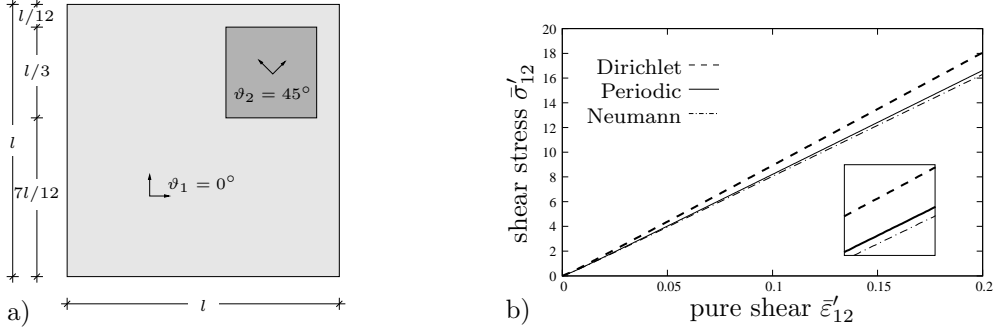


Figure 6.5: *Boundary-value-problem and stress-strain curves.* a) Dimension of boundary-value-problem with square eccentric inclusion, side length $l/3$, and preferred direction $\vartheta_2 = 45^\circ$. b) Macroscopic stress-strain curves showing stiffness of the microstructure and bound character of (D) Dirichlet and (N) Neumann boundary conditions.

displacement vector $\bar{d}_I = -\partial_{\bar{\varepsilon}} \bar{\pi}_{P,I}^T$ by function evaluations as

$$\bar{\sigma}_I = \begin{cases} \frac{1}{|\mathcal{B}|} \int_{\partial\mathcal{B}} \text{sym}[\alpha_D(\mathbf{u} - \bar{\varepsilon}\mathbf{x}) \otimes \mathbf{x}] dA \\ \frac{1}{|\mathcal{B}|} \int_{\partial\mathcal{B}^+} \text{sym}[\alpha_P(\llbracket \mathbf{u} \rrbracket - \bar{\varepsilon} \llbracket \mathbf{x} \rrbracket) \otimes \llbracket \mathbf{x} \rrbracket] dA \\ \alpha_N \left(\frac{1}{|\mathcal{B}|} \int_{\partial\mathcal{B}} \text{sym}[\mathbf{u} \otimes \mathbf{n}] dA - \bar{\varepsilon} \right) \end{cases} \quad \text{and} \quad \bar{d}_I = \begin{cases} \frac{1}{|\mathcal{B}|} \int_{\partial\mathcal{B}} \beta_D(\phi + \bar{\varepsilon}\mathbf{x}) \mathbf{x} dA \\ \frac{1}{|\mathcal{B}|} \int_{\partial\mathcal{B}^+} \beta_P(\llbracket \phi \rrbracket + \bar{\varepsilon} \llbracket \mathbf{x} \rrbracket) \llbracket \mathbf{x} \rrbracket dA \\ \beta_N \left(\frac{1}{|\mathcal{B}|} \int_{\partial\mathcal{B}} \phi \mathbf{n} dA + \bar{\varepsilon} \right) \end{cases} \quad (6.58)$$

for the three types of boundary conditions under consideration.

6.4. Representative numerical examples

The capability of the developed computational framework of homogenization in micro-electro-mechanics is demonstrated by means of two- and three-dimensional benchmarks. The examples describe domain wall movements in *piezoceramic materials* for macroscopic electric field and strain driven scenarios. The homogenization allows the determination of *macroscopic hysteresis curves*. We again consider barium titanate (BaTiO_3) in a polarized tetragonal state. The material parameter are identical to the previous chapter and not repeated here, see [Table 5.1](#).

6.4.1. Analysis of different homogenization boundary conditions

We first investigate the influence of the different boundary conditions $I = D, P, N$ for a simple microstructure, consisting of a stiff inclusion with rotated preferred direction. The geometry of the sample is shown in [Figure 6.5a](#). The square inclusion has a size of $l/3$. A structured mesh is used with 30×30 quadrilateral elements. The stiff inclusion has the modified Lamé parameters $\lambda'_2 = 11100.0$, $\mu'_2 = 3700.0$, and a rotated preferred direction $\vartheta_2 = 45^\circ$. The equilibrium state of the micro model is determined starting from a random noise of the polarization. We apply (D) Dirichlet-type boundary conditions for the displacement field and the electric potential and (P) periodic boundary conditions for the polarization in order to get a feasible starting point for the subsequent simulations. [Figure 6.5b](#) shows the stress-strain curve for a macroscopic pure shear load $\bar{\varepsilon}'_{12}$. Observe

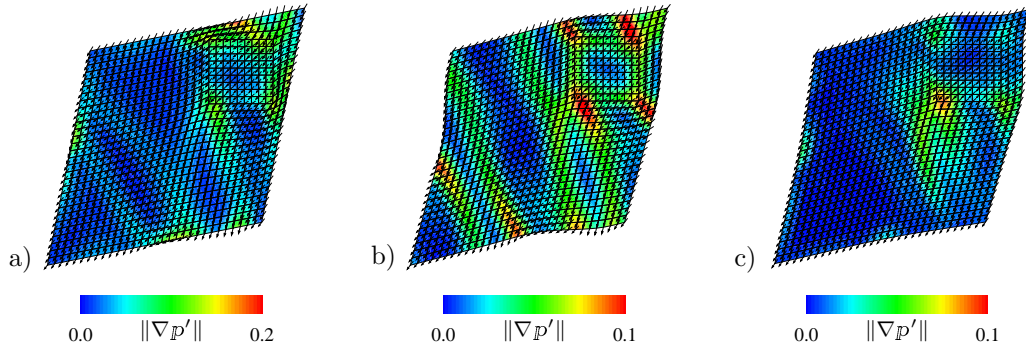


Figure 6.6: Comparison of polarization states for macroscopic shear deformation. The final domain state is obtained for a macroscopic pure shear loading and periodic boundary conditions for the polarization. a) Dirichlet, b) periodic, and c) Neumann-type surface constraints are chosen for displacement field and electric potential.

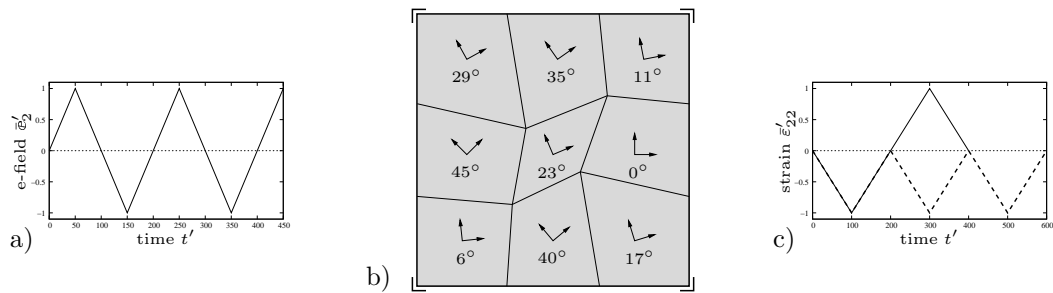


Figure 6.7: Boundary-value-problem and loading curves. Sawtooth-type loading for the a) electric and c) two mechanical loading processes. b) Representative volume element of nine grains characterized by different preferred directions $\{\vartheta_i\}_{i=1,9}$ and normalized edge length $l' = 100$. On the corner nodes, the mechanical $\tilde{\mathbf{u}}' = \mathbf{0}$ and electric fluctuations $\tilde{\phi}' = 0$ are suppressed. Each grain is discretized with 10×10 four node quadrilateral finite elements.

that for the mechanical problem, the (D) Dirichlet-type and (N) Neumann-type boundary conditions form upper and lower bounds of the mechanical stiffness. As expected, the (P) periodic boundary conditions render the best choice of surface constraints. Figure 6.6 shows the mechanically deformed sample and the evolved domains. The influence of the boundary conditions on the final state obtained by formation and evolution of the domains is observed. The (D) Dirichlet, (P) periodic, and (N) Neumann boundary conditions for the displacement field can be directly observed at the surface deformation of the microstructure.

6.4.2. Homogenization analysis of polycrystalline aggregate

Next, consider a two-dimensional example which analyses an idealized polycrystal consisting of only nine grains. Each grain has different preferred poling directions characterized by the lattice orientations $\{\vartheta_i\}_{i=1,9}$ as indicated in Figure 6.7. The different lattice orientations are chosen such that the gap between neighboring grains is maximized. The material parameters are identical in all grains. Goal is the determination of macroscopic hysteresis curves based on the proposed homogenization technique, where this microstructure is related to a macroscopic material point. Clearly, this idealized polycrystal can be easily extended to more complex structures consisting of more grains.

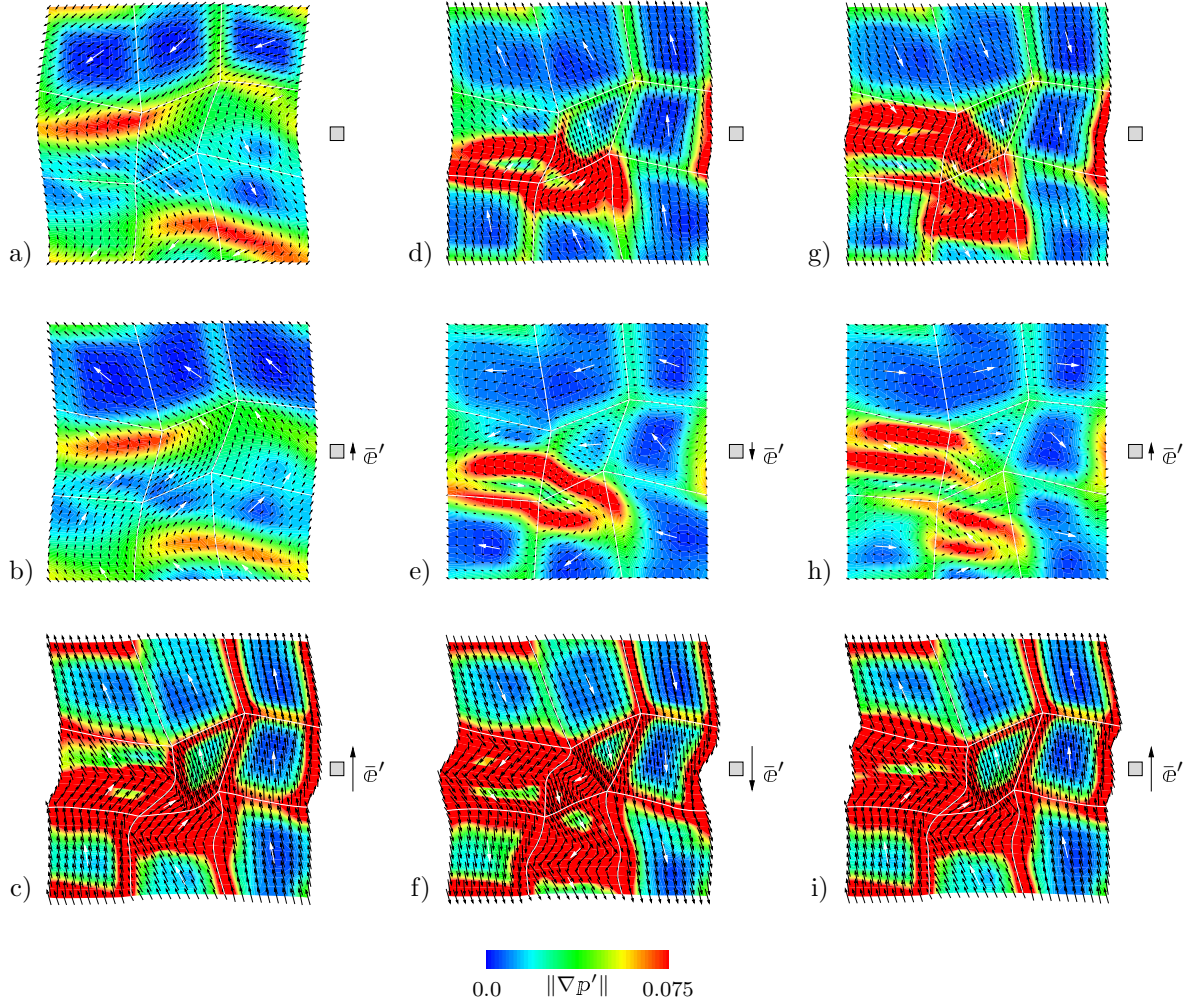


Figure 6.8: *Domain states of electric field driven homogenization.* Periodic boundary conditions (fluctuation magnified) are utilized, the contour shows the norm of the polarization gradient $\|\nabla P'\|$, and poling directions are indicated by white arrows. The snapshots are at time a) $t' = 0$, b) $t' = 10$, c) $t' = 50$, d) $t' = 100$, e) $t' = 110$, f) $t' = 150$, g) $t' = 200$, h) $t' = 210$, and i) $t' = 250$.

Construction of an initial equilibrium state. First, an artificial initial boundary-value-problem is solved that produces an appropriate starting point for the subsequent simulations of electric field and strain driven domain wall motions. To this end, a relaxation process of a random initial orientation to an equilibrium state of microscopic polarization is performed. The relaxation process causes the polarization to adjust in certain regions and domain walls start to appear. The final stage of the equilibrium state is shown in Figure 6.8a, where domain walls intersecting different grains appear. These domain walls are not restricted to the grain boundaries, i.e. transgranular domain walls are formed during the relaxation process. In the domains, that are regions separated by the walls, the polarization vectors are almost aligned. It is interesting to notice that the orientation differences of the polarization vectors across the domain walls within each grain are close to either 90° or 180° . Hence, the polarization vectors are aligned with preferred directions on either side of the walls. The varying lattice orientations of the grains intersected by the domain wall lead to its "zig-zag" shape.

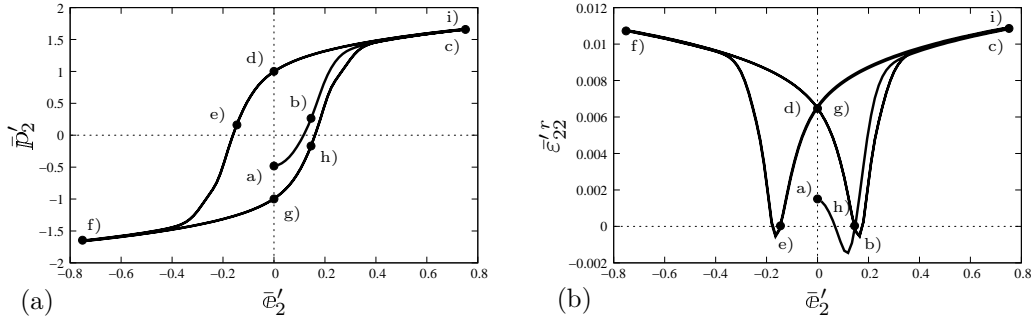


Figure 6.9: *Ferroelectric hysteresis curves of electric field driven homogenization.* a) Dielectric hysteresis and b) butterfly hysteresis characterizing dissipative ferroelectric processes and incorporating domain states of Figure 6.8.

Macroscopic electric field driven loading. Starting with the equilibrium state, we apply a sawtooth-type macroscopic electric field in vertical direction up to a maximum value of $\bar{e}'_2{}^{max} = 0.75$. Such a loading causes microscopic domain wall motions in the polycrystalline microstructure, where periodic boundary conditions are applied.

Domain wall motion. Figure 6.8 depicts the domain walls and the evolution of the polarization in the microstructure for a macroscopic electric field driven process. In order to visualize the periodicity of the microstructure, the displacement fluctuations are magnified. Solid white lines mark grain boundaries. The application of the electric loading causes the polarization towards the external field, however, aligned to the preferred directions $\{\vartheta_i\}_{i=1,9}$ in the grains. Figure 6.8a–c show the equilibrium state of the simulation and the subsequent motion of the domain walls. The last snapshot of this sequence, Figure 6.8c, corresponds to the point of maximum applied electric field. A careful observation of this figure reveals that this configuration has been obtained via the mechanisms of 90° and 180° domain wall switching. The polarization vectors are observed to still occupy the minima of the four-well phase separation potential. The full alignment of the polarization vectors with the external field, that are orientations that do not coincide with preferred directions, can only be achieved at higher field levels. One should further notice that the distribution of the polarization gradient and the alignment of the polarization itself are fully periodic on the boundary of the microstructure. Inversion of the macroscopic electric loading yields a stepwise alignment of the polarization initiated by reaching a certain threshold value, see Figure 6.8d–f. Thus, in a first stage the piezoelectric material behaves purely elastic. Reaching the coercive threshold, the polarization starts to switch, Figure 6.8e, and ends up at a stage where the polarization is nearly aligned with the reversed external field, see Figure 6.8f. A further inversion of the macroscopic electric field yields to the same characteristic domain wall motions and thus again to a reorientation of the polarization vectors as shown in the sequence Figure 6.8g–i.

Macroscopic hysteresis curves. Having analyzed the poling process via domain wall motions in the multi-grain aggregate, we now proceed to compute estimates of the macroscopic electro-mechanical overall response of polycrystals. The resulting dielectric and butterfly hystereses are depicted in Figure 6.9. These curves clearly illustrate the dissipative character and time dependency of the poling process as predicted by the phase field model at the micro-level. The dielectric hysteresis curve Figure 6.9a represents the plot of the averaged polarization \bar{p}'_2 against the homogenized electric field \bar{e}'_2 . The butterfly hysteresis Figure 6.9b shows the volume average of the remanent strain $\bar{\epsilon}'_{22}$ defined later

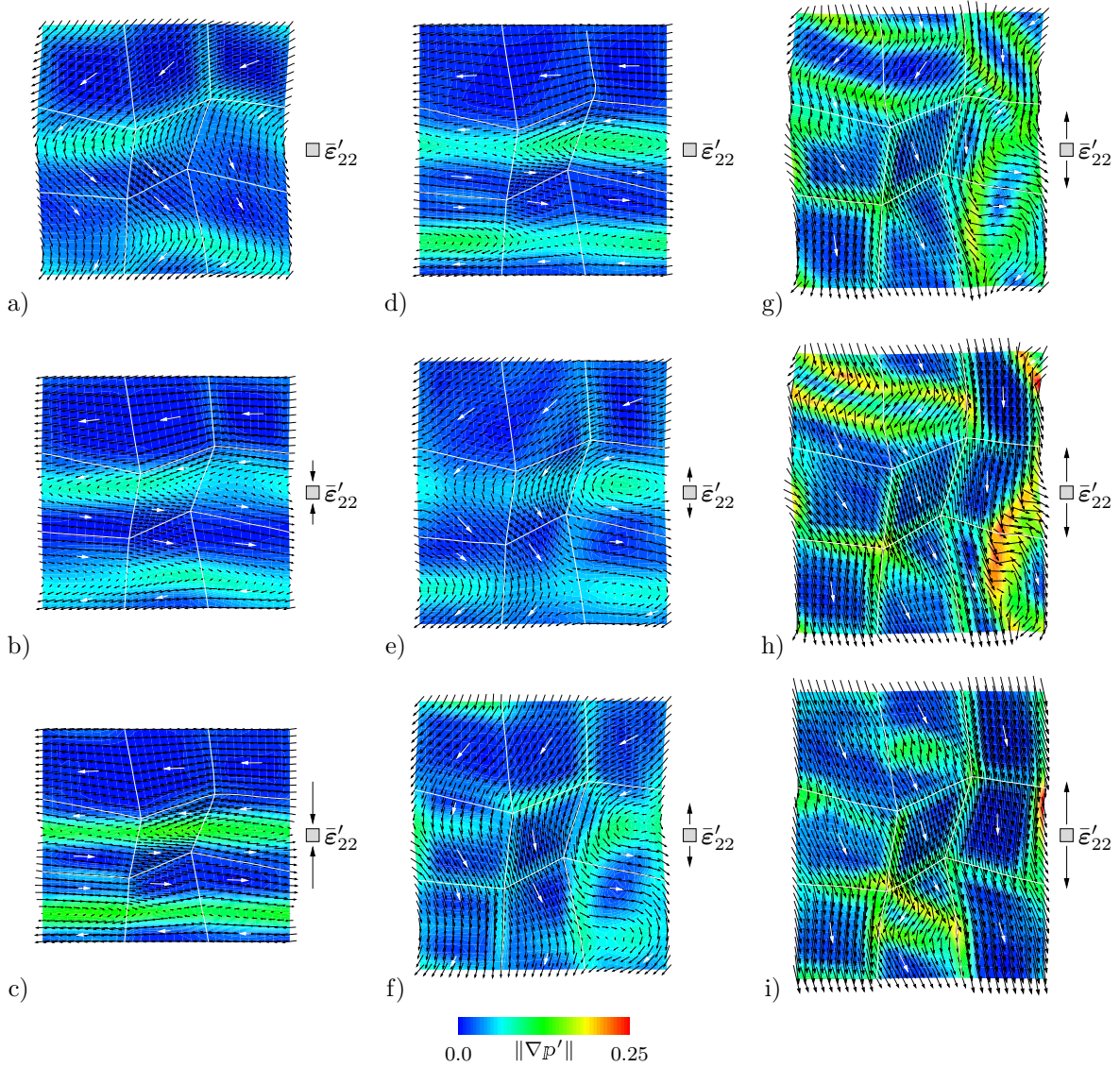


Figure 6.10: *Domain states of strain driven homogenization.* Periodic boundary conditions (fluctuation magnified) are utilized, the contour plots illustrate the norm of the polarization gradient $\|\nabla P'\|$, and poling directions in each grain are indicated by white arrows. The different snapshots are taken at time a) $t' = 0$, b) $t' = 50$, c) $t' = 100$, d) $t' = 200$, e) $t' = 235$, f) $t' = 250$, g) $t' = 265$, h) $t' = 280$, and i) $t' = 300$.

plotted against the average electric field. The poling states discussed earlier can be directly linked to the marked points in the hysteresis curves. After reaching the coercive field strength one can clearly observe the beginning of the switching process. The nearly alignment of the polarization in [Figure 6.9c](#) and [f](#) can be directly interpreted by a saturation of the microscopic polarization to the saturation value p_s and thus by a purely elastic behavior for increasing load.

Macroscopic strain driven loading. We consider now a purely mechanical loading of the polycrystalline aggregate by a macroscopic strain field according to the two loading patterns shown in [Figure 6.7c](#). Uniaxial compressive and tensile strains are applied in a sawtooth-like fashion.

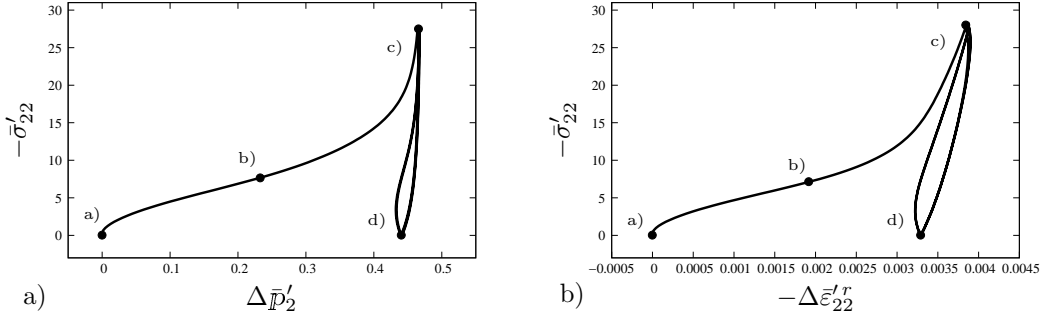


Figure 6.11: Ferroelastic hysteresis curves of strain driven homogenization. Plot of negative homogenized stress $-\bar{\sigma}'_{22}$ over a) change in average polarization $\Delta \bar{p}'_2$ and b) change in average remanent strain $\Delta \bar{\epsilon}'_{22}$ characterizing the phenomenon of mechanical depolarization. The curves are connected to the domain states in Figure 6.10 for three consecutive cycles of uniaxial compressive loading.

Domain wall motion. The domain wall motions caused by a macroscopic strain field are shown in Figure 6.10 on the deformed microstructure. The simulation starts from the equilibrium state. The loading is characterized by a compressive part followed by a tensile strain. For the uniaxial compressive strain under consideration, switching is initiated after passing a limit load such that the polarization orients in a direction perpendicular to the loading direction, see Figure 6.10b–c. Nevertheless, the polarization tries to align as closely as possible with the varying preferred or easy directions in each grain. Complete unloading, see Figure 6.10d, basically preserves the resulting domain structure. The subsequent uniaxial tensile loading again causes immense domain motions. According to the investigations of stress driven domain wall switching in Chapter 5, we realize a random reorientation of the polarization in the direction of the applied macroscopic tensile strain, see Figure 6.10e–i. For higher field levels, the polarization completely aligns with the tensile load, that is the polarization direction would overcome the minima of the four-well phase separation potential.

Macroscopic hysteresis curves. The ferroelastic hysteresis caused by three consecutive cycles of uniaxial compressive loading characterizes the phenomenon of *mechanical depolarization*. The plot of the relative change of macroscopic polarization $\Delta p' = p'_{in} - p'$ and homogenized remanent strain $\Delta \epsilon'^r = \epsilon'^r_{in} - \epsilon'^r$, respectively, over macroscopic compressive stress is shown in Figure 6.11. The initial states at the beginning of the depolarization process are denoted by p'_{in} and ϵ'^r_{in} . Here, we define the remanent strain based on the phenomenological ansatz $\epsilon'^r = \frac{3}{2} \varepsilon_s \frac{|p'|}{p_s} \text{dev}[\mathbf{a}' \otimes \mathbf{a}']$ as a deviatoric function of the polarization in terms of the polarization director $\mathbf{a}' := p'/|p'|$. As a consequence of an increasing compressive load, a gradual orientation of all longer c -axes close to a plane perpendicular to the mechanical stress takes place, see MOULSON & HERBERT [138]. Rather, the microscopic spontaneous polarization vectors of the unit cells become distributed randomly within or close to a plane perpendicular to the compressive load. This means that the material does no longer possess any resultant remanent polarization after being loaded by a compressive mechanical deformation of sufficient magnitude, which is why this process is called mechanical depolarization. Together with the remanent polarization, the macroscopic piezoelectric properties and, thereby, the most important features of a piezoceramic material are lost. The subsequent unloading of the microstructure causes only minor changes in the domain structure.

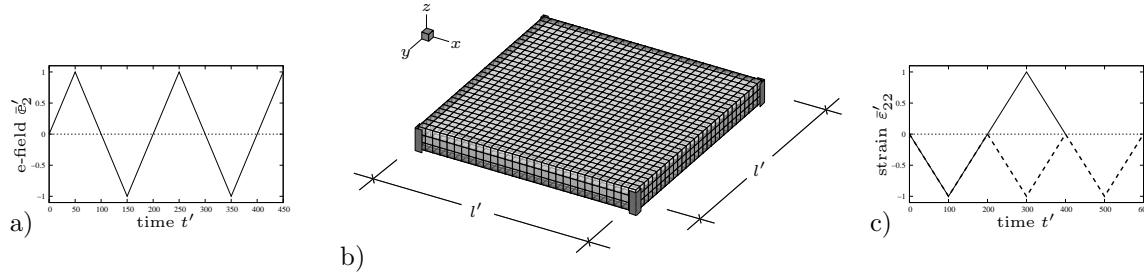


Figure 6.12: *Boundary-value-problem and loading curves.* Sawtooth-type loading for the a) electric and c) two mechanical loading processes. b) Thin single crystal representative volume element with normalized edge length $l' = 100$. On the corner nodes, the mechanical $\tilde{\mathbf{u}}' = \mathbf{0}$ and electric fluctuations $\tilde{\phi}' = 0$ are suppressed. The sample is discretized by $30 \times 30 \times 3$ eight node brick elements.

6.4.3. Three-dimensional homogenization of thin single crystal

We now extend the complexity by considering three-dimensional problems. Consider the homogenization of a thin single crystal with periodic boundary conditions in the x/z - and y/z -plane. Due to the thin specimen, no boundary conditions in z -direction are applied. The geometry is specified in Figure 6.12b. According to the applied periodic boundary conditions, the total displacement is fully prescribed at all corner nodes $\mathbf{u}_{cor} = \bar{\boldsymbol{\varepsilon}} \cdot \mathbf{x}_{cor}$, i.e. the fluctuations are suppressed. In analogy to the two-dimensional simulation, we consider sawtooth-type loading by a macroscopic electric field $\bar{\boldsymbol{\varepsilon}}'$ and a mechanical strain $\bar{\boldsymbol{\varepsilon}}'$, see Figure 6.12a and c. In a preprocessing step, an equilibrium state is determined for the microscopic polarization. This equilibrium state is then used as the starting configuration for the analysis of electric field and strain driven domain evolution.

Construction of an initial equilibrium state. First, the *relaxation process* of a random initial distribution of the microscopic polarization in a single domain sample with uniform lattice direction is carried out, Figure 6.13a. No macroscopic mechanical or electric loading is applied. The formation of the domains is fully governed by the evolution equation for the polarization field. The discretization is performed with a regular mesh consisting of $30 \times 30 \times 3$ hexahedral eight node elements. The single grain sample is subjected to *periodic boundary constraints* in the x/z - and y/z -plane for the mechanical and electric fluctuations, as well as the order parameter of the phase field model. Thus, in order to satisfy this constraint, one has to ensure that the initial random state of the microscopic polarization is periodic on the surface of the microstructure. The final stage shows the formation of a *laminate structure* of solely 90° walls, that is a stable twin-like structure with no further change with respect to time. It is also clear that the average polarization $\bar{\mathbf{p}} = \frac{1}{|\mathcal{B}|} \int_{\mathcal{B}} \mathbf{p} dV$ resulting from such a domain state is non-zero. The chosen boundary conditions and the periodic initialization of the order parameter on the surface of the microstructure ensure the evolution of a periodic microstructure.

Macroscopic electric field driven loading. Domain motions and homogenized hysteresis curves under a sawtooth-type macroscopic electric field are investigated. The maximum normalized field which is reached during the loading process depicted in Figure 6.12a is $e_2'^{max} = 1.0$ at a period of 200 time steps each cycle.

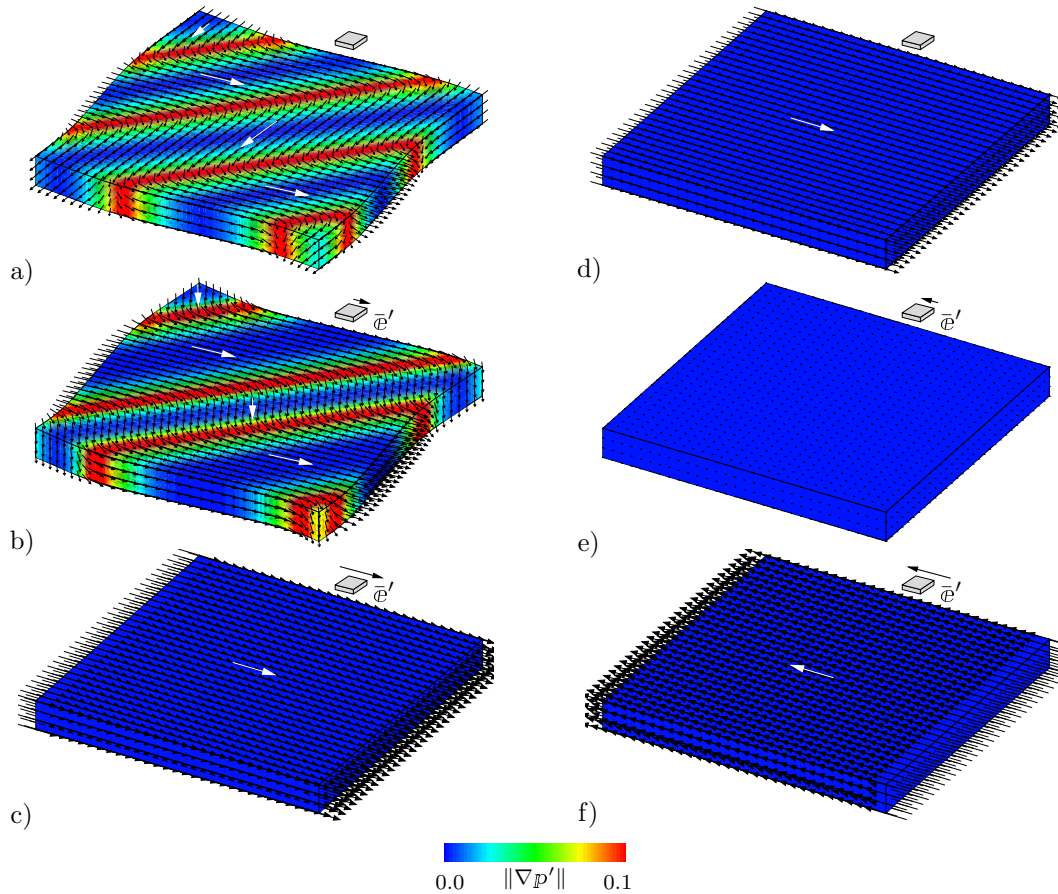


Figure 6.13: Domain states of electric field driven homogenization. Periodic boundary conditions (fluctuation magnified) are utilized, the contour plots show the norm of the polarization gradient $\|\nabla P'\|$, and poling directions in the thin single grain are indicated by white arrows. The different snapshots are at time a) $t' = 0$, b) $t' = 10$, c) $t' = 50$, d) $t' = 100$, e) $t' = 110$, and f) $t' = 150$.

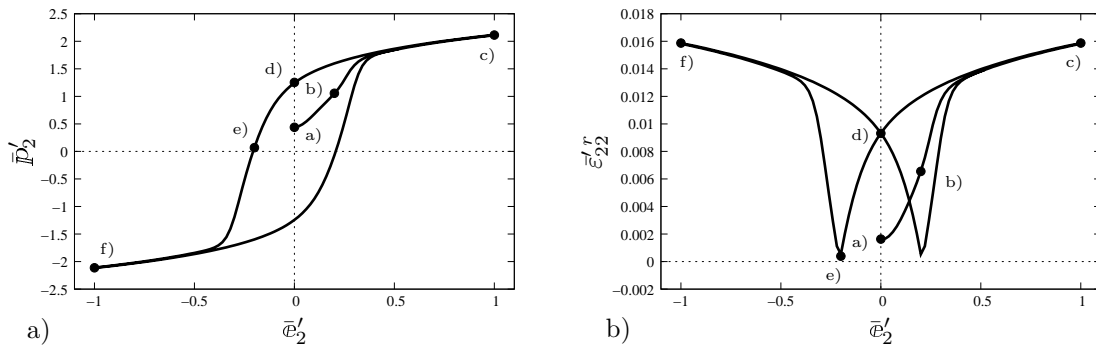


Figure 6.14: Ferroelectric hysteresis curves of electric field driven homogenization. a) Dielectric and b) butterfly hysteresis of thin single grain sample incorporating reference to domain states depicted in Figure 6.13.

Domain wall motion. Figure 6.13 shows six snapshots of domain changes caused by the applied macroscopic electric field. In the vicinity of the microstructure the applied macroscopic loading is shown. The linear increase of the electric field \bar{e}'_2 causes the laminate structure to vanish. The 90° domain walls dissolve completely for the maximum applied load, see Figure 6.13c. This results in a single domain structure where the polarization is completely aligned with the macro-field. The removal of the load and subsequent inver-

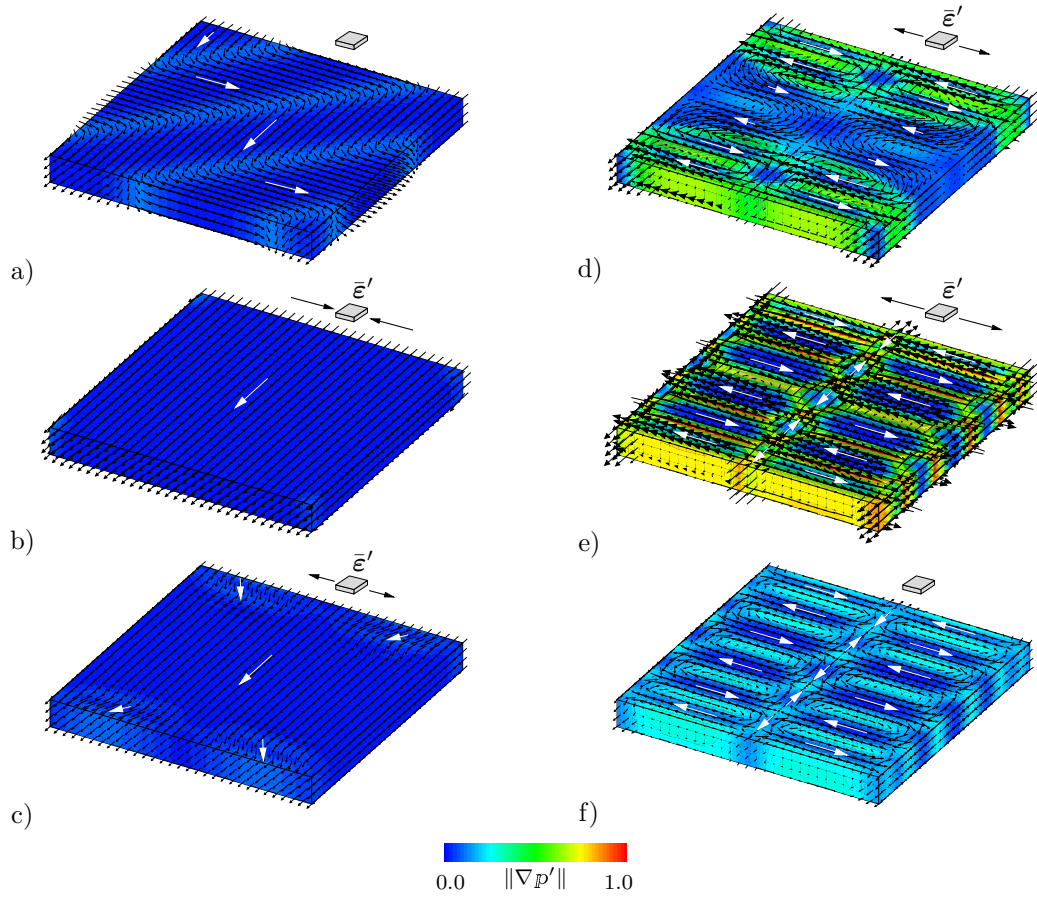


Figure 6.15: *Domain states for strain driven homogenization.* Periodic boundary conditions (fluctuation magnified) are utilized, the contour plots illustrate the norm of the polarization gradient $\|\nabla P'\|$, and poling directions in the thin single grain are indicated by white arrows. The different snapshots are at time a) $t' = 0$, b) $t' = 100$, c) $t' = 250$, d) $t' = 260$, e) $t' = 300$, and f) $t' = 400$.

sion is displayed in the remaining plots. [Figure 6.13e](#) shows the point where the single domain switches and aligns with the reversed direction of the electric field.

Macroscopic hysteresis curves. Each snapshot of the microstructure discussed previously is directly linked to a point in the macroscopic hysteresis curves shown in [Figure 6.14](#). The dielectric hysteresis as plot of macroscopic polarization over the applied electric field is recorded in [Figure 6.14a](#). It shows the typical shape, where switching of the polarization in the microstructure occurs after the coercive loading is achieved. For sufficiently strong fields a linear saturation behavior is observed and for small electric loading we rest in a linear application range. The plot of remanent strain over applied electric field is given by the so-called butterfly hysteresis curve, see [Figure 6.14b](#). Herein, the remanent strain is as previously defined a deviatoric function of the polarization. For more details about the derivation of the remanent strain see MIEHE & ROSATO [123].

Macroscopic strain driven loading. For the thin single grain specimen two macroscopic strain driven loadings with $\varepsilon_{22}^{\prime max} = 0.5$ as shown in [Figure 6.12c](#) are performed. Again, the domain wall motions and hysteresis phenomena are investigated.

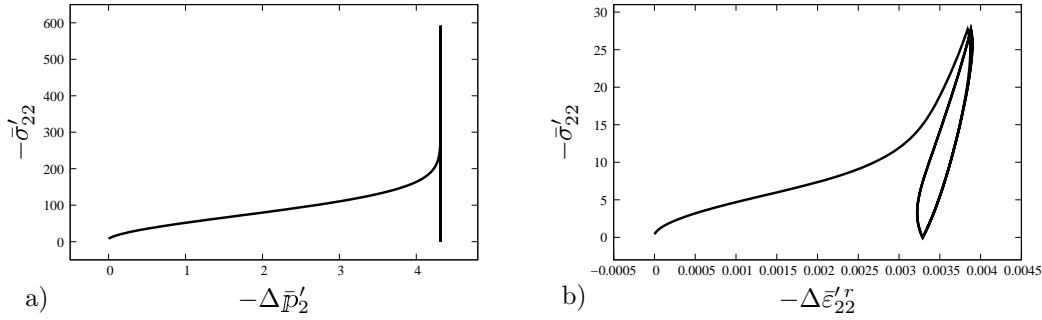


Figure 6.16: *Ferroelastic hysteresis curves of strain driven homogenization.* Plot of negative homogenized stress $-\bar{\sigma}'_{22}$ over a) change in average polarization $\Delta\bar{p}'_2$ and b) change in average remanent strain $\Delta\bar{\epsilon}'_{22}{}^r$ characterizing the phenomenon of mechanical depolarization for three consecutive cycles of uniaxial compressive loading.

Domain wall motion. The domain states are depicted in Figure 6.15 for different simulation states. For the initial compressive loading, the laminate structure vanishes and the microscopic polarization switches in the direction perpendicular to the applied macroscopic strain. After load removal and subsequent tensile loading, the formation of vortex-like domains is observed. The alignment in or against the direction of the tensile strain is preferred.

Macroscopic hysteresis curves. For the second loading history with three consecutive cycles of compressive loading, the hysteresis curves are shown in Figure 6.16. The left panel depicts the change in averaged polarization over the negative macroscopic stress. Due to the full alignment of the polarization perpendicular to the applied load, the specimen depolarizes completely. In contrast to the multi-grain sample, the additional compressive loading cycles do not cause any hysteresis phenomena for the depolarization plot Figure 6.16a. This is caused by the fact that in Figure 6.15b for the first maximum compressive load a complete alignment occurs perpendicular to the loading without polarization components in the direction of the load. Hence, we observe for the two consecutive compressive loading cycles no development and change of the polarization component in the direction of the applied strain, respectively. The right panel depicts the change in remanent strain $\Delta\bar{\epsilon}'_{22}{}^r$ over the negative macroscopic stress $\bar{\sigma}'_{22}$, where we observe the development of a small hysteresis.

— Part III —

**Modeling and Homogenization of
Electroactive Polymers at Large
Strains**

Multiplicative Electro-Elasticity of Electroactive Polymers Accounting for Micromechanically-Based Network Models

Electro-active polymers (EAPs) are materials with a polymer chain network microstructure, which exhibit coupled electro-mechanical behavior. EAP materials are divided into two main groups: electronic and ionic materials. In *electronic* EAPs, the activation is driven by Coulomb-type *electrostatic forces* between opposite charges (Maxwell stresses) which are created inside the dielectric as a result of an applied electric field. These materials allow fast response speeds, however, at the cost of high voltage. *Ionic* EAPs including gels and conductive polymers are actuated by electric field induced *diffusion of mobile ions* that causes a deformation. The recent developments with a particular focus on the constitutive modeling of electronic electroactive polymers DORFMANN & OGDEN [41], McMEEKING & LANDIS [113], VU & STEINMANN [196], ZHAO ET AL. [215], SUO ET AL. [176], PONTE CASTAÑEDA & SIBONI [151], THYLANDER ET AL. [186], JIMÉNEZ & McMEEKING [80], and ROSATO & MIEHE [156] will be particularly useful for our subsequent investigations. Recent numerical implementations of finite electro-mechanics combined with variational principles are proposed by VU ET AL. [197] and VU & STEINMANN [196] for non-dissipative as well as ROSATO & MIEHE [156] for dissipative material response.

This work focuses on the micro-mechanically based continuum modeling of electronic EAPs. These materials can further be subdivided into *dielectric elastomers*, which are activated by Coulomb forces, *ferroelectric polymers*, which exhibit spontaneous polarization and show piezoelectricity when poled and electrostriction in a non-poled phase, as well as *electrostrictive graft elastomers*, where the activation is caused by molecular alignment. All these materials have as a basic ingredient of their microstructure at least a fraction of an amorphous network consisting of cross-linked polymer chains similar to natural or synthetic rubbers. This network has an important effect on the electro-mechanical overall response, in particular, when the material undergoes large strains. There is a substantial body of literature for the construction of highly predictive micromechanically motivated models in the pure mechanical context such as the three chain model proposed by JAMES & GUTH [77], the eight chain model suggested by ARRUDA & BOYCE [2], as

well as the affine full network models considered in TRELOAR [191], TRELOAR & RIDING [193], and WU & VAN DER GIESSEN [206]. A further improvement provides the non-affine microsphere model proposed in MIEHE ET AL. [129], which allows a flexible modeling of the locking stretches in multi-dimensional deformations. A second ingredient to be incorporated in the modeling of EAPs are micromechanical assumptions for a *deformation-dependent electric permittivity*. For stretches well below the extension limit of the polymer chains and small degree of cross-linking, a polymer network is assumed to polarize as freely as a polymeric liquid and the permittivity is unaffected by the deformation. However, with increasing stretch the chains align and their mobility decreases. This effect hinders the orientation of molecules in an electric field and therefore reduces the electric permittivity. This dependence of the electric permittivity of matter on the stretch of the material was experimentally shown by KOFOD ET AL. [86] and WISSLER & MAZZA [205], among others. While isotropic in the undeformed state, an *anisotropy* is observed during deformation. For large deformations, stresses resulting from a varying permittivity differ considerably from the simple constant approach that is widely used in literature, see ZHAO & SUO [214]. The fundamental work of KUHN & GRÜN [98] uses statistical mechanics of freely jointed chain molecules to obtain a relation between the microscopic polarization of the polymer chains and the macroscopic birefringence. As suggested recently in JIMÉNEZ & MCMEECKING [80], this concept can directly be transferred to the electric permittivity which then becomes a function of the macroscopic deformation.

Goal of this paper is to outline a general constitutive model structure for EAPs that is open for a modular inclusion of micromechanical ingredients. In particular, the incorporation of the highly predictive *homogenization method* over the chain orientations space suggested in MIEHE ET AL. [129] is of interest. Conceptually, this is achieved by assuming a split of the energy function into an *elastic contribution* and an *electrostatic part*. The first part will be designed to include the *mechanical network model*, while the second part covers the *deformation-dependent electric permittivity*. A key aspect of this work is a modeling of the elastic contribution based on three alternative kinematic assumptions for the *macroscopic network deformation*

$$\Psi_{elas}(\mathbf{F}, \mathbf{E}) = \Psi_{net}(\mathbf{F}_{net}) \quad \text{with} \quad \mathbf{F}_{net} \in \{\mathbf{F}, \mathbf{F}\boldsymbol{\mathcal{E}}, \boldsymbol{\mathcal{E}}\mathbf{F}\} \quad (7.1)$$

which include the *multiplicative decomposition* of the deformation gradient into stress-free and stress-producing parts. The above ansatz allows for the incorporation of energy functions Ψ_{net} associated with complex mechanical network models *without any change*, see the recent work ZÄH & MIEHE [208] for more detail. The first approach $\mathbf{F}_{net} = \mathbf{F}$ is appropriate for *elastomers* with an ideal microstructure consisting of cross-linked polymer chains. The second and third kinematic assumptions are suitable for more complex microstructures, such as that of graft elastomers discussed in Chapter 2. Here, crystalline phases in the form of *particles with inherent dipoles* are embedded into an amorphous polymer network matrix. For an applied electric field, an electrically induced deformation of the composite microstructure occurs *solely due to the dipoles of the particles*. For small volume fractions and random placements of the embedded particles, this electrically induced deformation can be assumed to leave the random nature of the cross-linked polymer network structure unaltered. Hence, its behavior can be assumed to remain isotropic and governed by the network models reviewed above. Furthermore, the electrically induced deformation of the microstructure due to the dipoles in the particles can be assumed to

be *stress-free*. As a consequence, the stored elastic energy of the network cannot depend on the total deformation, but must be in addition a function of the electric field that drives the particle deformation. In order to achieve this, a key ingredient of our proposed framework is to define *separate constitutive functions* for a stress-free electrically induced stretch of the microstructure. Multiplicative splits into stress-free and stress-producing partial deformations do not commute for general non-coaxial deformation modes. Recall in this context the Kröner-Lee decomposition, rooted in the works KRÖNER [95] and LEE [104], which assumes first a stress-free deformation followed by a stress-producing deformation. This ansatz is well motivated when relating the plastic deformation solely to the micromechanical dislocation flow through an ideal lattice. The reverse setting, originally proposed by CLIFTON [33], lacks this micromechanical motivation and is commonly considered to be not appropriate for plasticity theory. Inspired by plasticity theory, a Lee-type multiplicative decomposition has already been applied to electro-mechanics by ROSATO & MIEHE [155, 156] and SKATULLA ET AL. [167]. We outline in this paper a unified modeling framework for EAPs that accounts for both types of multiplicative kinematics. The right (Lee-type) decomposition $\mathbf{F}_{net} = \mathbf{F}\mathbf{E}$ is based on a constitutive dependence of \mathbf{E} on the *Lagrangian electric field*. In contrast, the left (Clifton-type) decomposition $\mathbf{F}_{net} = \mathbf{E}\mathbf{F}$ assumes a dependence of \mathbf{E} on the *Eulerian (true) electric field*. In both cases, the electrically induced deformation is assumed to be *rotation-free*, representing material or spatial stretch tensors.

This chapter is organized as follows. [Section 7.1](#) summarizes general equations of finite electro-elasticity in a variational format, accounting for geometric settings in both the Lagrangian as well as the Eulerian configuration. This also includes a compact outline of potential-based finite element implementations. [Section 7.2](#) develops the modular framework for the alternative incorporation of polymer network models. This covers all details of the modeling, including the set up of coupled electro-mechanical tangent moduli. [Section 7.3](#) reviews micromechanical based network kernels, which can be included into the proposed modeling framework. Finally, [Section 7.4](#) reports on numerical simulations, which demonstrate the modeling capability of the proposed framework.

7.1. General equations of finite electro-elasticity

The primary fields and their gradients are already introduced in Part I dealing with fundamentals of mechanics and electrostatics, that is, the deformation map and electric potential. The gradients of these two fields are denoted as the deformation gradient and the Lagrangian electric field.

7.1.1. The variational principle and its Euler equations

The global equations of finite electro-elasticity can be derived from a variational principle. We focus exclusively on a constitutive description of electro-mechanics in terms of the electric enthalpy. Consider as a variational potential the electro-elastic enthalpy stored in the solid domain minus the external loading contributions

$$\Pi(\boldsymbol{\varphi}, \phi) := \int_B \Psi(\mathbf{F}, \mathbb{E}; \mathbf{X}) dV - \Pi_{ext}(\boldsymbol{\varphi}, \phi), \quad (7.2)$$

determined by the *enthalpy density function* Ψ that contains superimposed contributions from the solid matter embedded into the free space and the external part

$$\Pi_{ext}(\boldsymbol{\varphi}, \phi) = \int_{\mathcal{B}} \boldsymbol{\varphi} \cdot \varrho_0 \boldsymbol{\Gamma}^m dV + \int_{\partial \mathcal{B}_t} \boldsymbol{\varphi} \cdot \mathbf{T} dA - \int_{\mathcal{B}} \phi \rho_0^e dV - \int_{\partial \mathcal{B}_d} \phi \Sigma_f^e dA. \quad (7.3)$$

The constitutive enthalpy function is derived from an electro-elastic *stored energy function* Ψ' by a partial Legendre transformation with respect to the electric slot $\Psi(\mathbf{F}, \mathbb{E}; \mathbf{X}) = \inf_{\mathcal{D}} [\Psi'(\mathbf{F}, \mathcal{D}; \mathbf{X}) - \mathbb{E} \cdot \mathcal{D}]$. The canonical energy function Ψ' is weakly convex with respect to \mathbf{F} and \mathcal{D} . As a consequence, the enthalpy function Ψ is *weakly convex* with respect to \mathbf{F} but *concave* with respect to \mathbb{E} . With regard to the set up of specific enthalpy functions, we assume that an *extended* enthalpy function Ψ_{ext}

$$\Psi(\mathbf{F}, \mathbb{E}; \mathbf{X}) = \Psi_{ext}(\mathbf{F}, \text{cof}[\mathbf{F}], \det[\mathbf{F}], \mathbb{E}; \mathbf{X}) \quad (7.4)$$

is *convex* with respect to \mathbf{F} , $\text{cof}[\mathbf{F}]$, and $\det[\mathbf{F}]$, that is *polyconvex* with respect to \mathbf{F} in the sense of BALL [6], and *concave* with respect to \mathbb{E} . We consider this a suitable condition for the modeling of a stable electro-elastic material response. Furthermore, the enthalpy function Ψ must be *objective*, that is invariant with respect to rigid body motions $\boldsymbol{\varphi}^+ = \mathbf{Q}(t)\boldsymbol{\varphi} + \mathbf{c}(t)$ superimposed onto the current configuration. This is a priori satisfied by the *reduced form*

$$\Psi(\mathbf{F}, \mathbb{E}; \mathbf{X}) = \check{\Psi}(\mathbf{F}^T \mathbf{g} \mathbf{F}, \mathbf{F}^T \mathbf{e}; \mathbf{X}) = \check{\Psi}(\mathbf{g}, \mathbf{e}; \mathbf{F}, \mathbf{X}) \quad (7.5)$$

that depends on the right Cauchy-Green tensor $\mathbf{C} := \mathbf{F}^T \mathbf{g} \mathbf{F}$. The function $\check{\Psi}$ emphasizes the dependence of the enthalpy function on the Eulerian standard metric \mathbf{g} and the spatial electric field \mathbf{e} . This functional dependence is exploited within the subsequent *spatial geometric setting* of electro-elasticity, that is advantageous with regard to the numerical treatment due to its sparse structure based on symmetric incremental deformation tensors. With the potential Π defined in (7.2) at hand, the coupled boundary-value-problem of finite electro-elastostatics is governed by the variational principle

$$\boxed{\{\boldsymbol{\varphi}, \phi\} = \arg \left\{ \inf_{\boldsymbol{\varphi}} \sup_{\phi} \Pi(\boldsymbol{\varphi}, \phi) \right\}} \quad (7.6)$$

subject to Dirichlet-type boundary conditions $\boldsymbol{\varphi} = \boldsymbol{\varphi}_0$ on $\partial \mathcal{B}_{\boldsymbol{\varphi}}$ and $\phi = \phi_0$ on $\partial \mathcal{B}_{\phi}$. Here, the boundary $\partial \mathcal{B}$ of the solid is decomposed into $\partial \mathcal{B} = \partial \mathcal{B}_{\boldsymbol{\varphi}} \cup \partial \mathcal{B}_t = \partial \mathcal{B}_{\boldsymbol{\varphi}} \cup \partial \mathcal{B}_d$ with $\partial \mathcal{B}_{\boldsymbol{\varphi}} \cap \partial \mathcal{B}_t = \partial \mathcal{B}_{\boldsymbol{\varphi}} \cap \partial \mathcal{B}_d = \emptyset$.

Variation in material setting. Introducing fields of *virtual* deformation $\delta \boldsymbol{\varphi}$ and electric potential $\delta \phi$ satisfying $\delta \boldsymbol{\varphi} = \mathbf{0}$ on $\partial \mathcal{B}_{\boldsymbol{\varphi}}$ and $\delta \phi = 0$ on $\partial \mathcal{B}_{\phi}$, the necessary condition of the saddle point principle (7.6) reads

$$\delta \Pi = \int_{\mathcal{B}} \begin{bmatrix} \nabla \delta \boldsymbol{\varphi} \\ -\nabla \delta \phi \end{bmatrix} \cdot \begin{bmatrix} \partial_{\mathbf{F}} \Psi \\ \partial_{\mathbb{E}} \Psi \end{bmatrix} dV - \int_{\mathcal{B}} \begin{bmatrix} \delta \boldsymbol{\varphi} \\ -\delta \phi \end{bmatrix} \cdot \begin{bmatrix} \varrho_0 \boldsymbol{\Gamma}^m \\ \rho_0^e \end{bmatrix} dV - \int_{\partial \mathcal{B}} \begin{bmatrix} \delta \boldsymbol{\varphi} \\ -\delta \phi \end{bmatrix} \cdot \begin{bmatrix} \mathbf{T} \\ \Sigma_f^e \end{bmatrix} dA = 0 \quad (7.7)$$

in terms of the material constitutive expressions

$$\mathbf{P} := \partial_{\mathbf{F}} \Psi(\mathbf{F}, \mathbb{E}; \mathbf{X}) \quad \text{and} \quad \mathbb{D} := -\partial_{\mathbb{E}} \Psi(\mathbf{F}, \mathbb{E}; \mathbf{X}) \quad (7.8)$$

for the nominal stress tensor \mathbf{P} and the material electric displacement vector \mathbb{D} . Applying the Gauss theorem gives the two material field equations

$$\text{Div}[\mathbf{P}] + \varrho_0 \mathbf{\Gamma}^m = \mathbf{0} \text{ in } \mathcal{B} \quad \text{and} \quad \text{Div}[\mathbb{D}] = \rho_0^e \text{ in } \mathcal{B} \quad (7.9)$$

as the Euler equation of the variational principle (7.6). This is the static equilibrium condition on the mechanical side and the Gauss law on the electric side. Furthermore, we obtain from (7.7) the Neumann-type boundary conditions $\mathbf{P} \cdot \mathbf{N} = \mathbf{T}$ on $\partial\mathcal{B}_t$ and $\mathbb{D} \cdot \mathbf{N} = -\Sigma_f^e$ on $\partial\mathcal{B}_d$, where \mathbf{N} is the outward normal on $\partial\mathcal{B}$.

Linearization in material setting. The numerical treatment of the nonlinear problem (7.7) of finite electro-elasticity, e.g. by Newton-type iterative solvers, is based on the *linearization* of (7.7) at a given electro-mechanical state $\{\boldsymbol{\varphi}, \phi\}$, that is

$$\text{Lin}[\delta\Pi] := \delta\Pi(\delta\boldsymbol{\varphi}, \delta\phi; \boldsymbol{\varphi}, \phi) + \Delta[\delta\Pi](\delta\boldsymbol{\varphi}, \delta\phi, \Delta\boldsymbol{\varphi}, \Delta\phi; \boldsymbol{\varphi}, \phi) = 0. \quad (7.10)$$

It is solved for the *incremental* deformation $\Delta\boldsymbol{\varphi}$ and electric potential $\Delta\phi$, satisfying $\Delta\boldsymbol{\varphi} = \mathbf{0}$ on $\partial\mathcal{B}_\varphi$ and $\Delta\phi = 0$ on $\partial\mathcal{B}_\phi$. For dead external loads, the linear increment of the first variation takes the form

$$\Delta[\delta\Pi] = \int_{\mathcal{B}} \begin{bmatrix} \nabla\delta\boldsymbol{\varphi} \\ -\nabla\delta\phi \end{bmatrix} \cdot \begin{bmatrix} \partial_{\mathbf{F}\mathbf{F}}^2\Psi & \partial_{\mathbf{F}\mathbb{E}}^2\Psi \\ \partial_{\mathbb{E}\mathbf{F}}^2\Psi & \partial_{\mathbb{E}\mathbb{E}}^2\Psi \end{bmatrix} \cdot \begin{bmatrix} \nabla\Delta\boldsymbol{\varphi} \\ -\nabla\Delta\phi \end{bmatrix} dV \quad (7.11)$$

in terms of the material moduli

$$\mathbb{A} := \partial_{\mathbf{F}\mathbf{F}}^2\Psi(\mathbf{F}, \mathbb{E}; \mathbf{X}), \quad \mathbb{H} := \partial_{\mathbf{F}\mathbb{E}}^2\Psi(\mathbf{F}, \mathbb{E}; \mathbf{X}), \quad \mathbb{K} := \partial_{\mathbb{E}\mathbb{E}}^2\Psi(\mathbf{F}, \mathbb{E}; \mathbf{X}). \quad (7.12)$$

Note that these moduli govern the constitutive expressions of the *rates* of the nominal stresses and the material electric displacement

$$\begin{bmatrix} \dot{\mathbf{P}} \\ -\dot{\mathbb{D}} \end{bmatrix} = \begin{bmatrix} \mathbb{A} & \mathbb{H} \\ \mathbb{H}^T & \mathbb{K} \end{bmatrix} \cdot \begin{bmatrix} \dot{\mathbf{F}} \\ \dot{\mathbb{E}} \end{bmatrix}. \quad (7.13)$$

Variation in spatial setting. Using the relationship $\nabla(\cdot) = \nabla_{\mathbf{x}}(\cdot)\mathbf{F}$, characterizing a chain-rule operation, the necessary condition (7.7) can be recast for pure Dirichlet problems into the spatial form

$$\delta\Pi = \int_{\mathcal{B}} \begin{bmatrix} (\mathbf{g}\nabla_{\mathbf{x}}\delta\boldsymbol{\varphi})_s \\ -\nabla_{\mathbf{x}}\delta\phi \end{bmatrix} \cdot \begin{bmatrix} 2\partial_{\mathbf{g}}\tilde{\Psi} \\ \partial_{\mathbf{e}}\tilde{\Psi} \end{bmatrix} dV = 0 \quad (7.14)$$

in terms of the spatial constitutive expressions

$$\boldsymbol{\tau} = 2\partial_{\mathbf{g}}\tilde{\Psi}(\mathbf{g}, \mathbf{e}; \mathbf{F}, \mathbf{X}) \quad \text{and} \quad \tilde{\mathbf{d}} = -\partial_{\mathbf{e}}\tilde{\Psi}(\mathbf{g}, \mathbf{e}; \mathbf{F}, \mathbf{X}) \quad (7.15)$$

for the Kirchhoff stress $\boldsymbol{\tau}$ and the Kirchhoff-type electric displacement $\tilde{\mathbf{d}}$. For the sake of simplicity, external loading contributions are neglected. Here, $(\mathbf{g}\nabla_{\mathbf{x}}\delta\boldsymbol{\varphi})_s := \frac{1}{2}[(\mathbf{g}\nabla_{\mathbf{x}}\delta\boldsymbol{\varphi}) + (\mathbf{g}\nabla_{\mathbf{x}}\delta\boldsymbol{\varphi})^T]$ denotes the *symmetrized spatial gradient* of the virtual deformation $\delta\boldsymbol{\varphi}$. Applying the Gauss theorem gives the two spatial field equations

$$\text{div}[\boldsymbol{\tau}/J] = \mathbf{0} \text{ in } \varphi_t(\mathcal{B}) \quad \text{and} \quad \text{div}[\tilde{\mathbf{d}}/J] = 0 \text{ in } \varphi_t(\mathcal{B}) \quad (7.16)$$

as the Euler equations of the variational principle (7.6). This is the static equilibrium condition in terms of the *true* Cauchy stress $\boldsymbol{\sigma} := \boldsymbol{\tau}/J$ on the mechanical side and Gauss's law in terms of the *true* electric displacement $\mathbf{d} := \tilde{\mathbf{d}}/J$ on the electric side. In addition, we obtain from (7.14) due to the absence of loading terms the zero Neumann-type conditions $\boldsymbol{\sigma} \cdot \mathbf{n} = \mathbf{0}$ on $\varphi(\partial\mathcal{B}_t)$ and $\mathbf{d} \cdot \mathbf{n} = 0$ on $\varphi(\partial\mathcal{B}_d)$, where \mathbf{n} is the outward normal on the deformed surface $\varphi(\partial\mathcal{B})$.

Linearization in spatial setting. The spatial representation of the linearization (7.10) is obtained by replacing in the linear increment (7.11) material by spatial gradients via $\nabla(\cdot) = \nabla_x(\cdot)\mathbf{F}$, yielding

$$\Delta[\delta\Pi] = \int_{\mathcal{B}} \begin{bmatrix} \mathbf{g}\nabla_x\delta\varphi \\ -\nabla_x\delta\phi \end{bmatrix} \cdot \begin{bmatrix} \mathbf{a} & \mathbf{h} \\ \mathbf{h}^T & \mathbf{k} \end{bmatrix} \cdot \begin{bmatrix} \mathbf{g}\nabla_x\Delta\varphi \\ -\nabla_x\Delta\phi \end{bmatrix} dV \quad (7.17)$$

in terms of constitutive expressions for the spatial moduli

$$\mathbf{c} := 4\partial_{\mathbf{g}\mathbf{g}}^2\tilde{\Psi}(\mathbf{g}, \mathbf{e}; \mathbf{F}, \mathbf{X}), \quad \mathbf{h} := 2\partial_{\mathbf{g}\mathbf{e}}^2\tilde{\Psi}(\mathbf{g}, \mathbf{e}; \mathbf{F}, \mathbf{X}), \quad \mathbf{k} := \partial_{\mathbf{e}\mathbf{e}}^2\tilde{\Psi}(\mathbf{g}, \mathbf{e}; \mathbf{F}, \mathbf{X}), \quad (7.18)$$

where the mechanical moduli \mathbf{a} decomposes into *symmetric* material tangent and geometric stress terms

$$\mathbf{a} := \mathbf{c} + \mathbf{g}^{-1} \odot \boldsymbol{\tau} \quad \text{with} \quad \mathbf{a}^{abcd} := \mathbf{c}^{abcd} + \delta^{ac}\tau^{bd}. \quad (7.19)$$

Note that the moduli (7.18) govern the Lie derivatives (Oldroyd rates) of the *symmetric* Kirchhoff stress and the Kirchhoff-type electric displacement ¹

$$\begin{bmatrix} \mathcal{L}_v\boldsymbol{\tau} \\ -\mathcal{L}_v\tilde{\mathbf{d}} \end{bmatrix} = \begin{bmatrix} \mathbf{c} & \mathbf{h} \\ \mathbf{h}^T & \mathbf{k} \end{bmatrix} \cdot \begin{bmatrix} \frac{1}{2}\mathcal{L}_v\mathbf{g} \\ \mathcal{L}_v\mathbf{e} \end{bmatrix}. \quad (7.20)$$

The insertion of (7.19) into (7.17) allows the representation of the linear increment

$$\Delta[\delta\Pi] = \int_{\mathcal{B}} \begin{bmatrix} (\mathbf{g}\nabla_x\delta\varphi)_s \\ -\nabla_x\delta\phi \end{bmatrix} \cdot \begin{bmatrix} \mathbf{c} & \mathbf{h} \\ \mathbf{h}^T & \mathbf{k} \end{bmatrix} \cdot \begin{bmatrix} (\mathbf{g}\nabla_x\Delta\varphi)_s \\ -\nabla_x\Delta\phi \end{bmatrix} + \text{tr} [(\mathbf{g}\nabla_x\delta\varphi)\boldsymbol{\tau}(\nabla_x\Delta\varphi)^T] dV \quad (7.21)$$

in terms of the symmetrized spatial gradients $(\mathbf{g}\nabla_x\delta\varphi)_s$ and $(\mathbf{g}\nabla_x\Delta\varphi)_s$. Hence, when comparing the material and spatial representations (7.7) with (7.14) and (7.11) with (7.21), the *advantage of the spatial representations* (7.14) and (7.21) are obvious: First, they are formulated in terms of symmetric gradients of the virtual and incremental deformations allowing a reduced data implementation. Secondly, the spatial representations are sparse due to the diagonal form of the current metric $\mathbf{g} = \delta_{ab}$, in contrast to its material counterpart $\mathbf{C} := \mathbf{F}^T\mathbf{g}\mathbf{F}$ that is fully populated.

7.1.2. Finite element implementation of coupled problem

The spatial discretization of the coupled problem by a finite element method is considered. Let \mathfrak{T}^h denote a finite element triangulation of the domain \mathcal{B} . The index h indicates a typical mesh size based on E^h finite element domains $\mathcal{B}_e^h \in \mathfrak{T}^h$ and N^h global nodes. Here $d \in [2, 3]$ is the dimension of the problem.

FEM discretization of material setting. The constitutive state variables for the coupled two-field electro-mechanical problem are summarized in a generalized gradient field $\mathbf{F} := \{\nabla\varphi, -\nabla\phi\}$. Explicitly, we get the discrete global gradient

$$\mathbf{F} \approx \underline{\mathbf{F}}^h = \underline{\mathbf{B}}(\mathbf{X})\mathbf{d} \quad (7.22)$$

¹*Definition of Lie derivatives.* Lie derivatives of spatial objects are defined in [Subsection 3.1.4](#). This defines objective rates for the Kirchhoff stress $\mathcal{L}_v\boldsymbol{\tau} := \dot{\boldsymbol{\tau}} - \mathbf{l}\boldsymbol{\tau} - \boldsymbol{\tau}\mathbf{l}^T$ and the Kirchhoff-type electric displacement $\mathcal{L}_v\tilde{\mathbf{d}} := \dot{\tilde{\mathbf{d}}} - \mathbf{l}\tilde{\mathbf{d}}$ as well as for deformation rate $\mathcal{L}_v\mathbf{g} := \dot{\mathbf{g}}\mathbf{l} + \mathbf{l}^T\mathbf{g}$ and electric field $\mathcal{L}_v\mathbf{e} := \dot{\mathbf{e}} + \mathbf{l}^T\mathbf{e}$, where $\mathbf{l} := \dot{\mathbf{F}}\mathbf{F}^{-1}$ is the spatial velocity gradient.

that are the first and second derivatives of the enthalpy density function Ψ by the discretized spatial constitutive state vector \mathbf{f}^h . The geometric tangent matrix on element level can be computed as

$$\mathbf{g}_e^{d(I-1)+i,d(J-1)+i} = \int_{\mathcal{B}_e^h} (N_{,\mathbf{x}})_j^I \tau_{jk} (N_{,\mathbf{x}})_k^J dV \quad (7.37)$$

in terms of element nodes (I, J) and $i = 1, d$.

7.2. Constitutive modeling of multiplicative electro-elasticity

This section develops specific constitutive expressions for the electro-mechanical enthalpy function Ψ in dielectric elastomers, which are rooted in the micromechanics of polymer networks. The key concept is to develop representations of this function, that includes in a modular format a *mechanical network kernel*. This kernel is designed such that statistically-based free energies for polymer networks, such as outlined in TRELOAR [192], FLORY [47], ARRUDA & BOYCE [2], BOYCE & ARRUDA [23], and MIEHE ET AL. [129], are included without any change. In order to achieve this, novel structures of the enthalpy function are investigated. This covers in particular the alternative *multiplicative decomposition* of the deformation gradient into electrically-induced deformation and stress-producing parts. A general structure that includes three alternative approaches to the incorporation of the network kernels is developed and a closed-form representation for the stress and electric displacement is outlined.

7.2.1. Ingredient 1: Additive split of energy-enthalpy density

The additive decomposition of the total enthalpy function per unit volume of the reference configuration into an *elastic part* and an *electrostatic part* is assumed as

$$\Psi(\mathbf{F}, \mathbb{E}) = \Psi_{elas}(\mathbf{F}, \mathbb{E}) + \Psi_{elec}(\mathbf{F}, \mathbb{E}) \quad (7.38)$$

The first part Ψ_{elas} includes contributions due to the network deformation, which we root in micromechanically-based theories of statistical mechanics of polymers. For *multiplicative electro-mechanics* considered below, Ψ_{elas} depends on the electric field and includes an electrostatic contribution. Ψ_{elec} covers deformation-dependent contributions, including effects of the free space where the body is embedded in. For convenience, we drop in what follows the dependence of the constitutive functions on the position $\mathbf{X} \in \mathcal{B}$ and focus on *homogeneous* materials.

7.2.2. Ingredient 2: Volumetric-isochoric split of local deformation

Electroactive elastomers are weakly compressible as rubber-like materials. They undergo nearly incompressible elastic deformations. We account for this aspect by applying a penalty method that ensures approximately the incompressibility constraint $J = 1$. In the constitutive modeling, we account for this aspect by a multiplicative split of the deformation map \mathbf{F} , defining its *isochoric* and *volumetric part*

$$\bar{\mathbf{F}} := J^{-1/3} \mathbf{F} \quad \text{and} \quad J := \det[\mathbf{F}]. \quad (7.39)$$

As a consequence, the *elastic contribution* to the enthalpy function is assumed to decompose

$$\boxed{\Psi_{elas}(\mathbf{F}, \mathbb{E}) = U(J) + \bar{\Psi}_{elas}(\bar{\mathbf{F}}, \mathbb{E})} \quad (7.40)$$

into a volumetric contribution and an isochoric part, that includes an electrostatic expansion as considered below. The volumetric contribution U is considered as a penalty function which approximately enforces the incompressibility constraint. The above additive split induces a decomposition of the stress into spherical and deviatoric parts, where only the latter is considered to be of physical relevance.

7.2.3. Ingredient 3: Local electrically-induced deformation

The subsequent constructions of the elastic energy storage function $\bar{\Psi}_{elas}$ use as an input a constitutively defined, local homogeneous electrostrictive deformation $\bar{\mathbf{E}}(\mathbf{x})$ depending on the material or spatial electric field $\mathbf{x} := \{\mathbb{E}, \mathbf{e}\}$, respectively. This deformation is assumed to be a *volume-preserving spatial* or *material stretch tensor*, that is a priori constitutively defined based on experimental investigations. A simple example construction is as follows. Consider the stretch tensor

$$\mathbf{E}^{-1}(\mathbf{x}) := \begin{cases} \mathbf{1} - f \mathbf{n} \otimes \mathbf{n} & , \text{ for } |\mathbf{x}| \neq 0 \\ \mathbf{1} & , \text{ otherwise} \end{cases} \quad (7.41)$$

with $\mathbf{n} := \mathbf{x}/|\mathbf{x}|$, which describes an electrostrictive deformation aligned to the director \mathbf{n} . The determinant of this tensor is $D := \det[\mathbf{E}^{-1}] = 1 - f > 0$. The most simple assumption for the amount of electrically-induced stretching is

$$f = \hat{f}(|\mathbf{x}|) = c|\mathbf{x}|^2 < 1 \quad (7.42)$$

in terms of just one material parameter c . Note carefully that this simple choice can only be applied for electric fields strengths $|\mathbf{x}| < 1/\sqrt{c}$. We emphasize that this simple linear ansatz is only a model problem for possibly more complex constitutive functions \hat{f} , that can be fitted to experimental observations. Note that the above deformation \mathbf{E}^{-1} does not preserve the volume of the polymer network. The desired *isochoric stretch mode* is governed by the multiplicative definition $\bar{\mathbf{E}}^{-1} := D^{-1/3} \mathbf{E}^{-1}$. Taking into account the inverse of the sum of two square matrices, MILLER [135], we obtain a closed-form constitutive assumption for the *inverse isochoric stretch* induced by a spatial or material electric field

$$\bar{\mathbf{E}}(\mathbf{x}) = (1 - f)^{-2/3} [(1 - f) \mathbf{1} + f \mathbf{n} \otimes \mathbf{n}]. \quad (7.43)$$

It is used in the subsequent treatment as a part of the constitutive structure.

7.2.4. Ingredient 4: Local isochoric elastic network kernel

An important aspect of this work is the modular constitutive structure of electro-elasticity, that allows to include micromechanically-based network models for polymers without any change. This *micromechanical kernel* is assumed to define the energy $\bar{\Psi}_{elas}$ in (7.40) by the constitutive assumption

$$\boxed{\bar{\Psi}_{elas}(\bar{\mathbf{F}}, \mathbb{E}) = \bar{\Psi}_{net}(\bar{\mathbf{F}}_{net})} \quad (7.44)$$

in terms of the *elastic network storage function* $\bar{\Psi}_{net}$. This function is considered to be known from statistical approaches to finite elasticity of cross-linked polymer networks. We outline closed-form representations in [Section 7.3](#). The critical ingredient in the above constitutive equation is the definition of an *elastic network deformation* $\bar{\mathbf{F}}_{net}$. Here, we investigate the three possible assumptions

$$\bar{\mathbf{F}}_{net} := \begin{cases} \bar{\mathbf{F}} & \text{- case 1: total isochoric deformation,} \\ \bar{\mathbf{F}}\bar{\mathcal{E}}(\mathbb{E}) & \text{- case 2: right multiplicative decomposition,} \\ \bar{\mathcal{E}}(\mathfrak{e})\bar{\mathbf{F}} & \text{- case 3: left multiplicative decomposition.} \end{cases} \quad (7.45)$$

The first choice assumes the polymer network to be driven by the *total isochoric deformation* $\bar{\mathbf{F}}$. The second and third assumptions introduce *right* and *left multiplicative splits* of the total isochoric deformation, that is $\bar{\mathbf{F}} = \bar{\mathbf{F}}_{net}\bar{\mathcal{E}}^{-1}(\mathbb{E})$ and $\bar{\mathbf{F}} = \bar{\mathcal{E}}^{-1}(\mathfrak{e})\bar{\mathbf{F}}_{net}$, into electrically-induced deformations $\bar{\mathcal{E}}^{-1}$ and the stress-producing part $\bar{\mathbf{F}}_{net}$. These two geometric splits characterize the electrically-induced deformation part \mathcal{E} defined in [\(7.43\)](#) to be dependent on the material or spatial electric field $\mathfrak{x} := \{\mathbb{E}, \mathfrak{e}\}$, respectively. Restrictions and geometric meaning are discussed below.

7.2.5. Ingredient 5: Local electrostatic contribution to the energy

We outline a purely phenomenological structure of the electrostatic contribution to the enthalpy function per unit volume of the reference configuration [\(7.38\)](#). It is assumed to be *quadratic in the electric field*

$$\Psi_{elec}(\mathbf{F}, \mathbb{E}) = -\frac{J}{2}\mathbb{E} \cdot \hat{\mathcal{P}}(\mathbf{F}) \cdot \mathbb{E} \quad (7.46)$$

in terms of the deformation-dependent *electric permittivity tensor* $\hat{\mathcal{P}}$. The simplest constitutive ansatz for this tensor is assumed for *ideal dielectric elastomers*, that links in a linear format the spatial electric field to the dielectric displacement $d = \epsilon_1 e$. This contribution is formally identical to the free space contribution and motivated by a behavior of the cross-linked polymers at low stretches similar to polymer liquids. A deformation-dependent anisotropic permittivity tensor for elastomers that accounts for large strains was derived recently by JIMÉNEZ & MCMEEKING [\[80\]](#) by taking into account analogies to the micromechanics of birefringence in polymers. We combine these two assumptions by assuming a deformation-dependent permittivity of the form ²

$$\hat{\mathcal{P}}_1(\mathbf{F}) := \epsilon_1 \mathbf{C}^{-1} - \epsilon_2 J^{-2/3} [\text{tr}[\mathbf{C}]\mathbf{C}^{-1} - 3\mathbf{G}^{-1}] \quad (7.47)$$

in terms of the two material parameters ϵ_1 and ϵ_2 . Note that the factor $J^{-2/3}$ of the deformation-dependent terms enforces the associated stress contribution to be deviatoric.

² *Deformation-dependent permittivity tensor in spatial setting.* In the spatial setting, the Kirchhoff-type electric displacement is given by $\bar{d} := Jd = -\partial_e \Psi_{elec}(\mathbf{F}, \mathfrak{e})$ resulting in the push-forward of the deformation-dependent permittivity tensor

$$\Psi_{elec}(\mathbf{F}, \mathfrak{e}) = -\frac{J}{2} e \cdot \hat{\mathcal{P}}(\mathbf{F}) \cdot e \quad \text{with} \quad \hat{\mathcal{P}}_1(\mathbf{F}) = \mathbf{F}\hat{\mathcal{P}}_1(\mathbf{F})\mathbf{F}^T = \epsilon_1 \mathbf{g}^{-1} - \epsilon_2 J^{-2/3} [\text{tr}[\mathbf{b}]\mathbf{g}^{-1} - 3\mathbf{b}] .$$

Setting the material parameter $\epsilon_2 = 0$, we end up with the standard (deformation-independent) free space term in the Eulerian configuration used in electro-mechanics $\Psi_{free}(\mathbf{F}, \mathfrak{e}) = -\frac{\epsilon_1}{2} J(e \otimes e) : \mathbf{g}^{-1}$.

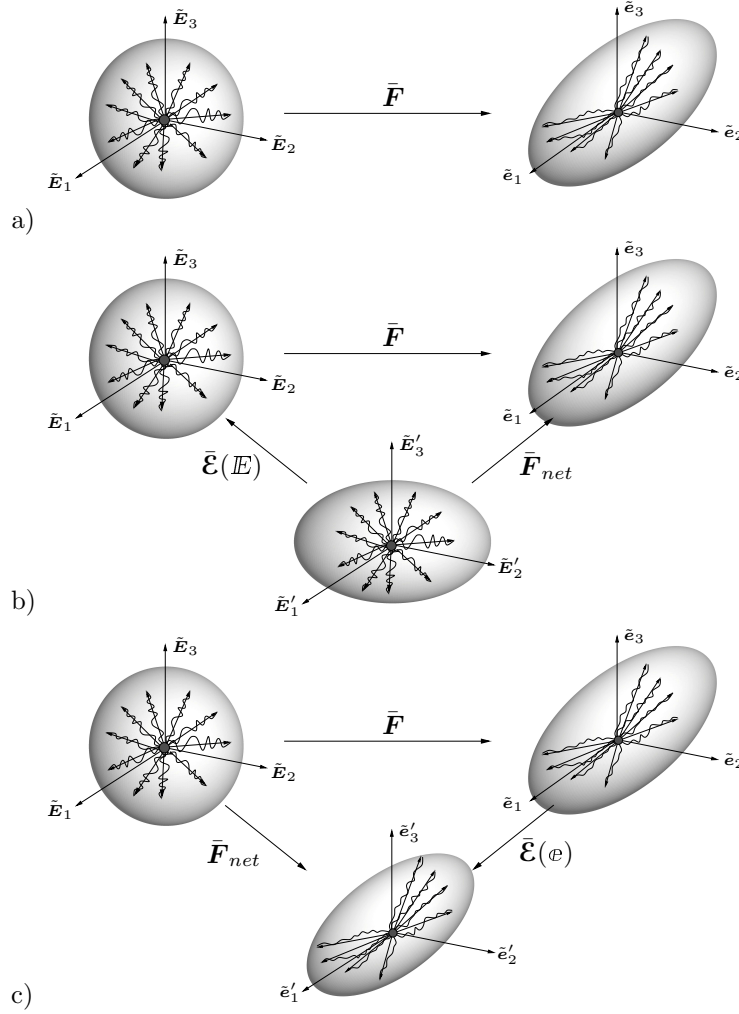


Figure 7.1: *Multiplicative decomposition of deformation gradient.* The isochoric part of the deformation gradient is decomposed into network contribution $\bar{\mathbf{F}}_{net}$ and local electrically-induced deformation $\bar{\mathcal{E}}(\mathbf{x})$. a) Total isochoric deformation $\bar{\mathbf{F}}_{net} = \bar{\mathbf{F}}$ representing an ideal dielectric material model. b) Right Lee-type multiplicative decomposition $\bar{\mathbf{F}}_{net} = \bar{\mathbf{F}}\bar{\mathcal{E}}(\mathbb{E})$ and c) left Clifton-type multiplicative decomposition $\bar{\mathbf{F}}_{net} = \bar{\mathcal{E}}(\mathbf{e})\bar{\mathbf{F}}$.

For materials which are dielectrically isotropic during straining, we may choose the simpler ansatz

$$\hat{\mathcal{P}}_2(\mathbf{F}) := \epsilon_0(1 + \hat{\chi}(J))\mathbf{C}^{-1} \quad \text{with} \quad \hat{\chi}(J) = \frac{\chi}{J}, \quad (7.48)$$

where χ is the constant electric susceptibility, see McMEEKING & LANDIS [113]. A possible, more phenomenological formulation has been used in VU ET AL. [197] in the form

$$\hat{\mathcal{P}}_3(\mathbf{F}) := \epsilon_0\mathbf{C}^{-1} - \frac{2c_1}{J}\mathbf{G}^{-1} - \frac{2c_2}{J}\mathbf{G}^{-1}\mathbf{C}\mathbf{G}^{-1}. \quad (7.49)$$

Note that all the above contributions to the electric enthalpy with deformation-dependent permittivity are isotropic functions of \mathbf{C} and $\mathbb{E} \otimes \mathbb{E}$.

7.2.6. Stress and electric displacement with isochoric stress kernel

With the enthalpy function (7.38) at hand, the material stresses (7.8)₁ take the form

$$\mathbf{P} = U' J \mathbf{F}^{-T} + \bar{\mathbf{P}}_{elas} : \mathbb{O} + \mathbf{P}_{Max} \quad (7.50)$$

in terms of the penalty-type elastic pressure contribution, a deviatoric contribution due to the network deformation and a Maxwell-type electrostatic contribution. Taking into account the three possible links (7.45) to the network model, we define the isochoric stress

$$\bar{\mathbf{P}}_{elas} := \begin{cases} \bar{\mathbf{P}}_{net} \\ \bar{\mathbf{P}}_{net} \bar{\mathbf{E}}(\mathbb{E}) \\ \bar{\mathbf{E}}^{(\varrho)} \bar{\mathbf{P}}_{net} \end{cases} \quad (7.51)$$

for the three cases considered in (7.45) in terms of the isochoric stress kernel

$$\bar{\mathbf{P}}_{net} := \partial_{\bar{\mathbf{F}}_{net}} \bar{\Psi}_{net}(\bar{\mathbf{F}}_{net}), \quad (7.52)$$

which we specify in the Section 7.3 for micromechanically motivated elastic network models. The second term is deviatoric and governed by the material deviatoric projection tensor

$$\mathbb{O} := \partial_{\mathbf{F}} \bar{\mathbf{F}} = J^{-1/3} (\mathbb{I} - \frac{1}{3} \mathbf{F} \otimes \mathbf{F}^{-T}) \quad (7.53)$$

in terms of the fourth-order identity tensor $\mathbb{I}_{ijkl} = \delta_{ik} \delta_{jl}$. The electrostatic stress contribution takes the form

$$\mathbf{P}_{Max} := \partial_{\mathbf{F}} \Psi_{elec}(\mathbf{F}, \mathbb{E}) = -\frac{J}{2} (\mathbb{E} \otimes \mathbb{E}) : \mathbb{R} + \Psi_{elec} \mathbf{F}^{-T}, \quad (7.54)$$

with $\mathbb{R} := \partial_{\mathbf{F}} \hat{\mathcal{P}}^3$, which is considered as a Maxwell tensor associated with the material. The structure of the material electric displacement (7.8)₂ obtained from the enthalpy function (7.38) appears in a similar format

$$\mathbb{D} = J \hat{\mathcal{P}} \cdot \mathbb{E} + \tilde{\mathbf{P}}_{elas} : \mathbb{G} \quad (7.56)$$

with $\mathbb{G} := -\partial_{\mathbb{E}} \bar{\mathbf{E}}(\mathbb{x})^4$. The first term is the pure electric contribution and the second term an additional electro-elastic coupling effect governed by

$$\tilde{\mathbf{P}}_{elas} := \begin{cases} \mathbf{0} \\ \bar{\mathbf{F}}^T \bar{\mathbf{P}}_{net} \\ \bar{\mathbf{P}}_{net} \bar{\mathbf{F}}^T \end{cases} \quad (7.58)$$

³ *Derivative of permittivity tensor.* Taking into account the deformation-dependent permittivity tensor (7.47), its derivative with respect to the deformation gradient reads

$$\mathbb{R} := [\partial_{\mathbf{F}} \hat{\mathcal{P}}]_{ijkl} = -\epsilon_1 \mathbb{J}_{ijkl} + \epsilon_2 J^{-2/3} (\frac{2}{3} (\text{tr}[\mathbf{C}] C_{ij}^{-1} - 3G_{ij}^{-1}) F_{lk}^{-1} - 2C_{ij}^{-1} F_{kl} + \text{tr}[\mathbf{C}] \mathbb{J}_{ijkl}), \quad (7.55)$$

where we defined the fourth order tensor $\mathbb{J}_{ijkl} := F_{ik}^{-1} C_{lj}^{-1} + F_{jk}^{-1} C_{li}^{-1}$.

⁴ *Derivative of electric induced deformation.* Taking into account the deformation-dependent inverse electric deformation tensor (7.43), its derivative with respect to the material electric field reads

$$\mathbb{G} := -[\partial_{\mathbb{E}} \bar{\mathbf{E}}]_{ijk} = c(1-f)^{-2/3} [\frac{2}{3} \mathcal{E}_{ij} \mathbb{x}_a - \mathcal{E}_{ia} \mathbb{x}_j - \mathcal{E}_{ja} \mathbb{x}_i] A_{ak} \quad \text{with} \quad A_{ak} = \begin{cases} \delta_{ak} & \text{- case 2} \\ F_{ka}^{-1} & \text{- case 3} \end{cases} \quad (7.57)$$

for the material $\mathbb{x}_i = \mathbb{E}_i$ and spatial electric field $\mathbb{x}_i = \varrho_i$ in case 2 and 3, respectively.

for the three cases considered in (7.45). Note that in the constitutive equations (7.50) and (7.56) everything is determined except the *stress kernel* $\bar{\mathbf{P}}_{net}$ in the *isochoric elastic deformation space*. This allows to *include all elastic network models* for polymers, see Section 7.3 for a specification. In this context, the functions (7.50) and (7.56) cover the most simple formulations of the response functions for electro-elastic polymers with complex elastic network kernels.

7.2.7. The coupled electro-elastic tangent moduli

The computation of the tangent moduli necessary for Newton-type solvers needs a further derivative of the above outlined constitutive functions. Due to the multiplicative split, these derivatives are demanding. Following MIEHE [115], we compute the coupled electro-mechanical moduli numerically. In order to get a compact formulation, we assemble the electro-mechanical variables in arrays, such that

$$\mathbf{S} := \begin{bmatrix} \partial_{\mathbf{F}}\Psi \\ \partial_{\mathbf{E}}\Psi \end{bmatrix} \quad \text{and} \quad \mathbf{F} := \begin{bmatrix} \mathbf{F} \\ \mathbf{E} \end{bmatrix} \quad (7.59)$$

denote material generalized stresses and deformations. The sensitivity of the generalized stress with respect to the generalized deformation defines the *material moduli*, which we assemble is a *material electro-mechanical coupling array*

$$\mathbf{C} := \begin{bmatrix} \partial_{\mathbf{F}\mathbf{F}}^2\Psi & \partial_{\mathbf{F}\mathbf{E}}^2\Psi \\ \partial_{\mathbf{E}\mathbf{F}}^2\Psi & \partial_{\mathbf{E}\mathbf{E}}^2\Psi \end{bmatrix}. \quad (7.60)$$

They determine the sensitivity $\Delta\mathbf{S}$ of the generalized stresses array with respect to the generalized deformation increment $\Delta\mathbf{F}$ according to $\Delta\mathbf{S} = \mathbf{C} \cdot \Delta\mathbf{F}$. Let the generalized stresses and deformation be rearranged in vector arrays, such that $\mathbf{S} = \mathbf{S}_I$ and $\mathbf{F} = \mathbf{F}_I$ for $I = 1, 12$. In order to determine a numerical approximation of the tangent matrix, assume a perturbation of a given generalized strain \mathbf{F} in the form

$$\mathbf{F}_{(J)}^\epsilon := \mathbf{F} + \epsilon\mathbf{E}_{(J)}, \quad (7.61)$$

where $\{\mathbf{E}_{(J)}\}_{J=1,12}$ are base vectors which span the \mathcal{R}^{12} . Based on this perturbation, define the columns of the electro-mechanical coupling array by the difference of perturbed generalized stresses relative to the current state

$$\mathbf{C}_{I(J)} \approx \frac{1}{\epsilon} [\hat{\mathbf{S}}_I(\mathbf{F} + \epsilon\mathbf{E}_{(J)}) - \hat{\mathbf{S}}_I(\mathbf{F})] \quad (7.62)$$

for $J = 1, 12$. This needs for twelve additional evaluations of the generalized stresses for perturbed penalized deformations, governed by the material constitutive functions (7.50) and (7.56).

7.3. Micromechanical kernel for elastic network response

An important aspect of this work is the modular structure of multiplicative electro-elasticity, that allows to include micromechanically-based network models for polymers

without any change. This *micromechanical kernel* is characterized by the isochoric network energy $\bar{\Psi}_{net}$ in (7.44), yielding the *elastic network stress kernel*

$$\bar{\mathbf{P}}_{net} = \partial_{\bar{\mathbf{F}}_{net}} \bar{\Psi}_{net}(\bar{\mathbf{F}}_{net}) \quad (7.63)$$

that takes into account the network structure of cross-linked polymer chains. We specify in this section the function $\bar{\Psi}_{net}$, that is linked to statistical mechanics of polymer networks. In classical entropy-based elasticity of polymer networks, the entropy s of a single polymer chain is governed by Boltzmann's equation. Hence, the free energy of a chain is

$$\psi = -\theta s \quad \text{with} \quad s = k \ln p, \quad (7.64)$$

where p is the probability density that describes the free chain response. k is the Boltzmann constant and $\theta > 0$ the absolute temperature. Now consider a single polymer consisting of N segments of equal length l as depicted in Figure 7.2a. The classical Gaussian statistics derived by KUHN [96, 97] considers the unconstrained chain with end-to-end distance $r := |\mathbf{r}| \ll L$ much smaller than the contour length $L := Nl$, that are moderate deformations of the chain. Here, the probability density per unit volume of a randomly jointed chain characterized by the end-to-end vector \mathbf{r} has the form

$$p(\mathbf{r}) = p_0 \exp[-\frac{3}{2}\lambda^2] \quad \text{with} \quad p_0 := (\frac{3}{2}Nl^2\pi)^{3/2} \quad (7.65)$$

in terms of the stretch $\lambda := r/r_0 \in [0, \sqrt{N}]$, see TRELOAR [192, p.47]. Here, $r_0 := \sqrt{N}l$ is the random-walk mean-square distance of a chain. Insertion of (7.65) into (7.64) gives the *free energy of the chain*

$$\psi(\lambda) = \frac{3}{2}k\theta\lambda^2 \quad (7.66)$$

as a function of the stretch λ . The simplest *network model* that links the response of a single polymer chain to the macroscopic deformation of a continuum is the *three-chain model*, which can be traced back to KUHN & GRÜN [98] and JAMES & GUTH [77]. It considers a network of n chains per unit volume and links the microscopic stretch λ of a single strain embedded in the continuum by an *affine deformation assumption* to the three macroscopic elastic principal stretches $\{\lambda_i\}_{i=1,3}$, obtained by the singular value decomposition of the (isochoric) elastic network deformation map of multiplicative electro-mechanics defined in (7.45), that is

$$\bar{\mathbf{F}}_{net} = \sum_{i=1}^3 \lambda_i \mathbf{n}_i \otimes \mathbf{N}_i \quad \text{with} \quad \det[\bar{\mathbf{F}}_{net}] = 1. \quad (7.67)$$

The elastic free energy of the network is constructed by taking the arithmetic average of *three representative chain energies* aligned with the macroscopic principal stretch directions as depicted in Figure 7.2b, that is

$$\bar{\Psi} = n \langle \psi \rangle \quad \text{with} \quad \langle \psi \rangle := \frac{1}{3} [\psi(\lambda_1) + \psi(\lambda_2) + \psi(\lambda_3)]. \quad (7.68)$$

Insertion of (7.66) into (7.68) and taking into account $\text{tr}[\bar{\mathbf{F}}_{net}^T \mathbf{g} \bar{\mathbf{F}}_{net}] = \lambda_1^2 + \lambda_2^2 + \lambda_3^2$ finally gives the classical closed-form *elastic free energy function* of the polymer network

$$\bar{\Psi}_{net}(\bar{\mathbf{F}}_{net}) = \frac{\mu}{2} \text{tr}[\bar{\mathbf{F}}_{net}^T \mathbf{g} \bar{\mathbf{F}}_{net}] \quad \text{with} \quad \mu := nk\theta. \quad (7.69)$$

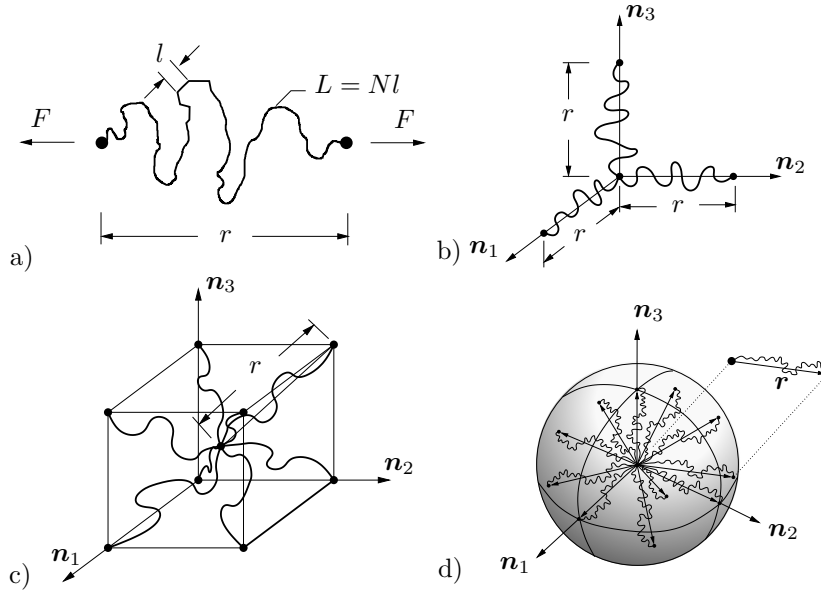


Figure 7.2: Network models for rubbery polymers. a) Single chain with N segments of length l , end-to-end distance r and contour length $L = Nl$. b) Three-chain model: Chains in principal stretch directions \mathbf{n}_i . c) Eight-chain model: Chains placed along the space-diagonals of a cube, all undergoing the same stretch. d) Microsphere model: Chain orientation continuum with directors \mathbf{r} , stretch fluctuation determined by a principle of minimum averaged energy.

In continuum mechanics, this energy function is known as the neo-Hookean free energy, which has through the above treatment a well-defined micromechanically motivated *network stiffness* μ . More advanced network theories of rubbery polymers applicable to large deformations replace the Gaussian statistics by the *inverse Langevin statistics*, developed by KUHN & GRÜN [98] and JAMES & GUTH [77], which takes account for the finite extensibility of the chain. It results in the free energy of a single chain

$$\psi(\lambda) = Nk\theta \left(\lambda_r \mathcal{L}^{-1}(\lambda_r) + \ln \left[\frac{\mathcal{L}^{-1}(\lambda_r)}{\sinh \mathcal{L}^{-1}(\lambda_r)} \right] \right), \quad (7.70)$$

which advances (7.66) for end-to-end distances r up to the limiting value L . Here, $\mathcal{L}(x) = \coth x - 1/x$ is the well-known Langevin function and $\lambda_r := r/L = \lambda/\sqrt{N} \in [0, 1)$ the relative stretch, see TRELOAR [192, p.103]. Furthermore, the restrictive affine deformation assumption can be relaxed by more advanced network models, such as the *non-affine microsphere network model* developed by MIEHE ET AL. [129], that links by a particular homogenization method on the unit sphere $\mathcal{S} \subset \mathcal{R}^2$ depicted in Figure 7.2d the microstretch λ of the single chain to the macroscopic deformation gradient (7.67) by the p-root average of the macroscopic stretch

$$\lambda = \langle \bar{\lambda} \rangle_p := \left[\frac{1}{|\mathcal{S}|} \int_{\mathcal{S}} \bar{\lambda}^p dA \right]^{1/p} \quad \text{with} \quad \bar{\lambda} := |\bar{\mathbf{F}}_{net} \mathbf{r}|, \quad (7.71)$$

where \mathbf{r} is the unit director to the surface of the sphere. The elastic free energy of the non-affine network model is derived as

$$\bar{\Psi}_{net}(\bar{\mathbf{F}}_{net}) = n\psi(\langle \bar{\lambda} \rangle_p). \quad (7.72)$$

This function describes the idealized network with free fluctuation of the chains between the cross-links of the network. An additional free energy representing the energy due to

Table 7.1: Material parameters used for numerical simulations.

no.	par.	name	unit	value
1.	κ	bulk modulus	N/mm ²	5.00×10^2
2.	μ	shear modulus	N/mm ²	1.00×10^{-2}
3.	N	number of chain segments	–	4.31
4.	p	non-affine averaging parameter	–	6.22
5.	c	electrostrictive coefficient	mm ² /kV ²	1.00×10^{-2}
6.	ϵ_0	vacuum permittivity	N/kV ²	8.854×10^{-6}
7.	ϵ_1	relative permittivity	N/kV ²	$8.00 \times \epsilon_0$
8.	ϵ_2	deformation dependent permittivity	N/kV ²	$0.01 \times \epsilon_1$

interaction of chains is added. The model is based on five physically motivated material parameters and shows excellent fits to multi-dimensional experimental results. We refer to MIEHE ET AL. [129] for more details. A straightforward derivation with respect to the elastic network deformation results in the missing ingredient for the micromechanically-based model

$$\bar{\mathbf{P}}_{net} = n\psi' \langle \bar{\lambda} \rangle_p^{1-p} \langle \bar{\lambda}^{p-2} \mathbf{t} \otimes \mathbf{r} \rangle, \quad (7.73)$$

where $\mathbf{t} = \bar{\mathbf{F}}_{net} \mathbf{r}$. Note that the average $\langle (\cdot) \rangle = \frac{1}{|\mathcal{S}|} \int_{\mathcal{S}} (\cdot) dA$ is taken over the unit sphere. $p > 0$ in (7.71) is a material parameter. For $p = 2$, the microsphere model degenerates to the *eight-chain model* proposed by ARRUDA & BOYCE [2] and visualized in Figure 7.2c,

$$\bar{\Psi}_{net}(\bar{\mathbf{F}}_{net}) = n\psi(\langle \bar{\lambda} \rangle_2) \quad \text{with} \quad \langle \bar{\lambda} \rangle_2 = \sqrt{\text{tr}[\bar{\mathbf{F}}_{net}^T \mathbf{g} \bar{\mathbf{F}}_{net}]/3}, \quad (7.74)$$

which is simpler due to its closed-form relationship to the invariant $\text{tr}[\bar{\mathbf{F}}_{net}^T \mathbf{g} \bar{\mathbf{F}}_{net}]$ of $\bar{\mathbf{F}}_{net}$ but of limited fitting capability. This summarizes our overview about physically motivated network models of rubber-like polymers. Further details can be found in the textbooks TRELOAR [192], FLORY [47], and DOI & EDWARDS [40], as well as in the papers BOYCE & ARRUDA [23] and MIEHE ET AL. [129].

7.4. Representative numerical examples

In the examples that follow, we demonstrate the salient features of the finite strain coupled electro-mechanical model. The micromechanical kernel for the elastic network response is the non-affine microsphere model developed in MIEHE ET AL. [129]. For this particular model the elastic free energy function is given in (7.72) in terms of the p-root average of the macroscopic stretch. The finite element discretization of the boundary-value-problems is performed by employing eight-node brick elements. The degrees of freedom at the nodes are the displacement field \mathbf{u} and the electric potential ϕ . The material parameters used in the subsequent numerical simulations are given in Table 7.1. Electroactive polymers sandwiched between two electrodes are considered. Application of voltage difference causes the polymer to extend in the direction perpendicular to the applied electric field.

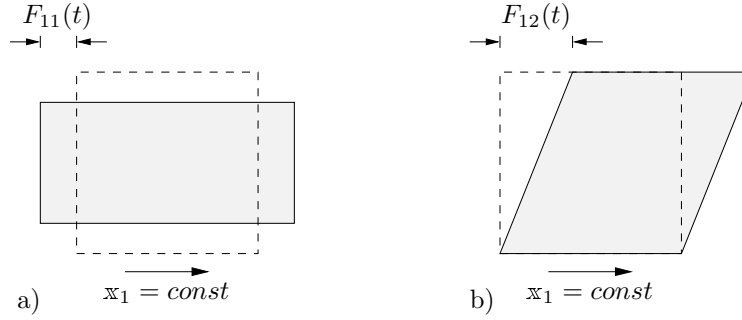


Figure 7.3: *Tensile and shear driver tests on EAP unit cube.* The illustrations show the cross-section. a) Tensile deformation and b) shear deformation is monotonically increased for constant material or spatial electric field $\mathbf{x}_1 := \{\mathbb{E}_1, \mathbf{e}_1\}$. These simple tests outline the differences between the multiplicative splits introduced as case 1–3.

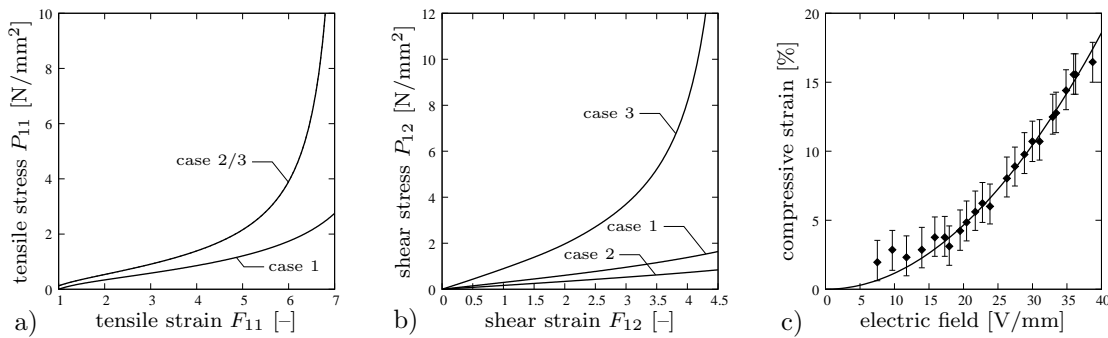


Figure 7.4: *Stress versus strain curves and experimental fit.* To demonstrate the capability of the models, we choose for this test $c = 1.0 \text{ mm}^2/\text{kV}^2$. a) Uniaxial response for cases 2 (constant \mathbb{E}_1) and 3 (constant \mathbf{e}_1) are identical due to the coaxiality of the isochoric deformation and the electrically-induced deformation. b) Simple shear test indicates differences between all three cases. c) Fitting numerical approach to experimental data taken from PELRINE ET AL. [145] for the commercially available elastomer HS3 silicone. The chosen material parameter for the quadratic electrostrictive function is $c = 1.16 \times 10^{-4} \text{ mm}^2/\text{V}^2$.

7.4.1. Model comparison and parameter identification

In order to compare the different multiplicative approaches outlined in Section 7.2, the results of simple tests are presented. These splits are labeled in the following simply by case 1–3. In the first example, we consider a tension test in a constant electric field $\mathbf{x} = [\mathbf{x}_1(t) \ 0 \ 0]^T \text{ kV/mm}$ aligned with the x -direction, see Figure 7.3a for the description of the boundary-value-problem. With this prescribed constant electric field $\mathbf{x}_1 = 0.5 \text{ kV/mm}$, we then compute the tensile nominal stress P_{11} for the three cases. The results are shown in Figure 7.4a, and we choose $c = 1.0 \text{ mm}^2/\text{kV}^2$ as well as for the non-affine microsphere model the parameters detected in MIEHE ET AL. [129] in order to demonstrate the capability of the three different types of models.

For the ideal dielectric (case 1), the applied Lagrangian electric field has a negligible influence on the stress-strain diagram. A first observation for the multiplicative splits 2 and 3 is that the stress response shows an offset compared with an ideal dielectric. The uniaxial response for case 2 with constant Lagrangian field \mathbb{E}_1 and case 3 with constant Eulerian field \mathbf{e}_1 are identical due to the fact that the isochoric deformation and the electrically-induced deformation are coaxial $\bar{\mathbf{F}}\bar{\mathbf{E}} = \bar{\mathbf{E}}\bar{\mathbf{F}}$. The second test highlights the differences within a simple shear test for a fixed electric field $\mathbf{x}_1 = 0.75 \text{ kV/mm}$,

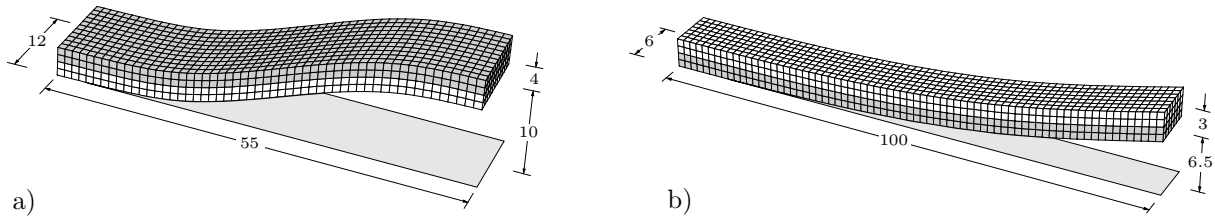


Figure 7.5: *Boundary-value-problems for electroactive polymers.* The white layer is the EAP material which extends in the direction perpendicular to the electric field, while the other strip (gray) is a polymer that does not deform in an electric field. Dimensions are in [mm]. a) Bimorph double-s-shaped actuator using symmetry properties. Electric potential is applied at the bottom surface, whereas intermediate layer separating both strips is fixed to zero. Finite element mesh with $54 \times 11 \times 4$ elements per edge. b) Starfish gripper where solely one finger is shown exemplarily. Electric potential is applied at the top surface, intermediate fixed to zero. Finite element mesh with $109 \times 6 \times 4$ elements per finger.

and increasing shear deformation $F_{12}(t)$, see Figure 7.3b. The plot in Figure 7.4b shows the nominal shear stress P_{12} versus the shear deformation F_{12} for the three cases under consideration. We observe that in comparison with case 1, the right Lee-type decomposition decreases the stiffness, while the left Clifton-type decomposition increases it. Experimental results on electroactive polymers are not easy to come by and therefore the results of PELRINE ET AL. [145, 144] on EAPs are quite valuable. Within the fitting process, the experimental data points of PELRINE ET AL. [145] are used representing the commercially available elastomer Dow Corning HS3 silicone. The graph in Figure 7.4c contains the experimental measurements as well as the model's response, showing the compressive engineering strain versus the applied electric field. In order to fit the simulation, the quadratic electrostrictive function with one additional material parameter presented in Subsection 7.2.3 has been used. This parameter is determined to the value $c = 1.16 \times 10^{-4} \text{ mm}^2/\text{V}^2$ with a standard error of 1.453% resulting in a good agreement with experimental observations.

7.4.2. Electroactive polymer as double-s-shaped actuator

A practical application, where the advantages of electroactive polymers come into play, is a bimorph double-s-shaped actuator. The inner layer is the EAP material which extends in the direction perpendicular to the electric field. Electric potential is applied at the bottom layer, whereas intermediate layer separating both strips is held constant at zero. The finite element discretization of one-fourth of the specimen using symmetry properties is shown in Figure 7.5a. A total number of 2376 three-dimensional brick elements is used for the mesh. If the intermediate layer is activated via the application of a voltage difference of $\Delta\phi = 23.1 \text{ kV}$, the curvature of the actuator can be accentuated. Figure 7.6 shows a sequence of deformation states for increasing potential difference $\Delta\phi$. The large mechanical deformations can be clearly observed for the electric loading under consideration. The coupling between electric and mechanical phenomena is caused by the *multiplicative split* of the deformation gradient, the subsequent computations performed by the microsphere model, and the electric part of the energy. In addition to the large deformation in vertical direction, we clearly observe bending in the transverse direction of the specimen in Figure 7.6d. This bending deformation in the actuator causes an inhomogeneous deformation state. It can be seen clearly with the help of the pole projections,

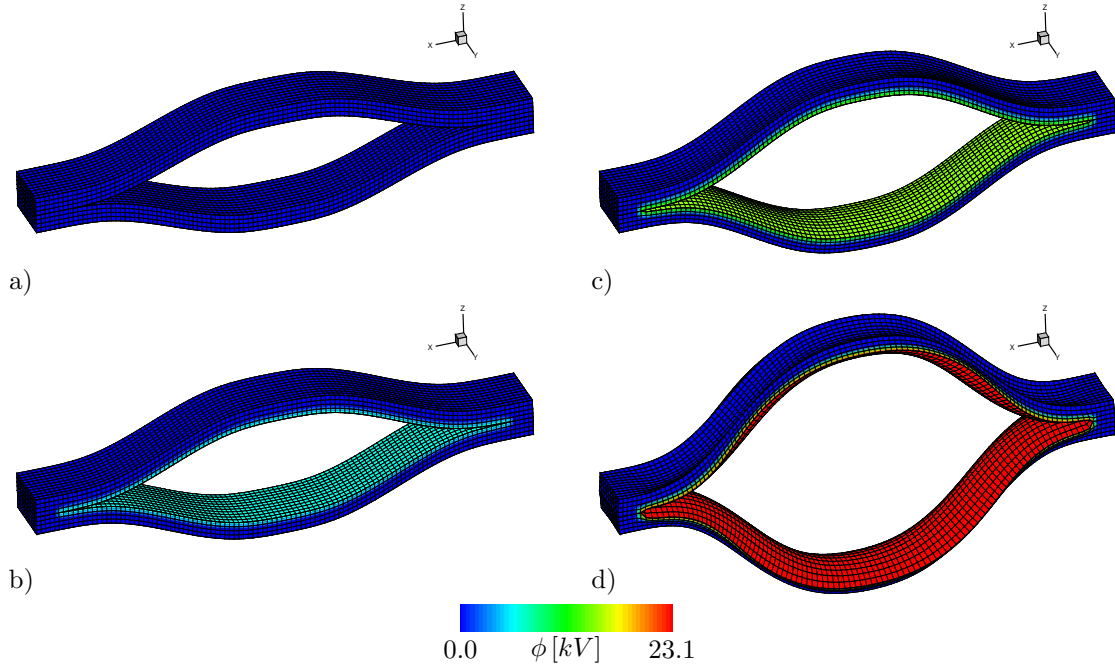


Figure 7.6: *Double-s-shaped actuator using bi-material strip.* The formation of an electric field by a potential difference $\Delta\phi$ between the bottom and intermediate electrode (not modeled numerically) causes a progressive thickness deformation combined with an in-plane curling.

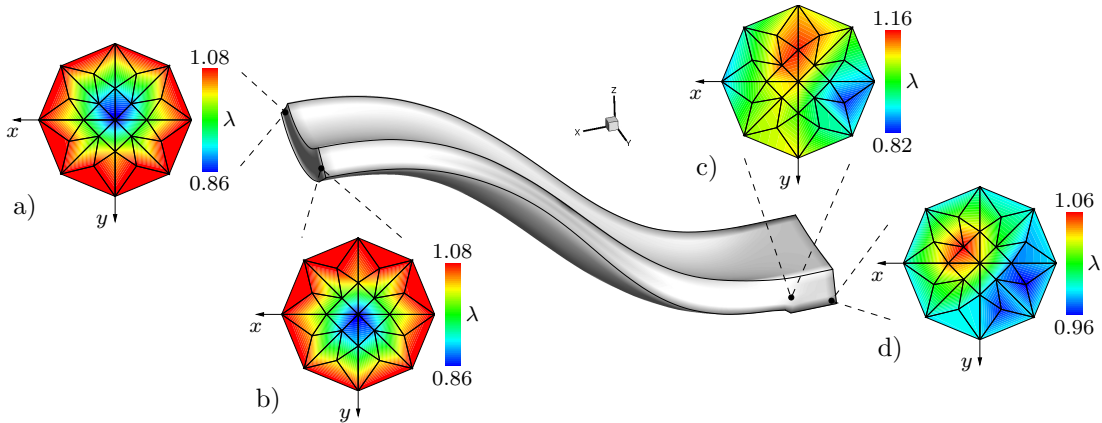


Figure 7.7: *Pole projection figures for double-s-shaped actuator.* The pole figures show the local deformation state λ of the microstructure at different points. Deformed geometry corresponds to that of [Figure 7.6d](#). Bending of actuator can be observed along the transverse direction.

that are plotted alongside the deformed body in [Figure 7.7](#). These pole projections give an insight in the deformation $\bar{\mathbf{F}}_{net}$ at their respective material points. Elements of the electroactive material experience a more pronounced anisotropic behavior. This is expected since an electric field causes an elongation perpendicular to itself and in addition the applied boundary conditions cause inhomogeneities. For the pole figure at the fixed points, the material behaves almost isotropic.

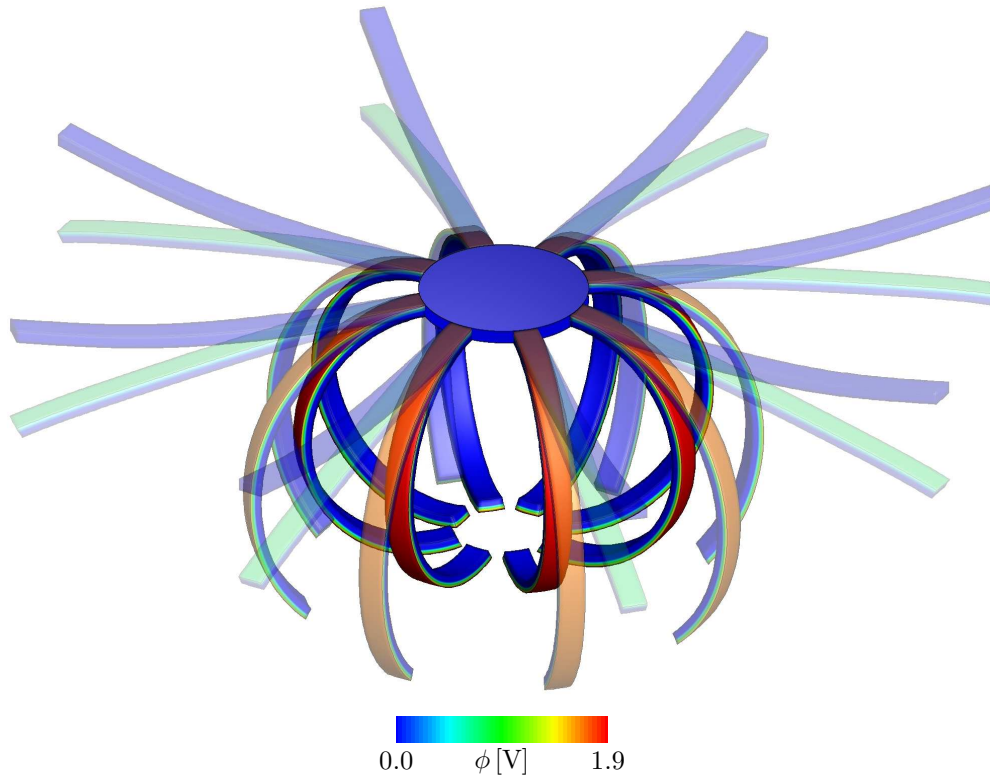


Figure 7.8: *Deformation process of starfish gripper.* The electrically induced differential extension along the longitudinal direction causes the gripper to progressively curl up with increasing potential difference $\Delta\phi$ between the two electrodes. The sequence of deformation is shown, where the contour plot is related to the electric potential with maximum value $\Delta\phi_{max} = 1.9$ V.

7.4.3. Electroactive polymer as starfish gripper

We demonstrate the capability of the proposed multiplicative split with respect to large deformations and rotations. To this end, we analyze a curved finger actuator in a “starfish” shape, consisting of two polymer strips glued together. While one of the materials is electroactive, the other is not. Furthermore, an electrode is placed between both strips, which is assumed to not hinder the deformation. As demonstrated in Figure 7.5b, a single finger (out of eight) has length $l = 100$ mm, width $b = 6$ mm, and height $t = 3$ mm. The left face has all mechanical displacements fixed to zero. A voltage difference of $\Delta\phi = 1.9$ V is applied in thickness direction of the electroactive polymer between the upper and intermediate electrode. The numerical simulation is performed on one quarter of the total geometry, where 5232 three-dimensional electro-mechanically coupled brick elements have been used (2616 elements per finger). The applied electric potential is monotonically increased and the series of pictures in Figure 7.8 shows the progressive deformation. In the initial state, the starfish is opened. The electric field causes the finger to close and objects can be grabbed. The applied potential difference causes the electroactive polymer to lengthen in the direction perpendicular to the field while having no effect on the dimensions of the other (non-active) polymer material. This differential contraction between the two layers, however, causes the actuator as a whole to curl like a finger with the electroactive material to be in the convex (outer) side. Symmetry conditions have been used in order to get the whole gripper consisting of eight fingers. The top plate in Figure 7.8 has been added in a post processing step.

Variational-Based Homogenization of Electro-Elasticity at Finite Strains

Due to their great coupling possibilities composites tailored by a polymer matrix and high dielectric inclusions are emerging in the last decade and hence became an extensive field of research. The aim is to achieve high coupling coefficients between the electric stimulus and mechanical output or vice versa. The main challenge in the development of dielectric elastomer actuators is the high driving voltage of up to $150 \text{ V}/\mu\text{m}$ needed for actuation, see ZHANG ET AL. [212]. Some examples of these so-called *smart* or *functional materials* are electroactive and electrostrictive materials, piezoelectrics, magnetostrictive materials, and shape memory alloys, to name a few, see SMITH [169]. The goal of this chapter is to determine optimal composite structures by including high dielectric filler particles into the polymer matrix in order to reduce the driving voltage. The fundamentals for the general nonlinear theory of electro-mechanically coupled material equations were proposed starting in the 1960s by TOUPIN [190], ERINGEN [42], MAUGIN [110], KOVETZ [94], and GRIFFITHS [52].

In fields where *large deformations* are needed, rigid and fragile materials such as piezoceramics are of no use. This is where soft active materials such as *electroactive polymers (EAPs)* are considered. Polymers are known to withstand deformations of several hundred percent and have many other attractive characteristics such as light weight, fracture tolerance, and they are cheap to manufacture as well as modify. The discovery and development of these materials were reported in the works of KORNBLUH ET AL. [89, 90] and PELRINE ET AL. [144, 145]. Their application as actuators, sensors, and energy harvesters is of high interest in recent research, see BAR-COHEN [7] and CARPI & SMELA [29]. Electroactive polymers consist of a thin layer of polymeric material coated with compliant electrodes on either side. Application of a voltage difference in terms of charge separation due to the polymer acting as an insulator between the two electrodes results in *Maxwell stresses* in response to charge attraction. The reduction in thickness is balanced out by area expansion, therefore the electrodes need to consist of flexible materials such as carbon grease to not hinder expansion of the polymer. The dielectric can either be used as an actuator by transforming electrical loading into mechanical response using the inverse piezoelectric effect or transducing mechanical energy into electrical signals by the direct

piezoelectric effect. Both effects are of interest for practical applications in bio-medical engineering, for example as artificial muscles that need high material expansibility or Braille displays, as well as in robotics and aerospace.

This technology becomes practical as soon as the material is robust, reliable, and long lived. However, electroactive polymers suffer from different types of *instabilities* such as unstable thinning of the actuator, local buckling induced by coexistent states, and electrical breakdown that have been analyzed both, analytically by ZHAO & SUO [213], ZHAO ET AL. [215], MOSCARDO ET AL. [136], LIU ET AL. [106] or BERTOLDI & GEI [16] and experimentally by PLANTE & DUBOWSKY [148]. When the applied voltage increases, the dielectric thins down and the same voltage produces a higher electric field that will further squeeze the polymer, possibly resulting in electrical breakdown. This failure mode known as *pull-in instability* represents the key issue preventing the realization of large and stable deformations. One also distinguishes between *structural instability*, namely instabilities in the global material response like buckling or wrinkling of the whole structure, and *local* or *material instability*, that is the formation of microstructures. Following the theory of bifurcation and stability for nonlinear elastic solids developed by HILL [61] and BIOT [18] the necessary condition for global material instability, i.e. loss of uniqueness of the solution, is determined by the loss of positive definiteness of the tangential stiffness matrix. Likewise, local stability issues are determined by investigating the positive definiteness of the *acoustic tensor*, see HILL [62], BAESU [4], BAESU ET AL. [5], and BERTOLDI & BOYCE [15]. Both these phenomena are well investigated in purely mechanical problems, see TRUESDELL & NOLL [194], OGDEN [142], MIEHE & SCHRÖDER [124] or MIEHE & LAMBRECHT [122] but are extended in this chapter to *electro-mechanically coupled problems* as recently outlined in MIEHE ET AL. [134].

An important aspect of the research in continuum micromechanics is the description of the macroscopic overall response of composites in an averaged or homogenized sense. Classical analytic estimates for the overall response of composites make often use of the fundamental result of ESHELBY [45] concerning the actuation strain field in an ellipsoidal inclusion. These approaches are in many circumstances restricted, especially with respect to the geometry of the representative microstructure and its constitutive response that is often assumed to be linearly elastic. Starting with the work of SUQUET [177] several numerical methods have been developed on the computational side which discretize fine-scale fields on the microstructure of a composite. These methods allow the analysis of general geometries and constitutive nonlinearities of composite representative volume elements and provide detailed information on fine-scale mechanisms. Numerical formulations for the analysis of representative cells of periodic composites have been outlined for example in SWAN [179], GOSH ET AL. [51], MOULINEC & SUQUET [137], and MICHEL ET AL. [114] based on discretizations of composite microstructures in terms of the finite element method or fast Fourier transforms. Finite element formulations in the large-strain context have been considered for instance in SMIT ET AL. [168] and MIEHE ET AL. [125, 126]. The investigation of variational-based homogenization methods for finite deformations is discussed in this chapter. The purely mechanical formulations outlined in MIEHE [116] and MIEHE ET AL. [127, 128] are extended to non-dissipative electro-mechanics.

The chapter is organized as follows: Section 8.1 outlines the micro-to-macro transition performed by a *variational principle of homogenization* determining a macroscopic potential density by the volume average of its microscopic counterpart. Hence, no explicit

constitutive material model is specified on the macroscale. The material behavior is determined by additional finite element computations on the representative volume element. The consistent generalized macro-stress and moduli expressions are determined including the softening part of the macro-stiffness due to the sensitivity of the microstructure with respect to the fluctuations. With this at hand, the variational formulation of the macroscopic response is considered in Section 8.2 including its finite element discretization. The macro-problem is fully governed by the homogenized generalized stress potential density determined by the microstructure. Afterwards, a local *structural stability criterion* for an enthalpy-based formulation is determined in Section 8.3. It is based on the combination of a Legendre transformation for the electric energy density and a minimization principle of electro-elastostatics. Section 8.4 discusses a macroscopic FE² driver for one-dimensional stress and deformation states assuming a homogeneous macroscopic boundary-value-problem. Finally, Section 8.5 outlines representative numerical examples applying the developed stability analysis and FE² driver to coupled electro-mechanics. The electric actuation response of varying volume fractions and various shapes of the inclusion for two-phase composites are investigated and compared.

8.1. Variational formulation of the homogenization problem

This section defines an average-type homogenization principle in finite electro-mechanics on a variational basis. We propose a new stationary principle for the homogenization problem, point out its Euler-Lagrange equations, and develop a unified matrix representation of its finite element discretization focusing on periodic boundary conditions. This formulation extends concepts proposed by MIEHE ET AL. [127, 128] to finite electro-mechanics.

8.1.1. Constraints on fine-scale fluctuation fields

Let $\varphi : (\mathbf{X}, t) \mapsto \mathbf{x} = \varphi(\mathbf{X}, t)$ denote the deformation map of the microstructure $\mathcal{B} \subset \mathcal{R}^3$, mapping points from the reference configuration to the current configuration. In complete analogy, $\phi : \mathcal{B} \times \mathcal{T} \rightarrow \mathcal{R}$ denotes the electric potential of the microstructure. The mechanical displacement is assumed to be driven by a prescribed macroscopic deformation gradient $\bar{\mathbf{F}}(t)$. Likewise the microscopic electric potential is governed by the macroscopic electric field $\bar{\mathbf{E}}(t)$ resulting in the additive split

$$\varphi(\mathbf{X}, t) = \bar{\mathbf{F}}(t)\mathbf{X} + \tilde{\varphi}(\mathbf{X}, t) \quad \text{and} \quad -\phi(\mathbf{X}, t) = \bar{\mathbf{E}}(t)\mathbf{X} - \tilde{\phi}(\mathbf{X}, t) \quad (8.1)$$

into linear parts $\bar{\mathbf{F}}\mathbf{X}$ and $\bar{\mathbf{E}}\mathbf{X}$ driven by the macroscale and superimposed fine-scale fluctuation fields $\tilde{\varphi}$ and $\tilde{\phi}$. Hence, the deformation gradient and electric field of the microstructure locally at $\mathbf{X} \in \mathcal{B}$ read

$$\mathbf{F} = \nabla\varphi = \bar{\mathbf{F}} + \nabla\tilde{\varphi} \quad \text{and} \quad \mathbf{E} = -\nabla\phi = \bar{\mathbf{E}} - \nabla\tilde{\phi} \quad (8.2)$$

additive decomposed into prescribed homogeneous parts $\bar{\mathbf{F}}$ and $\bar{\mathbf{E}}$ as well as a superimposed fluctuation gradients $\nabla\tilde{\varphi}$ and $\nabla\tilde{\phi}$. Following the arguments provided by NEMAT-NASSER [139], SCHRÖDER [161], and ZÄH & MIEHE [207] the macroscopic quantities are governed by surface data only

$$\bar{\mathbf{F}} = \frac{1}{|\mathcal{B}|} \int_{\partial\mathcal{B}} \varphi \otimes \mathbf{N} \, dA \quad \text{and} \quad \bar{\mathbf{E}} = \frac{1}{|\mathcal{B}|} \int_{\partial\mathcal{B}} -\phi \mathbf{N} \, dA. \quad (8.3)$$

As far as no holes, cracks or discontinuities are considered within the microstructure, the macroscopic quantities are obtained as the volume average of their microscopic counterparts, see [Chapter 4](#). As a consequence of the additive decomposition (8.1) the volume average of the fine-scale fluctuations vanish. Within this work, we restrict our self to non-trivial periodic boundary constraints for the microstructure

$$\tilde{\varphi}^+ = \tilde{\varphi}^- \text{ on } \partial\mathcal{B} \quad \text{and} \quad \tilde{\phi}^+ = \tilde{\phi}^- \text{ on } \partial\mathcal{B}. \quad (8.4)$$

Periodic boundary conditions applied to the faces of the representative volume element render the best choice even for non-periodic microstructures. This is due to the fact that the effective elastic constants derived under these conditions are always bounded by those obtained under prescribed Dirichlet (displacements) or Neumann (forces) boundary conditions. A detailed discussion of the three classical boundary conditions and a graphical representation of periodic constraints is given in [Chapter 4](#).

8.1.2. Variational formulation of the coupled homogenization problem

Let ψ denote an objective potential function associated with a general non-dissipative material behavior determining the stress and electric displacement of the microstructure. By the quasi-hyperelastic function evaluations

$$\begin{aligned} \mathbf{P} &= \partial_{\mathbf{F}}\psi(\mathbf{F}, \mathbb{E}) & \mathbf{A} &= \partial_{\mathbf{F}\mathbf{F}}^2\psi(\mathbf{F}, \mathbb{E}) \\ -\mathbb{D} &= \partial_{\mathbb{E}}\psi(\mathbf{F}, \mathbb{E}) & \mathbb{H} &= \partial_{\mathbf{F}\mathbb{E}}^2\psi(\mathbf{F}, \mathbb{E}) \\ & & \boldsymbol{\epsilon} &= \partial_{\mathbb{E}\mathbb{E}}^2\psi(\mathbf{F}, \mathbb{E}) \end{aligned} \quad (8.5)$$

we get the microscopic stress and electric displacement as well as corresponding moduli expressions at a local point $\mathbf{X} \in \mathcal{B}$ of the heterogeneous microstructure. The coupled micro-to-macro transition in finite electro-mechanics can be, due to the analogy to finite elasticity, compactly represented by a *variational principle of homogenization*

$$\boxed{\bar{\psi}(\bar{\mathbf{F}}, \bar{\mathbb{E}}) = \inf_{\tilde{\varphi}} \sup_{\tilde{\phi}} \frac{1}{|\mathcal{B}|} \int_{\mathcal{B}} \psi(\bar{\mathbf{F}} + \nabla\tilde{\varphi}, \bar{\mathbb{E}} - \nabla\tilde{\phi}) dV} \quad (8.6)$$

subjected to periodic boundary conditions (8.4). It defines the macroscopic stress potential as the stationary volume average of the micro-potential ψ for fluctuation fields satisfying the periodic boundary conditions. Such a variational principle is not only mathematically elegant, but also provides the basis for the finite element discretization. It leads to symmetric tangent matrices such that fast symmetric solvers can be applied in the numerical solution strategy to the highly nonlinear problem. The macro-potential $\bar{\psi}$ is assumed to define the macroscopic nominal stress $\bar{\mathbf{P}}$ and electric displacement $\bar{\mathbb{D}}$ as well as the mechanical, coupling, and electric moduli by

$$\begin{aligned} \bar{\mathbf{P}} &= \partial_{\bar{\mathbf{F}}}\bar{\psi}(\bar{\mathbf{F}}, \bar{\mathbb{E}}) & \bar{\mathbf{A}} &= \partial_{\bar{\mathbf{F}}\bar{\mathbf{F}}}^2\bar{\psi}(\bar{\mathbf{F}}, \bar{\mathbb{E}}) \\ -\bar{\mathbb{D}} &= \partial_{\bar{\mathbb{E}}}\bar{\psi}(\bar{\mathbf{F}}, \bar{\mathbb{E}}) & \bar{\mathbb{H}} &= \partial_{\bar{\mathbf{F}}\bar{\mathbb{E}}}^2\bar{\psi}(\bar{\mathbf{F}}, \bar{\mathbb{E}}) \\ & & \bar{\boldsymbol{\epsilon}} &= \partial_{\bar{\mathbb{E}}\bar{\mathbb{E}}}^2\bar{\psi}(\bar{\mathbf{F}}, \bar{\mathbb{E}}) \end{aligned} \quad (8.7)$$

The stationary variational principle (8.6) provides the shift of microscopic variables to their macroscopic counterparts, often denoted as micro-to-macro transition or scale bridging. The electro-mechanically coupled principle extends the average variational principle

of nonlinear elasticity PONTE CASTAÑEDA [149], PONTE CASTAÑEDA & SUQUET [152] and incremental principles for dissipative response MIEHE [116] to the coupled context.

The state of the microstructure is determined by the variational principle (8.6) expect rigid body motions which are excluded by adding some artificial constraints, that is, the fluctuations are suppressed on the corner nodes of the finite element mesh. The necessary condition of this principle results in the first variation with respect to the fluctuation fields

$$\begin{aligned} 0 = & \int_{\partial\mathcal{B}} \delta\tilde{\boldsymbol{\varphi}} \cdot (\partial_{\mathbf{F}}\psi\mathbf{N}) dA - \int_{\mathcal{B}} \delta\tilde{\boldsymbol{\varphi}} \cdot \text{Div}[\partial_{\mathbf{F}}\psi] dV \\ & - \int_{\partial\mathcal{B}} \delta\tilde{\phi}(\partial_{\mathbb{E}}\psi\mathbf{N}) dA - \int_{\mathcal{B}} \delta\tilde{\phi} \text{Div}[-\partial_{\mathbb{E}}\psi] dV. \end{aligned} \quad (8.8)$$

Due to the periodicity constraint on the fluctuation field, the latter can be recast into

$$\begin{aligned} 0 = & \int_{\partial\mathcal{B}} \delta\tilde{\boldsymbol{\varphi}} \cdot \frac{1}{2} [(\partial_{\mathbf{F}}\psi\mathbf{N})^+ + (\partial_{\mathbf{F}}\psi\mathbf{N})^-] dA - \frac{1}{|\mathcal{B}|} \int_{\mathcal{B}} \delta\tilde{\boldsymbol{\varphi}} \cdot \text{Div}[\partial_{\mathbf{F}}\psi] dV \\ & - \int_{\partial\mathcal{B}} \delta\tilde{\phi} \frac{1}{2} [(\partial_{\mathbb{E}}\psi\mathbf{N})^+ + (\partial_{\mathbb{E}}\psi\mathbf{N})^-] dA - \frac{1}{|\mathcal{B}|} \int_{\mathcal{B}} \delta\tilde{\phi} \text{Div}[-\partial_{\mathbb{E}}\psi] dV, \end{aligned} \quad (8.9)$$

where $(\cdot)^+$ and $(\cdot)^-$ denote quantities evaluated at associated points $\mathbf{X}^+ \in \partial\mathcal{B}^+$ and $\mathbf{X}^- \in \partial\mathcal{B}^-$ on the surface of the microstructure. For arbitrary virtual fluctuations $\{\delta\tilde{\boldsymbol{\varphi}}, \delta\tilde{\phi}\} \neq \mathbf{0}$, the Euler-Lagrange equations of the variational principle are obtained as the balance of linear momentum and the Gauss law

$$\begin{aligned} \text{Div}[\partial_{\mathbf{F}}\psi] = \mathbf{0} \text{ in } \mathcal{B} \quad \text{and} \quad (\partial_{\mathbf{F}}\psi\mathbf{N})^+ = -(\partial_{\mathbf{F}}\psi\mathbf{N})^- \text{ on } \partial\mathcal{B} \\ \text{Div}[-\partial_{\mathbb{E}}\psi] = 0 \text{ in } \mathcal{B} \quad \text{and} \quad (\partial_{\mathbb{E}}\psi\mathbf{N})^+ = -(\partial_{\mathbb{E}}\psi\mathbf{N})^- \text{ on } \partial\mathcal{B} \end{aligned} \quad (8.10)$$

The principle is consistent with an equilibrium state of the microstructure with anti-periodic tractions and surface charges on the boundary $\partial\mathcal{B}$.

8.1.3. Finite element solution of homogenization problem

An approximative numerical solution of the variational principle (8.6) is obtained by the finite element method. For this purpose, a general notation is adopted where the primary fluctuation fields are summed up in a single quantity leading to a generalized gradient

$$\tilde{\mathbf{d}} := \{\tilde{\boldsymbol{\varphi}}, -\tilde{\phi}\} \quad \text{and} \quad \tilde{\mathbf{F}} := \nabla\tilde{\mathbf{d}} = \{\nabla\tilde{\boldsymbol{\varphi}}, -\nabla\tilde{\phi}\}. \quad (8.11)$$

The additive decomposition of the deformation gradient and the electric field of the microstructure can be written in the format $\mathbf{F} = \bar{\mathbf{F}} + \tilde{\mathbf{F}}$, where the generalized homogeneous macroscopic part $\bar{\mathbf{F}} := \{\bar{\mathbf{F}}, \bar{\mathbb{E}}\}$ collects mechanical as well as electric contributions. The proposed notation leads to the representation of boundary conditions

$$\tilde{\mathbf{d}} \in \mathcal{W} := \{\tilde{\mathbf{d}} \in \mathcal{W}^{1,p}(\mathcal{B}) \mid \tilde{\mathbf{d}}^+ = \tilde{\mathbf{d}}^- \text{ on } \partial\mathcal{B}\}. \quad (8.12)$$

The variational principle of homogenization provides the starting point for the numerical implementation. To this end, the generalized fluctuation field and its gradient are discretized on element level by

$$\tilde{\mathbf{d}} \approx \tilde{\mathbf{d}}^h = \underline{\mathbf{N}}_e(\mathbf{X})\mathbf{d}_e \quad \text{and} \quad \tilde{\mathbf{F}} \approx \tilde{\mathbf{F}}^h = \underline{\mathbf{B}}_e(\mathbf{X})\mathbf{d}_e, \quad (8.13)$$

small strain context. Note that the first and second derivative of the energy functional ψ with respect to the generalized gradient are coupled finite element arrays stored in Voigt notation as

$$\mathbf{S} := \partial_{\mathbf{F}}\psi = \begin{bmatrix} \partial_{\mathbf{F}}\psi \\ \partial_{\mathbf{E}}\psi \end{bmatrix}_{12 \times 1} \quad \text{and} \quad \mathbf{C} := \partial_{\mathbf{FF}}^2\psi = \begin{bmatrix} \partial_{\mathbf{FF}}^2\psi & \partial_{\mathbf{FE}}^2\psi \\ \partial_{\mathbf{EF}}^2\psi & \partial_{\mathbf{EE}}^2\psi \end{bmatrix}_{12 \times 12} \quad (8.18)$$

Hence, the finite dimensional discretization of the variational principle of homogenization (8.6) can be written as

$$\boxed{\bar{\psi}(\bar{\mathbf{F}}) = \text{stat}_{\underline{\mathbf{d}}} \bar{\psi}^h(\bar{\mathbf{F}}, \underline{\mathbf{d}})} \quad (8.19)$$

The necessary condition of this discrete stationary problem

$$\bar{\psi}_{,\underline{\mathbf{d}}}^h = \mathbf{0} \quad (8.20)$$

provides a nonlinear algebraic system of equations for the determination of the global fluctuation field $\underline{\mathbf{d}}$ in the microstructure, usually solved by an iterative Newton-Raphson scheme yielding the update

$$\underline{\mathbf{d}} \leftarrow \underline{\mathbf{d}} - [\bar{\psi}_{,\underline{\mathbf{d}}\underline{\mathbf{d}}}^h]^{-1} [\bar{\psi}_{,\underline{\mathbf{d}}}^h] \quad (8.21)$$

till the residuum $\|\bar{\psi}_{,\underline{\mathbf{d}}}^h(\underline{\mathbf{d}}^*)\| < \text{tol}$ is smaller than a certain tolerance at the solution $\underline{\mathbf{d}}^*$ of (8.19). This outlines again the special character of the variational principle of homogenization, which governs the micro-to-macro transition and is fully characterized by the function $\bar{\psi}^h$ defined in (8.16).

8.1.4. Generalized macro-stress and moduli

With the solution of the variational principle $\underline{\mathbf{d}}^*$ at hand, the macroscopic stresses and moduli are computed based on a straightforward exploitation of definition (8.7). If a microscopic equilibrium state is reached at $\underline{\mathbf{d}}^*$, the generalized macro-stress is determined by the derivative of the function (8.16) with respect to the generalized gradient $\bar{\mathbf{F}}$ as

$$\bar{\mathbf{S}} := \partial_{\bar{\mathbf{F}}}\bar{\psi} = \bar{\psi}_{,\bar{\mathbf{F}}}^h + [\bar{\psi}_{,\underline{\mathbf{d}}\bar{\mathbf{F}}}^h][\underline{\mathbf{d}},\bar{\mathbf{F}}] = \bar{\psi}_{,\bar{\mathbf{F}}}^h, \quad (8.22)$$

that is the volume average of the microscopic counterpart defined in (8.17)₁. The last term vanishes due to the necessary condition (8.20) of the coupled problem. The second derivative specifies the coupled macro-moduli

$$\bar{\mathbf{C}} := \partial_{\bar{\mathbf{F}}\bar{\mathbf{F}}}^2\bar{\psi} = \bar{\psi}_{,\bar{\mathbf{F}}\bar{\mathbf{F}}}^h + [\bar{\psi}_{,\underline{\mathbf{d}}\bar{\mathbf{F}}\bar{\mathbf{F}}}^h][\underline{\mathbf{d}},\bar{\mathbf{F}}] = \bar{\psi}_{,\bar{\mathbf{F}}\bar{\mathbf{F}}}^h - [\bar{\psi}_{,\underline{\mathbf{d}}\bar{\mathbf{F}}\bar{\mathbf{F}}}^h][\bar{\psi}_{,\underline{\mathbf{d}}\underline{\mathbf{d}}}^h]^{-1}[\bar{\psi}_{,\underline{\mathbf{d}}\bar{\mathbf{F}}}^h] \quad (8.23)$$

in terms of the finite element matrices introduced in (8.17)_{3,4,5}. The sensitivity of the discrete fluctuation fields with respect to the macroscopic gradients is obtained by the implicit function theorem, that is the linearization of the microscopic equilibrium condition (8.20) in the form

$$\bar{\psi}_{,\underline{\mathbf{d}}\bar{\mathbf{F}}}^h + \bar{\psi}_{,\underline{\mathbf{d}}\underline{\mathbf{d}}\bar{\mathbf{F}}}^h \underline{\mathbf{d}},\bar{\mathbf{F}} = \mathbf{0} \quad \longrightarrow \quad \underline{\mathbf{d}},\bar{\mathbf{F}} = -[\bar{\psi}_{,\underline{\mathbf{d}}\underline{\mathbf{d}}}^h]^{-1}[\bar{\psi}_{,\underline{\mathbf{d}}\bar{\mathbf{F}}}^h]. \quad (8.24)$$

Observe that the coupled macro-moduli ¹ consist of the volume average of the microscopic moduli and a softening part, which is the consequence of the flexibility of the microstructure. In (8.23), the term $[\bar{\psi}_{,\underline{\mathbf{d}}\underline{\mathbf{d}}}^h]^{-1}[\bar{\psi}_{,\underline{\mathbf{d}}\bar{\mathbf{F}}}^h]$ is obtained by twelve backward substitutions for a triangular decomposition of the stiffness matrix $\bar{\psi}_{,\underline{\mathbf{d}}\underline{\mathbf{d}}}^h$ associated with the rows of $\bar{\psi}_{,\underline{\mathbf{d}}\bar{\mathbf{F}}}^h$.

¹An explicit representation of the coupled moduli is obtained by specifying the finite element discretization as $\tilde{\mathbf{F}} \approx \tilde{\underline{\mathbf{F}}}^h = \mathbf{B}_{\varphi}^e(\mathbf{X})\underline{\mathbf{d}}_{\varphi}^e$ and $\tilde{\mathbf{E}} \approx \tilde{\underline{\mathbf{E}}}^h = \mathbf{B}_{\varphi}^e(\mathbf{X})\underline{\mathbf{d}}_{\varphi}^e$. The global nodal fluctuations are

8.2. Variational formulation of the macroscopic response

Throughout this section quantities associated with the macroscopic scale will be labeled with a bar. The macroscopic body of interest is denoted by $\bar{\mathcal{B}} \subset \mathcal{R}^3$ and parametrized in the reference coordinates $\bar{\mathbf{X}} \in \bar{\mathcal{B}}$.

8.2.1. Variational formulation of finite electro-mechanics

Let $\bar{\varphi} : \bar{\mathcal{B}} \times \mathcal{R} \rightarrow \mathcal{R}^3$ and $\bar{\phi} : \bar{\mathcal{B}} \times \mathcal{R} \rightarrow \mathcal{R}$ denote the deformation map and electric potential of the macrostructure. Then, the macroscopic deformation gradient tensor and electric field vector are defined as $\bar{\mathbf{F}} = \bar{\nabla} \bar{\varphi}$ and $\bar{\mathbb{E}} = -\bar{\nabla} \bar{\phi}$, respectively. Based on the definition of the macro-potential density $\bar{\psi}$ through the variational principle of homogenization (8.6), a macroscopic variational principle of the coupled response is defined as

$$\boxed{\{\bar{\varphi}, \bar{\phi}\} = \arg \left\{ \inf_{\bar{\varphi}} \sup_{\bar{\phi}} \bar{\Pi}(\bar{\varphi}, \bar{\phi}) \right\}} \quad (8.25)$$

in terms of the stress potential for pure Dirichlet problems

$$\bar{\Pi}(\bar{\varphi}, \bar{\phi}) = \int_{\bar{\mathcal{B}}} \bar{\psi}(\bar{\mathbf{F}}, \bar{\mathbb{E}}) dV \quad (8.26)$$

neglecting body forces, surface tractions, and surface charges for the sake of brevity. A possible incorporation of external source terms is shown in [Chapter 7](#). The primary fields are subjected to Dirichlet boundary conditions in terms of prescribed displacements and electric potential on the surface of the macrostructure. Taking the first variation of (8.25), the balance of linear momentum and the Gauss law follow together with the homogeneous Neumann-type boundary conditions as the Euler-Lagrange equations

$$\begin{aligned} \text{Div}[\partial_{\bar{\mathbf{F}}} \bar{\psi}] &= \mathbf{0} \text{ in } \bar{\mathcal{B}} & \text{and} & & \partial_{\bar{\mathbf{F}}} \bar{\psi} \bar{\mathbf{N}} &= \mathbf{0} \text{ on } \partial \bar{\mathcal{B}}_t \\ \text{Div}[-\partial_{\bar{\mathbb{E}}} \bar{\psi}] &= 0 \text{ in } \bar{\mathcal{B}} & & & \partial_{\bar{\mathbb{E}}} \bar{\psi} \bar{\mathbf{N}} &= 0 \text{ on } \partial \bar{\mathcal{B}}_d \end{aligned} \quad (8.27)$$

Note that the macroscopic stress and electric displacement are defined through the variational principle of homogenization defining the macroscopic potential density $\bar{\psi}$.

then obtained by a standard finite element assembly procedure. With this at hand, the coupled moduli including softening terms are

$$\bar{\mathbf{C}} = \bar{\psi}_{,\bar{\mathbf{F}}\bar{\mathbf{F}}}^h - [\bar{\psi}_{,\bar{\mathbf{F}}\bar{\mathbf{d}}}^h][\bar{\psi}_{,\bar{\mathbf{d}}\bar{\mathbf{d}}}^h]^{-1}[\bar{\psi}_{,\bar{\mathbf{d}}\bar{\mathbf{F}}}^h] = \frac{1}{|\bar{\mathcal{B}}|} \mathbf{A}_{e=1}^{E^h} \int_{\mathcal{B}_e^h} \mathbf{C} dV - [\bar{\psi}_{,\bar{\mathbf{F}}\bar{\mathbf{d}}}^h][\bar{\psi}_{,\bar{\mathbf{d}}\bar{\mathbf{d}}}^h]^{-1}[\bar{\psi}_{,\bar{\mathbf{d}}\bar{\mathbf{F}}}^h]$$

where the generalized micro-moduli are defined in (8.18)₂ and

$$\bar{\psi}_{,\bar{\mathbf{d}}\bar{\mathbf{F}}}^h = \begin{bmatrix} \bar{\psi}_{,\bar{\mathbf{d}}_\varphi \bar{\mathbf{F}}}^h & \bar{\psi}_{,\bar{\mathbf{d}}_\varphi \bar{\mathbb{E}}}^h \\ \bar{\psi}_{,\bar{\mathbf{d}}_\phi \bar{\mathbf{F}}}^h & \bar{\psi}_{,\bar{\mathbf{d}}_\phi \bar{\mathbb{E}}}^h \end{bmatrix} \quad \text{and} \quad \bar{\psi}_{,\bar{\mathbf{d}}\bar{\mathbf{d}}}^h = \begin{bmatrix} \bar{\psi}_{,\bar{\mathbf{d}}_\varphi \bar{\mathbf{d}}_\varphi}^h & \bar{\psi}_{,\bar{\mathbf{d}}_\varphi \bar{\mathbf{d}}_\phi}^h \\ \bar{\psi}_{,\bar{\mathbf{d}}_\phi \bar{\mathbf{d}}_\varphi}^h & \bar{\psi}_{,\bar{\mathbf{d}}_\phi \bar{\mathbf{d}}_\phi}^h \end{bmatrix}$$

are the sensitivity and the global stiffness matrix of the finite element simulation.

8.2.2. Finite element discretization of the macroscopic response

In complete analogy to the micro-problem, the generalized displacement is introduced as $\bar{\mathbf{d}} := \{\bar{\varphi}, -\bar{\phi}\}$ defining the macroscopic gradient as $\bar{\mathbf{F}} = \bar{\nabla} \bar{\mathbf{d}} := \{\bar{\mathbf{F}}, \bar{\mathbf{E}}\}$. An approximative numerical solution of the stationary problem (8.25) can be obtained by the finite element method. To this end, the macroscopic displacement field and electric potential as well as their gradients are discretized by

$$\bar{\mathbf{d}} \approx \bar{\mathbf{d}}^h = \bar{\mathbf{N}}_e(\bar{\mathbf{X}}) \bar{\mathbf{d}}_e \quad \text{and} \quad \bar{\mathbf{F}} \approx \bar{\mathbf{F}}^h = \bar{\mathbf{B}}_e(\bar{\mathbf{X}}) \bar{\mathbf{d}}_e, \quad (8.28)$$

where the continuous body consists of \bar{E}^h finite elements $\bar{\mathcal{B}}_e^h \subset \bar{\mathcal{B}}$. Then,

$$\bar{\mathbf{d}} = \mathbf{A} \bar{\mathbf{d}}_e \in \mathcal{R}^{(d+1)\bar{N}^h} \quad (8.29)$$

is the finite-dimensional vector of nodal displacements associated with the finite element mesh of the macrostructure. Insertion of the approximations (8.28) into (8.25) defines the function

$$\bar{\Pi}^h(\bar{\mathbf{d}}) = \mathbf{A} \int_{\bar{\mathcal{B}}_e^h} \bar{\psi}(\bar{\mathbf{B}}_e \bar{\mathbf{d}}_e) dV. \quad (8.30)$$

The first and second derivative of this function define all macroscopic finite element arrays

$$\bar{\Pi}_{,\bar{\mathbf{d}}}^h = \mathbf{A} \int_{\bar{\mathcal{B}}_e^h} \bar{\mathbf{B}}_e^T \partial_{\bar{\mathbf{F}}} \bar{\psi} dV \quad \text{and} \quad \bar{\Pi}_{,\bar{\mathbf{d}}\bar{\mathbf{d}}}^h = \mathbf{A} \int_{\bar{\mathcal{B}}_e^h} \bar{\mathbf{B}}_e^T \partial_{\bar{\mathbf{F}}\bar{\mathbf{F}}}^2 \bar{\psi} \bar{\mathbf{B}}_e dV \quad (8.31)$$

needed below. Here, the first and second derivative of the homogenized generalized stress potential density $\bar{\psi}$ are the macro-stresses $\bar{\mathbf{S}} := \partial_{\bar{\mathbf{F}}} \bar{\psi}$ and the macro-moduli $\bar{\mathbf{C}} := \partial_{\bar{\mathbf{F}}\bar{\mathbf{F}}}^2 \bar{\psi}$ defined in (8.22) and (8.23), respectively. The consistent algorithmic moduli are characterized by the volume average of the microscopic moduli and a softening term due to the sensitivity of the microstructure. The finite-dimensional discretized form of the variational principle (8.25) then reads

$$\boxed{\bar{\mathbf{d}} = \arg \left\{ \text{stat}_{\bar{\mathbf{d}}} \bar{\Pi}^h(\bar{\mathbf{d}}) \right\}} \quad (8.32)$$

The necessary condition of this discrete stationary problem

$$\bar{\Pi}_{,\bar{\mathbf{d}}}^h = \mathbf{0} \quad (8.33)$$

provides a nonlinear algebraic system for the determination of the vector $\bar{\mathbf{d}}$ of discrete generalized displacements of the macrostructure. It can be solved by a Newton-Raphson iteration yielding the update equation

$$\bar{\mathbf{d}} \leftarrow \bar{\mathbf{d}} - [\bar{\Pi}_{,\bar{\mathbf{d}}\bar{\mathbf{d}}}^h]^{-1} [\bar{\Pi}_{,\bar{\mathbf{d}}}^h] \quad (8.34)$$

performed by a solver of linear equations. The iteration is terminated for $\|\bar{\Pi}_{,\bar{\mathbf{d}}}^h(\bar{\mathbf{d}}^*)\| < \text{tol}$, where $\bar{\mathbf{d}}^*$ is considered to be the solution of the macroscopic variational principle (8.32).

8.3. Infinitesimal material stability analysis

Starting point of the stability analysis is a *minimization structure* of the corresponding variational principle. This section outlines an extension of purely mechanical stability criteria to electro-mechanics. First, an energy-based formulation is concerned which is then transformed to a saddle point structure of the enthalpy-based formulation in terms of the deformation gradient and the electric field. The topic of structural and material stability analysis for coupled problems is discussed in more detail in the recent work MIEHE ET AL. [134]. A common structure for a local material stability analysis is outlined independent of the proposed variational-based homogenization framework. However, it is developed exemplary for the macroscopic material response discussed in the previous section. Theoretical investigations of stability problems are outlined in the books THOMPSON & HUNT [185] and PFLÜGER [147]. The numerical treatment is discussed in MIEHE & SCHRÖDER [124], SCHRÖDER [160], and MIEHE ET AL. [128].

8.3.1. Material stability analysis of the energy formulation

To analyze the material stability condition in coupled electro-mechanics, we start from a purely energetic formulation leading to a *minimization structure*. The energy density is constraint to be polyconvex in the deformation gradient $\bar{\mathbf{F}}$ and convex in the electric displacement vector $\bar{\mathbf{D}}$.

The canonical variational principle. Consider as a variational potential of electro-elastostatics the functional

$$\bar{\Pi}'(\bar{\varphi}, \bar{\mathbf{D}}) = \int_{\bar{\mathcal{B}}} \bar{\psi}'(\bar{\mathbf{F}}, \bar{\mathbf{D}}) dV \quad (8.35)$$

depending on the deformation field $\bar{\varphi}$ and the material electric induction $\bar{\mathbf{D}}$. Note that external source terms are neglected for the sake of brevity and we treat pure Dirichlet problems. The potential is governed by the energy density function $\bar{\psi}'$ that described locally the free energy per unit volume stored in the deformable dielectric. With this potential at hand, the coupled boundary-value-problem of finite electro-elastostatics is governed by the *minimization principle*

$$\{\bar{\varphi}, \bar{\mathbf{D}}\} = \arg \left\{ \inf_{\bar{\varphi} \in \mathcal{W}_{\bar{\varphi}}} \inf_{\bar{\mathbf{D}} \in \mathcal{W}_{\bar{\mathbf{D}}}} \bar{\Pi}'(\bar{\varphi}, \bar{\mathbf{D}}) \right\} \quad (8.36)$$

Within this variational principle, the space of admissible functions for the deformation field satisfies the Dirichlet boundary conditions

$$\bar{\varphi} \in \mathcal{W}_{\bar{\varphi}} := \{\bar{\varphi} \mid \bar{\varphi} = \bar{\varphi}_D \text{ on } \partial\bar{\mathcal{B}}\}. \quad (8.37)$$

The space of admissible functions for the electric displacement satisfies a priori the Gauss law for the conservation of charges

$$\bar{\mathbf{D}} \in \mathcal{W}_{\bar{\mathbf{D}}} := \{\bar{\mathbf{D}} \mid \text{Div}[\bar{\mathbf{D}}] = 0 \text{ in } \bar{\mathcal{B}} \text{ and } \bar{\mathbf{D}} \cdot \bar{\mathbf{N}} = 0 \text{ on } \partial\bar{\mathcal{B}}\}. \quad (8.38)$$

We refer to PONTE CASTAÑEDA & SIBONI [151] for a finite-strain constitutive theory of electro-active polymer composites via homogenization discussing the energy-based formulation in more detail.

Local material stability criterion. Introduce the state of the energy-based formulation characterized by a given deformation field and electric displacement

$$\bar{\mathbf{s}}' := \{\bar{\boldsymbol{\varphi}}, \bar{\mathbb{D}}\} \text{ in } \bar{\mathcal{B}} \quad (8.39)$$

which satisfy the electro-mechanical minimization principle (8.36). An electro-mechanical state $\bar{\mathbf{s}}'_1$ is said to be *globally stable* if

$$\bar{\Pi}'(\bar{\mathbf{s}}'_2) - \bar{\Pi}'(\bar{\mathbf{s}}'_1) > 0 \quad (8.40)$$

holds for any other admissible state $\bar{\mathbf{s}}'_2$ satisfying the essential boundary conditions $\bar{\boldsymbol{\varphi}}_2 \in \mathcal{W}_{\bar{\boldsymbol{\varphi}}}$ and $\bar{\mathbb{D}}_2 \in \mathcal{W}_{\bar{\mathbb{D}}}$. Then the state $\bar{\mathbf{s}}'_1$ provides an absolute minimum of the energy functional (8.35) and according to HILL [61] is said to be a unique solution. This assumption is too restrictive in finite elasticity, see OGDEN [142, pp.354]. However, if $\bar{\mathbf{s}}'_2 = \bar{\mathbf{s}}'_1 + \epsilon \delta \bar{\mathbf{s}}'$ is confined to a local neighborhood of $\bar{\mathbf{s}}'_1$, then (8.40) is a suitable *infinitesimal stability criterion*, see TRUESDELL & NOLL [194, pp.252]. Here, $\epsilon \delta \bar{\mathbf{s}}'$ is a scaled perturbation of the equilibrium state. A Taylor series expansion of the global stability criterion truncated after the quadratic term yields

$$\bar{\Pi}'(\bar{\mathbf{s}}'_2) - \bar{\Pi}'(\bar{\mathbf{s}}'_1) = \left. \frac{d}{d\epsilon} \right|_{\epsilon=0} \bar{\Pi}'(\bar{\mathbf{s}}'_1 + \epsilon \delta \bar{\mathbf{s}}') + \frac{1}{2!} \left. \frac{d^2}{d\epsilon^2} \right|_{\epsilon=0} \bar{\Pi}'(\bar{\mathbf{s}}'_1 + \epsilon \delta \bar{\mathbf{s}}') > 0, \quad (8.41)$$

where the first and second directional derivatives are identical to the first and second variation of the functional (8.35) at the equilibrium state $\bar{\mathbf{s}}'_1$. As the first variation indicates an equilibrium state and hence vanishes, we obtain

$$\bar{\Pi}'(\bar{\mathbf{s}}'_2) - \bar{\Pi}'(\bar{\mathbf{s}}'_1) = \frac{1}{2} \left. \frac{d^2}{d\epsilon^2} \right|_{\epsilon=0} \bar{\Pi}'(\bar{\mathbf{s}}'_1 + \epsilon \delta \bar{\mathbf{s}}') > 0 \quad (8.42)$$

for a locally stable deformation state $\bar{\mathbf{s}}'_1$. This second variation of the potential (8.35) at the equilibrium state may be computed in a straightforward manner by

$$\boxed{\bar{\Pi}(\bar{\mathbf{s}}'_2) - \bar{\Pi}(\bar{\mathbf{s}}'_1) = \frac{1}{2} \int_{\bar{\mathcal{B}}} \begin{bmatrix} \delta \bar{\mathbf{F}} \\ \delta \bar{\mathbb{D}} \end{bmatrix} \cdot \begin{bmatrix} \frac{\partial^2 \bar{\psi}'}{\partial \bar{\mathbf{F}} \partial \bar{\mathbf{F}}} & \frac{\partial^2 \bar{\psi}'}{\partial \bar{\mathbf{F}} \partial \bar{\mathbb{D}}} \\ \frac{\partial^2 \bar{\psi}'}{\partial \bar{\mathbb{D}} \partial \bar{\mathbf{F}}} & \frac{\partial^2 \bar{\psi}'}{\partial \bar{\mathbb{D}} \partial \bar{\mathbb{D}}} \end{bmatrix} \cdot \begin{bmatrix} \delta \bar{\mathbf{F}} \\ \delta \bar{\mathbb{D}} \end{bmatrix} dV > 0} \quad (8.43)$$

as the necessary condition to determine *stable equilibrium states* in a local neighborhood.

8.3.2. Material stability analysis of the enthalpy formulation

The stability analysis for a mixed enthalpy-based formulation leads to a saddle point structure. The electric enthalpy density is still constraint to be polyconvex in the deformation gradient but concave in the electric field due to the Legendre transformation.

The mixed variational principle. The electric enthalpy density function can be expressed in terms of the energy density function $\bar{\psi}'$ by a local Legendre transformation in the electric slot

$$\bar{\psi}(\bar{\mathbf{F}}, \bar{\mathbb{E}}) = \inf_{\bar{\mathbb{D}}} [\bar{\psi}'(\bar{\mathbf{F}}, \bar{\mathbb{D}}) - \bar{\mathbb{E}} \cdot \bar{\mathbb{D}}]. \quad (8.44)$$

This defines an enthalpy-based variational potential

$$\bar{\Pi}(\bar{\varphi}, \bar{\phi}) = \int_{\bar{\mathcal{B}}} \bar{\psi}(\bar{\mathbf{F}}, \bar{\mathbb{E}}) dV \quad (8.45)$$

depending on the deformation field $\bar{\varphi}$ and the material electric potential $\bar{\phi}$, see also (8.26) above. The boundary-value-problem of finite electro-elastostatics is then governed by the *saddle point principle*

$$\{\bar{\varphi}, \bar{\phi}\} = \arg \left\{ \inf_{\bar{\varphi} \in \mathcal{W}_{\bar{\varphi}}} \sup_{\bar{\phi} \in \mathcal{W}_{\bar{\phi}}} \bar{\Pi}(\bar{\varphi}, \bar{\phi}) \right\} \quad (8.46)$$

The space of admissible functions for the deformation map is still constraint by (8.37) and for the electric potential it provides an equipotential on the surface

$$\bar{\phi} \in \mathcal{W}_{\bar{\phi}} := \{\bar{\phi} \mid \bar{\phi} = \bar{\phi}_D \text{ on } \partial\bar{\mathcal{B}}\}. \quad (8.47)$$

Local material stability criterion. Introduce a mixed electro-mechanical state characterized by a given deformation field and electric potential

$$\bar{\mathbf{s}} := \{\bar{\varphi}, \bar{\phi}\} \text{ in } \bar{\mathcal{B}} \quad (8.48)$$

satisfying the saddle-point principle (8.46). Starting point for the determination of a local enthalpy-based stability criterion is again the minimizing structure of the energy-based formulation (8.41). The potential of electro-elastostatics (8.35) can be modified by the Legendre transformation for the electric energy

$$\bar{\psi}'(\bar{\mathbf{F}}, \bar{\mathbb{D}}) = \sup_{\bar{\mathbb{E}}} [\bar{\psi}(\bar{\mathbf{F}}, \bar{\mathbb{E}}) + \bar{\mathbb{D}} \cdot \bar{\mathbb{E}}] \quad (8.49)$$

such that it is governed by three independent fields, that is, the deformation map, the electric potential, and the electric induction. The local stability criterion in terms of these three fields then reads

$$\frac{1}{2} \int_{\bar{\mathcal{B}}} \begin{bmatrix} \delta \bar{\mathbf{F}} \\ \delta \bar{\mathbb{E}} \end{bmatrix} \cdot \begin{bmatrix} \partial_{\bar{\mathbf{F}} \bar{\mathbf{F}}}^2 \bar{\psi} & \partial_{\bar{\mathbf{F}} \bar{\mathbb{E}}}^2 \bar{\psi} \\ \partial_{\bar{\mathbb{E}} \bar{\mathbf{F}}}^2 \bar{\psi} & \partial_{\bar{\mathbb{E}} \bar{\mathbb{E}}}^2 \bar{\psi} \end{bmatrix} \cdot \begin{bmatrix} \delta \bar{\mathbf{F}} \\ \delta \bar{\mathbb{E}} \end{bmatrix} dV + 2\delta \bar{\mathbb{D}} \cdot \delta \bar{\mathbb{E}} > 0. \quad (8.50)$$

The necessary condition of the Legendre transformation $\bar{\mathbb{D}} = -\partial_{\bar{\mathbb{E}}} \bar{\psi}$ results in the elimination equation for the electric displacement

$$\delta \bar{\mathbb{D}} = -\partial_{\bar{\mathbb{E}} \bar{\mathbf{F}}}^2 \bar{\psi} : \delta \bar{\mathbf{F}} - \partial_{\bar{\mathbb{E}} \bar{\mathbb{E}}}^2 \bar{\psi} \cdot \delta \bar{\mathbb{E}}. \quad (8.51)$$

Insertion of the latter into the criterion (8.50) gives a statement for the local material stability of an enthalpy-based formulation to determine stable equilibrium states in a local neighborhood

$$\bar{\Pi}(\bar{\mathbf{s}}_2) - \bar{\Pi}(\bar{\mathbf{s}}_1) = \frac{1}{2} \int_{\bar{\mathcal{B}}} \begin{bmatrix} \delta \bar{\mathbf{F}} \\ \delta \bar{\mathbb{E}} \end{bmatrix} \cdot \begin{bmatrix} \partial_{\bar{\mathbf{F}} \bar{\mathbf{F}}}^2 \bar{\psi} & \mathbf{0} \\ \mathbf{0} & -\partial_{\bar{\mathbb{E}} \bar{\mathbb{E}}}^2 \bar{\psi} \end{bmatrix} \cdot \begin{bmatrix} \delta \bar{\mathbf{F}} \\ \delta \bar{\mathbb{E}} \end{bmatrix} dV > 0 \quad (8.52)$$

Note the decoupled structure enforcing the positive definiteness of the mechanical as well as (negative) electrical tangents.

8.4. FE² driver for homogeneous macro-problems

Consider the formulation of an algorithmic FE² driver for three-dimensional representative volume elements at the microscale. This driver solves *two nested boundary-value problems* coupled by the variational principle of homogenization outlined in Section 8.1. The inhomogeneous microscopic problem is solved by a finite element scheme while the macrostructure is assumed to be homogeneous. The goal is to *solve generalized stress and deformation driven processes* under the additional constraint of a macroscopic stress-free state ($\bar{\mathbf{P}} = \mathbf{0}$) and open circuit conditions ($\bar{\mathbf{D}} = \mathbf{0}$). This stress-free state is given up as soon as stresses or deformations are prescribed in a particular direction. For the sake of simplicity, the algorithm is described in a purely mechanical framework, but can be easily extended to coupled electro-mechanics.

The crucial ingredient is the definition of a vector of unknowns $\bar{\mathbf{u}}$ containing either the deformation gradient or stress field in the particular direction. As an example consider a two-dimensional model problem with $n = 4$ degrees of freedom where the deformation gradient in axial direction \bar{F}_{11} is prescribed. Consequently, the resultant axial stress \bar{P}_{11} is unknown and the vector $\bar{\mathbf{u}}$ becomes

$$\bar{\mathbf{u}} := [\bar{P}_{11}, \bar{F}_{22}, \bar{F}_{12}, \bar{F}_{21}]^T \in \mathcal{R}^4 \quad (8.53)$$

summing up axial nominal stress and remaining deformation gradient components. Note that the assumption of a macroscopic stress-free state defines all outstanding stress components to be zero and hence that the corresponding deformations need to be determined. On the other hand, a stress driven scenario would lead to a prescribed stress \bar{P}_{11} and consequently an unknown deformation gradient \bar{F}_{11} . A symbolic representation of the equilibrium stresses is defined as

$$\bar{\mathbf{P}}_{eq}(\bar{\mathbf{u}}) := [\bar{P}_{11}, \bar{P}_{22}, \bar{P}_{12}, \bar{P}_{21}]^T \in \mathcal{R}^4 \quad (8.54)$$

combining both the unknown entry \bar{P}_{11} and prescribed slots $\bar{P}_{22} = \bar{P}_{12} = \bar{P}_{21} = 0$. The vector of unknowns $\bar{\mathbf{u}}$ is determined by formulating the nominal stress residuum expression

$$\bar{\mathbf{R}}(\bar{\mathbf{u}}) := \bar{\mathbf{P}}(\bar{\mathbf{F}}(\bar{\mathbf{u}})) - \bar{\mathbf{P}}_{eq}(\bar{\mathbf{u}}) = \mathbf{0}, \quad (8.55)$$

where $\bar{\mathbf{P}}$ are the homogenized first Piola-Kirchhoff stresses obtained as volume averages by the finite element simulation on the representative volume element. In order to solve this nonlinear problem for the unknowns $\bar{\mathbf{u}}$ a standard Newton-Raphson scheme is applied leading to the linearization

$$\text{Lin } \bar{\mathbf{R}} = \bar{\mathbf{R}}_k + \left. \frac{d\bar{\mathbf{R}}}{d\bar{\mathbf{u}}} \right|_k \Delta\bar{\mathbf{u}}_{k+1} = \mathbf{0} \quad (8.56)$$

which defines the modified tangent operator incorporating both the stress and deformation driven scenario

$$\bar{\mathbf{K}} := \frac{d\bar{\mathbf{R}}}{d\bar{\mathbf{u}}} = \frac{d}{d\bar{\mathbf{u}}} [\bar{\mathbf{P}}(\bar{\mathbf{F}}) - \bar{\mathbf{P}}_{eq}] = \partial_{\bar{\mathbf{F}}}\bar{\mathbf{P}} \cdot \partial_{\bar{\mathbf{u}}}\bar{\mathbf{F}} - \partial_{\bar{\mathbf{u}}}\bar{\mathbf{P}}_{eq}. \quad (8.57)$$

The matrix $\bar{\mathbf{A}} := \partial_{\bar{\mathbf{F}}}\bar{\mathbf{P}}$ is the homogenized mechanical stiffness of the representative volume element including softening terms due to the sensitivity of the microstructure with

respect to the fluctuation (for the electro-mechanical model the fully coupled expression $\bar{\mathbf{C}}$ outlined in (8.23) needs to be taken into account). Furthermore, there are two auxiliary diagonal matrices which are not formulated explicitly during computation but given for completeness

$$\partial_{\bar{\mathbf{u}}}\bar{\mathbf{F}} = \text{diag}[\alpha_1, \alpha_2, \dots, \alpha_n] \quad \text{and} \quad \partial_{\bar{\mathbf{u}}}\bar{\mathbf{P}}_{eq} = \text{diag}[\beta_1, \beta_2, \dots, \beta_n], \quad (8.58)$$

where $\{\alpha_i\}_{i=1,n}$ is zero if the corresponding stress is unknown and one if the deformation is unknown. $\{\beta_i\}_{i=1,n}$ is defined in the opposite manner. For the simple two-dimensional model problem, these two matrices are

$$\partial_{\bar{\mathbf{u}}}\bar{\mathbf{F}} = \text{diag}[0, 1, 1, 1] \quad \text{and} \quad \partial_{\bar{\mathbf{u}}}\bar{\mathbf{P}}_{eq} = \text{diag}[1, 0, 0, 0]. \quad (8.59)$$

The modification of the tangent matrix by the latter two matrices is obtained for the two-dimensional example under consideration as

$$\bar{\mathbf{K}} = \begin{bmatrix} -1 & \bar{A}_{12} & \bar{A}_{13} & \bar{A}_{14} \\ 0 & \bar{A}_{22} & \bar{A}_{23} & \bar{A}_{24} \\ 0 & \bar{A}_{32} & \bar{A}_{33} & \bar{A}_{34} \\ 0 & \bar{A}_{42} & \bar{A}_{43} & \bar{A}_{44} \end{bmatrix}. \quad (8.60)$$

The update for the vector of unknowns $\bar{\mathbf{u}}$ is then obtained as

$$\Delta\bar{\mathbf{u}}_{k+1} = -\bar{\mathbf{K}}_k^{-1}\bar{\mathbf{R}}_k \quad (8.61)$$

The Newton-Raphson iteration is performed until convergence is obtained in the sense $\|\bar{\mathbf{R}}\| < \text{tol}$. The crucial components for the solution of stress as well as deformation driven scenarios are the two diagonal matrices outlined in (8.58). For the specific update of the unknown values $\bar{\mathbf{u}}$ these two matrices ensure that the solution is performed in an adequate manner. The prescribed stresses are, due to the additional constraint of a stress-free state, usually zero despite the one belonging to the prescribed deformation, which is handled by the update process.

8.5. Representative numerical examples

The limitation of EAPs to be applied as artificial muscles in industrial applications is their extensive power requirement for actuation. To improve the actuation response typical EAPs with low dielectric constant ($\chi < 10$) are doped with high dielectric filler particles ($\chi > 1000$). For the current study a polyurethane (PU) elastomer is used as the matrix material and BaTiO₃ particles are used as inclusions. Figure 8.1 depicts exemplarily the microscopic boundary-value-problem with spherical inclusion of radius $r = h = b = 10.3 \mu\text{m}$ and volume fraction of 17%. The dimension of the representative volume element is $30 \mu\text{m} \times 30 \mu\text{m} \times 30 \mu\text{m}$ and solely half of the matrix material is shown. We analyze altering volume fractions for a spherical inclusion and the shape of the inclusion characterized by the aspect ratio $\omega := h/b$ with the variational-based homogenization framework outlined previously. Furthermore, microscopic zones of electro-mechanical instability are determined and visualized for a selected microstructure.

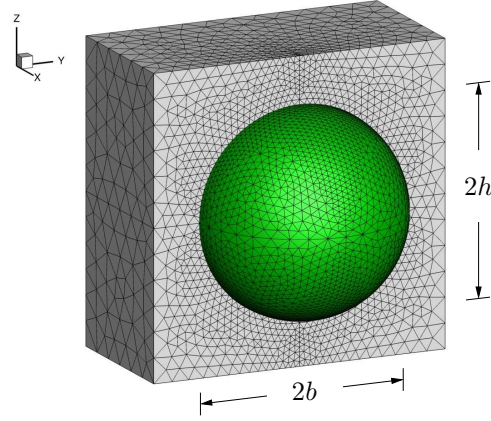


Figure 8.1: *Boundary-value-problem for two-phase composites.* Representative volume element of size $30 \mu\text{m} \times 30 \mu\text{m} \times 30 \mu\text{m}$ with stiff inclusion of high permittivity and aspect ratio $\omega = h/b$. The centers of inclusion and cubic matrix coincide in all treated cases. Exemplary a spherical inclusion discretized by 168,368 tetrahedron finite elements is shown.

8.5.1. Energy-enthalpy density function

This contribution outlines a simple model structure governing all relevant effects of coupled electro-mechanics. Two-phase composites are characterized by a polymeric matrix material such as polyurethane (PU) and stiff inclusions with high dielectric constant. The basic enthalpy density functions for the individual constituents are outlined in a modular format and normalization conditions developed. The electric enthalpy function of two-phase composites is additive decomposed into a mechanical and an electric part

$$\psi(\mathbf{F}, \mathbb{E}) = \psi_{mech}(\mathbf{F}) + \psi_{elec}(\mathbf{F}, \mathbb{E}). \quad (8.62)$$

Note that solely the electric part is assumed to be coupled to the deformation, a common assumption when dealing with ideal dielectrics.

The mechanical energy. The mechanical part of the two-phase composite is described by a neo-Hookean model for hyperelastic material response

$$\psi_{mech}(\mathbf{F}) = \frac{\mu}{2}(\text{tr}[\mathbf{C}] - 3) + \frac{\mu}{\beta}(J^{-\beta} - 1) \quad (8.63)$$

where μ is the shear modulus and β given in terms of the Poisson ration ν . The material parameter $\beta = \frac{\lambda}{\mu} = \frac{2\nu}{1-2\nu}$ can be interpreted as ratio between the first Lamé parameter λ and the shear modulus for homogeneous and isotropic materials in a small strain setting. For incompressible materials $\beta \rightarrow \infty$ due to $\nu \rightarrow 0.5$. The first term is formulated in terms of the right Cauchy-Green tensor $\mathbf{C} = \mathbf{F}^T \mathbf{g} \mathbf{F}$ as pull-back of the current metric to the reference configuration while the second depends on the determinant $J = \det[\mathbf{F}]$. Hence, the energy satisfies a priori the principle of material objectivity $\psi(\mathbf{Q}\mathbf{F}) = \psi(\mathbf{F})$ stating the independence of arbitrary rigid body rotations $\mathbf{Q} \in \mathcal{SO}(3)$ applied to the current configuration $\mathcal{S} = \varphi_t(\mathcal{B})$.

The electric enthalpy. The electric enthalpy is formulated such that it reflects the relation $d = \epsilon_0 e + \mathcal{P}$ for the electric induction in the current configuration. For a linear,

Table 8.1: Material parameters for polyurethane matrix and BaTiO₃ inclusion.

no.	para.	name	PU	BaTiO ₃	unit
1.	μ	shear modulus	1.6×10^{-6}	4.3×10^{-2}	N/ μm^2
2.	ν	Poisson ratio	0.35	0.32	–
3.	χ	electric susceptibility	4.7	1250	–

isotropic, dielectric material the polarization is assumed to be proportional to the electric field such that

$$d = \epsilon_0 e + p = \epsilon_0(1 + \tilde{\chi})e = \epsilon e \quad \text{with} \quad \tilde{\chi} = \frac{\rho\chi}{\rho_0} = \frac{\chi}{J} \quad (8.64)$$

due to the density dependent dielectric permittivity $\epsilon := \epsilon_0(1 + \tilde{\chi})$. This permittivity is formulated in terms of the deformation dependent term $\tilde{\chi} = \chi/J$ with constant electric susceptibility χ , see MCMEEKING & LANDIS [113]. A formulation of the electric enthalpy in terms of the reference electric field $\mathbb{E} = \mathbf{F}^T e$ results in the electric enthalpy

$$\psi_{elec}(\mathbf{F}, \mathbb{E}) = -\frac{\epsilon_0}{2}(1 + \frac{\chi}{J})J\mathbf{C}^{-1} : (\mathbb{E} \otimes \mathbb{E}). \quad (8.65)$$

The electric permittivity of free space is $\epsilon_0 = 8.854 \text{ N/MV}^2$, a physical constant which is the value of absolute dielectric permittivity of vacuum. The requirement for electrostriction, that is the independence of the direction of the electric field, is perfectly met by the quadratic term in \mathbb{E} .

Normalization. To obtain dimensionless quantities the enthalpy density $\psi(\mathbf{F}, \mathbb{E})$ is normalized by the shear modulus μ such that

$$\psi'(\mathbf{F}, \mathbb{E}') = \frac{1}{\mu}\psi(\mathbf{F}, \mathbb{E}). \quad (8.66)$$

For the two-phase composite under consideration this procedure defines a relative shear modulus with respect to one of the materials involved. Hence, we get for the additive split of the free energy-enthalpy the purely mechanical part and the electrostrictive coupling part

$$\psi'_{mech}(\mathbf{F}) = \frac{1}{2}(\text{tr}[\mathbf{C}] - 3) + \frac{1}{\beta}(J^{-\beta} - 1) \quad \text{and} \quad \psi'_{elec}(\mathbf{F}, \mathbb{E}') = -\frac{1}{2}(1 + \frac{\chi}{J})J\mathbf{C}^{-1} : (\mathbb{E}' \otimes \mathbb{E}'). \quad (8.67)$$

This defines the dimensionless first Piola-Kirchhoff stress, the electric field, and the electric induction by

$$\mathbf{P}' := \frac{\mathbf{P}}{\mu} = \partial_{\mathbf{F}}\psi', \quad \mathbb{E}' := \frac{\mathbb{E}}{\sqrt{\mu/\epsilon_0}}, \quad \mathbb{D}' := \frac{\mathbb{D}}{\sqrt{\mu\epsilon_0}} = -\partial_{\mathbb{E}'}\psi'. \quad (8.68)$$

The material parameters used for the two-phase composite in the subsequent simulations are outlined in [Table 8.1](#).

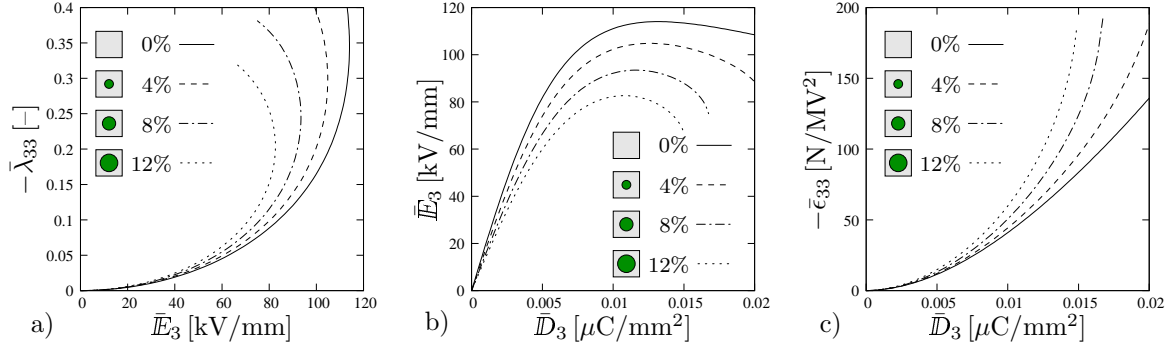


Figure 8.2: Analysis of different volume fractions for spherical inclusion. a) Influence of high dielectric filler particle on electro-mechanical response. b) Applied electric induction versus the resultant electric field showing a limit point followed by a decrease of the electric field. This limit point is usually denoted as the point of *electro-mechanical instability*. c) Increase in dielectric constant $\bar{\epsilon}_{33}$ for growing volume fraction.

8.5.2. Volume fraction of the inclusion

The two-phase composite is doped by high dielectric inclusions of different volume fractions. This procedure increases the macroscopic dielectric constant of the composite but retains the flexibility of the polymer matrix. Different volume fractions of 4%, 8%, and 12% for a spherical inclusion are considered. The radii for the three samples under consideration are $r_4 = 6.37 \mu\text{m}$ (4%), $r_8 = 8.02 \mu\text{m}$ (8%), and $r_{12} = 9.18 \mu\text{m}$ (12%). The representative volume element is driven by a macroscopic electric displacement \bar{D}_3 in vertical z -direction. The results are summarized in Figure 8.2. The consequence of a higher dielectric constant is that the electric field needed for an actuation strain $\bar{\lambda}_{33} = -0.2$ decreases from 105 kV/mm for the pure matrix material to 69 kV/mm for a volume fraction of 12%, see Figure 8.2a. The second plot compares the applied electric induction with the resultant electric field and shows a clear limit point followed by a decrease of the electric field. This limit point is usually denoted as the point of *electro-mechanical instability*. Hence, the high dielectric inclusion reduces the electric field to achieve similar deformation states at the expense of stability problems. The last plot Figure 8.2c shows the applied macroscopic electric displacement versus the dielectric constant $\bar{\epsilon}_{33} := -\partial\bar{D}_3/\partial\bar{E}_3$ as ratio between applied load and resultant electric field. Obviously, an increase in volume fraction increases the dielectric constant of the average macroscopic response. Experimental results comparing the volume fraction of the inclusion are outlined in HUANG ET AL. [69, 70] and ZHANG ET AL. [212, 209].

8.5.3. Shape of the inclusion

The actuation response of a pure matrix material is compared to two-phase composites with altering shape of the inclusion. Three cases of the dielectric inclusion with equal volume fraction of 4% are investigated: The spherical filler has dimension $\omega_o = 6.37 \mu\text{m}/6.37 \mu\text{m} = 1.00$, the vertical ellipsoidal inclusion (needle-shaped) with $\omega_{\perp} = 10.3 \mu\text{m}/5.0 \mu\text{m} = 2.06$ is stretched in the direction of the electric field, and the horizontal ellipsoidal inclusion (penny-shaped) with $\omega_{\perp} = 5.0 \mu\text{m}/10.3 \mu\text{m} = 0.48$ is stretched perpendicular to the electric field direction. Again, the representative volume element is driven by a macroscopic electric displacement \bar{D}_3 in vertical z -direction. All compo-

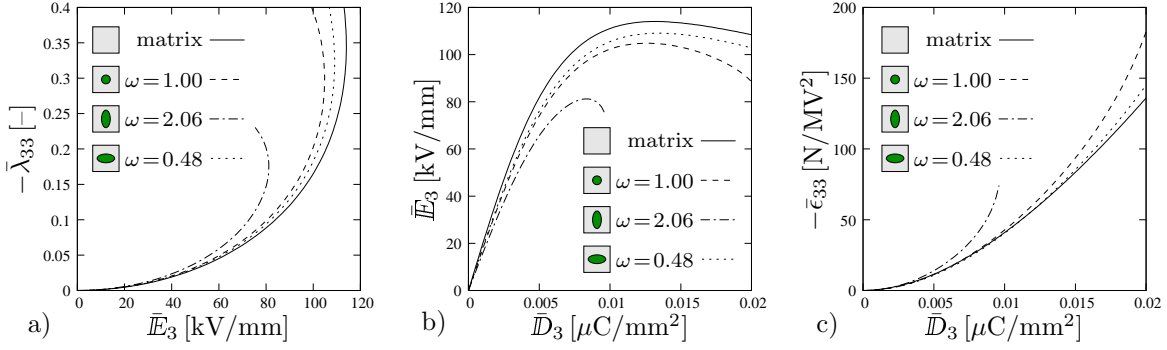


Figure 8.3: Analysis of shape of the inclusion. a) Influence of spherical or ellipsoidal shape of the inclusion on electro-mechanical response. b) Applied electric induction versus the resultant electric field showing a limit point followed by a decrease of the electric field. This limit point is usually denoted as the point of *electro-mechanical instability*. c) Increase in dielectric constant $\bar{\epsilon}_{33}$ for needle-shaped inclusions which are pronounced in the direction of the applied load.

nents of the generalized macro-stress are prescribed as zero and the remaining generalized deformations and electric field are determined. Figure 8.3 shows the results for such a scenario. The actuation curves comparing electric field and negative stretch in direction of the macro-loading are given in Figure 8.3a. The needle-shaped ellipsoidal inclusion elongated in the direction of the applied field with aspect ratio $\omega_{\pm} = 2.06$ shows a pronounced electro-active response under small fields and hence is advantageous to the pure matrix material and the other two inclusions. This increased actuation response is accompanied by an unstable behavior for smaller electric fields, that is the breakdown field decreases, see Figure 8.3b. Compared to the matrix material a volume fraction of solely 4% for the inclusion leads to a 20% smaller electric field needed to cause a compression of $\lambda_{33} = -0.16$ in z -direction. Figure 8.3c compares the increase in macroscopic dielectric constant $\bar{\epsilon}_{33}$ for the three specific shapes of the inclusion. Numerical simulations concerning the shape of the inclusion are performed in KEIP ET AL. [83]. Theoretical studies regarding the particle shape of magnetoelastic composites are given in SIBONI & PONTE CASTAÑEDA [166].

8.5.4. Material limit point analysis

The framework for local stability analysis shortly outlined in Section 8.3 is now combined with the computational homogenization scheme. In the following, the microstructure is checked by an accompanied material limit point analysis. The decoupling of the material stability criterion (8.52) demands that both purely mechanical and purely electric moduli are positive definite at each Gauss point of the discrete microstructure. For the electric part under consideration

$$-\boldsymbol{\epsilon} = -\partial_{\mathbb{E}\mathbb{E}}^2 \psi = -\partial_{\mathbb{E}\mathbb{E}}^2 \psi_{elec} = \epsilon_0 \left(1 + \frac{\chi}{J}\right) \mathbf{C}^{-1} \quad (8.69)$$

this condition is always satisfied due to the positive definiteness of the right Cauchy-Green tensor. Hence, the accompanied local stability check reduces to the analysis of the mechanical partition $\partial_{\mathbf{F}\mathbf{F}}^2 \psi$. This is performed by an eigenvalue criterion

$$\min[\lambda_i] \begin{cases} > 0 & \text{for a locally stable state,} \\ \leq 0 & \text{for a locally unstable state,} \end{cases} \quad (8.70)$$

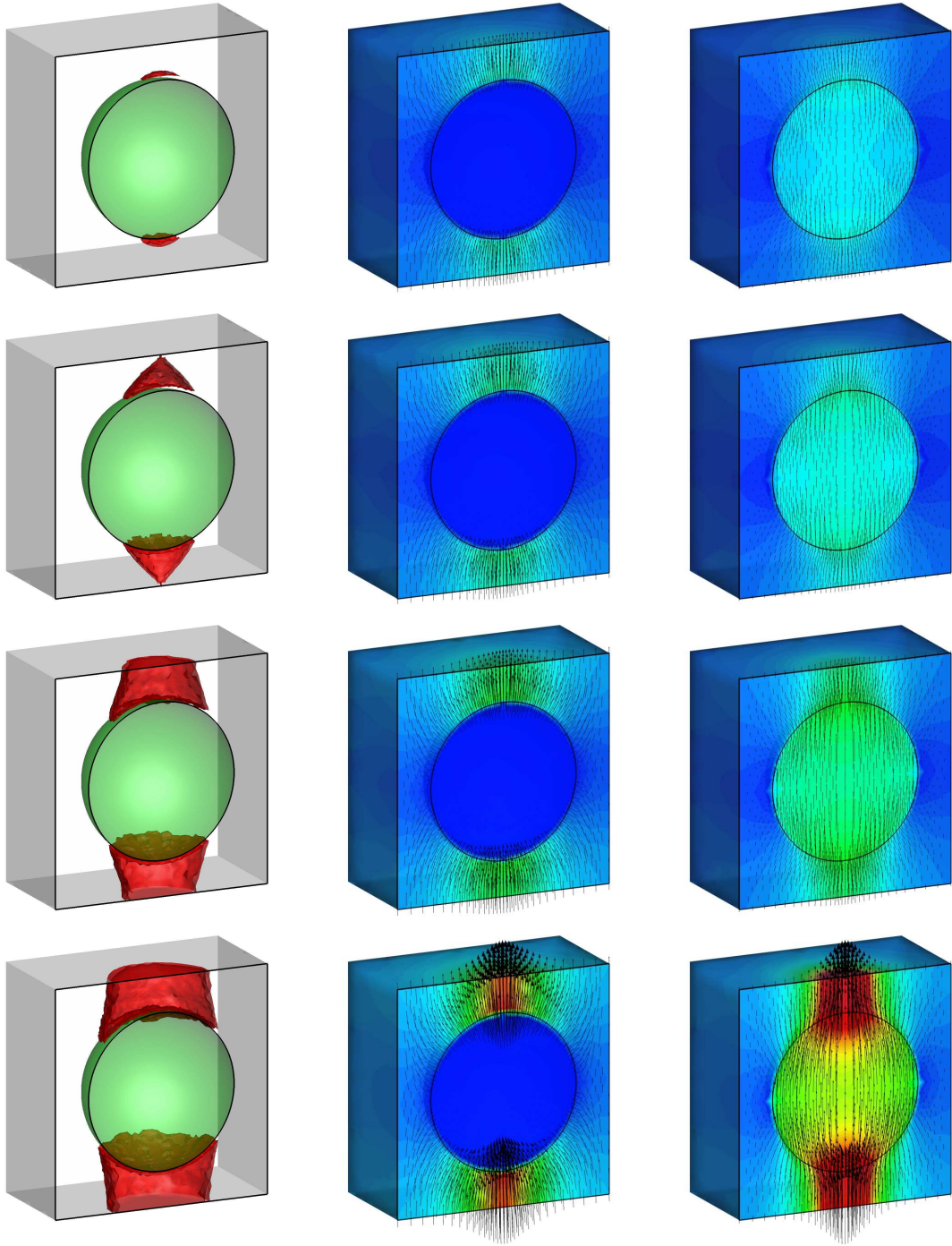


Figure 8.4: *Local material stability analysis of the microstructure.* The first column shows the development of the unstable zone in the microstructure. The red zone indicates elements with negative eigenvalue of the block diagonal stiffness matrix. The second and third column depicts the corresponding electric field E_3 and electric induction D_3 as contour plot as well as arrows.

where $\{\lambda_i\}_{i=1,9}$ are the eigenvalues of the mechanical tangent matrix. It demands a stable electro-mechanical response for positive eigenvalues. The nominal moduli as second derivative with respect to the asymmetric deformation gradient include rigid body rotations. These rotations are associated with three additional zero eigenvalues of the stiffness matrix. To get rid of them, the two-point nominal moduli are pulled-back to the reference configuration with $\mathbb{C}^{ABCD} = (F^{-1})^A_x \delta^{xa} [A_a^B D^D - \delta_{ab} S^{BD}] \delta^{yb} (F^{-1})^C_y$ in terms of

the symmetric second Piola-Kirchhoff stress $\mathbf{S} = \mathbf{F}^{-1}\mathbf{g}^{-1}\mathbf{P}$. Note that the tangent matrix is available in typical finite element implementations if Newton-Raphson schemes are applied for updates in iterative solvers.

Consider a spherical inclusion with radius $r = 10.3\ \mu\text{m}$ and volume fraction of 17% as shown in [Figure 8.1](#). To obtain a fine resolution of zones of instability within the microstructure the representative volume element is discretized by 168,368 tetrahedron finite elements. We investigate the development of unstable zones within the inhomogeneous body, where the block diagonal moduli are checked for loss of positive definiteness by determining their eigenvalues. [Figure 8.4](#) highlights unstable zones (elements) with eigenvalues smaller than zero. In the inhomogeneous case the unstable zones develop first on top and bottom of the inclusion and spread around. When observing the evolution of the electric field the tendencies of the development of instable zones are obvious. As the inclusion itself is a nearly perfect conductor, the electric field inside the inclusion tends to zero as the electric counterfield inside the inclusion negates the induced electric field (second column). Therefore, the largest electric potential difference appears at the bounding surface between the matrix and inclusion material at top and bottom of the inclusion. As a result the stiffness of the matrix material weakens most at these points and therefore material instability occurs by reaching a critical local value of the electric field. The unstable zones then follow the regions of high electric field.

Conclusion

This work was concerned with aspects of electro-mechanically coupled material models on different scales and with the development of new *variational-based homogenization techniques*. An important issue was—due to the proposed variational principles—the symmetric and compact format of the numerical implementation of the multifield problem.

The work was subdivided into three parts: [Part I](#) governed fundamentals of classical continuum mechanics and electrostatics. The main ingredients of electrostatics were provided by Coulomb’s law, Gauss’s law, and Faraday’s law formulated for the electrostatic case. The interaction of matter with electric fields was considered by additional electric force, couple, and energy supply terms within the balance equations. Furthermore, the basic principles of homogenization theory were briefly outlined such as the concept of representative volume elements and the separation of length scales hypothesis. [Part II](#) dealt with the small strain theory of *micro-electro-elasticity* describing piezoelectric ceramics. The dissipative response caused by polarization switching was described by a Ginzburg-Landau-type phase field model resolving the resultant domain structure. New rate-type and incremental *variational principles* for the coupled evolution problem were outlined and details of the micro-to-macro transition by an extended Hill-Mandel macrohomogeneity condition discussed. An important aspect for the design of a variational homogenization method was the definition of suitable boundary conditions at the micro-level, which also includes the phase field of electric polarization. The three classical types of surface conditions (Dirichlet, Neumann, periodic) were discussed and consistently transferred to the electro-mechanical context. Besides, [Part III](#) developed *finite strain material models* and bridging theorems for polymers. General equations of finite electro-elasticity in a variational format are reviewed, accounting for geometric settings in both the Lagrangian as well as the Eulerian configuration. All details of the modeling process were covered including the set up of coupled electro-mechanical tangent moduli by a numerical perturbation technique. In addition, a macroscopic FE² driver for the homogenization problem was developed, accounting for the consistent algorithmic tangent on the macroscale. Homogeneous macro-tests were performed and the relevant data transferred to the microscale via the boundary conditions. An innovative driving of the electric displacement as compared to the electric field was performed, allowing us to overcome points of electro-mechanical instability.

Bibliography

- [1] ARLT, G. [1990]: *Twinning in ferroelectric and ferroelastic ceramics: Stress relief*. Journal of Material Science, 25: 2655–2666.
- [2] ARRUDA, E. M.; BOYCE, M. C. [1993]: *A three-dimensional constitutive model for the large stretch behavior of rubber elastic materials*. Journal of the Mechanics and Physics of Solids, 41: 389–412.
- [3] BAŞAR, Y.; WEICHERT, D. [2000]: *Nonlinear Continuum Mechanics of Solids*. Springer.
- [4] BAESU, E. [2003]: *On electroacoustic energy flux*. Zeitschrift für angewandte Mathematik und Physik, 54(6): 1001–1009.
- [5] BAESU, E.; FORTUNE, D.; SOÓS, E. [2003]: *Incremental behaviour of hyperelastic dielectrics and piezoelectric crystals*. Zeitschrift für angewandte Mathematik und Physik, 54(1): 160–178.
- [6] BALL, J. M. [1977]: *Convexity conditions and existence theorems in nonlinear elasticity*. Archive of Rational Mechanics and Analysis, 63: 337–403.
- [7] BAR-COHEN, Y. [2002]: *Electro-active polymers: Current capabilities and challenges*. Proceedings of the SPIE Smart Structures and Materials Symposium, 4695-02: 1–6.
- [8] BAR-COHEN, Y.; ZHANG, Q. [2008]: *Electro-active polymer actuators and sensors*. MRS Bulletin, 33: 173–181.
- [9] BASSIOUNY, E.; MAUGIN, G. A. [1989]: *Thermodynamical formulation for coupled electromechanical hysteresis effects—III. Parameter identification*. International Journal of Engineering Science, 27(8): 975–987.
- [10] BASSIOUNY, E.; MAUGIN, G. A. [1989]: *Thermodynamical formulation for coupled electromechanical hysteresis effects—IV. Combined electromechanical loading*. International Journal of Engineering Science, 27(8): 989–1000.
- [11] BASSIOUNY, E.; GHALEB, A. F.; MAUGIN, G. A. [1988]: *Thermodynamical formulation for coupled electromechanical hysteresis effects—I. Basic equations*. International Journal of Engineering Science, 26(12): 1279–1295.
- [12] BASSIOUNY, E.; GHALEB, A. F.; MAUGIN, G. A. [1988]: *Thermodynamical formulation for coupled electromechanical hysteresis effects—II. Poling of ceramics*. International Journal of Engineering Science, 26(12): 1297–1306.
- [13] BENSOUSSAN, A.; LIONS, J. L.; PAPANICOLAOU, G. [1978]: *Asymptotic analysis for periodic structures*. In Lions, J. L.; Papanicolaou, G.; Rockafellar, R. T. (Editors), *Studies in Mathematics and its Applications*, Vol. 5. North-Holland Publishing Company.
- [14] BERDICHEVSKY, V. L. [2009]: *Variational Principles of Continuum Mechanics: II*.

- Applications*. Interaction of Mechanics and Mathematics. Springer-Verlag.
- [15] BERTOLDI, K.; BOYCE, M. C. [2008]: *Wave propagation and instabilities in monolithic and periodically structured elastomeric materials undergoing large deformations*. Physical Review B, 78(18): 184107.
- [16] BERTOLDI, K.; GEI, M. [2011]: *Instabilities in multilayered soft dielectrics*. Journal of the Mechanics and Physics of Solids, 59: 18–42.
- [17] BHATTACHARYA, K.; RAVICHANDRAN, G. [2003]: *Ferroelectric perovskites for electromechanical actuation*. Acta Materialia, 51: 5941–5960.
- [18] BIOT, M. A. [1965]: *Mechanics of incremental deformations*. John Wiley & Sons.
- [19] BISEGNA, P.; LUCIANO, R. [1996]: *Variational bounds for the overall properties of piezoelectric composites*. Journal of the Mechanics and Physics of Solids, 44(4): 583–602.
- [20] BISEGNA, P.; LUCIANO, R. [1997]: *On methods for bounding the overall properties of periodic piezoelectric fibrous composites*. Journal of the Mechanics and Physics of Solids, 45(8): 1329–1356.
- [21] BISHOP, J. F. W.; HILL, R. [1951]: *A theory of the plastic distortion of a polycrystalline aggregate under combined stresses*. Philosophical Magazine, 42: 414–427.
- [22] BISHOP, J. F. W.; HILL, R. [1951]: *A theoretical derivation of the plastic properties of a polycrystalline face-center metal*. Philosophical Magazine, 42: 1298–1307.
- [23] BOYCE, M. C.; ARRUDA, E. M. [2000]: *Constitutive models of rubber elasticity: A review*. Rubber Chemistry and Technology, 73: 504–523.
- [24] BRASSART, L.; STAINIER, L.; DOGHRI, I.; DELANNAY, L. [2011]: *A variational formulation for the incremental homogenization of elasto-plastic composites*. Journal of the Mechanics and Physics of Solids, 59(12): 2455–2475.
- [25] BROWN, JR., W. F. [1966]: *Magnetoelastic Interactions*, Vol. 9 of *Tracts in Natural Philosophy*. Springer-Verlag.
- [26] BUDIANSKY, B. [1965]: *On the elastic moduli of some heterogeneous materials*. Journal of the Mechanics and Physics of Solids, 13: 223–227.
- [27] BURYACHENKO, V. A. [2007]: *Micromechanics of Heterogeneous Materials*. Springer-Verlag.
- [28] CAO, W.; CROSS, L. E. [1991]: *Theory of tetragonal twin structures in ferroelectric perovskites with a first-order phase transition*. Physical Review B, 44(1): 5–12.
- [29] CARPI, F.; SMELA, E. [2009]: *Biomedical Applications of Electroactive Polymer Actuators*. John Wiley & Sons.
- [30] CHATZIGEORGIOU, G.; JAVILI, A.; STEINMANN, P. [2014]: *Unified magnetomechanical homogenization framework with application to magnetorheological elastomers*. Mathematics and Mechanics of Solids, 19: 193–211.
- [31] CHEN, W.; LYNCH, C. S. [1998]: *A micro-electro-mechanical model for polarization switching of ferroelectric materials*. Acta Materialia, 46(15): 5303–5311.
- [32] CHOUDHURY, S.; LI, Y. L.; KRILL III, C.; CHEN, L. Q. [2007]: *Effect of grain orientation and grain size on ferroelectric domain switching and evolution: Phase field simulations*. Acta Materialia, 55: 1415–1426.
- [33] CLIFTON, R. J. [1972]: *On the equivalence of $\mathbf{F}^e \mathbf{F}^p$ and $\mathbf{F}^p \mathbf{F}^e$* . Journal of Applied Mechanics, 39: 287–289.
- [34] DAMJANOVIC, D. [1998]: *Ferroelectric, dielectric and piezoelectric properties of ferroelectric thin films and ceramics*. Reports on Progress in Physics, 61: 1267–1324.

- [35] DESIMONE, A. [1993]: *Energy minimizers for large ferromagnetic bodies*. Archive for Rational Mechanics and Analysis, 125: 99–143.
- [36] DESIMONE, A.; JAMES, R. D. [2002]: *A constrained theory of magnetoelasticity*. Journal of the Mechanics and Physics of Solids, 50: 283–320.
- [37] DESIMONE, A.; KOHN, R. V.; MÜLLER, S.; OTTO, F. [2004]: *Recent analytical developments in micromagnetics*. Technical report, Max-Planck-Institut für Mathematik in den Naturwissenschaften, Leipzig.
- [38] DEVONSHIRE, A. F. [1949]: *XCVI. Theory of barium titanate – Part I*. Philosophical Magazine Series 7, 40(309): 1040–1063.
- [39] DEVONSHIRE, A. F. [1954]: *Theory of ferroelectrics*. Advances in Physics, 3: 86–130.
- [40] DOI, M.; EDWARDS, S. F. [1986]: *The Theory of Polymer Dynamics*. Clarendon Press.
- [41] DORFMANN, A.; OGDEN, R. W. [2005]: *Nonlinear electroelasticity*. Acta Mechanica, 174: 167–183.
- [42] ERINGEN, A. C. [1963]: *On the foundations of electroelastostatics*. International Journal of Engineering Science, 1(1): 127–153.
- [43] ERINGEN, A. C.; MAUGIN, G. A. [1990]: *Electrodynamics of Continua I: Foundations and Solid Media*. Springer-Verlag.
- [44] ERINGEN, A. C.; MAUGIN, G. A. [1990]: *Electrodynamics of Continua II: Fluid and Complex Media*. Springer-Verlag.
- [45] ESHELBY, J. D. [1957]: *The determination of the elastic field of an ellipsoidal inclusion and related problems*. Proceedings of the Royal Society of London (Serie A), 241: 367–396.
- [46] FEYEL, F.; CHABOCHE, J.-L. [2000]: *FE² multiscale approach for modelling the elastoviscoplastic behaviour of long fibre SiC/Ti composite materials*. Computer Methods in Applied Mechanics and Engineering, 183: 309–330.
- [47] FLORY, P. J. [1989]: *Statistical Mechanics of Chain Molecules*. Clarendon Press.
- [48] FRIED, E.; GURTIN, M. E. [1993]: *Continuum theory of thermally induced phase transitions based on an order parameter*. Physica D, 68: 326–343.
- [49] FRIED, E.; GURTIN, M. E. [1994]: *Dynamic solid-solid transitions with phase characterized by an order parameter*. Physica D, 72: 287–308.
- [50] GEERS, M. G. D.; KOUZNETSOVA, V. G.; BREKELMANS, W. A. M. [2010]: *Multi-scale computational homogenization: Trends and challenges*. Journal of Computational and Applied Mathematics, 234: 2175–2182.
- [51] GOSH, S.; LEE, K.; MOORTHY, S. [1996]: *Two-scale analysis of heterogeneous elastic-plastic materials with asymptotic homogenization and voronoi cell finite element model*. Computer Methods in Applied Mechanics and Engineering, 132: 63–116.
- [52] GRIFFITHS, D. J. [2012]: *Introduction to Electrodynamics*. Addison-Wesley, 4th Edition.
- [53] GURTIN, M. E. [1981]: *An Introduction to Continuum Mechanics*, Vol. 158 of *Mathematics in Science and Engineering*. Academic Press.
- [54] GURTIN, M. E. [1996]: *Generalized Ginzburg-Landau and Cahn-Hilliard equations based on a microforce balance*. Physica D, 92: 178–192.
- [55] GURTIN, M. E.; FRIED, E.; ANAND, L. [2010]: *The Mechanics and Thermodynamics of Continua*. Cambridge University Press.

- [56] HASHIN, Z. [1983]: *Analysis of composite materials – A survey*. ASME Journal of Applied Mechanics, 50: 481–505.
- [57] HASHIN, Z.; SHTRIKMAN, S. [1962]: *On some variational principles in anisotropic and nonhomogeneous elasticity*. Journal of the Mechanics and Physics of Solids, 10: 335–342.
- [58] HASHIN, Z.; SHTRIKMAN, S. [1963]: *A variational approach to the theory of the elastic behaviour of multiphase materials*. Journal of the Mechanics and Physics of Solids, 11: 127–140.
- [59] HAUPT, P. [2002]: *Continuum Mechanics and Theory of Materials*. Springer.
- [60] HILL, R. [1952]: *The elastic behaviour of a crystalline aggregate*. Proceedings of the Physical Society A, 65: 349–354.
- [61] HILL, R. [1957]: *On uniqueness and stability in the theory of finite elastic strains*. Journal of the Mechanics and Physics of Solids, 5: 229–241.
- [62] HILL, R. [1962]: *Acceleration waves in solids*. Journal of the Mechanics and Physics of Solids, 10: 1–16.
- [63] HILL, R. [1963]: *Elastic properties of reinforced solids: Some theoretical principles*. Journal of the Mechanics and Physics of Solids, 11: 357–372.
- [64] HILL, R. [1965]: *A self-consistent mechanics of composite materials*. Journal of the Mechanics and Physics of Solids, 13: 213–222.
- [65] HILL, R. [1972]: *On constitutive macro-variables for heterogeneous solids at finite strain*. Proceedings of the Royal Society of London (Series A), 326: 131–147.
- [66] HILL, R. [1984]: *On macroscopic effects of heterogeneity in elastoplastic media at finite strain*. Mathematical Proceedings of the Cambridge Philosophical Society, 95(3): 481–494.
- [67] HOLZAPFEL, G. A. [2000]: *Nonlinear solid mechanics*. John Wiley & Sons.
- [68] HU, H.-L.; CHEN, L.-Q. [1998]: *Three-dimensional computer simulation of ferroelectric domain formation*. Journal of the American Ceramic Society, 81(3): 492–500.
- [69] HUANG, C.; ZHANG, Q. M.; SU, J. [2003]: *High-dielectric-constant all-polymer percolative composites*. Applied Physics Letters, 82: 3502–3504.
- [70] HUANG, C.; ZHANG, Q. M.; DEBOTTON, G.; BHATTACHARYA, K. [2004]: *All-organic dielectric-percolative three-component composite materials with high electromechanical response*. Applied Physics Letters, 84(22): 4391–4393.
- [71] HUBER, J. E.; FLECK, N. A. [2001]: *Multi-axial electrical switching of a ferroelectric: Theory versus experiment*. Journal of Mechanics and Physics of Solids, 49: 785–811.
- [72] HUBER, J. E.; FLECK, N. A.; LANDIS, C. M.; McMEEKING, R. M. [1999]: *A constitutive model for ferroelectric polycrystals*. Journal of the Mechanics and Physics of Solids, 47: 1663–1697.
- [73] HWANG, S. C.; LYNCH, C. S.; McMEEKING, R. M. [1995]: *Ferroelectric/ferroelastic interactions and a polarization switching model*. Acta Metallurgica et Materialia, 43(5): 2073–2084.
- [74] IRODOV, I. E. [1986]: *Basic laws of electromagnetism*. CBS Publishers & Distributors.
- [75] JACKSON, J. D. [1999]: *Classical Electrodynamics*. John Wiley & Sons, 3rd Edition.
- [76] JAFFE, B.; COOK, W. R.; JAFFE, H. [1971]: *Piezoelectric Ceramics*. Academic Press.

- [77] JAMES, H. M.; GUTH, E. [1943]: *Theory of elastic properties of rubber*. The Journal of Chemical Physics, 11: 455–481.
- [78] JAMES, R. D.; KINDERLEHRER, D. [1990]: *Frustration in ferromagnetic materials*. Continuum Mechanics and Thermodynamics, 2: 215–239.
- [79] JAVILI, A.; CHATZIGEORGIOU, G.; STEINMANN, P. [2013]: *Computational homogenization in magneto-mechanics*. International Journal of Solids and Structures, 50(25–26): 4197–4216.
- [80] JIMÉNEZ, S. M. A.; MCMEECKING, R. M. [2013]: *Deformation dependent dielectric permittivity and its effect on actuator performance and stability*. International Journal of Non-Linear Mechanics, 57: 183–191.
- [81] KAMLAH, M. [2001]: *Ferroelectric and ferroelastic piezoceramics – Modelling of electromechanical hysteresis phenomena*. Continuum Mechanics and Thermodynamics, 13: 219–268.
- [82] KANOUTÉ, P.; BOSO, D. P.; CHABOCHE, J. L.; SCHREFLER, B. A. [2009]: *Multiscale methods for composites: A review*. Archives of Computational Methods in Engineering, 16(1): 31–75.
- [83] KEIP, M.-A.; STEINMANN, P.; SCHRÖDER, J. [2014]: *Two-scale computational homogenization of electro-elasticity at finite strains*. Computer Methods in Applied Mechanics and Engineering, 278: 62–79.
- [84] KHALAQUZZAMAN, M.; XU, B.-X.; RICKER, S.; MÜLLER, R. [2012]: *Computational homogenization of piezoelectric materials using FE^2 to determine configurational forces*. Technische Mechanik, 32(1): 21–37.
- [85] KLINKEL, S. [2006]: *A phenomenological constitutive model for ferroelastic and ferroelectric hysteresis effects in ferroelectric ceramics*. International Journal of Solids and Structures, 43: 7197–7222.
- [86] KOFOD, G.; SOMMER-LARSEN, P.; KORNBLUH, R.; PELRINE, R. [2003]: *Actuation response of polyacrylate dielectric elastomers*. Journal of Intelligent Material Systems and Structures, 14: 787–793.
- [87] KONTOSOS, A.; LANDIS, C. M. [2009]: *Computational modeling of domain wall interactions with dislocations in ferroelectric crystals*. International Journal of Solids and Structures, 46: 1491–1498.
- [88] KONTOSOS, A.; LANDIS, C. M. [2010]: *Phase-field modeling of domain structure energetics and evolution in ferroelectric thin films*. Journal of Applied Mechanics, 77: 041014.
- [89] KORNBLUH, R.; PELRINE, R.; JOSEPH, J. [1995]: *Elastomeric dielectric artificial muscle actuators for small robots*. Proceedings of the Materials Research Society.
- [90] KORNBLUH, R.; PELRINE, R.; JOSEPH, J.; HEYDT, R.; PEI, Q.; CHIBA, S. [1999]: *High-field electrostriction of elastomeric polymer dielectrics for actuation*. Proceedings of the SPIE: Smart Structures and Materials, 3669: 149–161.
- [91] KOUZNETSOVA, V. [2002]: *Computational homogenization for the multi-scale analysis of multi-phase materials*. Ph.D. Thesis, Institute of Mechanics of Materials, TU Eindhoven.
- [92] KOUZNETSOVA, V.; GEERS, M. G. D.; BREKELMANS, W. A. M. [2002]: *Multiscale constitutive modelling of heterogeneous materials with a gradient-enhanced computational homogenization scheme*. International Journal for Numerical Methods in Engineering, 54: 1235–1260.
- [93] KOUZNETSOVA, V. G.; GEERS, M. G. D.; BREKELMANS, W. A. M. [2004]:

- Multi-scale second-order computational homogenization of multi-phase materials: A nested finite element solution strategy.* Computer Methods in Applied Mechanics and Engineering, 193: 5525–5550.
- [94] KOVETZ, A. [2000]: *Electromagnetic Theory*. Oxford University Press.
- [95] KRÖNER, E. [1960]: *Allgemeine Kontinuumstheorie der Versetzungen und Eigenspannungen*. Archive for Rational Mechanics and Analysis, 4: 273–334.
- [96] KUHN, W. [1934]: *Über die Gestalt fadenförmiger Moleküle in Lösungen*. Kolloid-Zeitschrift, 68: 2–15.
- [97] KUHN, W. [1936]: *Beziehungen zwischen Molekülgröße, statistischer Molekülgestalt und elastischen Eigenschaften hochpolymerer Stoffe*. Kolloid-Zeitschrift, 76: 258–271.
- [98] KUHN, W.; GRÜN, F. [1942]: *Beziehungen zwischen elastischen Konstanten und Dehnungsdoppelbrechung hochelastischer Stoffe*. Kolloid Zeitschrift, 101: 248–271.
- [99] LAHELLEC, N.; SUQUET, P. [2007]: *On the effective behavior of nonlinear inelastic composites: I. Incremental variational principles*. Journal of the Mechanics and Physics of Solids, 55(9): 1932–1963.
- [100] LANDAU, L. D.; LIFSHITZ, E. M. [1935]: *On the theory of the dispersion of magnetic permeability in ferromagnetic bodies*. Physikalische Zeitschrift der Sowjetunion, 8: 153–169.
- [101] LANDAU, L. D.; LIFSHITZ, E. M. [1960]: *Electrodynamics of Continuous Media*. Pergamon Press.
- [102] LANDIS, C. M. [2002]: *Fully coupled, multi-axial, symmetric constitutive laws for polycrystalline ferroelectric ceramics*. Journal of Mechanics and Physics of Solids, 50: 127–152.
- [103] LANDIS, C. M. [2004]: *Non-linear constitutive modelling of ferroelectrics*. Current Opinion in Solid State and Materials Science, 8: 59–69.
- [104] LEE, E. H. [1969]: *Elastic-plastic deformation at finite strains*. Journal of Applied Mechanics, ASME, 36: 1–6.
- [105] LINES, M. E.; GLASS, A. M. [1977]: *Principles and Applications of Ferroelectrics and Related Materials*. Clarendon Press.
- [106] LIU, Y.; LIU, L.; YU, K.; SUN, S.; LENG, J. [2009]: *An investigation on electromechanical stability of dielectric elastomers undergoing large deformation*. Smart Materials and Structures, 18: 095040.
- [107] LYNCH, C. S. [1996]: *The effect of uniaxial stress on the electro-mechanical response of 8/65/35 PLZT*. Acta Materialia, 44(10): 4137–4148.
- [108] MANDEL, J. [1972]: *Plasticité classique et viscoplasticité*. In *CISM Courses and Lectures No. 97*. Springer-Verlag.
- [109] MARSDEN, J. E.; HUGHES, T. J. R. [1983]: *Mathematical foundations of elasticity*. Prentice-Hall.
- [110] MAUGIN, G. A. [1988]: *Continuum Mechanics of Electromagnetic Solids*. Elsevier.
- [111] MAUGIN, G. A.; ERINGEN, A. C. [1977]: *On the equations of the electrodynamics of deformable bodies of finite extent*. Journal de Mécanique, 16: 101–147.
- [112] McMEEKING, R. M.; LANDIS, C. M. [2002]: *A phenomenological multi-axial constitutive law for switching in polycrystalline ferroelectric ceramics*. International Journal of Engineering Science, 40: 1553–1577.
- [113] McMEEKING, R. M.; LANDIS, C. M. [2005]: *Electrostatic forces and stored energy for deformable dielectric materials*. Journal of Applied Physics, 72: 581–590.

- [114] MICHEL, J. C.; MOULINEC, H.; SUQUET, P. [1999]: *Effective properties of composite materials with periodic microstructure: A computational approach*. Computer Methods in Applied Mechanics and Engineering, 172: 109–143.
- [115] MIEHE, C. [1996]: *Numerical computation of algorithmic (consistent) tangent moduli in large-strain computational inelasticity*. Computer Methods in Applied Mechanics and Engineering, 134: 223–240.
- [116] MIEHE, C. [2002]: *Strain-driven homogenization of inelastic microstructures and composites based on an incremental variational formulation*. International Journal for Numerical Methods in Engineering, 55: 1285–1322.
- [117] MIEHE, C. [2003]: *Computational micro-to-macro transitions of discretized microstructures of heterogeneous materials at finite strains based on the minimization of averaged incremental energy*. Computer Methods in Applied Mechanics and Engineering, 192: 559–591.
- [118] MIEHE, C. [2011]: *A multi-field incremental variational framework for gradient-type standard dissipative solids*. Journal of Mechanics and Physics of Solids, 59(4): 898–923.
- [119] MIEHE, C. [2013]: *Geometrical methods of nonlinear continuum mechanics and continuum thermodynamics*. Lecture Notes.
- [120] MIEHE, C. [2014]: *Theoretical and computer-oriented material theory*. Lecture Notes.
- [121] MIEHE, C.; BAYREUTHER, C. G. [2007]: *On multiscale fe analyses of heterogeneous structures: From homogenization to multigrid solvers*. International Journal for Numerical Methods in Engineering, 71: 1135–1180.
- [122] MIEHE, C.; LAMBRECHT, M. [2003]: *Analysis of micro-structure development in shearbands by energy relaxation of incremental stress potentials: Large-strain theory for standard dissipative materials*. International Journal for Numerical Methods in Engineering, 58: 1–41.
- [123] MIEHE, C.; ROSATO, D. [2011]: *A rate-dependent incremental variational formulation of ferroelectricity*. International Journal of Engineering Science, 49: 466–496.
- [124] MIEHE, C.; SCHRÖDER, J. [1994]: *Post-critical discontinuous localization analysis of small-strain softening elastoplastic solids*. Archive of Applied Mechanic, 64: 267–285.
- [125] MIEHE, C.; SCHOTTE, J.; SCHRÖDER, J. [1999]: *Computational micro-macro transitions and overall moduli in the analysis of polycrystals at large strains*. Computational Materials Science, 16: 372–382.
- [126] MIEHE, C.; SCHRÖDER, J.; SCHOTTE, J. [1999]: *Computational homogenization analysis in finite plasticity. Simulation of texture development in polycrystalline materials*. Computer Methods in Applied Mechanics and Engineering, 171(3–4): 387–418.
- [127] MIEHE, C.; SCHOTTE, J.; LAMBRECHT, M. [2002]: *Homogenization of inelastic solid materials at finite strains based on incremental minimization principles. application to the texture analysis of polycrystals*. Journal of the Mechanics and Physics of Solids, 50: 2123–2167.
- [128] MIEHE, C.; SCHRÖDER, J.; BECKER, M. [2002]: *Computational homogenization analysis in finite elasticity: material instabilities on the micro- and macro-scales of periodic composites and their interaction*. Computer Methods in Applied Mechanics and Engineering, 191: 4971–5005.

- [129] MIEHE, C.; GÖKTEPE, S.; LULEI, F. [2004]: *A micro-macro approach to rubber-like materials. Part I: The non-affine micro-sphere model of rubber elasticity*. Journal of the Mechanics and Physics of Solids, 52: 2617–2660.
- [130] MIEHE, C.; DETTMAR, J.; ZÄH, D. [2010]: *Homogenization and two-scale simulations of granular materials for different microstructural constraints*. International Journal for Numerical Methods in Engineering, 83: 1206–1236.
- [131] MIEHE, C.; KIEFER, B.; ROSATO, D. [2011]: *An incremental variational formulation of dissipative magnetostriction at the macroscopic continuum level*. International Journal of Solids and Structures, 48: 1846–1866.
- [132] MIEHE, C.; ROSATO, D.; KIEFER, B. [2011]: *Variational principles in dissipative electro-magneto-mechanics: A framework for the macro-modeling of functional materials*. International Journal for Numerical Methods in Engineering, 86: 1225–1276.
- [133] MIEHE, C.; ZÄH, D.; ROSATO, D. [2012]: *Variational-based modeling of micro-electro-elasticity with electric field- and stress-driven domain evolution*. International Journal for Numerical Methods in Engineering, 91(2): 115–141.
- [134] MIEHE, C.; VALLICOTTI, D.; ZÄH, D. [2015]: *Computational structural and material stability analysis in finite electro-elasto-statics of electro-active materials*. Submitted to the International Journal for Numerical Methods in Engineering.
- [135] MILLER, K. S. [1981]: *On the inverse of the sum of matrices*. Mathematics Magazine, 54(2): 67–72.
- [136] MOSCARDO, M.; ZHAO, X.; SUO, Z.; LAPUSTA, Y. [2008]: *On designing dielectric elastomer actuators*. Journal of Applied Physics, 104: 093503.
- [137] MOULINEC, H.; SUQUET, P. [1998]: *A numerical method for computing the overall response of nonlinear composites with complex microstructure*. Computer Methods in Applied Mechanics and Engineering, 157: 69–94.
- [138] MOULSON, A. J.; HERBERT, J. M. [2003]: *Electroceramics: Materials, Properties, Applications*. John Wiley & Sons, 2nd Edition.
- [139] NEMAT-NASSER, S. [1999]: *Averaging theorems in finite deformation plasticity*. Mechanics of Materials, 31: 493–523.
- [140] NEMAT-NASSER, S.; HORI, M. [1999]: *Micromechanics: Overall properties of heterogeneous materials*, Vol. 36 of *North-Holland series in Applied Mathematics and Mechanics*. Elsevier Science Publisher B. V., 2nd Edition.
- [141] OGDEN, R. W. [1972]: *Large deformation isotropic elasticity: On the correlation of theory and experiment for incompressible rubberlike solids*. Proceedings of the Royal Society London A, 326: 565–584.
- [142] OGDEN, R. W. [1984]: *Nonlinear Elastic Deformations*. John Wiley & Sons.
- [143] PAO, Y.-H.; HUTTER, K. [1975]: *Electrodynamics for moving elastic solids and viscous fluids*. Proceedings of the IEEE, 63: 1011–1021.
- [144] PELRINE, R.; KORNBLUH, R. D.; JOSEPH, J. [1998]: *Electrostriction of polymer dielectrics with compliant electrodes as a means of actuation*. Sensors and Actuators A: Physical, 64: 77–85.
- [145] PELRINE, R.; KORNBLUH, R.; JOSEPH, J.; HEYDT, R.; PEI, Q.; CHIBA, S. [2000]: *High-field deformation of elastomeric dielectrics for actuators*. Materials Science and Engineering: C, 11(2): 89–100.
- [146] PENFIELD, P.; HAUS, H. A. [1967]: *Electrodynamics of Moving Media*. M.I.T. Press.
- [147] PFLÜGER, A. [1974]: *Stabilitätsprobleme der Elastostatik*. Springer.

- [148] PLANTE, J.-S.; DUBOWSKY, S. [2006]: *Large-scale failure modes of dielectric elastomer actuators*. International Journal of Solids and Structures, 43: 7727–7751.
- [149] PONTE CASTAÑEDA, P. [1991]: *The effective mechanical properties of nonlinear isotropic composites*. Journal of the Mechanics and Physics of Solids, 39: 45–71.
- [150] PONTE CASTAÑEDA, P. [1992]: *New variational principles in plasticity and their application to composite materials*. Journal of the Mechanics and Physics of Solids, 40: 1757–1788.
- [151] PONTE CASTAÑEDA, P.; SIBONI, M. H. [2012]: *A finite-strain constitutive theory for electro-active polymer composites via homogenization*. International Journal of Non-Linear Mechanics, 47: 293–306.
- [152] PONTE CASTAÑEDA, P.; SUQUET, P. [1997]: *Nonlinear composites*. Vol. 34 of *Advances in Applied Mechanics*, pp. 171–302. Elsevier.
- [153] REUSS, A. [1929]: *Berechnung der Fließgrenze von Mischkristallen aufgrund der Plastizitätsbedingung für Einkristalle*. Zeitschrift für angewandte Mathematik und Mechanik, 9: 49–58.
- [154] ROSATO, D. [2010]: *On the Formulation and Numerical Implementation of Dissipative Electro-Mechanics at Large Strains*. Ph.D. Thesis, Institute of Applied Mechanics (CE), Chair I, University of Stuttgart.
- [155] ROSATO, D.; MIEHE, C. [2009]: *On the formulation and numerical implementation of dissipative electro-mechanics at large strains*. Proceedings in Applied Mathematics and Mechanics, 9: 343–344.
- [156] ROSATO, D.; MIEHE, C. [2014]: *Dissipative ferroelectricity at finite strains. variational principles, constitutive assumptions and algorithms*. International Journal of Engineering Science, 74: 163–189.
- [157] SANCHEZ-PALENCIA, E. [1980]: *Non-Homogeneous Media and Vibration Theory*, Vol. 127 of *Lecture Notes in Physics*. Springer-Verlag.
- [158] SCHRADE, D.; MÜLLER, R.; GROSS, D.; UTSCHIG, T.; SHUR, V. Y.; LUPASCU, D. C. [2007]: *Interaction of domain walls with defects in ferroelectric materials*. Mechanics of Materials, 39: 161–174.
- [159] SCHRADE, D.; MÜLLER, R.; XU, B. X.; GROSS, D. [2007]: *Domain evolution in ferroelectric materials: A continuum phase field model and finite element implementation*. Computer Methods in Applied Mechanics and Engineering, 196: 4365–4374.
- [160] SCHRÖDER, J. [2000]: *Homogenisierungsmethoden der nichtlinearen Kontinuumsmechanik unter Beachtung von Stabilitätsproblemen*. Habilitationsschrift, Institut für Mechanik (Bauwesen), Lehrstuhl, I, Universität Stuttgart. Bericht Nr. I-7.
- [161] SCHRÖDER, J. [2009]: *Derivation of the localization and homogenization conditions for electro-mechanically coupled problems*. Computational Materials Science, 46: 595–599.
- [162] SCHRÖDER, J.; KEIP, M.-A. [2012]: *Two-scale homogenization of electromechanically coupled boundary value problems*. Computational Mechanics, 50(2): 229–244.
- [163] SCHRÖDER, J.; ROMANOWSKI, H. [2005]: *A thermodynamically consistent mesoscopic model for transversely isotropic ferroelectric ceramics in a coordinate-invariant setting*. Archive of Applied Mechanics, 74: 863–877.
- [164] SEGURADO, J.; LLORCA, J. [2002]: *A numerical approximation to the elastic properties of sphere-reinforced composites*. Journal of the Mechanics and Physics of Solids, 50(10): 2107–2121.

- [165] SHU, Y. C.; BHATTACHARYA, K. [2001]: *Domain patterns and macroscopic behaviour of ferroelectric materials*. Philosophical Magazine B, 81(12): 2021–2054.
- [166] SIBONI, M. H.; PONTE CASTAÑEDA, P. [2012]: *A magnetically anisotropic, ellipsoidal inclusion subjected to a non-aligned magnetic field in an elastic medium*. Comptes Rendus Mécanique, 340(4–5).
- [167] SKATULLA, S.; SANSOUR, C.; AROCKIARAJAN, A. [2012]: *A multiplicative approach for nonlinear electro-elasticity*. Computer Methods in Applied Mechanics and Engineering, 245–246: 243–255.
- [168] SMIT, R. J. M.; BREKELMANS, W. A. M.; MEIJER, H. E. H. [1998]: *Prediction of the mechanical behavior of nonlinear heterogeneous systems by multi-level element modeling*. Computer Methods in Applied Mechanics and Engineering, 155: 181–192.
- [169] SMITH, R. [2005]: *Smart Material Systems: Model Development*. SIAM, Society for Industrial and Applied Mathematics.
- [170] STEINMANN, P.; VU, D. K. [2012]: *Computational challenges in the simulation of nonlinear electroelasticity*. Computer Assisted Methods in Engineering and Science, 19: 199–212.
- [171] SU, J.; HARRISON, J. S.; CLAIR, T. L.; BAR-COHEN, Y.; LEARY, S. [1999]: *Electrostrictive graft elastomers and applications*. Materials Research Society Proceedings, 600: 131–136.
- [172] SU, J.; OUNAIES, Z.; HARRISON, J. S. [1999]: *Ferroelectric and piezoelectric properties of blends of poly(vinylidene fluoride trifluoroethylene) and a graft elastomer*. Materials Research Society Proceedings, 600: 95–100.
- [173] SU, J.; HARRISON, J. S.; ST. CLAIR, T. L. [2003]: *Electrostrictive graft elastomers*. United States Patent, US 6,515,077 B1.
- [174] SU, Y.; LANDIS, C. M. [2007]: *Continuum thermodynamics of ferroelectric domain evolution: Theory, finite element implementation, and application to domain wall pinning*. Journal of the Mechanics and Physics of Solids, 55: 280–305.
- [175] SUN, C.; WANG, Y.; ZHANG, C.; ZHOU, E.; SU, J. [2008]: *A modified self-consistent computational model for an electrostrictive graft elastomer*. Smart Materials and Structures, 17: 025007.
- [176] SUO, Z.; ZHAO, X.; GREENE, W. H. [2008]: *A nonlinear field theory of deformable dielectrics*. Journal of the Mechanics and Physics of Solids, 56: 467–486.
- [177] SUQUET, P. M. [1987]: *Elements of homogenization for inelastic solid mechanics*. In Sanchez-Palenzia, E.; Zaoui, A. (Editors), *Lecture Notes in Physics: Homogenization Techniques for Composite Materials*, pp. 193–278. Springer-Verlag.
- [178] SUQUET, P. M. [1993]: *Overall potential and extremal surfaces of power law or ideal plastic materials*. Journal of the Mechanics and Physics of Solids, 41: 981–1002.
- [179] SWAN, C. C. [1994]: *Techniques for stress- and strain-controlled homogenization of inelastic periodic composites*. Computer Methods in Applied Mechanics and Engineering, 117: 249–267.
- [180] TALBOT, D. R. S.; WILLIS, J. R. [1985]: *Variational principles for nonlinear inhomogeneous media*. IMA Journal of Applied Mathematics, 35: 39–54.
- [181] TALBOT, D. R. S.; WILLIS, J. R. [1987]: *Bounds and self-consistent estimates for the overall properties of nonlinear composites*. IMA Journal of Applied Mathematics, 39: 215–240.
- [182] TALBOT, D. R. S.; WILLIS, J. R. [1992]: *Some explicit bounds for the overall behaviour of nonlinear composites*. International Journal of Solids and Structures,

- 29: 1981–1987.
- [183] TERADA, K.; KIKUCHI, T. [2001]: *A class of general algorithms for multi-scale analyses of heterogeneous media*. Computer Methods in Applied Mechanics and Engineering, 190: 5427–5464.
- [184] TERADA, K.; HORI, M.; KYOYA, T.; KIKUCHI, N. [2000]: *Simulation of the multi-scale convergence in computational homogenization approaches*. International Journal of Solids and Structures, 37(16): 2285–2311.
- [185] THOMPSON, J. M. T.; HUNT, G. W. [1973]: *A general theory of elastic stability*. Wiley.
- [186] THYLANDER, S.; MENZEL, A.; RISTINMAA, M. [2012]: *An electromechanically coupled micro-sphere framework: application to the finite element analysis of electrostrictive polymers*. Smart Materials and Structures, 21.
- [187] TIERSTEN, H. F. [1971]: *On the nonlinear equations of thermo-electroelasticity*. International Journal of Engineering Science, 9(7): 587–604.
- [188] TOLAND, J. F.; WILLIS, J. R. [1989]: *Duality for families of natural variational principles in nonlinear electrostatics*. SIAM Journal on Mathematical Analysis, 20(6): 1283–1292.
- [189] TOUPIN, R. [1960]: *Stress tensors in elastic dielectrics*. Archive for Rational Mechanics and Analysis, 5: 440–452.
- [190] TOUPIN, R. A. [1956]: *The elastic dielectric*. Journal of Rational Mechanics and Analysis, 5(6): 849–915.
- [191] TRELOAR, L. R. G. [1954]: *The photoelastic properties of short-chain molecular networks*. Transactions of the Faraday Society, 50: 881–896.
- [192] TRELOAR, L. R. G. [1975]: *The Physics of Rubber Elasticity*. Clarendon Press, 3rd Edition.
- [193] TRELOAR, L. R. G.; RIDING, G. [1979]: *A non-Gaussian theory of rubber in biaxial strain. I. Mechanical properties*. Proceedings of the Royal Society London A, 369: 261–280.
- [194] TRUESDELL, C.; NOLL, W. [1965]: *The nonlinear field theories of mechanics*. In Fluegge, S. (Editor), *Handbuch der Physik Bd. III/3*. Springer-Verlag.
- [195] VOIGT, W. [1887]: *Über die Beziehung zwischen den beiden Elastizitätskonstanten isotroper Körper*. Annalen der Physik, 38: 573–587.
- [196] VU, D. K.; STEINMANN, P. [2007]: *Nonlinear electro- and magneto-elastostatics: Material and spatial settings*. Technical report, Chair of Applied Mechanics, University of Kaiserslautern.
- [197] VU, D. K.; STEINMANN, P.; POSSART, G. [2007]: *Numerical modelling of nonlinear electroelasticity*. International Journal for Numerical Methods in Engineering, 70: 685–704.
- [198] WANG, J.; KAMLAH, M. [2009]: *Three-dimensional finite element modeling of polarization switching in a ferroelectric single domain with an impermeable notch*. Smart Materials and Structures, 18(10): 104008.
- [199] WANG, J.; ZHANG, T.-Y. [2007]: *Phase field simulations of polarization switching-induced toughening in ferroelectric ceramics*. Acta Materialia, 55: 2465–2477.
- [200] WANG, J.; SHI, S.-Q.; CHEN, L.-Q.; LI, Y.; ZHANG, T.-Y. [2004]: *Phase field simulations of ferroelectric/ferroelastic polarization switching*. Acta Materialia, 52: 749–764.
- [201] WANG, Y.; SUN, C.; ZHOU, E.; SU, J. [2004]: *Deformation mechanisms of*

- electrostrictive graft elastomer*. *Smart Materials and Structures*, 13: 1407–1413.
- [202] WILLIS, J. R. [1981]: *Variational and related methods for the overall properties of composites*. *Advances in Applied Mechanics*, 21: 1–78.
- [203] WILLIS, J. R. [1986]: *Variational estimates for the overall response of an inhomogeneous nonlinear dielectric*. In Ericksen, J. L.; Kinderlehrer, D.; Kohn, R.; Lions, J.-L. (Editors), *Homogenization and Effective Moduli of Materials and Media*, pp. 247–263. Springer.
- [204] WILLIS, J. R. [1989]: *The structure of overall constitutive relations for a class of nonlinear composites*. *IMA Journal of Applied Mathematics*, 43: 231–242.
- [205] WISSLER, M.; MAZZA, E. [2007]: *Electromechanical coupling in dielectric elastomer actuators*. *Sensors and Actuators A*, 138: 384–393.
- [206] WU, P. D.; VAN DER GIESSEN, E. [1993]: *On improved network models for rubber elasticity and their applications to orientation hardening in glassy polymers*. *Journal of the Mechanics and Physics of Solids*, 41: 427–456.
- [207] ZÄH, D.; MIEHE, C. [2013]: *Computational homogenization in dissipative electro-mechanics of functional materials*. *Computer Methods in Applied Mechanics and Engineering*, 267: 487–510.
- [208] ZÄH, D.; MIEHE, C. [2015]: *Multiplicative electro-elasticity of electroactive polymers accounting for micromechanically-based network models*. Submitted to *Computer Methods in Applied Mechanics and Engineering*.
- [209] ZHANG, J. X.; LI, Y. L.; SCHLOM, D. G.; CHEN, L. Q.; ZAVALICHE, F.; RAMESH, R.; JIA, Q. X. [2007]: *Phase-field model for epitaxial ferroelectric and magnetic nanocomposite thin films*. *Applied Physics Letters*, 90: 052909.
- [210] ZHANG, W.; BHATTACHARYA, K. [2005]: *A computational model of ferroelectric domains. Part I: Model formulation and domain switching*. *Acta Materialia*, 53: 185–198.
- [211] ZHANG, W.; BHATTACHARYA, K. [2005]: *A computational model of ferroelectric domains. Part II: Grain boundaries and defect pinning*. *Acta Materialia*, 53: 199–209.
- [212] ZHANG, X. Q.; WISSLER, M.; JAEHNE, B.; BROENNIMANN, R.; KOVACS, G. [2004]: *Effects of crosslinking, prestrain, and dielectric filler on the electromechanical response of a new silicone and comparison with acrylic elastomer*. *Proceedings of SPIE*, 5385: 78–86.
- [213] ZHAO, X.; SUO, Z. [2007]: *Method to analyze electromechanical stability of dielectric elastomers*. *Applied Physics Letters*, 91: 061921.
- [214] ZHAO, X.; SUO, Z. [2008]: *Electrostriction in elastic dielectrics undergoing large deformation*. *Journal of Applied Physics*, 104(12): 123530.
- [215] ZHAO, X.; HONG, W.; SUO, Z. [2007]: *Electromechanical hysteresis and coexistent states in dielectric elastomers*. *Physical Review B*, 76: 134113.
- [216] ZHOU, D.; KAMLAH, M.; MUNZ, D. [2001]: *Rate dependence of soft PZT ceramics under electric field loading*. *Proceedings of the SPIE*, 4333: 64–70.
- [217] ZHOU, D.; KAMLAH, M.; MUNZ, D. [2005]: *Effects of bias electric fields on the non-linear ferroelastic behavior of soft lead zirconate titanate piezoceramics*. *Journal of the American Ceramic Society*, 88 (4): 867–874.
- [218] ZOHDI, T. I.; WRIGGERS, P. [2005]: *An introduction to computational micromechanics*. In Pfeiffer, F.; Wriggers, P. (Editors), *Lecture Notes in Applied and Computational Mechanics*, Vol. 20. Springer-Verlag.

In dieser Schriftenreihe bisher erschienene Berichte

- I-1 (1996) *Theoretische und algorithmische Konzepte zur phänomenologischen Beschreibung anisotropen Materialverhaltens*, J. Schröder, Dissertation, 1996.
- I-2 (1996) *Zur Theorie und Numerik finiter elastoplastischer Deformationen von Schalentragwerken*, B. Seifert, Dissertation, 1996.
- I-3 (1996) *Zur Modellierung des künstlichen Infrarot-Dichroismus in Polymerfolien bei großen Verformungen*, J. Buhler, Dissertation, 1996.
- I-4 (1998) *Verfahren zur Ermittlung der Erdbebenlasten mit Berücksichtigung des stochastischen Charakters des Bebens*, S. Zhang, Dissertation, 1998.
- I-5 (1998) *Zur Beschreibung finiter Deformationen von Polymeren: Experimente, Modellbildung, Parameteridentifikation und Finite-Elemente- Formulierung*, J. Keck, Dissertation, 1998.
- I-6 (1999) *Berechnungsverfahren instationär erregter Systeme im Frequenzbereich*, A. Jaworek, Dissertation, 1999.
- I-7 (2000) *Homogenisierungsmethoden der nichtlinearen Kontinuumsmechanik unter Beachtung von Stabilitätsproblemen*, J. Schröder, Habilitation, 2000.
- I-8 (2002) *Theorie und Numerik von Materialinstabilitäten elastoplastischer Festkörper auf der Grundlage inkrementeller Variationsformulierungen*, M. Lambrecht, Dissertation, 2002.
- I-9 (2002) *Mikromechanisch motivierte Modelle zur Beschreibung finiter Deformationen gummiartiger Polymere: physikalische Modellbildung und numerische Simulation*, F. Lulei, Dissertation, 2002.
- I-10 (2003) *Adaptive Finite-Elemente-Berechnungen der nichtlinearen Festkörpermechanik bei kleinen und großen Verzerrungen*, A. Koch, Dissertation, 2003.
- I-11 (2003) *Theorie und Numerik der Parameteridentifikation von Materialmodellen der finiten Elastizität und Inelastizität auf der Grundlage optischer Feldmeßmethoden*, G. Scheday, Dissertation, 2003.
- I-12 (2004) *Approaches to the Description of Anisotropic Material Behaviour at Finite Elastic and Plastic Deformations, Theory and Numerics*, N. Apel, Dissertation, 2004.
- I-13 (2004) *Temperaturabhängige Beschreibung visko-elasto-plastischer Deformationen kurzglasfaserverstärkter Thermoplaste: Modellbildung, Numerik und Experimente*, S. Rieger, Dissertation, 2004.
- I-14 (2005) *Zur Parameteridentifikation komplexer Materialmodelle auf der Basis realer und virtueller Testdaten*, A. Rieger, Dissertation, 2005.
- I-15 (2005) *Viskoelastisches Verhalten von Elastomeren bei finiten Verzerrungen: Experimente, Modellierung und Simulationen*, H. Zecha, Dissertation, 2005.
- I-16 (2005) *Mehrskalenmodelle in der Festkörpermechanik und Kopplung von Mehrgittermethoden mit Homogenisierungsverfahren*, C. G. Bayreuther, Dissertation, 2005.

- I-17 (2005) *Static and Dynamic Homogenization Analyses of Discrete Granular and Atomistic Structures on Different Time and Length Scales*, J. Dettmar, Dissertation, 2005.
- I-18 (2006) *Incompatibility and Instability Based Size Effects in Crystals and Composites at Finite Elastoplastic Strains*, M. Becker, Dissertation, 2006.
- I-19 (2007) *Aspects of Energy Minimization in Solid Mechanics: Evolution of Inelastic Microstructures and Crack Propagation*, E. Gürses, Dissertation, 2007.
- I-20 (2007) *Micro-Macro Approaches to Rubbery and Glassy Polymers: Predictive Micromechanically-Based Models and Simulations*, S. Göktepe, Dissertation, 2007.
- I-21 (2008) *Material Forces in Finite Inelasticity and Structural Dynamics: Topology Optimization, Mesh Refinement and Fracture*, D. Zimmermann, Dissertation, 2008.
- I-22 (2010) *Thermoviscoplasticity of Glassy Polymers: Experimental Characterization, Parameter Identification and Model Validation*, J. Méndez Diez, Dissertation, 2010.
- I-23 (2010) *On the Formulation and Numerical Implementation of Dissipative Electro-Mechanics at Large Strains*, D. Rosato, Dissertation, 2010.
- I-24 (2010) *A variational framework for gradient-extended dissipative continua: Application to damage mechanics, fracture, and plasticity*, F. Welschinger, Dissertation, 2010.
- I-25 (2013) *Variational Multifield Modeling of the Formation and Evolution of Laminate Microstructure*, F. Hildebrand, Dissertation, 2013.
- I-26 (2013) *On the Computational Modeling of Micromechanical Phenomena in Solid Materials*, C. Linder, Habilitation, 2013.
- I-27 (2013) *Hybrid Micro-Macro Modeling of Texture Evolution in Polycrystal Plasticity Based on Microstructural Reorientation Continua*, I. Zimmermann, Dissertation, 2013.
- I-28 (2014) *Finite Element based Electronic Structure Calculations*, V. Schauer, Dissertation, 2014.
- I-29 (2014) *A Thermodynamically Consistent Phase Field Approach to Fracture*, M. Hofacker, Dissertation, 2014.
- I-30 (2014) *Multi-level Description of Failure Phenomena with the Strong Discontinuity Approach*, A. Raina, Dissertation, 2014.
- I-31 (2014) *Phase Field Modeling of Fracture in Rubbery and Glassy Polymers at Finite Thermo-Viscoelastic Deformations*, L. Schänzel, Dissertation, 2014.
- I-32 (2014) *Variational Homogenization in Electro-Mechanics: From Micro-Electro-Elasticity to Electroactive Polymers*, D. Zäh, Dissertation, 2014.